KAMIL BECHTA

MODELING OF DIRECTIONAL RADIO LINKS AND THE ACCURACY OF 5G LINK BUDGET ESTIMATION

MODELOWANIE RADIOWEGO ŁĄCZA KIERUNKOWEGO A POPRAWNOŚĆ ESTYMACJI BILANSU ENERGETYCZNEGO W SYSTEMACH 5G

DOCTORAL DISSERTATION

Supervisors:

Cezary ZIÓŁKOWSKI, Ph.D. D.Sc. Eng., Prof. of MUT

Jan M. KELNER, Ph.D. D.Sc. Eng.

Warsaw 2021

Abstract

MODELING OF DIRECTIONAL RADIO LINKS AND THE ACCURACY OF 5G LINK BUDGET ESTIMATION

Author: **Kamil BECHTA, M.Sc. Eng.**

Supervisors: **Cezary ZIÓŁKOWSKI, Ph.D. D.Sc. Eng., Prof. of MUT**

Jan M. KELNER, Ph.D. D.Sc. Eng.

The main objective of this dissertation is the assessment of accuracy of 5G radio link budget estimation from the perspective of joint modelling of directional antenna beam pattern and angular spread phenomenon, due to impact of this estimation on the efficiency of 5G network planning and optimization.

First are clarified the definitions of nominal antenna pattern (as measured in anechoic chamber) and effective antenna pattern (as determined in scattering environment). Afterwards presented are simulation results of 5G network performance, which indicate significant overestimation if nominal antenna patterns are assumed during evaluation instead of effective antenna patterns. This part is concentrated on radio link budget for serving and interfering downlink (DL) signals in millimeter-wave cell and indicates methods for its accurate calculation. Additionally, a method for improvement of DL signal to interference plus noise ratio (SINR) by optimization of effective antenna pattern is proposed and evaluated. This method is based on the patented proprietary algorithm, which matches the geometry of antenna array to the azimuth and zenith angular spread in the given channel. In the consequence the effective antenna pattern, understood as a spatial filter of multipath components, is optimized and its effective antenna gain is maximized.

The next study evaluates for 5G the accuracy of methods for assessment of radio frequency (RF) electromagnetic field (EMF) exposure inherited from previous systems. It is presented that legacy methods may lead to significant overestimation of the maximum RF EMF exposure associated with 5G base station (BS) in scattering environment if nominal antenna pattern is assumed instead of effective antenna pattern. Therefore, a simple solution is proposed to improve

the accuracy of RF EMF exposure assessment, which is indicated in the latest version of standard 62232 defined by International Electrotechnical Commission (IEC). Proposed solution is based on closed-form formulas, which allow to extrapolate the maximum exposure by calculation and comparison of effective antenna gains. Obtained values of RF EMF exposure are more accurate than estimated based on nominal antenna gains and at the same time do not require comprehensive system-level simulation with 3D channel model.

By the example of Citizens Broadband Radio Service (CBRS) it is presented how the accurate modeling of antenna pattern may improve performance of radio resources distribution in spectrum sharing environment. Obtained simulation results allow to assess the accuracy of interference evaluation and channels distribution between CBRS devices (CBSD) if centralized controller for spectrum access system (SAS) does not have enough knowledge about effective antenna pattern. It is also indicated that for the assumed scenario of CBRS network implementation the mutual interference between each pair of CBSDs can be significantly underestimated, which in consequence leads to insufficient co-existence conditions, if nominal antenna pattens are used by SAS instead of effective patterns. Therefore, a proposal for improvement of standards relevant for CBRS networks is made.

The final study allows to compare different approaches for joint modeling of antenna pattern and angular spread phenomenon in scattering environment. The concept of effective antenna pattern is compared with multi-elliptical propagation model (MPM) approach. This comparison is enabled by the use of common input data. Comparable simulation results, obtained from both approaches for selected simulation scenarios, allow to conclude that MPM model ensures good accuracy without the need for full 3D channel modeling in time-consuming and computational power-consuming statistical simulations.

Findings and conclusions of all studies included in this dissertation are aligned with the thesis stated in its introduction and can be considered as a noticeable contribution to the current state of the art.

Streszczenie

MODELOWANIE RADIOWEGO ŁĄCZA KIERUNKOWEGO A POPRAWNOŚĆ ESTYMACJI BILANSU ENERGETYCZNEGO W SYSTEMACH 5G

Autor: mgr inż. Kamil BECHTA

Promotorzy: dr hab. inż. Cezary ZIÓŁKOWSKI, prof. WAT

dr hab. inż. Jan M. KELNER

Głównym celem niniejszej rozprawy jest ocena poprawności estymacji bilansu energetycznego łącza radiowego w systemach 5G z punktu widzenia wspólnego modelowania charakterystyki anteny kierunkowej i zjawiska kątowego rozproszenia mocy w kanale radiowym. Poprawność tej estymacji jest istotna ze względu na jej bezpośredni wpływ na efektywność procesu planowania i optymalizacji sieci 5G.

W pierwszej kolejności wprowadzone są definicje nominalnej charakterystyki antenowej (zmierzonej w komorze bezechowej) oraz skutecznej charakterystyki antenowej (określonej w kanale radiowym z rozproszeniami). Następnie przedstawione są wyniki symulacyjnych badań wydajności sieci 5G, które wskazują na jej znaczące przeszacowanie jeżeli skuteczne charakterystyki zostaną zastąpione podczas modelowania charakterystykami nominalnymi. Ta część analizy jest skoncentrowana na bilansie energetycznym użytecznego i zakłócającego łącza radiowego dla sygnałów przesyłanych w łączu w dół (DL) w komórce radiowej pracującej na falach milimetrowych oraz przedstawia metody jego poprawnej estymacji. Zaproponowana jest również metoda poprawy stosunku mocy sygnału użytecznego do szumi i interferencji w łączu w dół (DL SINR) polegająca na optymalizacji skutecznej charakterystyki antenowej. Metoda ta bazuje na opatentowanym algorytmie dopasowującym wymiary układu antenowego do kątowego rozproszenia mocy w płaszczyznach poziomej i pionowej, w wyniku czego kształt skutecznej charakterystyki antenowej (rozumianej jako filtr przestrzenny) zostaje zoptymalizowany, a jej zysk zmaksymalizowany.

W toku kolejnych badań sprawdzona zostaje dokładność oceny ekspozycji na promieniowanie elektromagnetyczne (PEM) pochodzące od stacji bazowych 5G według metod stosowanych dla dotychczasowych systemów radiowych. Wyniki przeprowadzanych symulacji wskazują na możliwość znaczącego przeszacowania maksymalnej ekspozycji na PEM od stacji bazowych 5G znajdujących się w środowisku z rozproszeniami, bądź w przypadku braku bezpośredniej widoczności ze stacją bazową (non-line-of-sight, NLOS), jeżeli skuteczne charakterystyki antenowe nie są znane. W związku z tym, zaproponowana jest metoda poprawy dokładności oceny ekspozycji na PEM, która została wspomniana w najnowszej wersji standardu 62232 przygotowanego przez Międzynarodową Komisję Elektrotechniczną (International Electrotechnical Commission, IEC). Metoda ta bazuje na uproszczonym wyznaczaniu wartości skutecznych zysków antenowych oraz ich porównaniu. Uzyskane w ten sposób wartości ekspozycji na PEM są dokładniejsze niż w przypadku wykorzystania nominalnych charakterystykach antenowych, a przy tym nie wymagają przeprowadzania czasochłonnych symulacji z wykorzystaniem pełnego modelu kanału radiowego.

Wykorzystując model symulacyjny sieci radiowej CBRS (Citizens Broadband Radio Service) zbadany jest wpływ dokładności wyznaczania skutecznej charakterystyki antenowej na wydajność rozdziału zasobów radiowych w systemach z dynamicznym dostępem do widma. Uzyskane wyniki symulacji pozwalają ocenić dokładność oszacowywania poziomu wzajemnych zakłóceń oraz sposobu rozdziału kanałów radiowych pomiędzy stacjami bazowymi systemu CBRS (CBRS Devices, CBSD), gdy centralny kontroler odpowiedzialny za rozdział zasobów (Spectrum Access System, SAS) nie posiada wystarczającej wiedzy o skutecznych charakterystykach antenowych stacji CBSD. Założony scenariusz symulacyjny wskazuje, że wzajemne zakłócenia pomiędzy stacjami CBSD zostają znacząco niedoszacowane przez kontroler SAS w sytuacji gdy dysponuje on tylko nominalnymi charakterystykami antenowymi, w konsekwencji czego minimalne wymagania ko-egzystencji pomiędzy stacjami CBSD nie zostają spełnione. W związku z powyższym wskazane zostają miejsca, w których standardy odpowiedzialne za funkcjonowanie systemu CBRS powinny zostać poprawione.

Celem ostatniego badania jest analiza porównawcza dwóch metod wspólnego modelowania charakterystyki anteny kierunkowej i zjawiska kątowego rozproszenia mocy w kanale radiowym. Podejście z wyznaczaniem i wykorzystaniem skutecznej charakterystyki antenowej jest porównane z metodyką modelowania kątowego rozproszenia mocy według wielo-eliptycznego modelu kanału (multi-elliptical propagation model, MPM). Porównanie jest przeprowadzone poprzez wykorzystania tych samych założeń symulacyjnych oraz parametrów wejściowych. Zbliżone wyniki badań wykonanych według obu podejść pozwalają uznać metodę z wykorzystaniem modelu MPM za skuteczną, a jednocześnie niewymagającą czasochłonnych symulacji z wykorzystaniem pełnego modelu kanału radiowego.

Wyniki badań wchodzących w skład niniejszej rozprawy oraz wnioski wyciągnięte na ich podstawie są zgodne z postawioną na początku tezą oraz mogą stanowić zauważalny wkład w obecny stan wiedzy.

Contents

1 List of Publications

This dissertation consists of an overview and of the following publications which are referred to in the text by their Arabic numerals. Copies of publications are included in the Appendix.

[1] **K. Bechta**, M. Rybakowski, F. Hsieh, D. Chizhik, "Modeling of radio link budget with beamforming antennas for evaluation of 5G systems", *2018 IEEE 5G World Forum (5GWF)*, 9-11 July 2018, Silicon Valley, CA, USA, DOI: 10.1109/5GWF.2018.8516969.

[2] **K. Bechta**, M. Rybakowski, J. Du, "Impact of Effective Antenna Pattern on Millimeter Wave System Performance in Real Propagation Environment", *European Conference on Antennas and Propagation (EuCAP)*, 31 March-5 April 2019, Krakow, Poland.

[3] **K. Bechta**, M. Rybakowski, J. Du, "Efficiency of Antenna Array Tapering in Real Propagation Environment of Millimeter Wave System", *European Conference on Antennas and Propagation (EuCAP)*, 31 March-5 April 2019, Krakow, Poland.

[4] **K. Bechta**, J. Du, M. Rybakowski, "Optimized Antenna Array for Improving Performance of 5G mmWave Fixed Wireless Access in Suburban Environment", *2019 IEEE 5G World Forum (5GWF)*, 30 Sept.-2 Oct. 2019, Dresden, Germany, DOI: 10.1109/5GWF.2019.8911630.

[5] ***** J. Du, M. Rybakowski, **K. Bechta** and R. A. Valenzuela, "Matching in the Air: Optimal Analog Beamforming under Angular Spread", under review before planned submission to *IEEE Transactions on Communications*. (arxiv:1910.11054)

[6] **K. Bechta**, J. Du, M. Rybakowski, "Rework the Radio Link Budget for 5G and Beyond," *IEEE Access*, vol. 8, 211585–211594, 19 November 2020, DOI: 10.1109/ACCESS.2020.3039423. **<u>(IF-2020: 3.745, 100 pkt. MEiN)</u>**

[7] **K. Bechta**, C. Grangeat, J. Du, "Impact of Effective Antenna Pattern on Radio Frequency Exposure Evaluation for 5G Base Station with Directional Antennas", *2020 XXXIIIrd General Assembly and Scientific Symposium of the International Union of Radio Science (URSI GASS 2020)*, 29 Aug.-5 Sept. 2020, Rome, Italy, DOI: 10.23919/URSIGASS49373.2020.9232371.

[8] **** K. Bechta**, C. Grangeat, J. Du, M. Rybakowski, „Analysis of 5G Base Station RF EMF Exposure Evaluation Methods in Scattering Environments", under review before planned submission to *IEEE Access*.

[9] **K. Bechta**, "Centralized Spectrum Sharing and Coordination Between Terrestrial and Aerial Base Stations of 3GPP-Based 5G Networks", *International Journal of Electronics and Telecommunications (IJET)*, 2021, Vol. 67, No. 2, pp. 301-308, DOI: 10.24425/ijet.2021.135980. **(40 pkt. MEiN)**

[10] **K. Bechta**, J. Du, M. Rybakowski, „Impact of Effective Antenna Pattern on Estimation of Interference in Citizens Broadband Radio Service", accepted for presentation during *European Conference on Networks and Communications (EuCNC 2021)*, 8-11 June 2021, Porto, Portugal.

[11] **K. Bechta**, C. Ziółkowski, J.M. Kelner, L. Nowosielski, "Downlink Interference in Multi-Beam 5G Macro-Cell", *2020 23rd International Microwave and Radar Conference (MIKON 2020)*, 5-8 Oct. 2020, Warsaw, Poland, DOI: 10.23919/MIKON48703.2020.9253919.

[12] **K. Bechta**, C. Ziółkowski, J.M. Kelner, L. Nowosielski, "Modeling of downlink interference in massive MIMO 5G macro-cell", *Sensors (Switzerland)*, 2021, 21(2), pp. 1–17, 597, DOI: 10.3390/s21020597. **(IF-2020: 3.275, 100 pkt. MEiN)**

[13] **K. Bechta**, C. Ziółkowski, J.M. Kelner, L. Nowosielski, "Inter-beam co-channel downlink and uplink interference for 5G new radio in mm-wave bands", *Sensors (Switzerland)*, 2021, 21(3), pp. 1–20, 793, DOI: 10.3390/s21030793. **(IF-2020: 3.275, 100 pkt. MEiN)**

[14] S. Kim, E. Visotsky, P. Moorut, **K. Bechta**, A. Ghosh, C. Dietrich, "Coexistence of 5G With the Incumbents in the 28 and 70 GHz Bands", *IEEE Journal on Selected Areas in Communications (IEEE JSAC)*, Volume: 35, Issue: 6, 1254 – 1268, June 2017, DOI: 10.1109/JSAC.2017.2687238. **(IF-2017: 7.172, 200 pkt. MEiN)**

* Not yet published. Includes extension of publications [4] and [6].

** Not yet published. Includes extension of publication [7].

2 Author's Contribution

Listed publications were prepared as part of research and development projects conduced in Nokia Technology Center Wroclaw (Poland) in cooperation with Nokia Bell Labs Murray Hill, NJ (USA), Nokia Technology Center Paris-Saclay (France) and Military University of Technology in Warsaw (Poland).

Publication [1]: ”Modeling of radio link budget with beamforming antennas for evaluation of 5G systems”
The author had the main responsibility on the manuscript. The author prepared the concept of the manuscript together with Mr. Rybakowski. The author prepared the simulation model together with Dr. Hsieh and Dr. Chizhik. Simulation studies and analysis of the simulation results were done by the author.

Publication [2]: ”Impact of Effective Antenna Pattern on Millimeter Wave System Performance in Real Propagation Environment”
The author had the main responsibility on the manuscript. The author prepared the concept of the manuscript and the simulation model. Simulation studies were done by the author. Analysis of the simulation results were done by the author together with Mr. Rybakowski and Dr. Du.

Publication [3]: ”Efficiency of Antenna Array Tapering in Real Propagation Environment of Millimeter Wave System”
The author had the main responsibility on the manuscript. The author prepared the concept of the manuscript together with Mr. Rybakowski. The author prepared the simulation model for this manuscript. Simulation studies were done by the author. Analysis of the simulation results were done by the author together with Mr. Rybakowski and Dr. Du.

Publication [4]: ”Optimized Antenna Array for Improving Performance of 5G mmWave Fixed Wireless Access in Suburban Environment”
The author had the main responsibility on the manuscript. The author prepared the concept of the manuscript together with Dr. Du. The author prepared the simulation model for this manuscript. Simulation studies were done by the author. Analysis of the simulation results were done by the author together with Mr. Rybakowski and Dr. Du.

Publication [5]: ”Matching in the Air: Optimal Analog Beamforming under Angular Spread”
The author prepared the concept of the manuscript together with Dr. Du, Mr. Rybakowski and Dr. Valenzuela. The author performed measurements together with Mr. Rybakowski. The author prepared the simulation model for this manuscript. Simulation studies were done by the author. Analysis of the simulation results were done by the author together with Mr. Rybakowski, Dr. Du and Dr. Valenzuela.

Publication [6]: ”Rework the Radio Link Budget for 5G and Beyond”
The author had the main responsibility on the manuscript. The author prepared the concept of the manuscript together with Dr. Du. The author prepared the simulation model for this manuscript. Simulation studies were done by the author. Analysis of the simulation results were done by the author together with Mr. Rybakowski and Dr. Du.

Publication [7]: ”Impact of Effective Antenna Pattern on Radio Frequency Exposure Evaluation for 5G Base Station with Directional Antennas”
The author had the main responsibility on the manuscript. The author prepared the concept of the manuscript together with Mr. Grangeat. The author prepared the simulation model for this manuscript. Simulation studies were done by the author. Analysis of the simulation results were done by the author together with Mr. Grangeat and Dr. Du.

Publication [8]: ”Analysis of 5G Base Station RF EMF Exposure Evaluation Methods in Scattering Environments”
The author had the main responsibility on the manuscript. The author prepared the concept of the manuscript together with Mr. Grangeat and Dr. Du. The author prepared the simulation model for this manuscript. Simulation studies were done by the author. Analysis of the simulation results were done by the author together with Mr. Grangeat, Dr. Du and Mr. Rybakowski.

Publication [9]: ”Centralized Spectrum Sharing and Coordination Between Terrestrial and Aerial Base Stations of 3GPP-Based 5G Networks”
The author had the main responsibility on the manuscript. The author prepared the concept of the manuscript. The author prepared the simulation model for this manuscript. Simulation studies and analysis of the simulation results were done by the author.

Publication [10]: ”Impact of Effective Antenna Pattern on Estimation of Interference in Citizens Broadband Radio Service”

The author had the main responsibility on the manuscript. The author prepared the concept of the manuscript. The author prepared the simulation model for this manuscript. Simulation studies were done by the author. Analysis of the simulation results were done by the author together with Dr. Du and Mr. Rybakowski.

Publication [11]: ”Downlink Interference in Multi-Beam 5G Macro-Cell”

The author had the main responsibility on the manuscript. The author prepared the concept of the manuscript together with Prof. Ziółkowski, Prof. Kelner and Prof. Nowosielski. The author prepared the simulation model together with Prof. Kelner. Simulation studies were done by the author together with Prof. Kelner. Analysis of the simulation results were done by the author together with Prof. Ziółkowski, Prof. Kelner and Prof. Nowosielski.

Publication [12]: ”Modeling of downlink interference in massive MIMO 5G macro-cell”

The author had the main responsibility on the manuscript. The author prepared the concept of the manuscript together with Prof. Ziółkowski, Prof. Kelner and Prof. Nowosielski. The author prepared the simulation model together with Prof. Kelner. Simulation studies were done by the author together with Prof. Kelner. Analysis of the simulation results were done by the author together with Prof. Ziółkowski, Prof. Kelner and Prof. Nowosielski.

Publication [13]: ”Inter-beam co-channel downlink and uplink interference for 5G new radio in mm-wave bands”

The author had the main responsibility on the manuscript. The author prepared the concept of the manuscript together with Prof. Ziółkowski, Prof. Kelner and Prof. Nowosielski. The author prepared the simulation model together with Prof. Kelner. Simulation studies were done by the author together with Prof. Kelner. Analysis of the simulation results were done by the author together with Prof. Ziółkowski, Prof. Kelner and Prof. Nowosielski.

Publication [14]: ”Coexistence of 5G With the Incumbents in the 28 and 70 GHz Bands”

The author prepared the concept of the manuscript together with Dr. Kim, Dr. Visotsky, Mr. Moorut, Dr. Gosh and Dr. Dietrich. The author prepared the simulation model for this manuscript together with Dr. Kim and Dr. Visotsky. Analysis of the simulation results were done by the author together with Dr. Kim, Dr. Visotsky, Mr. Moorut, Dr. Gosh and Dr. Dietrich.

3 Overview of the dissertation

3.1 Introduction

Unlike any other mobile communication systems developed and implemented in the past, the 5th generation (5G) of cellular communication standards has capabilities to become enabler and fundamental part of the next Industrial Revolution – Industry 4.0. The fourth Industrial Revolution aims to expand digitalization and automation from the sector of services, such as banking and the media, towards industries handling with heavy equipment, production lines and physical materials. These general use cases require reliable, scalable and mobile solutions which cannot be always ensured by wired networks or wireless-local-access-network (WLAN) standards, like IEEE-802.11.

From the beginning of the work on beyond-4G (the 4th generation of mobile communication systems) requirements, which has started a decade ago and is continued until now, the use cases for heavy industry were considered as a significant differentiator of the next cellular communication standard and a driver for new inventios. Therefore, at the current stage of 5G development the following characteristics give it the advantage to be the key part of Industry 4.0:

- High data throughput and cell capacity,
- New spectrum bands with wider channel bandwidths,
- Ultra-reliable low latency communication,
- Network slicing,
- Edge computing,
- Internet of Things,
- Open Radio Access Networks.

Even though the novel part of 5G relies on digitalization and cloud computing, it is still radio-based communication system and in this area also introduces significant improvements. The most representative examples are utilization of millimeter wave (mmWave) bands and implementation of beamforming antenna patterns, which are the key enablers of high data throughput and cell capacity in 5G system. However, such improvements may bring challenges at the early stage of implementation, if feasibility studies are not conducted with comprehensive and well verified models. Therefore, it is particularly important to identify potential root-causes of inaccurate modeling before wide-range deployments of 5G begin. In traditional cellular systems where omni-directional or sectoral antennas are deployed, the antenna half-power beam-widths (HPBW) are much larger than angular spread of the radio channels. Therefore, the impact of channel angular spread on radio link budget is negligible and the simplified model works. However, 5G is adapted to use - in both sub-6GHz and mmWave bands - antenna arrays whose beam-width is comparable to or smaller than channel angular spread. The complex relation between 5G narrow-beam directional antennas and channel angular spread should be carefully examined and properly accounted for in 5G radio link budget calculation. Inheriting the simplified radio link budget model from previous generations would lead to noticeable difference in estimated values of received power as compared to detailed simulation results using three-dimensional (3D) channel modeling. This dissertation investigates, in the series of simulations and measurements, the model for radio link budget estimation important from the perspective of 5G network planning and optimization (NPO), and proposes its improvements.

3.2 Motivation for the dissertation

In the early 2016 the 3rd Generation Partnership Project (3GPP), a standardization body, started a study on radio frequency (RF) and co-existence aspects for the New Radio (NR) standard version of 5G. The outcome of this study, consisting mostly in system-level simulation results contributed by members of 3GPP, is summarized in the 3GPP Technical Report (TR) 38.803.

Nokia, as one of the key members of 3GPP, performed and contributed simulation results of serving and interfering radio link budgets according to scenarios and methods agreed during evaluation of 5G co-existence aspects by 3GPP. These results were later used for determination of RF requirements for Release-15 NR standard, as included in 3GPP Technical Specification (TS) 38.104. Release-15 is the first full set of 5G standards developed by 3GPP, which in majority rely on link-level and system-level simulation studies conducted according to 3D channel model for frequencies from 0.5 to 100 GHz defined in TR 38.901. In this document 3GPP has provided instruction on how to generate statistical 3D channel models, which include all the necessary radio propagation phenomena that must be considered during comprehensive simulation to provide estimation of 5G radio link budget and performance.

Part of Nokia’s contributions to TR 38.803 and TS 38.104 were prepared in Nokia Technology Center Wroclaw. During this work it has been noticed that accurate modeling of 5G radio link budget for beamformed antenna patterns should be performed with appropriate channel models, especially for angular spread, due to the fact that the use of beamforming and spatial filtering of multipath propagation components is sensitive to time-variant radio channel conditions. Therefore, the simulation study has been initiated and supported by laboratory measurements to validate the concept of effective antenna pattern, as determined in given scattering environment, in contrary to nominal antenna pattern, as measured in anechoic chamber. The main difference between effective and nominal antenna patterns comes from the fact that the first one is 'drawn' in 3D space by multipath components (rays) with different angles of departure (AoD), angles of arrival (AoA), delays and powers, whereas the second one results from single direct path (ray) only. In consequence, the shapes and gains of both patterns may be significantly different, especially if effective pattern is determined in the environment with rich scattering. Initial simulation studies indicated that signal to interference plus noise ratio (SINR) in typical 5G downlink (DL) transmission can be significantly overestimated if spatial filtering of radiated energy by directional antenna patterns of transmitter (Tx) and receiver (Rx) is neglected during modeling, i.e. when nominal antenna gains are used instead of effective antenna gains in simple radio link budget models, e.g. (D-1):

$$P_{Rx} = \frac{P_{Tx} G_{Tx} G_{Rx}}{PL}, \tag{D-1}$$

where, P_{Rx} indicates power of signal (from serving or interfering link) at the output of Rx antenna, whereas P_{Tx} indicates power at the input of Tx antenna. G_{Tx} and G_{Rx} represent gains (nominal or effective) of Tx and Rx antennas, respectively, path loss between Tx and Rx antennas is indicated by PL, and other losses are neglected for simplicity. In the consequence of inaccurately modeled radio link budget, being a part of 5G NPO process, the wrongly estimated SINR gives inaccurate picture of system performance, capacity and coverage. Under- or overestimation of these parameters lead in turn to suboptimal deployments of evaluated 5G networks, which in most cases would be adjustable only after initial field measurements under real operation conditions. These initial findings were the motivation for all following studies contributed to this dissertation.

3.3 Summary of studies, objectives and contributions of the dissertation

Results of all studies presented in this dissertation come down to a common denominator and constitute its main thesis: **Mapping the impact of angular spread phenomenon on the beamformed antenna patterns significantly improves the accuracy of radio link budget**

estimation and the efficiency of 5G NPO process. However, before conclusions on the improvement of estimation accuracy were drawn, evaluation of different approaches had been made for series of propagation environments and 5G use cases. Therefore, following subsections give an overview of all conducted and published studies, where each of them has its own objectives and contributions to the state of the art but at the same time is aligned with the main thesis and objective of this dissertation, as stated above.

First are clarified the definitions of nominal and effective antenna patterns, as well as presented are simulation results of 5G network performance evaluated when nominal and effective antenna patterns are assumed. This part, as presented in publications [1] – [6], is concentrated on radio link budget for serving and interfering DL signals in 5G mmWave cell and indicates methods for its accurate calculation. Additionally, a method for improvement of DL SINR by optimization of effective antenna pattern is proposed and evaluated. This method is based on the patented proprietary algorithm, which matches the geometry of antenna array to the azimuth and zenith angular spread in the given channel. In the consequence the effective antenna pattern, understood as a spatial filter of multipath components, is optimized and its effective antenna gain is maximized.

Publications [7] and [8] evaluate for 5G the accuracy of methods for assessment of RF electromagnetic field (EMF) exposure inherited from previous systems. It has been presented in [7] and [8] that legacy methods may lead to significant overestimation of the maximum RF EMF exposure associated with 5G base station (BS) (gNodeB) in scattering environment if nominal antenna pattern is assumed instead of effective antenna pattern. Therefore, a simple solution is proposed in [8] to improve the accuracy of RF EMF exposure assessment, which is indicated in the latest version of standard 62232 defined by International Electrotechnical Commission (IEC). Proposed solution is based on closed-form formulas, which allow to extrapolate the maximum exposure by calculation and comparison of effective antenna gains. Obtained values of RF EMF exposure are more accurate than estimated based on nominal antenna gains and at the same time do not require comprehensive system-level simulation with 3D channel model.

By the example of Citizens Broadband Radio Service (CBRS) it was presented how the accurate modeling of antenna pattern may improve performance of radio resources distribution in spectrum sharing environment. Results of studies published in [9] and [10] allow to assess the accuracy of interference evaluation and channels distribution between CBRS devices (CBSD) if centralized controller for spectrum access system (SAS) does not have enough knowledge about effective antenna pattern. Simulation results from [10] indicate that for the assumed scenario of

CBRS network implementation the mutual interference between each pair of CBSDs can be significantly underestimated, which in consequence leads to insufficient co-existence conditions, if nominal antenna pattens are used by SAS instead of effective patterns. Therefore, a proposal for improvement of standards relevant for CBRS networks was made.

In the end, publications [11] – [14] allow to compare different approaches for joint modeling of antenna pattern and angular spread phenomenon in scattering environment. The concept of effective antenna pattern has been compared with multi-elliptical propagation model (MPM) approach. This comparison was enabled by the use of common input data, which was the 3GPP 3D channel model of TR 38.901. Comparable simulation results, obtained from both approaches for selected simulation scenarios, allow to conclude that MPM model ensures good accuracy without the need for full 3D channel modeling in time-consuming and computational power-consuming statistical simulations.

3.3.1 Accurate modeling of radio link budget for evaluation of performance in cellular 5G system

3.3.1.1 Description of studies

When designing an antenna, one of the main objectives is to obtain a specific radiation pattern. In case of antenna arrays of 5G the expectations are mostly high maximum gain and low level of side lobes. Antenna pattern which has been determined by design and validated by measurements in an anechoic chamber is referred to hereinafter as *nominal antenna pattern* of the antenna.

With increasing number of antenna elements in the array, the maximum gain $g_{\max}^{Nom}$ of the nominal antenna array pattern increases and its HPBW decreases. These relations are described by (D-2) [6]:

$$g_{\max}^{Nom} = \frac{2}{B_{ho} \cdot B_{vo}} = N \cdot G_e , \tag{D-2}$$

where B_{ho} and B_{vo} are the nominal root mean square (RMS) beam-width in horizontal and vertical planes (in radians), respectively, N is the number of antenna elements in the array, and G_e is the gain of a single antenna element.

In practical channel scattering environment, which differs significantly from anechoic chamber propagation conditions, the maximum realizable gain and associated HPBW of an antenna array differ from their nominal values and are hereinafter referred to as effective. Therefore, the antenna pattern measured in a scattering environment is defined as *effective antenna pattern* for that channel.

Nominal antenna pattern and nominal gain are antenna specific, whereas effective antenna patterns and the corresponding effective gains change depending on a channel. The difference between nominal and effective antenna patterns depends on an angular spread in the scattering environment introduced by a real deployment scenario. According to [6], (D-3) – (D-5) describe how the effective antenna gains g^{Eff} can be analytically obtained from nominal antenna gains g^{Nom} and power angular spectrum (PAS) p of the assumed propagation environment.

$$g^{Eff}\left(\phi_0,\theta_0\right)=\int_{-180^\circ}^{180^\circ}\int_{-90^\circ}^{90^\circ} g^{Nom}\left(\phi_0-\phi,\theta_0-\theta\right)\cdot p\left(\phi,\theta\right)d\phi d\theta\,, \qquad \text{(D-3)}$$

$$g_{Az}^{Eff}\left(\phi_0\right)=\int_{-180^\circ}^{180^\circ} g_{Az}^{Nom}\left(\phi_0-\phi\right)\cdot p_{Az}\left(\phi\right)d\phi\,, \qquad \text{(D-4)}$$

$$g_{Ele}^{Eff}\left(\theta_0\right)=\int_{-90^\circ}^{90^\circ} g_{Ele}^{Nom}\left(\theta_0-\theta\right)\cdot p_{Ele}\left(\theta\right)d\theta\,, \qquad \text{(D-5)}$$

where ϕ and θ define angular domain in azimuth and elevation, respectively, whereas ϕ_0 and θ_0 indicate the main beam orientation angles in azimuth and elevation, respectively. g_{Az}^{Nom}, g_{Ele}^{Nom}, g_{Az}^{Eff} and g_{Ele}^{Eff} indicate nominal and effective antenna gains if only azimuth or elevation plane is considered, respectively, whereas p_{Az} and p_{Ele} represent realizations of PAS in azimuth and elevation, respectively. Effective antenna gains g^{Eff} when calculated for full ranges of beam orientation angles, i.e. $\phi_0\in\left[-180^\circ;180^\circ\right)$ and $\theta_0\in\left[-90^\circ;90^\circ\right]$, allows to obtain 3D effective antenna pattern in given propagation conditions specified by PAS p. For illustration, Figure D-1 (Figure 3 of [8] and Figure 1 of [2]) presents example comparison of horizontal cuts for nominal and effective patterns of practical gNodeB antenna arrays in urban macro (UMa) propagation environment determined by 3GPP TR 38.901. Presented patterns were obtained as mean value from realization of (D-4) during 1000 Monte Carlo statistical simulation drops. Additional examples of horizontal and vertical cuts of 3D effective antenna patterns are illustrated in publications

[2],[3],[4],[8] and [10], for $M \times N$ antenna array, where M indicates number of antenna elements in each column and N indicates number of antenna elements in each row of antenna array:

- Figures 1 and 2 of [2]: Horizontal and vertical patterns of 16×16 antenna array in UMa environment in 28 GHz band;
- Figures 3 and 4 of [2]: Horizontal and vertical patterns of 8×8 antenna array in urban micro street canyon (UMi SC) environment in 28 GHz band;
- Figure 2 of [3]: Horizontal patterns of 16×16 antenna array in UMa environment in 28 GHz band with applied Chebyshev window for tapering of side lobes;
- Figure 6 of [3]: Horizontal patterns of 8×8 antenna array in UMi SC environment in 28 GHz band with applied Chebyshev window for tapering of side lobes;
- Figures 3 and 4 of [4]: Horizontal patterns of 8×8 antenna array in suburban fixed wireless access (SubU FWA) environment in 28 GHz band;
- Figure 2 of [8]: Horizontal patterns for broadcast and traffic signals of commercially available antenna panel for massive multiple-input-multiple-output (mMIMO) 5G system in UMa environment in 3.5 GHz band;
- Figures 3 and 4 of [10]: Horizontal and vertical patterns of commercially available antenna panel for CBRS system in UMa environment in 3.5 GHz band.

All abovementioned effective antenna patterns were determined for PAS per given propagation conditions defined by 3GPP in TR 38.901. As can be noticed, each of those figures includes effective patterns individually for line-of-sight (LOS) and non-LOS (NLOS) conditions. This approach is due to the fact that angular spread of LOS and NLOS conditions differs significantly and leads to different effective patterns. In case of LOS, the drop in effective antenna gain (in reference to nominal antenna gain) is noticeably lower than in case of NLOS. However, the widening of HPBW (in reference to nominal antenna pattern), and therefore the increase of side lobes levels, is significant in both LOS and NLOS. Obtained simulation results of effective antenna gains and HPBWs in different propagation environments and frequency bands are collected in Table I of [2], Table II of [3], Table I of [6] and Table II of [8].

All indicated deviations from nominal antenna pattern shape and gain depend on angular spread in given propagation scenario, as well as on parameters of nominal antenna pattern, and should be taken into account during radio link budget modeling for serving and interfering signals of 5G system with beamforming. Therefore, several simulation scenarios were investigated and

(a)

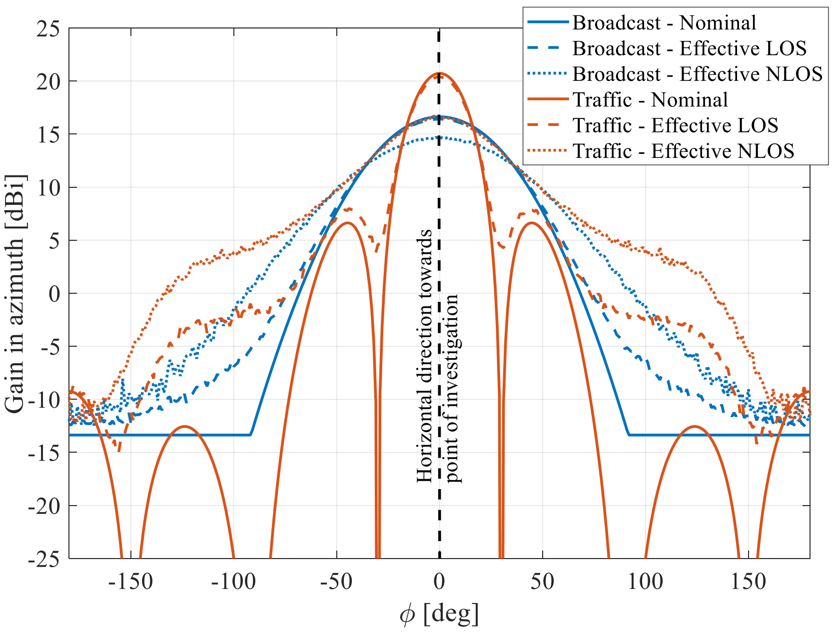

(b)

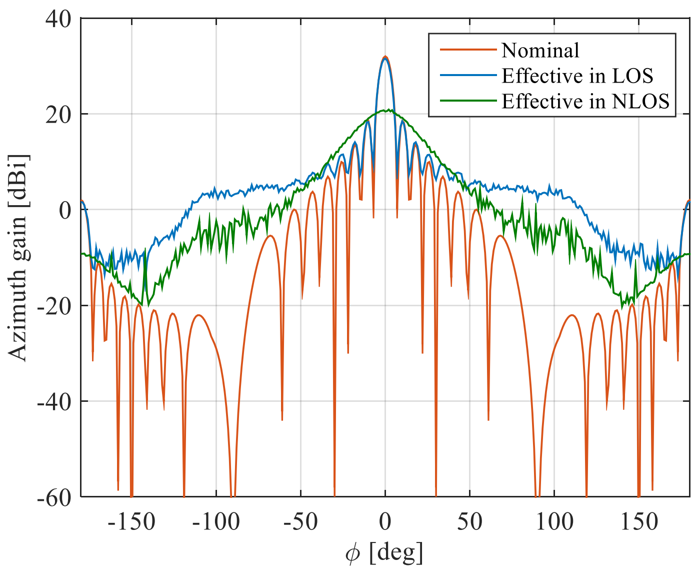

Figure D-1. Example comparison of nominal and effective antenna patters in 3GPP UMa environment for (a) Commscope “RRZZHHTTS4-65B-R7” antenna in 3.5 GHz band (Figure 3 of [8]) and (b) 16×16 antenna array in 28 GHz band (Figure 1 of [2])

published in [1],[2] and [4], to illustrate the error in modeling of DL SINR in mmWave 5G cell, if effective antenna pattern is not considered during calculation of radio link budget. In case of UMa environment it has been presented in Figures 5 and 8 of [1] and Figure 10 of [2] that overestimation of DL SINR can be as high as 20 dB. Overestimation of DL SINR obtained for UMi SC is lower but still can reach more than 10 dB, as presented in Figure10 of [2], whereas simulation results included in Figure 9 of [4] indicate overestimation of more than 5 dB in case of SubU FWA environment. Mentioned simulation results assume that both LOS and NLOS conditions occur in DL transmission, however it should be noted that significant overestimation in DL SINR is mainly due to NLOS conditions. In the presence of a strong direct path in LOS condition, the effective antenna gain is close to nominal value, whereas in NLOS conditions the effective gain is noticeably lower than nominal value. This difference in the gains causes overestimation of power in DL signal of serving link (DL S) if nominal pattern is used. On the other hand, angular spread of radiated energy in horizontal plane causes increased effective gain of side lobes as compared to nominal values in both LOS and NLOS conditions. This is the reason of underestimation of power in DL signal of interfering links (DL I), because the major part of interference is received by the side lobes. Therefore, the use of nominal pattern causes overestimation of DL S and underestimation of DL I, which leads to significantly overestimated DL SINR in all simulated deployment scenarios, as described in more details in [2] and [6].

All abovementioned simulation results, partially presented also in Figure D-2 (Figure 5 of [6]), clearly show that a simplified method with nominal pattern for 5G network estimation can give an erroneous picture of performance metrics which cannot be met in real field deployments. Therefore, to avoid inaccurate calculation of radio link budget while maintaining its simplicity, in

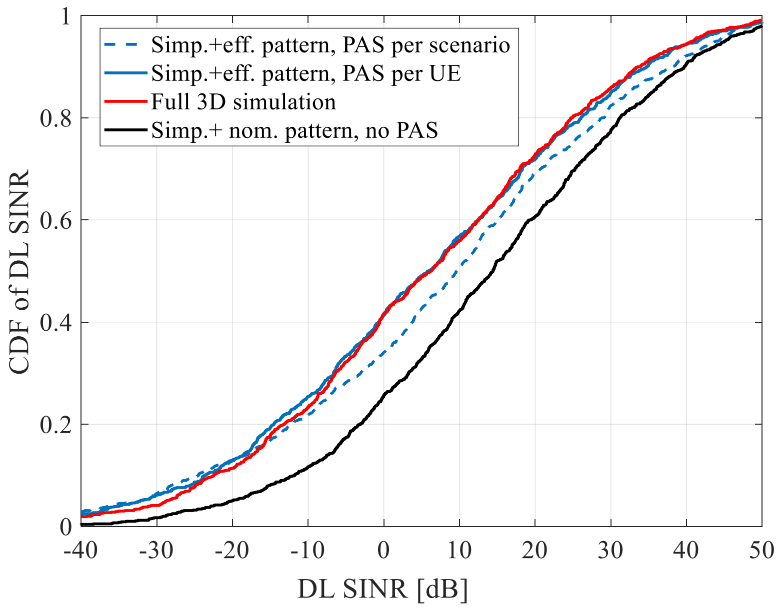

Figure D-2. CDFs of DL SINR for mmWave 3GPP UMi SC deployment scenario (combined LOS and NLOS links) obtained by different approaches of link budget calculation (Figure 5 of [6]) section III of [6] a method was proposed how to replace the nominal antenna gain by effective gain. It should be noted, that the proposed method can be used in case of analog beamforming or panel-based hybrid beamforming where the beamforming vector can be drawn from Grid of Beams (GoB) codebook, conventional Fourier transform based beamforming, or other advanced beamforming techniques such as eigen-based beamforming (EBB) and zero forcing beamforming. Accuracy of the proposed method has been evaluated in the UMi SC simulation scenario for 8×8 antenna array of gNodeB operating in 28 GHz frequency band. As presented in Figure 5 of [6], and reproduced in Figure D-2, the cumulative distribution functions (CDF) of DL SINR obtained by the proposed method can be within 1 dB of difference in reference to full-scale 3D simulation results (treated as ground truth for 3GPP related studies). This comparison indicates high accuracy of proposed method in contrary to calculation results for nominal antenna pattern, which can be over 10 dB too optimistic at 10%-tile and over 8 dB at median.

3.3.1.2 Objectives and contributions of studies published in [1] – [6]:

The main objectives and contributions of presented studies were:

- Clarification on definitions of nominal and effective antenna patterns,
- Determination of the method (mathematical equations) for calculation of effective antenna pattern based on nominal antenna pattern and PAS in given propagation environment,
- Comparison of 5G system performance evaluations obtained based on nominal and effective antenna patterns,
- Proposal of simplified method for radio link budget calculation with effective antenna gains and evaluation of its accuracy.

3.3.2 Optimization of antenna pattern shape for improvement of radio link budget

3.3.2.1 Description of studies

Directional antenna performs spatial filtering of electromagnetic energy from the space, and it is reasonable to match the antenna pattern to the angular spread of the channel in given propagation conditions. To prove this concept a series of simulations and measurements were performed. In the result of conducted studies, two detailed solutions have been derived for:

- estimation of angular spread in given propagation conditions based on measurements of signal strength using three or more different sub-array configurations on Tx side of radio link, as described in detail in section III-B of [5],

- optimization of antenna array geometry for maximization of the energy radiated to or captured from the space under given channel angular spread constraints, as described in detail in section III-A of [5].

Both presented solutions are part of International Patent Application No.PCT/IB2019/053142.

If assume that angular spread in the place of gNodeB antenna array deployment is known, (either from statistical channel models, like 3GPP TR 38.901, or estimated based on the first of abovementioned methods), optimization of effective gain of this antenna array may be obtained according to the second of abovementioned methods. Summary of this method is included in [4] and [6] and reproduced in the following paragraphs.

For this method it is assumed that N antenna elements, arranged in rectangular/square shape, form a uniform planar array of size $(K_1;K_2)$, with:

$$K_1K_2 \le N \, . \tag{D-6}$$

The array of $(K_1;K_2)=(1;N)$ corresponds to a horizontally deployed uniform linear array, whereas $K_2=1$ indicates a vertically deployed uniform linear array. Let B_{ve} and B_{he} be the nominal beam-widths of the antenna elements whose gain is G_e. The nominal RMS beam-widths B_{v0} and B_{h0} of the analog beams formed by antenna array of size $(K_1;K_2)$ can be approximately described as:

$$B_{v0}=\frac{B_{ve}}{K_1}, B_{h0}=\frac{B_{he}}{K_2} \; . \tag{D-7}$$

The effective beamforming gain can be determined based on nominal antenna pattern and channel angular spread as:

$$G\left(N,B_{ve},B_{he},\sigma_v,\sigma_h\right)=\frac{2}{\sqrt{\left(\frac{B_{ve}}{K_1}\right)^2+\sigma_v^2}\sqrt{\left(\frac{B_{he}}{K_2}\right)^2+\sigma_h^2}} \, , \tag{D-8}$$

where σ_h and σ_v are the RMS azimuth spread of departure (ASD) and RMS zenith spread of departure (ZSD), respectively.

Since the effective gain (D-8) depends on the panel geometry $(K_1;K_2)$, and B_{ve} and B_{he} are determined by the antenna element via $G_e=2/\left(B_{ve}B_{he}\right)$, the array geometry $(K_1;K_2)$ can be optimized to maximize the effective beamforming gain G stated in (D-8) subject to the size constraint (D-6). While ignoring the integer constraint on array dimension K_1 and K_2, the effective beamforming gain is maximized if and only if the array geometry is given by:

$$K_1 = \sqrt{\frac{NB_{ve}\sigma_h}{B_{he}\sigma_v}}, K_2 = \sqrt{\frac{NB_{he}\sigma_v}{B_{ve}\sigma_h}} \quad . \tag{D-9}$$

The nearest integer pair close to $\left(K_1;K_2\right)$ as specified by (D-9) and satisfying the total elements constraint (D-6) gives the best analog beamforming gain and constitutes the *optimal antenna array pattern*.

The principle of the invented method for antenna pattern optimization assumes that the shape of the pattern, understood here as a spatial filter, is matched to the azimuth and zenith angular spreads in a considered scattering environment by modification of antenna array geometry under constant number of antenna array elements. This method has been verified by system level simulations and laboratory measurements for determination of the optimal antenna array geometry for uniform planar arrays with analog beamforming. Simulations performed for UMi SC environment and presented in Figure 6 of [5] indicate that optimization of antenna pattern shape, due to re-configuration of uniform planar antenna array geometry from 8×16 to 42×3, allows to increase the DL SINR by around 6.6 dB. Optimization of antenna array geometry from 8×8 to 16×4, as presented in Figure D-3 (a) (Figure 4 of [4]) for SubU FWA environment, allows to increase the DL SINR by almost 2 dB in single user (SU)-MIMO scenario, which is presented in Figure D-3 (b) (Figure 9 of [4]). Higher value of DL SINR leads to improvement of DL cell capacity by around 60% for 10%-tile of CDF as presented in Figure D-3 (c) (Figure 10 of [4]), which can be understood as cell edge capacity improvement.

However, some concerns may be raised regarding the impact of antenna pattern widening in horizontal plane (due to optimization) on interference in multi-user (MU) scenario. Therefore, additional simulation results were presented in [6] to quantify the impact of antenna array optimization on DL performance in MU-MIMO scenario. Simulation results for antenna arrays with 64 and 144 elements were obtained for 2 or 4 simultaneously served user equipment (UE) per cell in SubU FWA scenario. In these cases, the improvement in DL SINR is still noticeable and varies between 1.2 dB and 2 dB, as presented in Figure 11 and summarized in Tables V and VI of [6]. These results prove that proposed method allows to improve radio link budget even in the presence

(a)

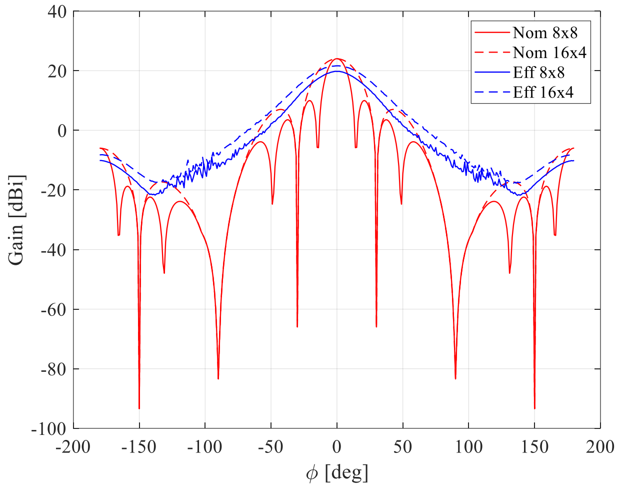

(b)

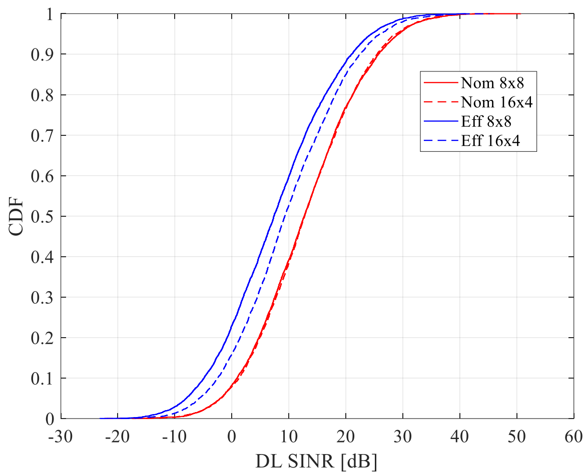

(c)

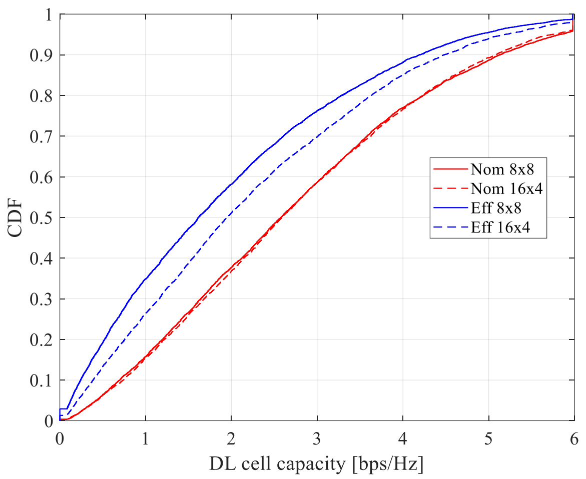

Figure D-3. (a) Horizontal cuts of nominal and effective antenna patterns for 8x8 and 16x4 configurations in NLOS (Figure 4 of [4]), (b) CDFs of DL SINR (Figure 9 of [4]) and (c) CDFs of DL cell capacity (Figure 10 of [4]), for mmWave SubU FWA deployment scenario with SU-MIMO of intra-cell interference, which is beneficial especially in challenging propagation conditions of mmWave bands.

To verify the effectiveness of the presented method of antenna pattern optimization, a proof-of-concept laboratory measurements were carried-out using a commercially available 28 GHz 16×16 array (Nokia AEUA AirScale Multi Antenna Array, 2Tx-2Rx, 512 antenna elements, 64 dBm of max equivalent isotropic radiated power - EIRP) as the Tx, and a 10 dBi horn antenna as

Figure D-4. Lab measurement setup for both LOS (left) and NLOS (right) where a 28 GHz phased array of 16×16 was used as the transmitter and a 10 dBi horn as the receiver (Figure 7 of [5])

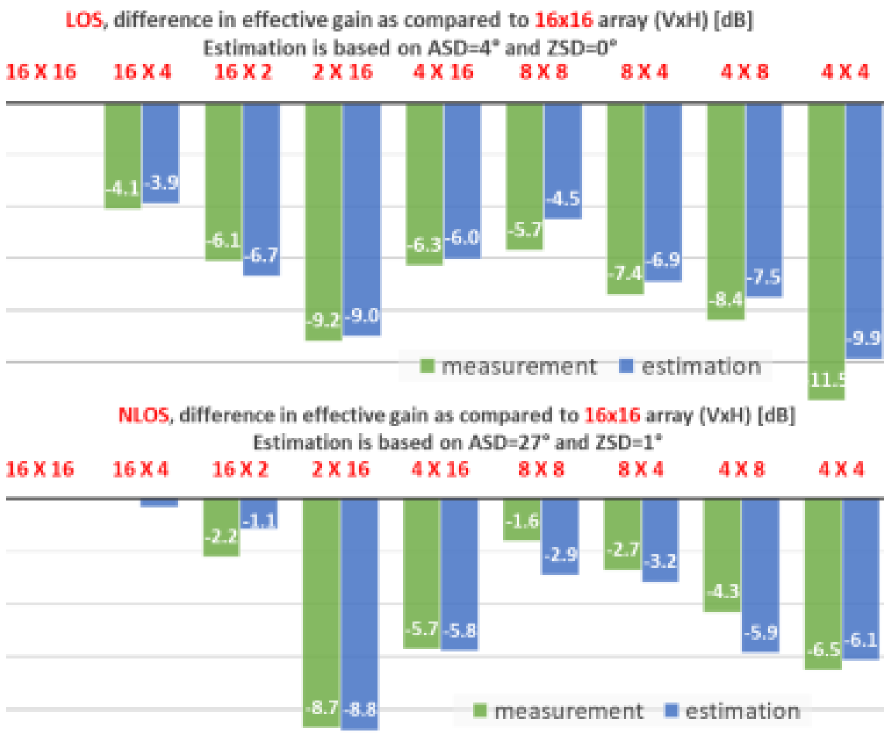

Figure D-5. Lab measurement results and estimated effective beamforming gains for LOS (upper) and NLOS (lower) (Figure 8 of [5]) the Rx. Detailed description of measurement procedure as well as post-processing of results is included in section IV-C of [5]. Measurements were performed in LOS and NLOS conditions for nine antenna array geometries (16×16, 16×4, 16×2, 2×16, 4×16, 8×8, 8×4, 4×8 and 4×4). Figure D-4 (Figure 7 of [5]) illustrates configured measurement setup. Based on measurement results of received power the relative effective antenna array gains were determined for all measured geometries in relation to 16×16 geometry. In parallel, the azimuth and zenith angular spreads were estimated in given propagation conditions according to the method presented in section III-B of [5]. Estimated values of angular spread allowed to calculate the relative effective antenna gains for all assumed array geometries according to the closed-form formula (D-8). Comparison of relative effective antenna gains obtained from measurements and estimations/calculations demonstrate good match, but first off all indicates that antenna array geometry can be optimized to improve effective antenna gain, as presented in Figure D-5 (Figure 8 of [5]). For example, in LOS the 16×2 sub-array has similar gain as the 8×8 by using 2 times less antenna elements, which indicates that effective antenna gain 'saturates' in analog beamforming and under given angular spread cannot be further improved, even by higher number of antenna elements in the array. In NLOS, the effective antenna gain of 16×2 array is only 2.2 dB worse than 16×16, whereas the effective gain of 2×16 array is 8.7 dB worse, clearly demonstrated the need of array optimization.

3.3.2.2 Objectives and contributions of studies published in [4] – [6]:

The main objectives and contributions of presented studies were:

- Preparation of the method for antenna array optimization under given angular spread conditions for improvement of effective gain (subject of International Patent Application No.PCT/IB2019/053142),
- Preparation of the method for angular spread estimation based on minimal number of signals measured from different antenna sub-arrays of Tx (subject of International Patent Application No.PCT/IB2019/053142),
- Evaluation of prepared methods by full-scale 3D statistical simulations and lab measurements,
- Demonstration of efficiency of the method for antenna array optimization in the realistic simulation scenarios of 5G mmWave networks.

3.3.3 Estimation of RF EMF exposure associated with gNodeB in scattering environment

3.3.3.1 Description of the study

Together with the introduction of 5G the methods for assessment of RF EMF exposure inherited from previous systems are being updated to account for actual transmitting, beamforming and beam-steering performances. The IEC develops and validates methods for assessing the RF EMF exposure due to BS in the standard IEC 62232. When the assessment is performed in-situ, it is recommended to extrapolate the maximum level of exposure (usually associated with traffic signal) from measurement of stable signals, such as broadcast signal with gNodeB. A comparative analysis of extrapolation method based on nominal and effective antenna pattern of gNodeB is presented in [7] and [8]. This analysis shows that extrapolation method with nominal antenna pattern may conduct to significant overestimation of the maximum RF exposure in case of NLOS conditions, up to several dB, depends on design of evaluated beam patterns.

In the study presented in [7] and [8] a commercially available 5G antenna pattern for 3.5 GHz band (Commscope "RRZZHHTTS4-65B-R7") was assumed with three different propagation environments according to 3GPP TR 38.901 – UMi SC, UMa and rural macro (RMa). This study concentrates on estimation of the extrapolation factor $F_{extBeam}$, as included in (D-10) ((1) of [8]).

$$E_{asmt} = E_{broadcast} \times \sqrt{F_{extBeam} \times F_{BW} \times F_{PR} \times F_{TDC}}\ , \tag{D-10}$$

where E_{asmt} and $E_{broadcast}$ are the extrapolated electric field strength of traffic signal in V/m and evaluated (measured) electric field strength of broadcast signal in V/m per given orthogonal frequency-division multiplexing (OFDM) resource element in 5G NR frame, respectively. $F_{extBeam}$ is extrapolation factor corresponding to the ratio of the EIRP envelope of all traffic signals to the EIRP envelope of the broadcast signal in the direction of the measurement location. F_{BW}, F_{PR} and F_{TDC} are remaining extrapolation factors corresponding respectively to the ratio of the total carrier bandwidth and the subcarrier frequency spacing of the broadcast signal, the power reduction factor (if the actual maximum approach is used) and the maximum technology duty cycle of all signals. Equation (D-10) is derived from the standard IEC 62232, which includes more accurate description of all above parameters.

Obtained simulation results, as presented in Figure 4 of [8], indicate that extrapolation factor can be overestimated in NLOS conditions even by 3.7 dB, 3.6 dB and 2.0 dB in assumed UMi SC, UMa and RMa scenarios, respectively, if high values of angular spread are assumed. Direct reason for this overestimation are the differences between nominal and effective patterns of broadcast and traffic beams, as presented in Figure D-1 (a) (Figure 3 of [8]), whereas consequences of this overestimation may be unnecessary limited DL transmit power of the gNodeB or overestimate of the RF EMF compliance distances.

Potential overestimation can be reduced by using effective antenna pattern in scattering environments in order to better represent the actual propagation conditions, such as those found in urban or dense urban areas. In such actual propagation conditions it is recommended to perform extrapolation of the maximum exposure with appropriate channel models, especially for angular spread, due to the fact that the use of beamforming and spatial filtering is sensitive to time-variant radio channel conditions. A simple method to improve the accuracy of RF EMF exposure extrapolation from broadcast signal measurements is introduced in section IV of [8], leveraging joint modeling of antenna beam pattern and PAS. As an input to the method the following parameters are required:

- maximum nominal gain ($g_{\max}^{Nom}$) in linear scale,
- nominal HPBW of the main beam in horizontal plane (B_h) in radians,
- nominal HPBW of the main beam in vertical plane (B_v) in radians,
- RMS azimuth angular spread (σ_h) of assumed scattering environment in radians,
- RMS elevation angular spread (σ_v) of assumed scattering environment in radians.

The RMS azimuth σ_h and elevation σ_h angular spread of the channel can be obtained either from standard propagation models, like 3GPP TR 38.901, or by performance angular spread estimation using the method prescribed in section III-B of [5]. Other methods for RMS angular spread determination are not precluded, e.g. ray-racing simulations assuming realistic model of deployment scenario, but it has to be noted that the accuracy of selected method impacts directly the accuracy of $F_{extBeamEff}$ estimation, as RMS angular spread determines effective antenna gain which is required for calculation of $F_{extBeamEff}$. If statistical channel models are selected for determination of RMS angular spread, it is important to consider also standard deviation and not only the mean value of angular spread for given propagation conditions and frequency band. Due to lack of single model which represents accurately all possible radio channels occurring in realistic propagation environments, this approach for RMS angular spread determination allows to obtain the range of $F_{extBeamEff}$ values which are expected to be the most representative. Having wider range of $F_{extBeamEff}$ values gives the freedom to select the one which is expected to provide the most accurate RF EMF exposure estimation or the one which gives the most conservative RF EMF exposure estimation, but still lower than estimated on the basis of nominal antenna gains. Proposed method for $F_{extBeamEff}$ estimation requires conversion of nominal HPBW, B_h^{Nom} and B_v^{Nom}, to corresponding nominal RMS beam-widths, B_{h0}^{Nom} and B_{v0}^{Nom}, and corresponding nominal gain $g_{\max 0}^{Nom}$. Conversion is based on the assumption that RMS beam-width is approximated by standard deviation of Gaussian distribution functions which describes the antenna pattern. The complete calculation method consists in the following steps:

1. Convert nominal HPBW of broadcast and traffic beams, B_h^{Nom} and B_v^{Nom}, to RMS beam-widths, B_{h0}^{Nom} and B_{v0}^{Nom}, according to (D-11) and (D-12), respectively:

$$B_{h0}^{Nom} = \frac{B_h^{Nom}}{2\sqrt{\ln(4)}} \,, \tag{D-11}$$

$$B_{v0}^{Nom} = \frac{B_v^{Nom}}{2\sqrt{\ln(4)}} \,. \tag{D-12}$$

2. Calculate RMS nominal gains $g_{\max 0}^{Nom}$ of broadcast and traffic beams according to (D-13):

$$g_{\max 0}^{Nom} = \frac{2}{B_{h0}^{Nom} \cdot B_{v0}^{Nom}} \,. \tag{D-13}$$

3. Calculate RMS effective gain $g_{\max 0}^{Eff}$ of broadcast and traffic beams according to (D-14), using RMS azimuth angular spread of assumed scattering environment (σ_h) and RMS elevation angular spread of assumed scattering environment (σ_v):

$$g_{\max 0}^{Eff} = \frac{2}{\sqrt{\left(B_{h0}^{Nom}\right)^2 + \left(\sigma_h\right)^2} \cdot \sqrt{\left(B_{v0}^{Nom}\right)^2 + \left(\sigma_v\right)^2}} \,. \tag{D-14}$$

4. Calculate maximum effective gain $g_{\max}^{Eff}$ of broadcast and traffic beams according to (D-15):

$$g_{\max}^{Eff} = \frac{g_{\max}^{Nom} \cdot g_{\max 0}^{Eff}}{g_{\max 0}^{Nom}} \,. \tag{D-15}$$

5. Calculate effective extrapolation factor $F_{extBeamEff}$ as a ratio between maximum effective gains of traffic and broadcast beams according to (D-16).

$$F_{extBeamEff} = \frac{traffic\_g_{\max}^{Eff}}{broadcast\_g_{\max}^{Eff}} . \tag{D-16}$$

The presented method is limited only to use cases when maximum exposure is investigated in parts of the 5G cell where the main lobes of broadcast and traffic beams are pointed, as it allows only for approximation of maximum effective gain of given beam pattern. This method is valid for codebook-based type of beamforming, where patterns and gains of broadcast and traffic beams are predefined and known before implementation. In that sense the proposed method can be used for beamforming implementations like beam sweeping or GoB, SU-MIMO, MU-MIMO and mMIMO. In more advanced types of beamforming, like EBB, where beam weight factors (BWF) are determined 'online' based on the actual channel state information (CSI), the general concept of maximum exposure extrapolation based on comparison of broadcast and traffic beams is not applicable, because patterns and gains of these beams are not known in advance.

In Figure D-6 (Figure 6 of [8]) compared are simulated values of $F_{extBeamEff}$ obtained from full-scale 3D simulation in NLOS for UMi SC, UMa and RMa scenarios, and corresponding results of calculations according to the above simplified method. As can be noticed, calculated extrapolation factor demonstrates good alignment with results of statistical simulations, if the same values of angular spread are used by both methods. However, proposed calculation method is less computational power- and time-consuming than full statistical simulations. At the same time this method gives an overview of statistically representative range of extrapolation factor, if proper statistical distribution of angular spread is selected for calculation, i.e. mean value and standard deviation of angular spread are assumed. Even if the exact value of angular spread in the point of maximum RF EMF exposure estimation is not known, the range of calculated extrapolation factor allows to select the value which leads to the most conservative exposure estimation but at the same time is not excessively overestimated, because effective antenna gains of broadcast and traffic beam patterns are assumed for extrapolation instead of corresponding nominal gains. These conclusions allowed to include the presented method in the latest version of the standard IEC 62232, as part of its section B.8. (*Extrapolation for massive MIMO and beamforming BS*).

(a)

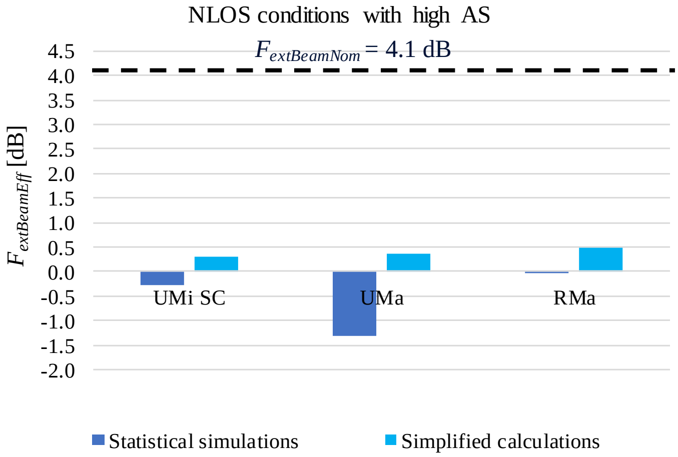

(b)

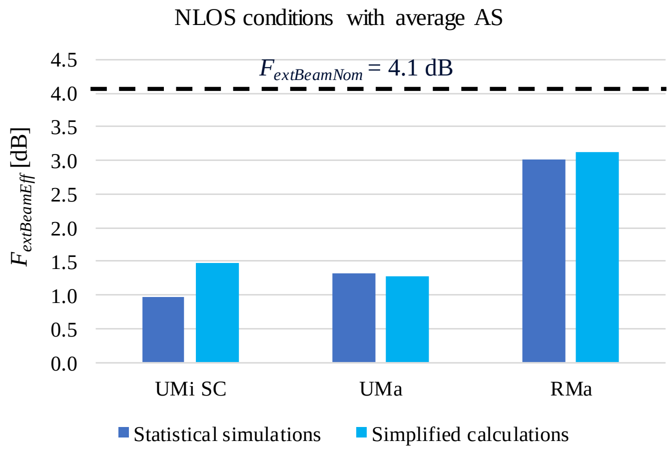

(c)

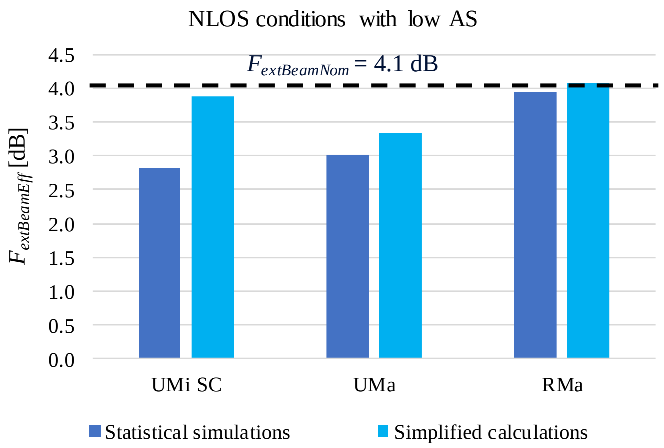

Figure D-6. Comparison of simulated and calculated values of effective extrapolation factor in NLOS conditions for practical antenna and 3GPP propagation environments of UMi SC, UMa and RMa. Calculations based on (a) mean value of angular spread plus twice standard deviation (NLOS conditions with high angular spread), (b) mean values of angular spread (NLOS conditions with average angular spread) and (c) mean value of angular spread minus twice standard deviation (NLOS conditions with low angular spread) (Figure 6 of [8])

3.3.3.2 Objectives and contributions of the study published in [7] – [8]:

The main objectives and contributions of presented study were:

- Determination, by full-scale 3D statistical simulations, of extrapolation factor for maximum RF EMF exposure estimation based on the effective antenna gains of broadcast and traffic beams in scattering environment and its comparison to nominal extrapolation factor,
- Proposal of simplified method for calculation of effective extrapolation factor and comparison of its results with the outcomes of full-scale 3D statistical simulation,
- Inclusion of obtained results as a part of the standard IEC 62232.

3.3.4 Meaning of effective antenna pattern in spectrum sharing environment

3.3.4.1 Description of the study

Results of the analysis presented in [10] indicate the impact of accuracy in antenna pattern modeling on performance evaluation in spectrum sharing environment. Intention of this study was to assess the difference in parameters of 3.5 GHz CBRS network when nominal and effective antenna patterns of CBSDs are assumed for interference evaluation. The current practice of using nominal antenna pattern for estimation of interference conditions between CBSDs does not address the antenna gain degradation and antenna pattern reshaping caused by angular spread in scattering propagation environment.

System level simulations have been conducted and presented in [10] using a model of commercially available antenna of CBSD (Nokia Integrated Directional Antenna AAQA for AirScale Micro Remote Radio Head) in UMa scenario with full 3D channel model according to 3GPP TR 38.901. Figure D-7 (Figures 3 and 4 of [10]) illustrates comparison of nominal and simulated effective antenna pattern cuts in horizontal and vertical planes, respectively. These patterns were used during simulations to determine interference conditions between CBSDs, which were further applied by proprietary algorithm for channels distribution inside CBRS network. Assumed algorithm is based on Kohonen neural networks, as described in detail in [9], and is subject of International Patent Application No.PCT/FI2017/050149.

Figure D-8 (a) (Figure 5 of [10]) presents CDFs of point-to-point interference between each pair of CBSDs obtained for nominal and effective antenna patterns from system level simulations for realistic scenario [10]. Comparison of CDFs reveals that the value of interference between each pair of investigated CBSDs can be underestimated by 6 dB if nominal antenna pattern is assumed

(a)

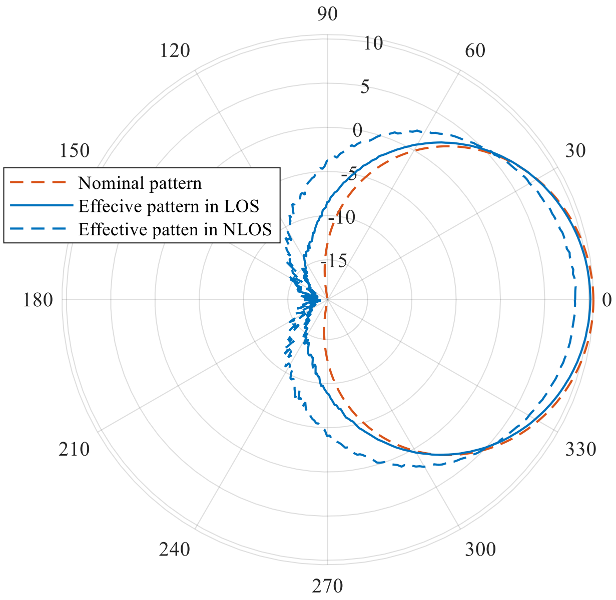

(b)

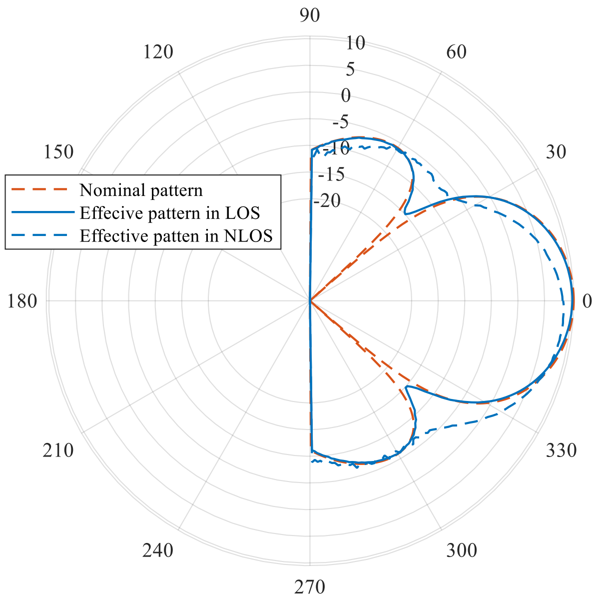

Figure D-7. Comparison of (a) horizontal cuts and (b) vertical cuts of nominal and effective patterns of assumed antenna model in 3GPP UMa environment (Figures 3 and 4 of [10])

in link budget calculation instead of effective antenna pattern. In consequence, the number of separate radio channels required to ensure co-existence between CBSDs is also different, as obtained from assumed Kohonen algorithm implemented by SAS controller. According to Figure D-8 (b) (Figure 6 of [10]), the minimal number of channels are 8 and 10 for nominal and effective patterns (in median), respectively. In other words – when nominal pattern is used for determination of interference conditions between CBSDs in UMa propagation environment, some cells suffer interference originated from other cells, because 2 additional channels are missing to ensure sufficient co-existence conditions.

Evaluation presented in [10] has been performed for the 4G long-term-evolution (LTE) type of CBSDs access points and associated antenna model. In case of 5G NR standard, which is adapted

(a)

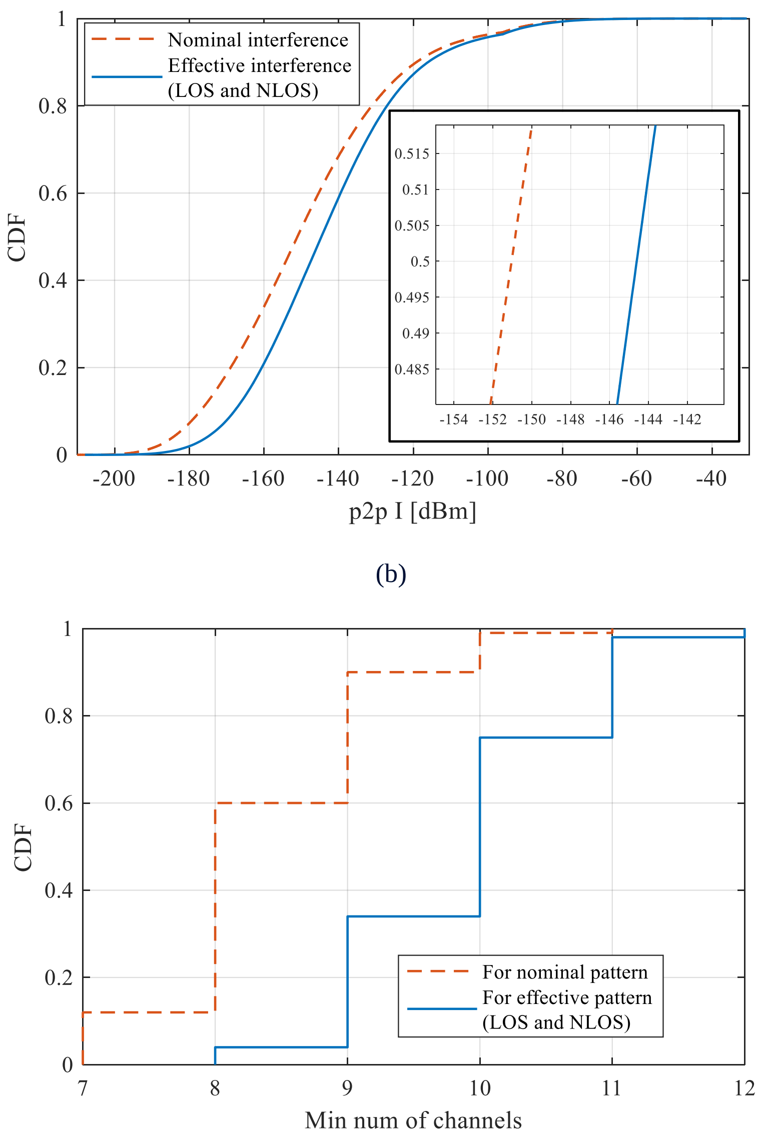

Figure D-8. CDFs of (a) point-to-point interference between each pair of CBSDs estimated with nominal and effective antenna patterns (Figure 5 of [10]) and (b) minimal number of channels required to ensure co-existence between each pair of CBSDs estimated with nominal and effective antenna patterns (Figure 6 of [10]) to utilize antenna arrays for shaping high gain narrow-beam antenna patterns via different beamforming techniques, the impact of scattering environments on effective antenna pattern is more visible. Considering that at the beginning of 2020 the CBRS Alliance, an industry organization focused on developments of CBRS, together with Federal Communication Commission (FCC) in USA enabled support for 5G NR deployments using shared spectrum in the 3.5 GHz band, the first CBSD implementations based on 5G NR standards are expected in 2021. Therefore, studies conducted in [10] suggest that enhancements of requirements applicable to CBRS system, as developed and maintained by Wireless Innovation Forum (WInnForum), should be introduced to consider effective antenna pattern for improvement of performance in future CBRS network with 5G NR implementations. In particular, specifications WINNF-TS-3002 and WINNF-TS-5006 should be updated to include definitions of effective antenna patterns, as described by (D-3) – (D-5), for more accurate determination of interference conditions in CBRS system and more efficient spectrum utilization.

3.3.4.2 Objectives and contributions of the study published in [9] – [10]:

The main objectives and contributions of presented study were:

- Evaluation, by full-scale 3D statistical simulations, what is the impact of inaccurate modeling of antenna pattern on efficiency of radio resources distribution in spectrum sharing system deployed in scattering environment,
- Indication of the approach for enhancement of requirements ensuring co-existence and efficient radio channels distribution between CBSDs.

3.3.5 Effective antenna pattern vs. MPM, as different approaches for joint modeling of antenna pattern and angular spread phenomenon in scattering environment

3.3.5.1 Description of studies

Joint modeling of beamforming and angular spread phenomenon is required to obtain an accurate estimation of realistic interference levels, as spatial filtering of multipath components by antenna pattern is sensitive to time-variant radio channel conditions. Such an approach to the modeling of 5G systems performance is more complex than simple link budget calculation, where nominal antenna gains of Tx and Rx are assumed on top of path loss model. This problem has been already investigated and described in section 3.3.1, where 3GPP channel models of TR 38.901 were used as a basis for calculations of effective antenna patterns. Determination of effective antenna pattern is then one of the approaches for modeling of angular spread impact on antenna pattern and gain in scattering environment. However, accurate estimation of effective gain may also be time-consuming, especially if is based on statistical sample of PAS generated per-UE, as indicated in Figure D-2 (Figure 5 of [6]). Therefore, an alternative approach for calculation of link budget with directional antennas in scattering environment has been described in [11] – [13]. This method, which is based on MPM geometrical channel model, presents comparable accuracy to effective antenna approach but requires less complex calculations. Comparison of both methods, i.e. effective antenna pattern based on the 3GPP channel model and MPM, is presented in section 3 of [12], where Figures 2 and 3 illustrate detailed flow charts with step-by-step instruction for each approach. Even though the aim of both methods is the same, i.e. joint modeling of beamforming and angular spread phenomenon for accurate link budget estimation, they differ in detail. For example, according to 3GPP channel model, the PAS does not depend on the assumed antenna pattern and is specific for given propagation environment. Parameters of Tx and Rx antennas are considered separately, when channel coefficients for each multipath cluster and each Tx and Rx element of antenna arrays are generated. Only afterwards the results of the spatial filtering of multipath components (clusters and rays) by the Tx and Rx nominal antenna patterns are known. In contrary, the MPM calculates the PAS using spatial filtering of multipath components by the Rx antenna pattern as seen on this antenna output. Just before that, the AoA histograms are multiplied with the proper powers to obtain the PAS seen around the Rx antenna, and at this stage the local scattering components and direct path for LOS conditions are also considered.

Effectiveness of both approaches in evaluation of interference inside 5G cell have been compared by system level simulations. Publications [12] and [13] include results of simulations conducted for 5G mMIMO cell in 3.5 GHz band and 5G small cell in mmWave band (28 GHz), respectively. In both cases realistic beam patterns and simulation parameters, according to 3GPP and International Telecommunication Union (ITU), were used. One of the conclusions, drawn after this comparison, is that for 80% of simulated samples of DL intra-cell signal-to-interference ratio (SIR) the difference between results obtained by the MPM and the 3GPP model is within 2 dB or less for LOS conditions of the UMa network operating in a 3.5 GHz band, as can be seen on Figure D-9 (Figures 7 and 8 of [12]). In the case of NLOS, the difference between both channel models is more visible. This may result from the fact that in the MPM the scatterer locations are limited to

(a)

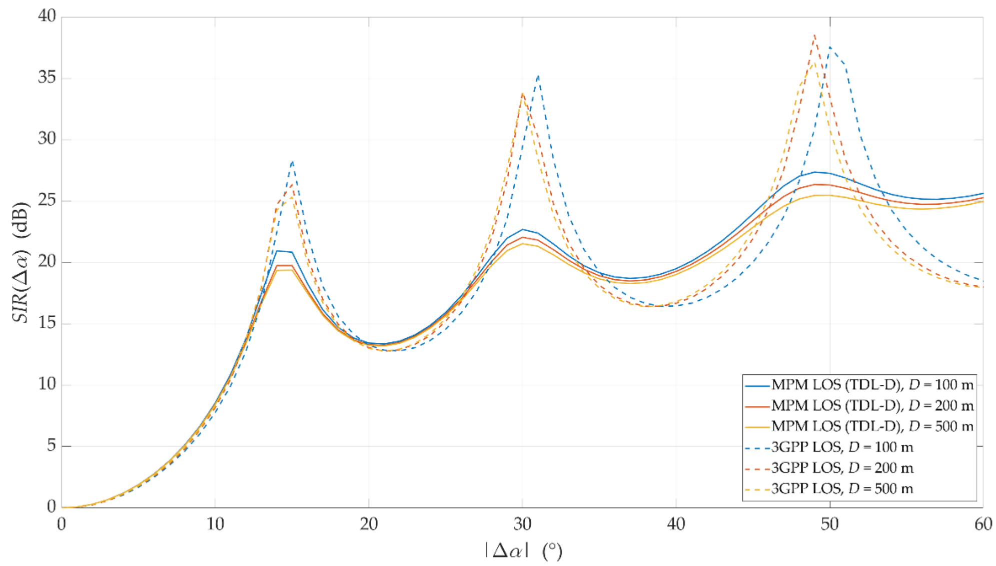

(b)

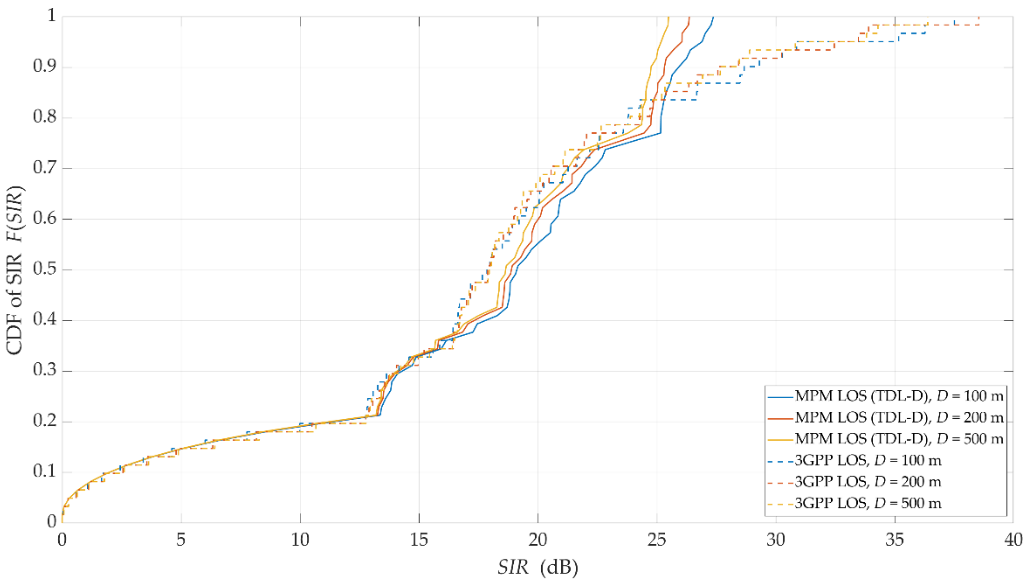

Figure D-9. (a) SIRs vs. angle of beam separation for LOS and different UE–gNodeB distances obtained for the MPM and 3GPP model (Figure 7 of [12]), and (b) CDFs of SIR for LOS and selected distances obtained for the MPM and 3GPP model (Figure 8 of [12])

the defined multi-elliptical structure related to the power delay profile (PDP) of the assumed propagation conditions, whereas in the statistical 3GPP channel model, the potential positions of the scatterers are characterized by more spatial variation. Nevertheless, both approaches demonstrate good practical solutions for accurate estimation of link budget for 5G system and beyond, and can be valid state of the art for the future studies. Especially in the context of complex co-existence studies, like presented in [14] for 5G and incumbents in the 28 GHz and 70 GHz Bands, the accurate modeling of interference, SIR and SINR is required. Even though simulation results presented in [14] were obtained from complex scenarios which assumed realistic deployment of 5G cells and incumbents, as well as 3GPP path loss models for UMa and RMa, the full 3D channel modeling was not performed. Therefore, the impact of angular spread on antenna patterns was not fully modeled and obtained values of interference are expected to be underestimated in relation to realistic values, especially for radio links which assumed NLOS between interfering and interfered antennas. The new studies are then planned to evaluate interference between 5G and incumbents in the 28 GHz and 70 GHz bands with the use of effective antenna pattern approach or MPM, which will complement results presented in [14].

3.3.5.2 Objectives and contributions of studies published in [11] – [13]:

The main objectives and contributions of presented studies were:

- Comparison of effectiveness of different approaches for joint modeling of antenna pattern and angular spread phenomenon in scattering environment,
- Justification that MPM approach can be considered as a reasonable alternative to the commonly used 3GPP channel model, especially if the performance assessment is required for strictly determined PDP.

3.4 Conclusion

The outcome of all studies conducted and published in [1] – [14] are several conclusions which indicate how the neglecting of a comprehensive modeling of beamforming and angular spread phenomenon in scattering environment can distort estimations of 5G system performance and negatively impact the NPO process. Therefore, these conclusions prove the main thesis stated at the beginning of this dissertation, i.e. **Mapping the impact of angular spread phenomenon on the beamformed antenna patterns significantly improves the accuracy of radio link budget estimation and the efficiency of 5G NPO process**. In line with this thesis the following main contributions to the current state of the art have been made, as a result of the conducted studies:

- Concept of effective antenna pattern was introduced and the method for effective gain estimation was presented, together with the proposal for improvement of accuracy in simplified radio link budget calculations,

- Invention of optimal antenna array geometry was made to increase the effective gain of antenna array under given angular spread conditions, together with the method for angular spread estimation based on minimal number of measurement results (International Patent Application No.PCT/IB2019/053142),
- Simple method for calculation of effective extrapolation factor was proposed and indicated in the standard IEC 62232 to improve estimation of maximum RF EMF exposure in scattering environments,
- Enhancements for current requirements from WInnForum specifications WINNF-TS-3002 and WINNF-TS-5006 are indicated to improve spectrum utilization inside CBRS system, especially under deployments of 5G NR-based CBSDs,
- Justification that MPM approach can be considered as a reasonable alternative to the commonly used 3GPP channel model, especially if the performance assessment is required for strictly determined PDP.

4 List of Figures

5 List of Abbreviations

3D	Three Dimensional
3GPP	3rd Generation Partnership Project
4G	4th generation of mobile communication systems
5G	5th generation of mobile communication systems
AoA	Angle of Arrival
AoD	Angle of Departure
AS	Angular Spread
ASD	Azimuth Spread of Departure
BS	Base Station
BWF	Beam Weight Factors
CBRS	Citizens Broadband Radio Service
CBSD	CBRS Device
CDF	Cumulative Distribution Function
CSI	Channel State Information
DL	Downlink
EBB	Eigen-based Beamforming
EIRP	Equivalent Isotropic Radiated Power
EMF	Electro-Magnetic Field
FCC	Federal Communication Commission
FWA	Fixed Wireless Access
gNodeB	Base station of 5G system
GoB	Grid of Beams
HPBW	Half Power Beam Width
IEC	International Electrotechnical Commission
IEEE	Institute of Electrical and Electronics Engineers
ITU	International Telecommunication Union
LOS	Line of Sight
LTE	Long Term Evolution
MIMO	Multiple Input Multiple Output

mMIMO	Massive MIMO
mmWave	Millimeter wave frequency band (30 GHz – 300 GHz)
MPM	Multi-elliptical Propagation Model
MU	Multi User
NLOS	Non Line of Sight
NPO	Network Planning and Optimization
NR	New Radio
OFDM	Orthogonal Frequency-Division Multiplexing
PAS	Power Angular Spectrum
PDP	Power Delay Profile
RF	Radio Frequency
RMa	Rural Macro
RMS	Root Mean Square
Rx	Receiver
SAS	Spectrum Access System
SINR	Signal to Interference plus Noise Ratio
SIR	Signal to Interference Ratio
SU	Single User
SubU	Suburban
TR	Technical Report
TS	Technical Specification
Tx	Transmitter
UE	User Equipment
UMa	Urban Macro
UMi SC	Urban Micro Street Canyon
WInnForum	Wireless Innovation Forum
WLAN	Wireless Local Access Network
ZSD	Zenith Spread of Departure

6 Appendix

This Appendix includes author's publications listed in Section 1 and Table A-1:

Table A-1. Titles of publications constituting the dissertation

Item	Publication's title
[1]	Modeling of radio link budget with beamforming antennas for evaluation of 5G systems
[2]	Impact of Effective Antenna Pattern on Millimeter Wave System Performance in Real Propagation Environment
[3]	Efficiency of Antenna Array Tapering in Real Propagation Environment of Millimeter Wave System
[4]	Optimized Antenna Array for Improving Performance of 5G mmWave Fixed Wireless Access in Suburban Environment
[5]	Matching in the Air: Optimal Analog Beamforming under Angular Spread
[6]	Rework the Radio Link Budget for 5G and Beyond
[7]	Impact of Effective Antenna Pattern on Radio Frequency Exposure Evaluation for 5G Base Station with Directional Antennas
[8]	Analysis of 5G Base Station RF EMF Exposure Evaluation Methods in Scattering Environments
[9]	Centralized Spectrum Sharing and Coordination Between Terrestrial and Aerial Base Stations of 3GPP-Based 5G Networks
[10]	Impact of Effective Antenna Pattern on Estimation of Interference in Citizens Broadband Radio Service
[11]	Downlink Interference in Multi-Beam 5G Macro-Cell
[12]	Modeling of downlink interference in massive MIMO 5G macro-cell
[13]	Inter-beam co-channel downlink and uplink interference for 5G new radio in mm-wave bands
[14]	Coexistence of 5G With the Incumbents in the 28 and 70 GHz Bands

Modeling of radio link budget with beamforming antennas for evaluation of 5G systems

Kamil Bechta, Marcin Rybakowski
Mobile Networks
Nokia
Wroclaw, Poland

Frank Hsieh[1], Dmitry Chizhik[2]
Nokia Bell Labs
Naperville, IL, USA[1]
Murray Hill, NJ, USA[2]

***Abstract*—Development of next generation mobile communication system (5G) is progressing rapidly. Standardization and regulatory bodies like 3rd Generation Partnership Project (3GPP) or International Telecommunication Union (ITU) are working on definition of requirements which will enable global usage of 5G and ensure sufficient co-existence with previous generations of mobile communication systems like Universal Mobile Telecommunication System (UMTS) or Long Term Evolution (LTE), as well as with other users of radio spectrum like satellite or radars. One of the key factors which distinguish 5G from previous technologies is the ability to operate in radio bands not accessible for LTE, i.e. higher than 6GHz. However, worse radio propagation conditions on higher frequencies require the usage of more directional antennas with higher maximum gains to compensate higher path loss in radio link budget. Particularly important in system evaluation and co-existence studies is correct modeling of power budget of radio link with directional antennas, both serving link and interfering link, as it impacts final signal to interference and noise ratio (SINR), which is the basis of 5G requirements evaluation. In this paper authors are concentrated on the methods of system level simulation modeling of serving link and interfering link with directional antennas on both sides of the link. For assumed simulation scenarios it is shown that use of idealized antenna gain, that neglects the angle spread, leads to an overestimation of received power of serving link by around 15dB. A simple approximate evaluation method is shown to be within less than 2dB of the detailed 3D channel simulation.**

***Index Terms*—5G, link budget, spatial filtering, beamforming, antenna pattern, channel model, effective antenna gain.**

I. Introduction

3GPP work on New Radio (NR) specification is ongoing and progressing well. Impressive content of Release 15 NR Work Item [1] motivates involved partners like radio access network equipment vendors, user equipment vendors, test equipment vendors and mobile network operators to work in unprecedented speed. It is enough to say that work on Release 8 Work Item of LTE system [2] took almost two times longer period, with relatively lower content of features, than is foreseen for Release 15 NR Work Item.

To progress according to time plan agreed in [1], 3GPP allows to reuse LTE requirements in NR specifications if feasible and technically acceptable. It happens especially in case of specifications for Frequency Range 1, which covers requirements of equipment intended for deployment in radio frequency bands below 6GHz.

As can be predicted, the set of necessary NR requirements is highly correlated with LTE requirements, although numerical values of these requirements can differ between LTE and NR. If application of LTE requirement for NR is not feasible from technical point of view, 3GPP performs new study, usually supported by simulation campaigns, based on which missing requirements are determined. However, in some cases 3GPP applies the same simulation methodologies as used during standardization processes in the past, which may be not accurate enough due to the high complexity of NR system.

In system level simulation, it is very important to correctly model the antenna gains of transmitter and receiver for the calculation of serving signal and interfering signal. This is particularly crucial in case of antennas with narrow beams and applied specific beamforming scheme.

The same approach should be also used in simple link budget based estimation where only path loss model formula and ideal antenna gains are used. The impact of radio channel on effective antenna gain should be taken into account in this kind of calculation, as omitting of this effect could lead to significant inaccuracy [4].

Following sections of this paper concentrate on presentation of three methods of antenna gains reconstruction, i.e. gains of transmitting antenna and receiving antenna which are used for calculation of serving and interfering signal received power during system level simulations. Presented methods are further compared and evaluated from the point of view of final results accuracy and calculation complexity.

This study is concentrated on mm-Wave frequency bands with antenna arrays and analog beamforming, where single RF chain per polarization is connected to antenna array and beam steering is realized by analog phase shifters.

II. Methods for Modeling of Antenna Gain for Serving and Interfering Links

A. Omni-directional path loss model with applied ideal antenna patterns gain

First method, the simplest and commonly used for high level analysis, is using antenna gains determined geometrically by the line between antenna of transmitter and antenna of receiver. In other words, the intersecting point of the line of sight (LOS) and the transmit or receive antenna pattern is taken as the transmit or receive antenna gain for the radio link. The same way is used for determination of transmitter's antenna gain and receiver's antenna gain. This method is used e.g. in [5] for calculation of link budget for serving signal as well as for interfering signal, where determined antenna gain is called as "directional array gain". Equations (1) and (2) present how this gain is determined from 3D antenna pattern.

$$G^i_{Tx} = g_{Tx}(\phi^{AoD}_{i,LOS} - \phi^{AoD}_{i,BF}, \theta^{ZoD}_{i,LOS} - \theta^{ZoD}_{i,BF}) \qquad (1)$$

$$G^i_{Rx} = g_{Rx}(\phi^{AoA}_{i,LOS} - \phi^{AoA}_{i,BF}, \theta^{ZoA}_{i,LOS} - \theta^{ZoA}_{i,BF}) \qquad (2)$$

In equations (1) and (2), G^i_{Tx} and G^i_{Rx} indicate constant gains of transmitting and receiving antennas respectively for radio link i, which carries whole power between transmitter and receiver. Implication of this is allocation of the same antenna gain to all multipath components. These gains are obtained from 3D patterns $g_{Tx}(\phi^{AoD}, \theta^{ZoD})$ and $g_{Rx}(\phi^{AoA}, \theta^{ZoA})$ of transmitting and receiving antennas respectively. $\phi^{AoD}_{i,LOS}$, $\theta^{ZoD}_{i,LOS}$, $\phi^{AoA}_{i,LOS}$ and $\theta^{ZoA}_{i,LOS}$ represent angles of LOS direction between transmitter and receiver in azimuth and elevation for radio link i. $\phi^{AoD}_{i,BF}$, $\theta^{ZoD}_{i,BF}$, $\phi^{AoA}_{i,BF}$ and $\theta^{ZoA}_{i,BF}$ represents directions in azimuth and elevation for which main beams of transmitting and receiving antennas are pointed, in case of radio link i. Graphical illustration of above relations is presented in Fig. 1 on example of receiving antenna in horizontal plane.

Key element of radio link budget is path loss, which determines what portion of energy radiated by transmitter's antenna is lost due to propagation in radio channel before it reaches receiver's antenna. Path loss for given propagation conditions is usually defined based on measurements performed with omni-directional antennas with wide vertical patterns, to maximize probability of capturing all multipath components. Therefore, in system level simulations which assume antennas with wide beams, there is no need for additional modeling of the impact of antenna pattern on the energy carried by multipath components – similarly to omni-directional measurements performed to determine path loss, simulations with omni-directional antennas assume that all multipath components are magnified by the same constant antenna gain. Additional modeling is required in case of system level simulations with narrow-beam antennas, where antenna gain is not constant and multipath components are not magnified in the same way.

Taking previous paragraph into account, radio link budget calculation with antenna gains determined according to method described in this section is correct only in case of omni-directional antennas or sectoral antennas with wide beam-widths. Therefore, resulting antenna gain obtained by this method can be called "omni-gain". Elements of statistical channel model utilized by omni-gain method are limited only to pathloss and shadow fading (black boxes in Fig. 2). However, if narrow-beam antennas are assumed for system level simulations, effect of not uniform magnification of multipath components should be additionally modeled to reflect realistic power conditions in radio channel.

B. 3D spatial channel model with applied antenna beamforming

Second method requires detailed simulation modeling of propagation phenomena for given radio channel. From the point of view of link budget with narrow-beam directional antennas, especially important is accurate reconstruction of angles of departure and angles of arrival of multipath components, and relation of these angles with 3D patterns of directional antennas of transmitter and receiver. This reconstruction can be done either by ray-tracing modeling or based on statistical model of radio channel. In this paper, statistical channel model is used to generate parameters of propagation phenomena and then to perform link budget calculations in the form of system level simulations.

Main difference between first method described in section II.A and method described in this section, is the way how the directional antennas of transmitter and receiver contribute to the outcome power of link budget. Omni-gain method assumes constant antenna gains of transmitter and receiver in link budget calculation for single realization of radio channel, as presented in equations (1) and (2). It means that all multipath components in the spatial domain are magnified by the same antenna gain, which is equivalent to the situation where all multipath components have the same angles of departure and angles of arrival. Such scenario is unrealistic even for LOS propagation conditions, where non-zero energy is carried by multipath components with angles of departure and angles of arrival different than angles of direct path.

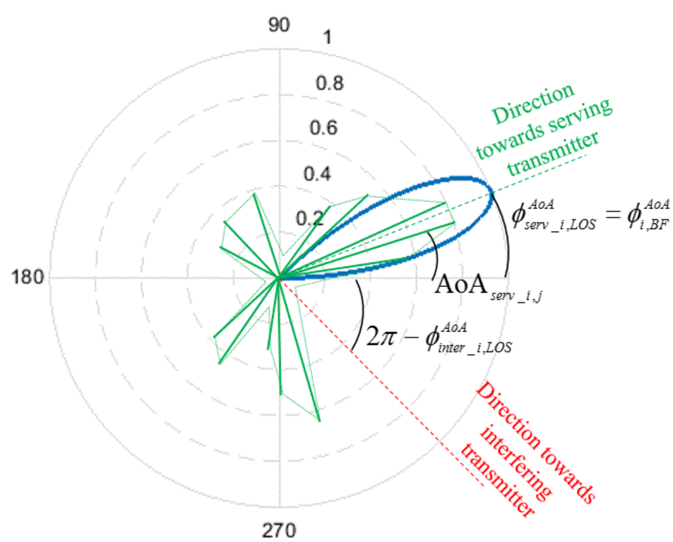

Fig. 1. Illustration of relation between receiving antenna pattern orientation in azimuth, angles towards serving/interfering transmitters and AoA of multipath components for serving link. Blue solid line presents example antenna pattern and green solid lines present example multipath components amplitudes.

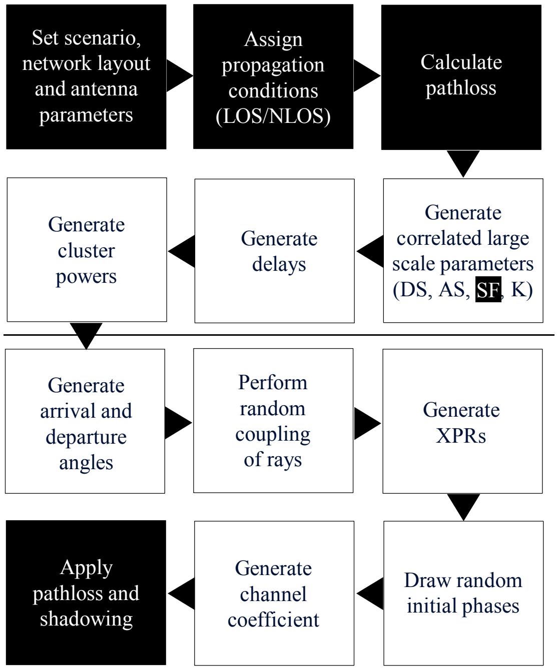

Fig. 2 Block diagram of statistical channel model reconstruction according to 3GPP [3]. Omni-gain method requires reconstruction of elements from black blocks only, whereas spatial filtering method reconstructs all illustrated channel model elements.

The second method by the usage of full 3D channel model assumes realistic modeling of spatial relation of angles of departure and angles of arrival of all multipath components with corresponding antenna patterns of transmitter and receiver, which can be called as “spatial filtering” of multipath components by antenna patterns of transmitter and receiver. Fig. 1 presents graphical illustration of this process in horizontal plane in case of receiving antenna. In this method each multipath component is magnified by gain represented by spatial pattern of receiving and transmitting antennas which correspond to angles of departure and angles of arrival of this multipath component.

$$G_{Tx}^{i,j} = g_{Tx}(\mathrm{AoD}_{i.j} - \phi_{i,BF}^{AoD}, \mathrm{ZoD}_{i.j} - \theta_{i,BF}^{ZoD}) \tag{3}$$

$$G_{Rx}^{i,j} = g_{Rx}(\mathrm{AoA}_{i.j} - \phi_{i,BF}^{AoA}, \mathrm{ZoA}_{i.j} - \theta_{i,BF}^{ZoA}) \tag{4}$$

In equations (3) and (4), $G_{Tx}^{i,j}$ and $G_{Rx}^{i,j}$ indicate gains of transmitting and receiving antennas respectively for multipath j of radio link i. $\mathrm{AoD}_{i.j}$, $\mathrm{ZoD}_{i.j}$, $\mathrm{AoA}_{i.j}$ and $\mathrm{ZoA}_{i.j}$ represent azimuth angle of departure, zenith angle of departure, azimuth angle of arrival and zenith angle of arrival respectively for multipath j of radio link i. $\phi_{i,BF}^{AoD}$, $\theta_{i,BF}^{ZoD}$, $\phi_{i,BF}^{AoA}$ and $\theta_{i,BF}^{ZoA}$ represents angles in azimuth and elevation for which main beams of transmitting and receiving antennas are pointed, in case of radio link i.

Spatial filtering method requires relatively higher complexity of simulation model and computation resources than omni-gain method, which comes from more detailed modeling of propagation phenomena, especially multipath propagation embedded in 3D channel model procedures. Comparison of simulation model components required by both methods is illustrated in Fig. 2 in the form of block diagram. This figure presents 3D channel model reconstruction procedure according to 3GPP as described in [3]. Simulations with omni-gain method reconstruct only elements marked by black blocks, whereas spatial filtering method requires reconstruction of all channel model elements presented in Fig. 2.

It should be noted that 3GPP statistical channel model described in [3] is based on measurements and ray-tracing simulation campaign. Therefore, it can be assumed that simulation results obtained according to spatial filtering method and based on this statistical model are good approximation of realistic results. As omni-gain method does not require reconstruction of all channel model components presented in Fig. 1, especially cluster powers and angles of departure and arrival, it is expected to be less accurate than spatial filtering method.

C. Omni-directional path loss model with applied effective antenna patterns gain

As described in [4], ideal maximum gain of directional antenna, measured in anechoic chamber, differs from the gain obtained in field measurements in case of analog beamforming when all antenna elements are connected to single radio frequency (RF) chain. In ideal case where as many RF chains as the antenna elements are used (full digital beamforming), and perfect channel state information can be obtained, generalized beamforming will provide full array gain, in absolute value, that grows linearly with the number of antenna elements. However, in practice the number of RF chains are limited due to hardware and cost constraints, and perfect channel state information is not available. Therefore, the full array gain indicated by generalized beamforming is out of reach. Instead, beam-steering approach is used to harvest the beamforming gain. Given limited number of RF chains and non-zero channel angular spread, the effective beamforming gain will saturate at the limit imposed by the angular spread of the channel. Simplified formula which indicates relation between ideal and effective antenna parameters is presented by equation (5) [4].

$$G_{Eff} = \frac{2}{B_v B_h} \tag{5}$$

$$B_v = \sqrt{B_{v0}^2 + \mathrm{ZS}^2} \tag{6}$$

$$B_h = \sqrt{B_{h0}^2 + \mathrm{AS}^2} \tag{7}$$

In equation (5) G_{Eff} is the effective gain, which is calculated based on effective root mean square (RMS) antenna beam-width in vertical (B_v) and horizontal (B_h) planes. B_{v0} and B_{h0} in (6) stand for nominal RMS antenna beam-width in vertical and horizontal planes respectively, whereas

ZS and AS indicate zenith angle spread and azimuth angle spread (of departure for transmitting antenna and arrival for receiving antenna).

System level simulation results included in section III.B indicate that applying the effective gain allows for the modeling accuracy of spatial filtering but keeps simulation complexity at the level of the omni-gain method.

In case of beamforming, beams are steered/optimized to maximize the power of serving signal and therefore the strongest multipath components (or the strongest cluster) of serving link are transmitted and received by main beams of transmitting and receiving antennas. This situation does not apply for interfering link, where positions of antennas are random in reference to angles of departure and angles of arrival of multipath components and therefore simple determination of effective gain is not possible for interfering links, which is the limitation from the point of view of system level simulations. Therefore, if beamforming is assumed at transmitter and receiver this method applies only for link budged calculations of serving link because effective gain can be estimated only for boresight direction of antenna pattern and in case of interfering links most of energy is received from directions other than boresight direction.

III. Comparison of System Level Simulation Results

Methods of modeling of antenna gains for serving and interfering links described in section II have been applied in system level simulations. This section presents simulation results of downlink (DL) budget for serving signal, DL budget for interfering signal and DL SINR obtained by different methods of antenna gain calculation.

A. System level simulation assumptions

System level simulations have been performed for two different sets of assumptions. First set has been agreed in 3GPP as part of Release 14 Study Item of NR and used for co-existence study [5]. Second set is the outcome of working group WP5D discussions in ITU-R on parameters for evaluation of IMT-2020 system [6][7]. Both sets, therefore, were aimed to represent typical parameters in studies which are the basis of future standards and recommendations for 5G system. Table 1 includes the most important simulation assumptions from [5] and [6][7].

B. System level simulation results

Direct comparison of impact of ideal antenna gain, spatial filtering and effective antenna gain on link budget calculation outcome is done based on Fig. 3 and Fig. 6 presenting cumulative distribution function (CDF) of received power of serving link (serving signal). Two main observations can be made here:

- Omni-gain method with ideal antenna gain overestimates received power of serving link in comparison to spatial filtering method. This is understandable, because first method assumes magnification of all multipath components' power by maximum or almost maximum gains of transmitting and receiving antennas, which is unrealistic due to different angles of arrival and angles of departure of multipath components, especially in dispersive environments like urban. Second method assumes realist magnification of multipath components' power by gains (maximum or almost maximum only in case of main multipath component/cluster) of transmitting and receiving antennas corresponding with different angles of arrival and angles of departure of these multipath components, which leads to lower total received power than obtained by first method.
- Results obtained with effective antenna gain have good alignment with results for spatial filtering method, when effective antenna gain is applied instead of ideal antenna gain for omni-gain method.

Based on above observations a general conclusion can be drawn for system level simulations of link budget with directional antennas – statistically correct results can be obtained for serving link (serving signal) if effective antenna gain is applied in omni-gain method, i.e. effective antenna gain replaces ideal antenna gain in omni-gain method. This approach allows to obtain accuracy similar to spatial filtering method with computation complexity of omni-gain method.

Table 1. Main System Level Simulation Assumptions

	3GPP [5]	**ITU-R [6][7]**
	Base Station	
Network topology and characteristics	Urban Macro; 19 sites, 3 cells (sectors) per site; ISD=200 m	Outdoor Urban hotspot (Urban Micro); 30BS s/km^2
Frequency	30 GHz	24.35 GHz
Channel bandwidth	200 MHz	
Antenna height (radiation centre)	25 m (above ground level)	6 m (above ground level)
Downtilt	0 °	10 °
Radio channel model	3GPP UMa [3]	3GPP UMi_SC [3]
	Antenna Characteristics	
Antenna pattern	Refer to Recommendation ITU-R M.2101 [8]	
Element gain	8 dBi	5 dBi
Antenna array configuration (Row × Column)	8x16 elements	8x8 elements
Conducted power (before Ohmic loss) per antenna element	22 dBm/200 MHz	10 dBm/200 MHz
	User Equipment	
User Equipment density for simultaneously transmitting terminals	1 UE/cell (sector)	3 UEs/cell
Antenna height (radiation center)	Outdoor: 1.5 m Indoor: 1.5 m – 22.5 m	1.5 m
Orientation in azimuth	-90 ° to +90 ° in the direction of the BS	-60 ° to +60 ° in the direction of the BS
Orientation in elevation	Fixed 90 °	-90 ° to +90 ° in the direction of the BS
Noise figure	9 dB	10 dB
	Antenna Characteristics	
Antenna pattern	Refer to Recommendation ITU-R M.2101 [8]	
Element gain	5 dBi	5 dBi
Antenna array configuration (Row × Column)	2x2 elements	4x4 elements

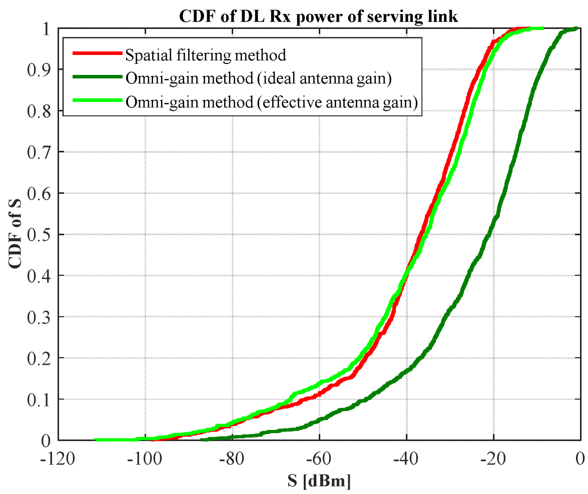

Fig. 3. System level simulation results for serving link (assumptions from 3GPP [5]).

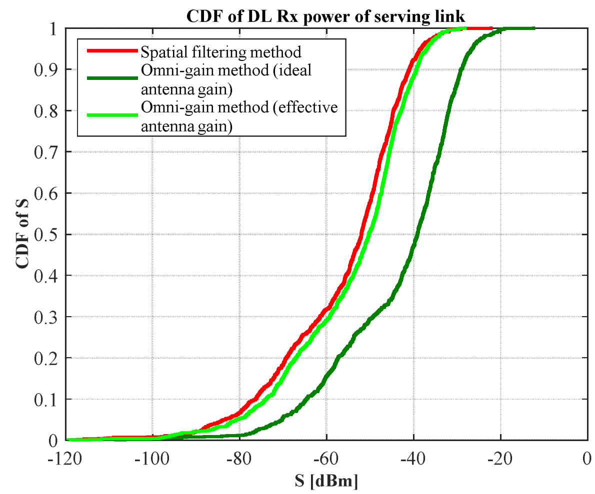

Fig. 6. System level simulation results for serving link (assumptions from ITU-R [6][7]).

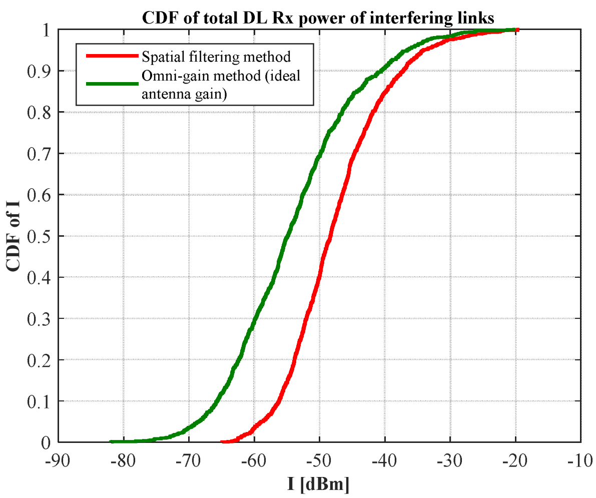

Fig. 4. System level simulation results for interfering link (assumptions from 3GPP [5]).

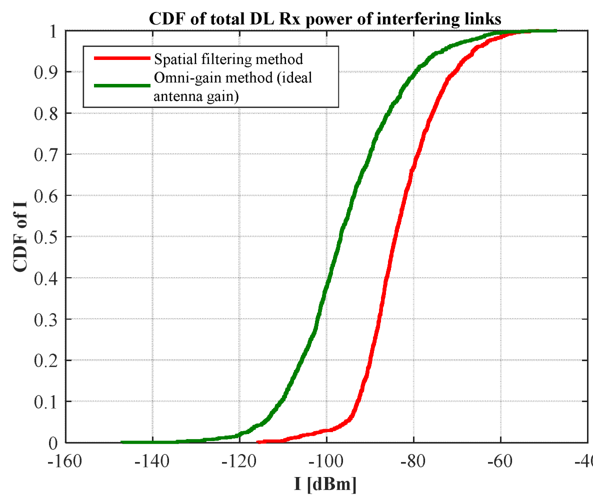

Fig. 7. System level simulation results for interfering links (assumptions from ITU-R [6][7]).

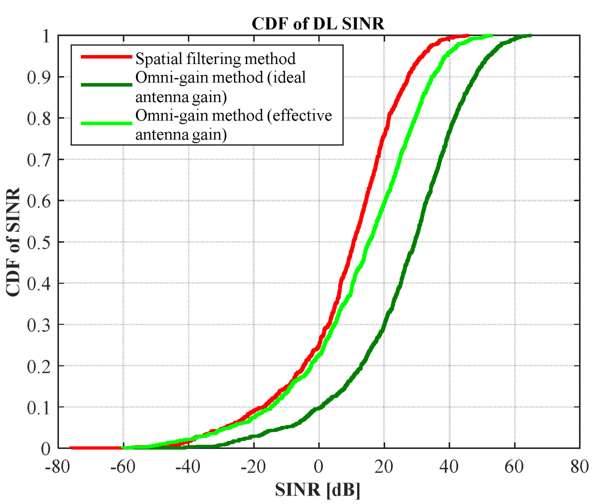

Fig. 5. System level simulation results of SINR (assumptions from 3GPP [5]).

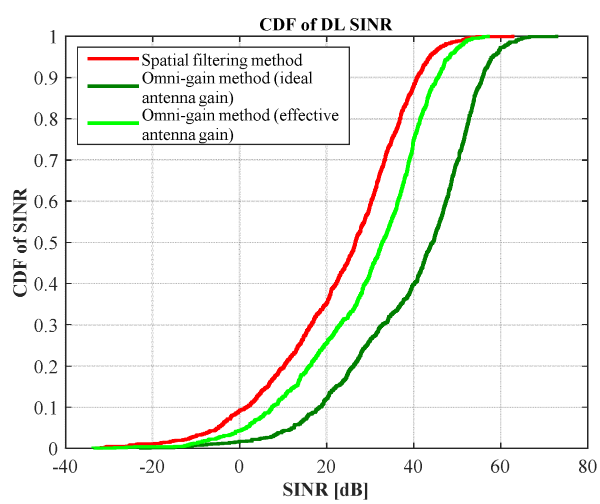

Fig. 8. System level simulation results of SINR (assumptions from ITU-R [6][7]).

TABLE 2. COMPARISON OF RADIO CHANNEL MODELING METHODS

Method	Simulation complexity	Applicability	Accuracy
Omni-gain (ideal antenna gain)	Low	Serving link Interfering link	Low
Spatial filtering	High	Serving link Interfering link	High
Omni-gain (effective antenna gain)	Low	Serving link	High

Looking at remaining simulation results, further difference between the omni-gain method with ideal antenna gain and the spatial filtering method are visible. In case of CDF of total received power from all interfering links presented in Figs. 4 and 7, simulation results indicate that the omni-gain method underestimates interfering signal power in reference to the spatial filtering method. However, it should not be taken as the spatial filtering method always results in higher interference power than the omni-gain method. This situation depends on assumed beam-width of antennas, radio channel dispersion as well as positions of receiver, transmitter of serving signal and transmitters on interfering signals.

Using the spatial filtering method in calculation of link budget with directional antennas leads then to statistically lower power of serving signal and higher power of interfering signal in comparison to omni-gain method with ideal antenna gain for presented scenarios, which in turn causes difference in SINR statistics. Figs. 5 and 8 present CDF of SINR which is noticeably lower in case of spatial filtering method. Value of SINR determined during system level simulations which are part of 5G system performance evaluation or co-existence study has direct impact on final requirements, recommendations or regulations. For example, simulation study performed by 3GPP and summarized in [5] aimed to define Adjacent Channel Leakage Ratio (ACLR) and Adjacent Channel Selectivity (ACS) requirements for ensuring intra-system and inter-system co-existence for NR equipments. Determination of these requirements was based on the radio channel capacity change in the victim system upon the presence of interference from the aggressor system. As channel capacity depends on SINR, particularly important is accurate calculation of received power of serving link and interfering links. Therefore, it is crucial to correctly perform system level simulations, where link budget calculations lead to realistic outcome values.

Final short summary of comparison between all described methods is presented in Table 2, where attributes like simulation complexity, applicability and accuracy are considered.

IV. CONCLUSION

Main purpose of this publication is to present results of link budget calculations in system level simulations using different methods of modeling the gains of directional antennas. A commonly used simple method has been compared with detailed and comprehensive approach, which led to noticeable difference in final simulation results.

The spatial filtering method employed in a 3D channel model provides more realistic simulation results than the omni-gain method. It should be ensured that studies of key 5G system requirements use accurate simulation methodology and avoid using the omni-gain method in scenarios where directional antennas are deployed. If simplified simulations have to be performed, it is suggested to apply the effective antenna gain.

Wrongly estimated SINR gives inaccurate picture of system performance, capacity and coverage as well as may lead to suboptimal deployments of first 5G networks, which in most cases will be adjustable only after initial filed measurements under real operation conditions.

Not only intra-system performance of first 5G deployments can be impacted by inaccurately determined co-existence requirements but also performance of other systems working in the same or adjacent frequency bands can be impacted, as underestimated or overestimated power of interference signals originated in 5G network may lead to wrongly concluded co-existence conditions.

Next publications are going to further compare presented methods of directional radio link budget calculations from the point of view of impact on final 5G requirements, especially co-existence. Comparison will be presented not only for channel model utilized by 3GPP [3] but also for NYU channel model [9] which is less dispersive, as channel dispersion has direct impact on difference in outcomes of omni-gain method and spatial filtering method.

REFERENCES

[1] 3GPP Radio Access Network Working Group, “Revised WID on New Radio Access Technology”, RP-171485.

[2] 3GPP Radio Access Network Working Group, “Revised LTE WIDs”, RP-060747.

[3] 3GPP Radio Access Network Working Group, “Study on channel model for frequencies from 0.5 to 100 GHz (Release 14)”, 3GPP TR 38.901 V14.2.0.

[4] J. Du, E. Onaran, D. Chizhik, S. Venkatesan, R. A. Valenzuela, “Gbps User Rates Using mmWave Relayed Backhaul with High Gain Antennas”, IEEE Journal on Selected Areas in Communications 2017.

[5] 3GPP Radio Access Network Working Group, “Study on New Radio Access Technology; RF and co-existence aspects (Release 14)”, 3GPP TR 38.803 V14.0.0.

[6] ITU-R WP5D, “Liaison Statement To Task Group 5/1, Attachment 2 On Spectrum Needs To A Liaison Statement To Task Group 5/1”, Document 5-1/36-E, 28 February 2017.

[7] ITU-R TG 5/1, “System Parameters And Propagation Models To Be Used In Sharing And Compatibility Studies”, Annex 1 to Document 5-1/173-E, 2 October 2017.

[8] ITU-R, “Modelling and simulation of IMT networks and systems for use in sharing and compatibility studies”, Recommendation ITU-R M.2101-0.

[9] M. K. Samimi and T. S. Rappaport, “3-D millimeter-wave statistical channel model for 5G wireless system design,” IEEE Transactions on Microwave Theory and Techniques, vol. 64, no. 7, pp. 2207–2225, July 2016.

[2]

Impact of Effective Antenna Pattern on Millimeter Wave System Performance in Real Propagation Environment

Kamil Bechta[1], Marcin Rybakowski[1], Jinfeng Du[2]
[1] NOKIA, Mobile Networks, Wroclaw, Poland, kamil.bechta@nokia.com
[2] NOKIA, Bell Labs, Holmdel, NJ 07733, USA

***Abstract*—Utilization of large antenna arrays in millimeter wave bands is one of the main differentiators in the forthcoming deployment of new mobile communication systems. However, the prevailing simulation practice for link budget, inter-site interference and co-existence studies is to use nominal antenna pattern rather than the effective pattern, leading to inaccurate received power and interference level estimation. We visualize the impact of three-dimensional (3D) channel models of 3rd Generation Partnership Project (3GPP) on effective antenna array patterns and find that the downlink (DL) Signal to Interference plus Noise Ratio (SINR) can be overestimated by 10 to 17 dB in Non Line of Sight (NLOS) scenario when using nominal beam pattern rather than effective pattern.**

***Index Terms*—angular spread, effective gain, link budget, millimeter wave.**

I. Introduction

One of the main differentiators of 5th generation of mobile communication systems (5G) is utilization of frequency bands above 6 GHz, not used by previous generations like 3G and 4G. Negative impact of higher carrier frequencies on propagation conditions in practice is mitigated by arrays with more antenna elements, which increases effective aperture of the antenna. Another advantage of antenna array is concentration of transmitted power in the direction of receiver by shaping antenna pattern in the form of spatial beams on both sides of radio link. With increasing number of antenna elements in the array the nominal gain of the antenna array increases and the half-power beam-width (HPBW) decreases. In more challenging propagation conditions, the maximum realizable antenna array gain, the effective beam pattern and its associated HPBW differ from nominal values. Difference between nominal and the effective patterns in the radio channel with scattering depends on angular spread introduced by the real radio channel. In [1] authors presented estimation of effective antenna gain based on root-mean square (RMS) angular spread of statistical channel model, whereas measurement results for indoor and suburban propagation conditions are reported in [2] and [3], respectively. In both measurement scenarios the 90% effective azimuth gain degradation of 4.5 dB or more was observed in reference to the nominal gain of 14.5 dBi. This demonstrates that nominal antenna patterns, as measured in anechoic chamber, are valid only in free space propagation conditions. This conclusion is particularly important in the context of simulation campaigns which aim to estimate performance of 5G system before the commercial deployment begins. Reliable simulation results ensure correctness of minimum requirements for 5G equipment and help to better optimize first 5G networks deployed in the field.

The need for effective antenna pattern inclusion in system level simulations of mobile networks have been already indicated in [4], where the performance of Long Term Evolution (LTE) system was evaluated via simulation using nominal and effective antenna patterns. The effective antenna pattern was obtained by convolution of nominal antenna pattern and Power Angular Spectrum (PAS) for assumed propagation environment model. Simulation results presented in [4] indicate that up to 40% deviation from realistic value of LTE downlink (DL) throughput can occur when nominal antenna pattern is assumed instead of effective antenna pattern. Study for 5G scenario with analog beamforming in millimeter waves (mmWave) range was presented in [5]. In that case the simulation results of radio link budget for serving link and interfering links were presented for nominal antenna gain and effective antenna gain. Effective antenna gain was obtained by spatial filtering of multipath components modeled with 3rd Generation Partnership Project (3GPP) approach [7] by nominal antenna pattern. Final results obtained from that study indicate that DL can be overestimated even by 20 dB if nominal antenna pattern is assumed instead of effective antenna pattern, for scenario used in simulations.

Studies presented in [4] and [5] both assumed omni-directional path loss model defined by 3GPP in [6] and [7] respectively. By default, these path loss models assume omni-directional antennas on both sides of simulated radio link. When directional antennas are used, the effective antenna pattern should be determined for that specific environment, as presented in [4] and [5], because nominal antenna gain is not valid for environments other than free space, as proven by measurement results in [2] and [3]. Even though 3GPP in [7] introduced possibility for spatial filtering of clustered delay line (CDL) models by antenna pattern, this approach is not commonly used in 5G system evaluation as it does not provide effective antenna pattern model for simple link budget calculation. However, it has been noticed in 3GPP [8] that the spatial filtering of the CDL models from

[7] using the base station (BS) antenna pattern has a major impact on the channel seen by the user equipment (UE). Simple model of effective antenna pattern has been proposed in [4], however, so far has not been validated for 5G channel model [7] and antenna patterns of large antenna arrays. Partial solution has been proposed in [9], where correction factor is applied on top of directional path loss model to calculate link budget for other directions of transmitter (Tx) and receiver (Rx) antennas than boresight alignment.

In the remaining part of this paper we present continuation of study included in [5]. In Sec. II effective antenna patterns are presented for different antenna array sizes and channel models defined by 3GPP [7]. Comparison of link budget simulation results for serving link and interfering links and the impact of effective antenna pattern on 5G system performance are included in Sec. III. Conclusion is in Sec. IV.

II. Effective Antenna Pattern

Nominal antenna array patterns follow the model presented in [7] and [10]. Each effective antenna pattern has been obtained as an average from 1000 convolutions of nominal antenna pattern with single realization of PAS generated according to statistical model described in [7].

Nominal antenna array gain in the free space propagation conditions can be expressed by following equation [1]:

$$g_{\max}^{Nom} = \frac{2}{B_{ho} \cdot B_{vo}} = N \cdot G_e \tag{1}$$

where $g_{\max}^{Nom}$ is the maximum nominal antenna array gain, B_{ho} and B_{vo} are the nominal RMS beamwidth in horizontal and vertical planes (in radians), respectively, N is the number of antenna elements in the array, and G_e is the gain of single antenna element. Equations (2)-(4) give the overview how effective antenna patterns have been obtained.

$$g^{Eff}(\phi_0,\theta_0) = \int_{-180^\circ}^{180^\circ}\int_{0^\circ}^{180^\circ} g^{Nom}(\phi,\theta)\cdot p(\phi-\phi_0,\theta-\theta_0)\,d\phi d\theta \tag{2}$$

$$g_{Az}^{Eff}(\phi_0) = g^{Eff}(\phi_0,\theta_0=90^\circ) = \int_{-180^\circ}^{180^\circ} g^{Nom}(\phi,\theta=90^\circ)\cdot p_{Az}(\phi-\phi_0)d\phi \tag{3}$$

$$g_{Ele}^{Eff}(\theta_0) = g^{Eff}(\phi_0=0^\circ,\theta_0) = \int_{0^\circ}^{180^\circ} g^{Nom}(\phi=0^\circ,\theta)\cdot p_{Ele}(\theta-\theta_0)d\theta \tag{4}$$

In above equations g^{Eff} indicates three-dimensional (3D) effective antenna pattern, whereas g^{Nom} indicates 3D nominal antenna pattern. g_{Az}^{Eff} and g_{Ele}^{Eff} indicate azimuth and elevation cuts of effective antenna pattern, ϕ and θ define angular domain in azimuth and elevation, respectively, whereas ϕ_0 and θ_0 indicate boresight direction between Tx and Rx in azimuth and elevation, respectively. p_{Az} and p_{Ele} represent realizations of PAS in azimuth and elevation.

RMS azimuth spread of departure and arrival (ASD and ASA) and RMS zenith spread of departure and arrival (ZSD and ZSA) used in simulations are presented in Table I. However, it should be noted that final characteristics of multipath components used in convolution operation depends not only on general RMS angular spread but also on other parameters, e.g. cluster angular spread, delay spread and scaling factors as defined in [7]. All these together determines the shape of effective antenna pattern for given realization of radio channel between transmitter and receiver.

Effective patterns of antenna arrays are presented in Figures 1-6 and can be summarized as follow:

- Due to presence of strong directive path in line of sight (LOS) condition, effective antenna gain of main lobe is close to nominal gain, whereas in Non Line of Sight (NLOS) conditions, where strong directive path is not present, effective gain of main lobe is noticeably lower.
- Angular spread of radiated energy in horizontal plane causes increase of effective antenna gain of side lobes in reference to nominal gain of side lobes in both LOS and NLOS conditions. This is more visible on Rx side, which is characterized by higher angular spread than Tx side.
- Change in the level of side lobes is less visible in vertical plane due to lower angular spread than in horizontal plane. Additionally, effective pattern of Tx antenna array is shifted in angular domain by several degrees due to statistical offset in zenith of departure modeled in [7].

III. Simulation Results of 5G System Performance

This section presents results of system level simulations of 5G network performance. Simulated were two scenarios: Urban Macro (UMa) and Urban Micro Street Canyon (UMi SC) according to simulation assumptions made by 3GPP in [11], which include 3D channel model and 3D antenna patterns. Main parameters of simulation scenarios are summarized in Table II.

Table I Parameters of Antenna Array and Channel Model

Channel model	3GPP UMa **[7]**		3GPP UMi SC **[7]**	
	LOS	**NLOS**	**LOS**	**NLOS**
Array size of BS	16x16		8x8	
RMS ASD [deg]	16.6	21.6	13.7	15.6
RMS ZSD [deg]	0.6	2.8	1.2	1.1
Nominal gain [dBi]	32.0		26.0	
Effective gain [dBi]	31.5	21.0	25.5	17.5
Nom. HPBW in az. [deg]	6.3		12.6	
Eff. HPBW in az. [deg]	6.6	26.0	13.0	43.2
Array size of UE	2x2			
RMS ASA [deg]	64.6	48.9	41.0	49.3
RMS ZSA [deg]	8.9	11.1	3.8	7.3
Nominal gain [dBi]	11.0		11.0	
Effective gain [dBi]	10.5	6.0	10.5	6.0
Nom. HPBW in az. [deg]	50.2		50.2	
Eff. HPBW in az. [deg]	50.4	166.0	50.8	167.0

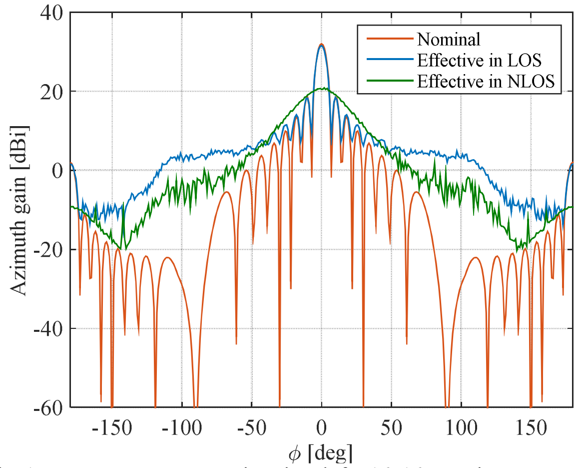

Fig. 1. Tx antenna pattern cut in azimuth for 16x16 array in UMa

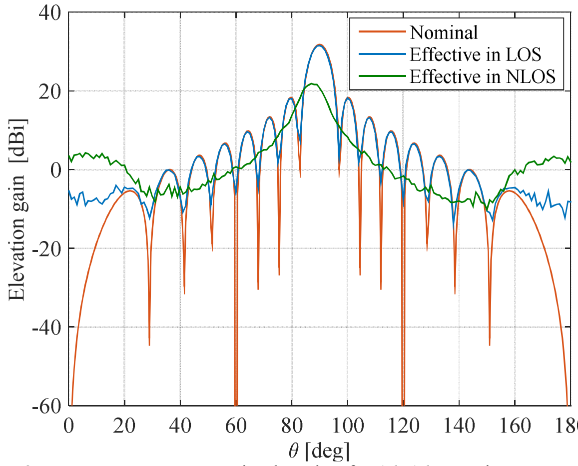

Fig. 2. Tx antenna pattern cut in elevation for 16x16 array in UMa

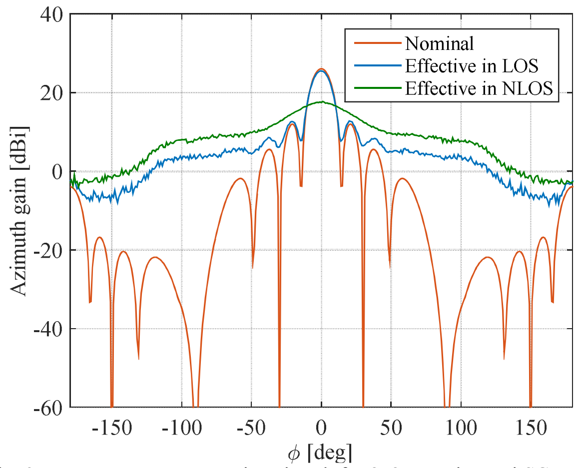

Fig. 3. Tx antenna pattern cut in azimuth for 8x8 array in UMi SC

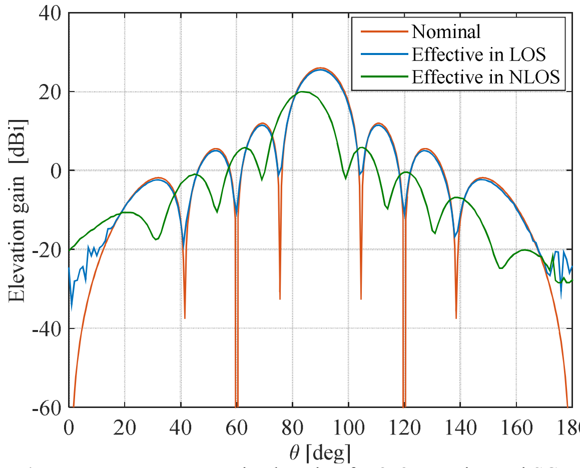

Fig. 4. Tx antenna pattern cut in elevation for 8x8 array in UMi SC

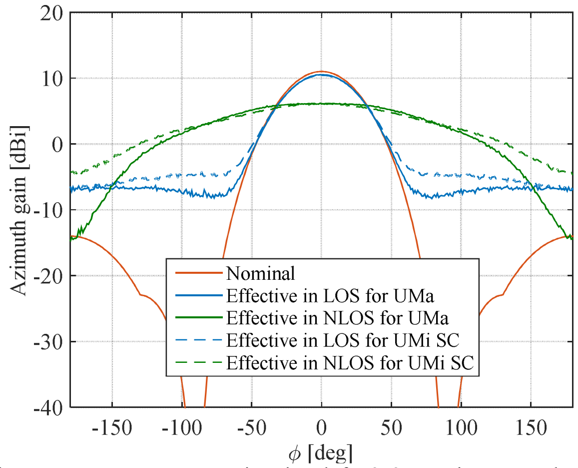

Fig. 5. Rx antenna pattern cut in azimuth for 2x2 array in UMa and UMi

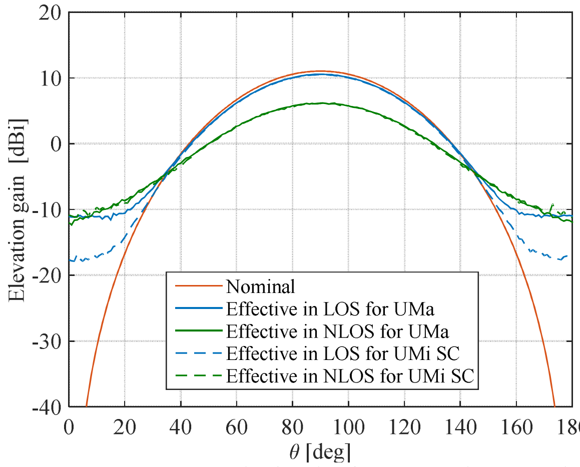

Fig. 6. Rx antenna pattern cut in elevation for 2x2 array in UMa and UMi

Outcome of simulations are cumulative distribution function (CDF) curves, which present DL Rx power from serving link (DL *S*), total DL power of inter-cell interfering links (DL *I*) and DL Signal to Interference plus Noise Ratio (DL *SINR*). DL *S* and DL *I* have been calculated as link budget presented in (5):

$$P_{Rx} = \frac{P_{Tx} \cdot G_{Tx} \cdot G_{Rx}}{PL} \tag{5}$$

where P_{Rx} and P_{Tx} are Rx and Tx power respectively, whereas G_{Rx} and G_{Tx} are Rx and Tx antenna gains used for

[2]

calculation of given radio link. *PL* indicates path loss of given radio link.

When power budget of link *i*, either for serving link or interfering link, was calculated, gains of Tx/Rx antennas were determined by Gn^{i}_{Tx}/Gn^{i}_{Rx} or Ge^{i}_{Tx}/Ge^{i}_{Rx} for nominal or effective antenna patterns respectively. These gains are presented by (6)-(9).

$$Gn^{i}_{Tx} = g^{Nom}_{Tx}\left(\phi^{AoD}_{i,LOS} - \phi^{AoD}_{i,BF}, \theta^{ZoD}_{i,LOS} - \theta^{ZoD}_{i,BF}\right) \quad (6)$$

$$Gn^{i}_{Rx} = g^{Nom}_{Rx}\left(\phi^{AoA}_{i,LOS} - \phi^{AoA}_{i,BF}, \theta^{ZoA}_{i,LOS} - \theta^{ZoA}_{i,BF}\right) \quad (7)$$

$$Ge^{i}_{Tx} = \sum_{j=1}^{N_i} Gn^{i,j}_{Tx} \cdot P_{i,j} = g^{Eff}_{Tx}\left(\phi^{AoD}_{i,LOS} - \phi^{AoD}_{i,BF}, \theta^{ZoD}_{i,LOS} - \theta^{ZoD}_{i,BF}\right) \quad (8)$$

$$Ge^{i}_{Rx} = \sum_{j=1}^{N_i} Gn^{i,j}_{Rx} \cdot P_{i,j} = g^{Eff}_{Rx}\left(\phi^{AoA}_{i,LOS} - \phi^{AoA}_{i,BF}, \theta^{ZoA}_{i,LOS} - \theta^{ZoA}_{i,BF}\right) \quad (9)$$

Gains of (6)-(9) are obtained from 3D nominal/effective patterns $g_{Tx}(\phi^{AoD}, \theta^{ZoD})$ and $g_{Rx}(\phi^{AoA}, \theta^{ZoA})$ of transmitting and receiving antennas, respectively. $\phi^{AoD}_{i,LOS}$, $\theta^{ZoD}_{i,LOS}$, $\phi^{AoA}_{i,LOS}$ and $\theta^{ZoA}_{i,LOS}$ represent angles of LOS direction between Tx and Rx in azimuth and elevation for radio link i. $\phi^{AoD}_{i,BF}$, $\theta^{ZoD}_{i,BF}$, $\phi^{AoA}_{i,BF}$ and $\theta^{ZoA}_{i,BF}$ represents directions in azimuth and elevation for which main beams of transmitting and receiving antennas are pointed (beamformed), in case of radio link i. In (8) and (9), $Gn^{i,j}_{Tx}$ and $Gn^{i,j}_{Rx}$ indicate nominal gains of transmitting and receiving antennas respectively for multipath j of radio link i and with more details are presented in [5]. $P_{i,j}$ is the power carried by multipath j ($j = 1,2,...,N_i$) of radio link i and $\sum_{j=1}^{N_i} P_{i,j} = 1$.

Simulation results of DL *S* are presented in Figs. 7 and 8 for UMa and UMi SC, respectively. LOS and NLOS propagation conditions have been plotted separately for better illustration of effective gain impact on final results. It should be noted here that DL *S* is calculated under assumption that beam-steering is realized on both sides of radio links and therefore gains of main beams of Tx and Rx antennas apply. Because of that, in LOS conditions the difference between DL *S* curves for nominal pattern and effective pattern is much smaller than the difference between the same curves in NLOS conditions, as suggested by the effective antenna patterns illustrated on Figs. 1-6. Obtained results indicate that use of nominal antenna gain in link budget calculation of DL *S* with beam-steering leads to overestimation of received power in reference to calculations with effective antenna gain. In LOS this difference is in the range of 1 – 2 dB, whereas in NLOS it increases to 15 – 17 dB for assumed simulation scenarios.

For DL *I* (Fig. 9) the situation is opposite, i.e. usage of nominal antenna gain causes underestimation of interference power in reference to results obtained for effective antenna gain. It happens because directions of most of interfering links are aligned with sidelobes of Tx and Rx antennas. Figures 1, 3 and 5 show that effective azimuth level of side-lobes is noticeably higher than the nominal level for both LOS and NLOS and therefore leads to higher values of received interference power.

Overestimated DL *S* and underestimated DL *I* cause that effective DL *SINR* is lower than the nominal DL *SINR*, which is illustrated on Fig. 10. In UMi SC scenario the difference is up to 10 dB, whereas for UMa even up to 17 dB.

TABLE II GENARAL SIMULATION ASSUMPTION

	UMa	**UMi SC**
Base Station		
Network topology and characteristics	19 sites, 3 cells (sectors) per site; ISD = 200 m	3 cluster circles are in a macro cell. 1 cluster circle has 1 micro BS. Micro cell radius = 28.9 m
Frequency/Channel bandwidth	28 GHz / 200MHz	
Antenna height (radiation center)	25 m (above ground level)	10 m (above ground level)
Radio channel model	3GPP UMa [7]	3GPP UMi SC [7]
Element gain	8 dBi	
Antenna array configuration	16x16 elements	8x8 elements
Conducted power (before Ohmic loss)	43 dBm/200 MHz	33 dBm/200 MHz
User Equipment		
User Equipment density for simultaneously transmitting terminals	1 UE/macro cell (sector)	1 UEs/micro cell
Antenna height (radiation center)	Outdoor (80% of UEs): 1.5 m Indoor (20% of UEs): 1.5-22.5 m	Outdoor (20% of UEs): 1.5 m Indoor (80% of UEs): 1.5-22.5 m
Orientation in azimuth / elevation	-90 ° to +90 ° in the direction of the BS / Fixed 90 °	
Noise figure	10 dB	
Element gain	5 dBi	
Antenna array configuration	2x2 elements	

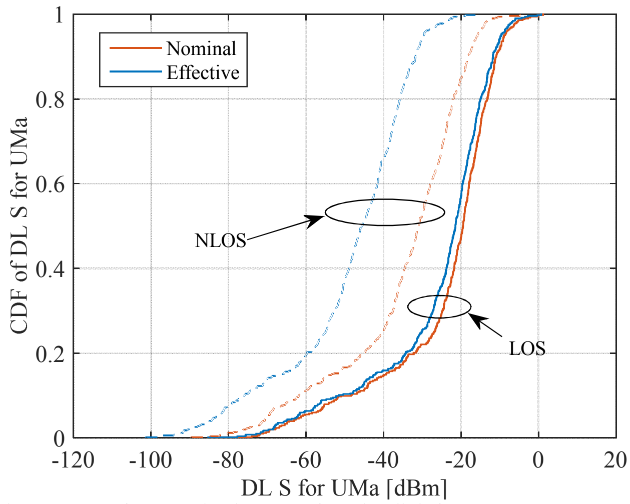

Fig. 7. CDFs of DL received power of serving link for UMa

[2]

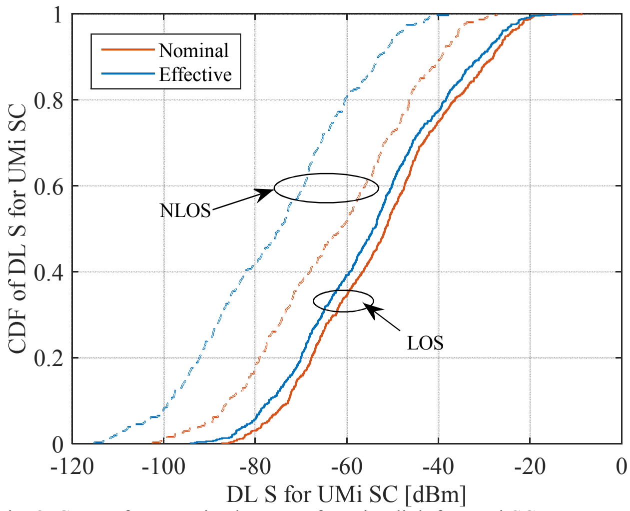

Fig. 8. CDFs of DL received power of serving link for UMi SC

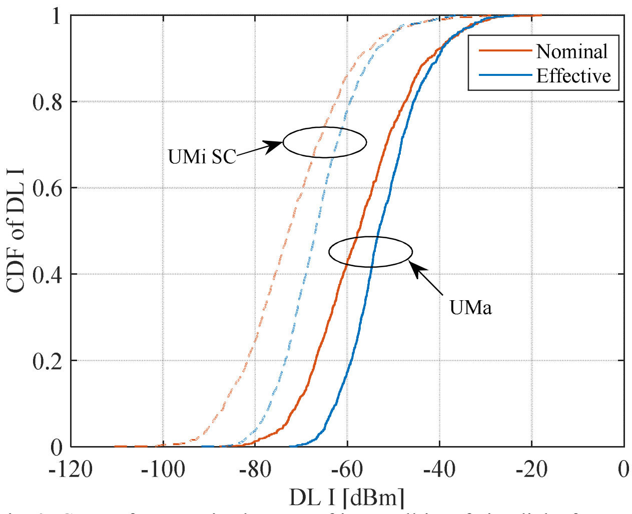

Fig. 9. CDFs of DL received power of inter-cell interfering links for UMa and UMi SC (combined LOS and NLOS links)

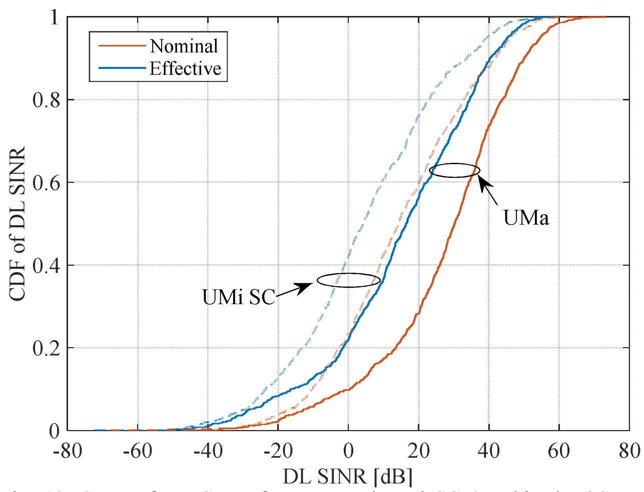

Fig. 10. CDFs of DL SINR for UMa and UMi SC (combined LOS and NLOS links)

IV. CONCLUSION

We have presented simulation results visualizing the impact of 3GPP UMa and UMi SC channel models on effective antenna array patterns. It has been described that simplified 5G system level simulations, where nominal antenna array pattern is assumed instead on effective (realistic for given radio channel) pattern, lead to inaccurate link budget results. Especially, for NLOS conditions the SINR can be overestimated even by 17 dB.

SINR wrongly estimated due to usage of inaccurate antenna patterns gives inaccurate picture of system performance, capacity and coverage. It may lead to suboptimal deployments of first 5G networks, which in most cases will be adjustable only after initial filed measurements under real operation conditions. Not only intra-system performance of first 5G deployments can be impacted by wrongly determined co-existence requirements but also performance of other systems working in the same or adjacent frequency bands can be impacted, as underestimated or overestimated power of interference signals originated in 5G network may lead to wrongly concluded co-existence conditions.

REFERENCES

[1] J. Du, E. Onaran, D. Chizhik, S. Venkatesan, R. A. Valenzuela, “Gbps User Rates Using mmWave Relayed Backhaul with High Gain Antennas”, IEEE Journal on Selected Areas in Communications, vol. 35, pp. 1363-1372, Jun. 2017.

[2] D. Chizhik, J. Du, R. Feick, M. Rodriguez, G. Castro, R. A. Valenzuela, “Path loss, beamforming gain and time dynamics measurements at 28 GHz for 90% indoor coverage”, European Conference on Antennas and Propagation (EuCAP), 2018.

[3] J. Du, D. Chizhik, R. Feick, M. Rodriguez, G. Castro, R. A. Valenzuela, “Suburban Fixed Wireless Access Channel Measurements and Models at 28 GHz for 90% Outdoor Coverage”, arXiv: 1807:03763, 2018.

[4] D. A. Zarbouti, G. V. Tsoulos, G. E. Athanasiadou, ”Effective radiation pattern concept for wireless systems analysis”, Electronics Letters, vol. 53, pp. 1160-1162, Aug. 2017.

[5] K. Bechta, M. Rybakowski, F. Hsieh, D. Chizhik, „Modeling of radio link budget with beamforming antennas for evaluation of 5G systems”, IEEE 5G World Forum, 2018.

[6] 3GPP Radio Access Network Working Group, “Study on channel model for LTE (Release 12)”, 3GPP TR 36.873 V12.2.0.

[7] 3GPP Radio Access Network Working Group, “Study on channel model for frequencies from 0.5 to 100 GHz (Release 15)”, 3GPP TR 38.901 V15.0.0.

[8] Keysight, “Updated channel model spatial filtering using 38.803 gNB Tx antenna assumptions”, 3GPP TSG-RAN WG4 Meeting #84bis, 2017.

[9] J. M. Kelner, C. Ziolkowski, “Path Loss Model Modification for Various Gains and Directions of Antennas”, European Conference on Antennas and Propagation (EuCAP), 2018.

[10] 3GPP Radio Access Network Working Group, “Radio Frequency (RF) requirement background for Active Antenna System (AAS) Base Station (BS) (Release 13)”, 3GPP TR 37.842 V13.0.0.

[11] 3GPP Radio Access Network Working Group, “Study on New Radio Access Technology; RF and co-existence aspects (Release 14)”, 3GPP TR 38.803 V14.0.0.

[3]

Efficiency of Antenna Array Tapering in Real Propagation Environment of Millimeter Wave System

Kamil Bechta[1], Marcin Rybakowski[1], Jinfeng Du[2]
[1] NOKIA, Mobile Networks, Wroclaw, Poland, kamil.bechta@nokia.com
[2] NOKIA, Bell Labs, Holmdel, NJ 07733, USA

***Abstract*—In real propagation conditions the angular spread of radio channel reshapes the effective antenna pattern and impacts the efficiency of tapering method in comparison to the nominal antenna pattern determined in anechoic chamber. This paper presents corresponding simulation results obtained for Urban Macro (UMa) and Urban Micro Street Canyon (UMi SC) channel models of 3rd Generation Partnership Project (3GPP). Simulations indicate that for effective antenna pattern the first Sidelobe Suppression Level (SSL) can decrease to 16 dB, in Line of Sight (LOS) conditions, or even to 2 dB, in Non Line of Sight (NLOS) conditions, in comparison to SSL of 20 dB for the nominal antenna pattern.**

***Index Terms*—angular spread, antenna array, effective gain, millimeter wave, side lobe level, tapering.**

I. Introduction

Deployment of 5th generation of mobile communication system (5G) in millimeter wave (mmWave) frequency range is, in majority of cases, connected with implementation of directional antennas with high maximum gains. In practice such gains are obtained by applying appropriate weights of antenna elements in large antenna arrays, such that the main lobe with maximum gain of transmitter (Tx) radiation pattern would point towards receiver (Rx). However, next to the main lobe there are also side lobes which radiate/capture energy to/from undesired directions.

Usually, the difference between the main lobe gain and the first side lobe gain, commonly referred as the first Sidelobe Suppression Level (SSL), is around 13 dB for square antenna arrays [1]. In practice this difference can be further increased by application of tapering method, i.e. attenuation of amplitude of outer antenna elements in the array [1]. In the result of tapering the loss in nominal gain of main lobe is observed but SSL could be improved significantly. Application of tapering helps to decrease the energy radiated/captured to/from undesired directions and therefore minimize the power of interference in radio channel.

Recent publications like [2] and [3] show designs of modern antennas for mmWave to achieve higher efficiency of side-lobe suppression for nominal antenna patterns, i.e., determined in anechoic chamber. These designs, however, do not illustrate the efficiency of tapering in real radio channel. Studies and measurements presented in [4], [5] and [6] confirm that effective antenna pattern (in real radio channel) differs from nominal antenna pattern in both Line of Sight (LOS) and Non Line of Sight (NLOS) conditions, whereas this difference is more visible in NLOS case.

In this paper we present comparison of nominal and effective patterns of antenna arrays obtained from simulations. Antenna array model and radio channel model used in simulations follow 3rd Generation Partnership Project (3GPP) specifications [7] and [8], respectively. Simulations have been carried out using two different antenna array sizes and two different propagation environments. For each case the antenna patterns with and without tapering are presented.

II. Simulation Results

This section presents nominal and effective antenna patterns for 16x16 and 8x8 arrays of antenna elements in horizontal plane. Nominal patterns follow the model of Active Antenna System (AAS) from [7], whereas effective patterns [9][10] have been obtained as a result of convolution operation of nominal pattern with power angular spectrum (PAS) of assumed propagation environment, i.e., Urban Macro (UMa) and Urban Micro Street Canyon (UMi SC) as defined in [8]. Main parameters of assumed nominal antenna arrays and radio channels are included in Table I, whereas the convolution operation for effective antenna pattern determination can be stated as

$$g_{Az}^{Eff}(\phi_0) = g^{Eff}(\phi_0, \theta_0 = 90^\circ) = \int_{-180^\circ}^{180^\circ} g^{Nom}(\phi, \theta = 90^\circ) \cdot p_{Az}(\phi - \phi_0) d\phi \quad (1)$$

In (1) g^{Eff} indicates three-dimensional (3D) effective antenna pattern and g^{Nom} indicates 3D nominal antenna pattern. g_{Az}^{Eff} is then azimuth cut of effective antenna pattern, ϕ and θ define angular domain in horizontal and vertical planes, respectively, whereas ϕ_0 and θ_0 indicate boresight direction between Tx and Rx in horizontal and vertical planes, respectively. p_{Az} represents realizations of PAS in horizontal plane.

Chebyshev window [1] has been used to obtain 20 dB of SSL for both assumed antenna arrays of 16x16 and 8x8.

Figures 1-4 illustrate Tx antenna pattern cuts in horizontal planes for 16x16 array and UMa propagation

[3]

environment, whereas Figs. 5-8 include the same pattern for 8x8 array and UMi SC.

Figures 1 and 5 present impact of real radio channel on antenna patterns without tapering. Following effects can be observed here:

- Due to presence of strong directive path in LOS condition, effective antenna gain of main lobe is close to nominal gain, whereas in NLOS conditions, where strong directive path is not present, effective antenna gain of main lobe is noticeably reduced.
- Angular spread of radiated energy causes increase of effective level of side lobes in reference to nominal gain of side lobes, in both LOS and NLOS conditions. The nulls, which are very deep in nominal antenna pattern, are completely flatten in effective antenna pattern. Therefore, it is difficult to determine the location of side lobes. However, the network which is dimensioned based on nominal antenna pattern, and especially directions of nulls and side lobes, will suffer in real environment due to higher interference level from these directions.

Figures 2 and 6 illustrate impact of tapering with Chebyshev window on nominal and effective antenna patterns. For nominal pattern the SSL of 20.6 dB and 21.5 dB have been obtained for 16x16/UMa and 8x8/UMi SC simulation scenarios, respectively, in line with the assumed parameter of tapering window.

In case of effective pattern in LOS conditions (Figs. 3 and 7) the SSL of 18.9 dB and 16.3 dB is observed for 16x16/UMa and 8x8/UMi SC, respectively. Impact of angular spread is visible with lower efficiency of tapering, which decreases further for the next side lobes (like 2nd and 3rd side lobes, etc.). However, it can be concluded that in LOS conditions the tapering method still improves the SSL in comparison to corresponding values before tapering, i.e. 13 dB. Unfortunately, this conclusion does not apply in NLOS conditions (Figs. 4 and 8), where one can observe significant drop in SSL measured at the azimuth angle corresponding to the first side lobe of nominal antenna pattern. For 16x16/UMa case the obtained SSL is equal to 2.3 dB, whereas for 8x8/UMi SC it increases to 3.4 dB when we compare the same angles of position of first side lobes. Simulated values of SSL, as well as other parameters of nominal and effective antenna patterns, are summarized in Table II.

Since the main objective of tapering is to drop side lobes gain of antenna pattern, which helps to minimize intra-cell and inter-cell interference of mobile communications system, it is important to understand what is the efficiency of this method in realistic propagation conditions. Presented simulation results indicate that angular spread in real radio channel impacts the effective pattern of antenna, and therefore changes the effective SSL. In LOS conditions the tapering still helps to improve system's signal to interference plus noise ratio (SINR), which is visible on Figs. 3 and 7, where drop in gain of main lobe maintains to be lower than the drop in gain of first side lobe. However, the reduction of tapering effectiveness even in LOS should be taken into account during the network deployment, where the interference from side lobes is crucial for performance evaluation. In NLOS conditions the same level of gain's drop is observed for main lobe and side lobes (Figs. 4 and 8), which suggests that tapering is not an efficient method for system's SINR improvement in NLOS conditions.

TABLE I. PARAMETERS OF NOMINAL ANTENNAS AND PROPAGATION CONDITIONS

Array size	16x16	8x8
Channel model	3GPP UMa [8]	3GPP UMi SC [8]
Carrier frequency	28 GHz	
Element spacing	$\lambda/2$	$\lambda/2$
Aperture size	73.5 cm^2	18.4 cm^2
Single element gain	8 dBi	
Half power beamwidth (HPBW) of single element	65 deg	

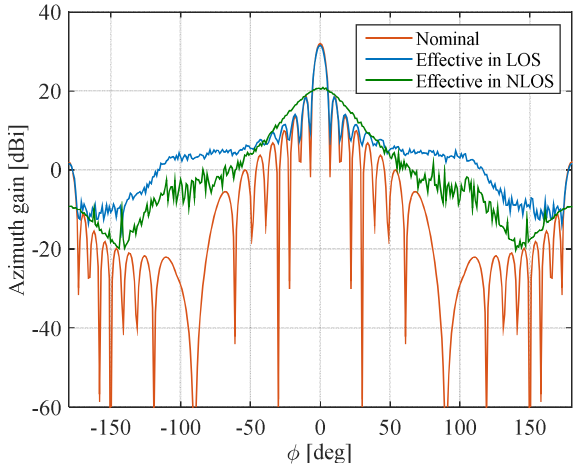

Fig. 1. Tx antenna pattern cut in horizontal plane for 16x16 array in UMa without tapering

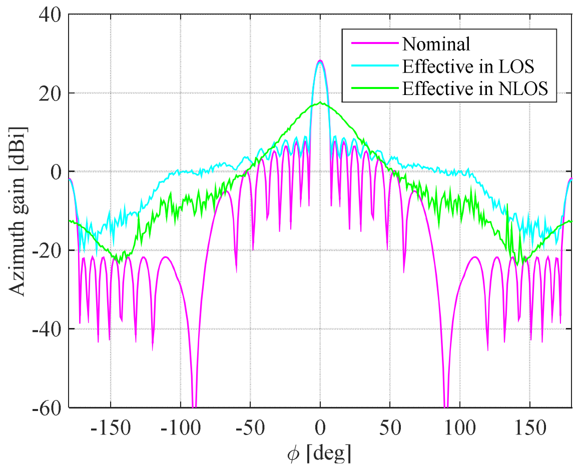

Fig. 2. Tx antenna pattern cut in horizontal plane for 16x16 array in UMa with tapering

[3]

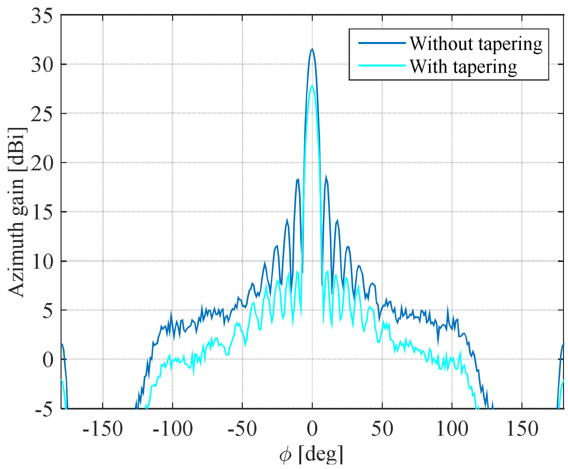

Fig. 3. Effective Tx antenna pattern cut in horizontal plane for 16x16 array in UMa for LOS conditions

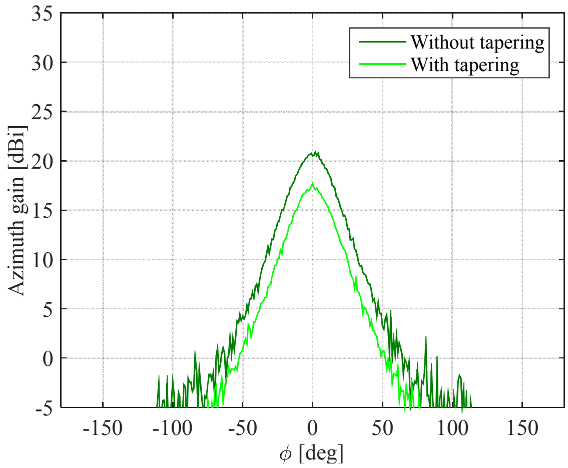

Fig. 4. Effective Tx antenna pattern cut in horizontal plane for 16x16 array in UMa for NLOS conditions

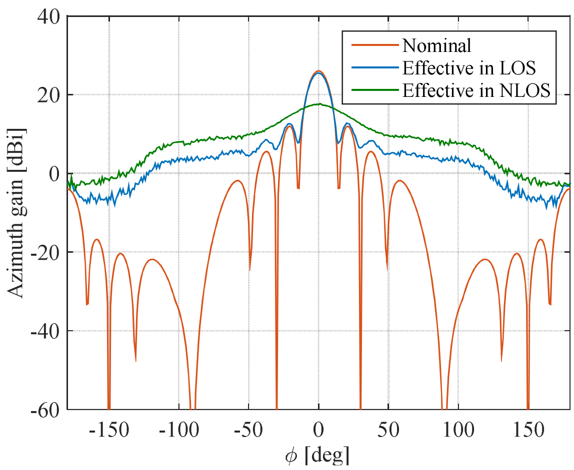

Fig. 5. Tx antenna pattern cut in horizontal plane for 8x8 array in UMi SC without tapering

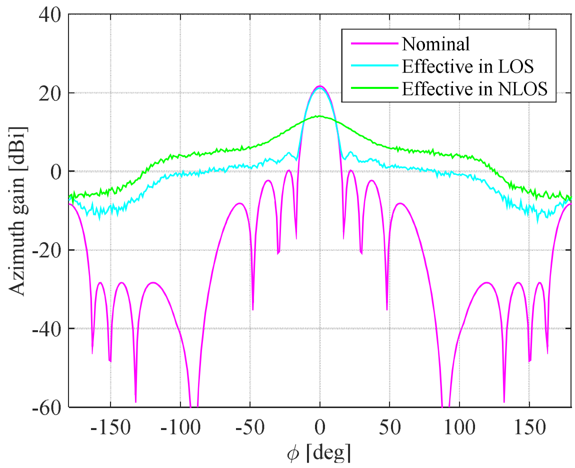

Fig. 6. Tx antenna pattern cut in horizontal plane for 8x8 array in UMi SC with tapering

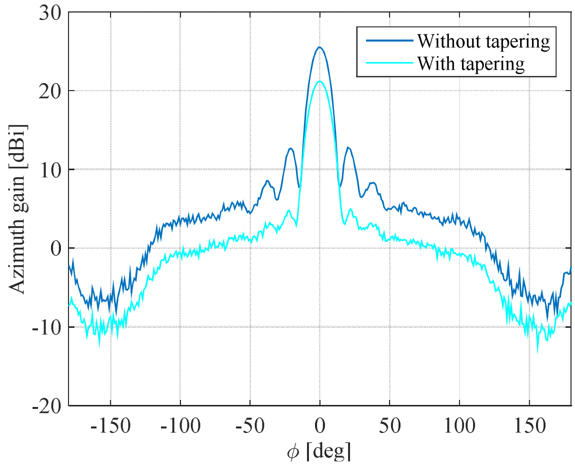

Fig. 7. Effective Tx antenna pattern cut in horizontal plane for 8x8 array in UMi SC for LOS conditions

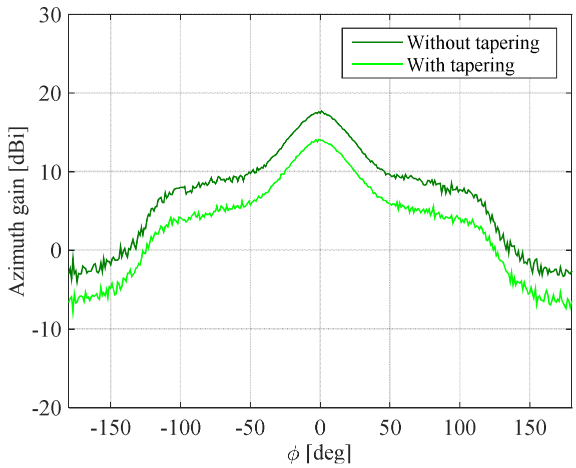

Fig. 8. Effective Tx antenna pattern cut in horizontal plane for 8x8 array in UMi SC for NLOS conditions

[3]

TABLE II. SUMMARY OF SIMULATION RESULTS

Array size	16x16		8x8	
Channel model	3GPP UMa [8]		3GPP UMi SC [8]	
	LOS	**NLOS**	**LOS**	**NLOS**
Root mean square (RMS) Azimuth Spread of Departure [deg]	16.64	21.60	13.70	15.62
Nominal gain [dBi]	32.0		26.0	
Effective gain [dBi]	31.5	21.0	25.5	17.5
Nom. HPBW in horizontal plane [deg]	6.3		12.6	
Eff. HPBW in horizontal plane [deg]	6.6	26.0	13.0	43.2
Nom. SSL in horizontal plane after tapering [dB]	20.6		21.5	
Eff. SSL in horizontal plane after tapering [dB]	18.9	2.3	16.3	3.4

III. CONCLUSION

Effective antenna pattern determined by the propagation environment depends on the angular spread of energy in real radio channel. The difference between the effective antenna pattern and the nominal pattern, as defined in anechoic chamber, reflects the changing in efficiency of tapering method in “free space” and real propagation environments of cellular systems. Simulation results indicate that in LOS conditions the tapering is able to improve system’s SINR, whereas in NLOS conditions the efficiency of tapering drops significantly. Proper design of antenna array with applied tapering should then take into account realistic propagation conditions in the place of deployment, which would help to determine effective antenna gain and therefore realistic system’s performance in LOS and NLOS conditions.

REFERENCES

[1] C. A. Balanis, “Antenna Theory: Analysis and Design”, Wiley, 3rd Edition.

[2] G. Sun et al., “An Antenna Array Sidelobe Level Reduction Approach through Invasive Weed Optimization”, International Journal of Antennas and Propagation, Volume 2018, Article ID 4867851.

[3] C. Mao, M. Khalily, P. Xiao, T. W. C. Brown, S. Gao, “Planar Sub-Millimeter-Wave Array Antenna with Enhanced Gain and Reduced Sidelobes for 5G Broadcast Applications”, IEEE Transactions on Antennas and Propagation, Vol. 67, pp. 160-168, Jan. 2019.

[4] J. Du, E. Onaran, D. Chizhik, S. Venkatesan, R. A. Valenzuela, “Gbps User Rates Using mmWave Relayed Backhaul with High Gain Antennas”, IEEE Journal on Selected Areas in Communications, vol. 35, pp. 1363-1372, Jun. 2017.

[5] D. Chizhik, J. Du, R. Feick, M. Rodriguez, G. Castro, R. A. Valenzuela, “Path loss, beamforming gain and time dynamics measurements at 28 GHz for 90% indoor coverage”, European Conference on Antennas and Propagation (EuCAP), 2018.

[6] J. Du, D. Chizhik, R. Feick, M. Rodriguez, G. Castro, R. A. Valenzuela, “Suburban Fixed Wireless Access Channel Measurements and Models at 28 GHz for 90% Outdoor Coverage”, arXiv: 1807:03763, 2018.

[7] 3GPP Radio Access Network Working Group, “Radio Frequency (RF) requirement background for Active Antenna System (AAS) Base Station (BS) (Release 13)”, 3GPP TR 37.842 V13.0.0.

[8] 3GPP Radio Access Network Working Group, “Study on channel model for frequencies from 0.5 to 100 GHz (Release 15)”, 3GPP TR 38.901 V15.0.0.

[9] K. Bechta, M. Rybakowski, F. Hsieh, D. Chizhik, „Modeling of radio link budget with beamforming antennas for evaluation of 5G systems”, IEEE 5G World Forum, 2018.

[10] K. Bechta, M. Rybakowski, J. Du, “Impact of Effective Antenna Pattern on Millimeter Wave System Performance in Real Propagation Environment”, European Conference on Antennas and Propagation (EuCAP), 2019.

Optimized Antenna Array for Improving Performance of 5G mmWave Fixed Wireless Access in Suburban Environment

Kamil Bechta
Mobile Networks
Nokia
Wroclaw, Poland
kamil.bechta@nokia.com

Jinfeng Du
Bell Labs
Nokia
Holmdel, NJ, USA
jinfeng.du@nokia-bell-labs.com

Marcin Rybakowski
Mobile Networks
Nokia
Wroclaw, Poland
marcin.rybakowski@nokia.com

***Abstract*—One of the first implementations of 5th generation of mobile communication system (5G) will be Fixed Wireless Access (FWA), allowing to provide wideband Internet access to areas inaccessible for optical fiber. Early deployments of FWA in millimetre wave (mmWave) frequency range and with analog beamforming will require accurate evaluation of system performance to ensure that realistic performance in the field meets expectations. In this paper we show that simplified approach for link budget calculation, where the impact of mmWave channel angular spread and the directional antenna pattern are not sufficiently modeled, may lead to overestimation of cell edge capacity by over two times for 5G FWA network in suburban environment. Additionally, we demonstrate that optimization of antenna pattern, by modification of antenna array configuration for analog beamforming matched to angular spread in suburban radio channel, may lead to improvement of 5G FWA cell edge capacity by 60%.**

Keywords—5G, angular spread, fixed wireless access, mmWave, suburban.

I. Introduction

Very first deployments of 5th generation of mobile communication system (5G) are concentrated on enhanced mobile broadband (eMBB) service to satisfy growing demands of end users. Due to limited availability of mobile user devices supporting 3rd Generation Partnership Project (3GPP) standard of New Radio (NR), the earliest deployments of 5G are aiming to provide several Gbps through Fixed Wireless Access (FWA) service. Large channel bandwidth, of several hundreds of MHz, ensured by deployment in millimetre wave (mmWave) frequency range in connection with analog beamforming and multiple-input multiple-output (MIMO) technique allow to provide data throughput comparable to optical fiber access. FWA becomes a particularly convenient solution for mobile network operators (MNOs) who intend to provide eMBB services, like wideband Internet access, to areas where installation of optical fiber infrastructure is difficult or unprofitable.

5G market analysts predict significant growth of FWA deployments in the next few years, e.g. [1] claims the grow from USD 396 million in 2019 to USD 46,366 million by 2026, at a Compound Annual Growth Rate of 97.47% from 2019 to 2026. In the light of these significant investments, it is particularly important to ensure that FWA network is optimally designed and deployed, especially from the point of view of challenges introduced by analog beamforming and radio propagation in mmWave bands.

In this paper we present system level study of 5G mmWave FWA network of small cells in suburban area. We concentrate in particular on the interaction between the narrow beamwidth antenna array of Base Station (BS), via analog beamforming, and the angular spread in multipath propagation environment as determined by Power Angular Spectrum (PAS). In Section II we clarify the difference between the nominal antenna pattern, as measured in anechoic chamber, and the effective antenna pattern, which is experienced in realistic propagation environment. This section introduces also the concept of antenna pattern optimization, which for given scattering environment helps to maximize the signal strength via analog beamforming. Section III includes system level simulation results of 5G FWA network performance, calculated for nominal and effective antenna patterns, and illustrates the improvement of the performance due to introduction of optimized antenna. Conclusion is presented in Section IV.

II. Effective and Optimal Antenna Patterns

With increasing number of antenna elements in the array the *nominal* gain of the antenna array, as measured in anechoic chamber, increases and the half-power beam-width (HPBW) decreases. In scattering environment, the maximum realizable antenna array gain, the *effective* beam pattern and its associated HPBW differ from nominal values. Difference between the nominal and the effective patterns in the radio channel with scattering depends on the angular spread introduced by the real deployment scenarios. Results of measurement campaigns presented in [2] and [3] show that the effective azimuth gain degradation of 4.5 dB or more, in reference to the nominal gain of 14.5 dBi, can be experience by more than half of users in non-line-of-sight (NLOS) propagation conditions. This demonstrates the importance of using effective antenna patterns in non-free space propagation conditions. Fig. 1 illustrates a sample beam pattern of antenna with nominal gain of 14.5 dBi measured in a NLOS environment [4].

Differences between nominal and effective antenna patterns are particularly important in the context of simulation campaigns which aim to estimate performance of 5G system before the commercial deployment begins. Reliable simulation results ensure correctness of minimum requirements for 5G equipment and help to better optimize first 5G networks deployed in the field. Therefore, effective antenna pattern should be used during evaluation studies.

The impact of different propagation conditions on beamforming gain was observed in [5] where the effect of cluster of scatterers for sector beam was investigated.

The need for effective antenna pattern inclusion in system level simulations of mobile networks have been already indicated in [6], where the performance of 4G system was evaluated via simulation using nominal and effective antenna patterns. Simulation results presented in [6] indicate that up to 40% deviation from realistic value of 4G downlink (DL) throughput can occur when nominal antenna pattern is assumed instead of effective antenna pattern. In [7] the performance of 5G system deployed in Urban Macro (UMa) and Urban Micro Street Canyon (UMi SC) environments, as defined by 3GPP in [8], was compared on the basis of system level simulations. In both cases it was observed that DL Signal to Interference plus Noise Ratio (SINR) can be overestimated by 10 to 17 dB in NLOS scenario when nominal beam pattern is used instead of effective pattern.

Effective antenna patterns assumed in [7] are also evaluated in this paper. Even though the array size and carrier frequency are the same in these two studies, the effective pattern is different due to change of propagation environment, i.e. from urban to suburban. In both cases the effective antenna patter has been obtained as an average from 1000 convolutions of nominal antenna pattern with single realization of PAS generated according to statistical model describing given environment. Equations (2)-(4) of [7] define effective antenna pattern in 3D, azimuth cut and elevation cut, respectively.

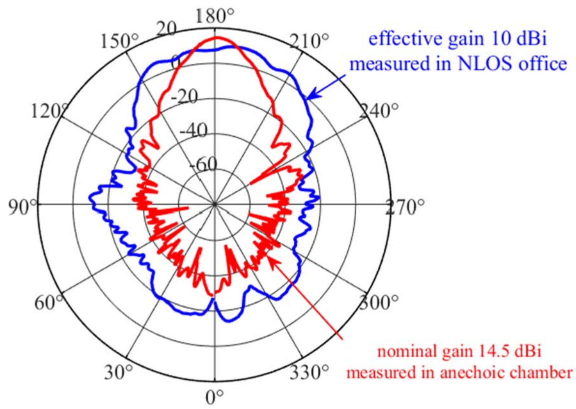

Fig. 1. The phenomenon of "widened" effective beamwidth from a NLOS measurement at 28 GHz (4.5 dB loss has been observed compared to its nominal value) [4].

TABLE I. ANGULAR SPREAD MODEL ASSUMED FOR SYSTEM STUDY OF 5G FWA IN SUBURBAN AREA AT 28 GHZ (AZIMUTH SPREAD OF DEPARTURE, ASD; ZENITH SPREAD OF DEPARTURE, ZSD; AZIMUTH SPREAD OF ARRIVAL, ASA; ZENITH SPREAD OF ARRIVAL, ZSA)

Propagation condition	**$\log_{10}$ (ASD/1°)**	**$\log_{10}$ (ZSD/1°)**	**$\log_{10}$ (ASA/1°)**	**$\log_{10}$ (ZSA/1°)**
LOS	$\mu = 1.14$ $\sigma = 0.41$ [8]	$\mu = 0.15$ $\sigma = 0.35$ [8]	$\mu = 1.21$ $\sigma = 0.12$ [3]	$\mu = 0.58$ $\sigma = 0.28$ [8]
VLOS	$\mu = 0.82$ $\sigma = 0.24$ [3]	$\mu = 0.05$ $\sigma = 0.35$ [8]	$\mu = 1.21$ $\sigma = 0.12$ [3]	$\mu = 0.86$ $\sigma = 0.31$ [8]
NLOS	$\mu = 0.82$ $\sigma = 0.24$ [3]	$\mu = 0.05$ $\sigma = 0.35$ [8]	$\mu = 1.21$ $\sigma = 0.12$ [3]	$\mu = 0.86$ $\sigma = 0.31$ [8]

As 3GPP in [8] does not define channel model for suburban environment, the simulation study presented in this paper in based on UMi SC model improved by statistics obtained for suburban area during measurement campaign presented in [3]. TABLE I includes the main angular spread characteristics of channel model assumed in simulation study presented in this paper.

One can notice that in TABLE I the azimuth angular spread is in all cases higher than the zenith angular spread and this relation is valid also in majority of other channel models. LOS states for line-of-sight conditions, whereas VLOS indicates Vegetation LOS, where direct visibility between radio transmitter and receiver is obstructed by vegetation, typical for suburban area.

As directional antenna is performing spatial filtering of electromagnetic energy from the space, it is reasonable to match the antenna pattern to PAS in given propagation conditions. In most of environments the angular spread in horizontal plane is higher than in vertical plane. Therefore, the optimal shape of antenna pattern, i.e. the one which will allow to maximize the energy radiated to or captured from the space, should be wide in horizontal plane and narrow in vertical. Fig. 2 in simplified way illustrates the relation between the shapes of standard (symmetrical) beam, channel angular spread and the optimal beam.

In [4] we presented detailed solution for determination of optimal antenna array geometry for uniform planar arrays in case of analog beamforming, i.e., where all antenna elements (radiators) are connected to a single transmission/reception chain. For convenience, the fundamental part of solution from [4] is disclosed below.

We assumed that N antenna elements, arranged in rectangular/square shape, form a uniform planar array of size (K_1; K_2), with:

$$K_1 K_2 \leq N \qquad (1)$$

Array of (K_1; K_2)=(1; N) corresponds to a horizontally deployed uniform linear array, whereas K_2=1 indicates a vertically deployed uniform linear array. Let B_{ve} and B_{he} be the nominal beamwidths of the antenna elements whose gain is G_e. The ideal RMS beamwidths B_{v0} and B_{h0}, which shall be observed in free space or anechoic chamber, of the analog beams formed by antenna array of size (K_1; K_2) can be approximately described as:

$$B_{v0} = \frac{B_{ve}}{K_1}, B_{h0} = \frac{B_{he}}{K_2} \qquad (2)$$

Since the directional gain can be related to the RMS beamwidths [7], the effective beamforming gain can be determined based on the nominal antenna pattern and channel angular spread as:

$$G(N, B_{ve}, B_{he}, \sigma_v, \sigma_h) = \frac{2}{\sqrt{\left(\frac{B_{ve}}{K_1}\right)^2 + \sigma_v^2}\sqrt{\left(\frac{B_{he}}{K_2}\right)^2 + \sigma_h^2}} \qquad (3)$$

where σ_h and σ_v state for RMS azimuth spread of departure (ASD) and RMS zenith spread of departure (ZSD), respectively.

Since the effective gain (3) depends on the panel geometry (K_1; K_2), and B_{ve} and B_{he} are determined by the antenna element via G_e=2/($B_{ve}B_{he}$), we can optimize the array geometry (K_1; K_2) to maximize the effective beamforming gain G stated in (3) subject to the size constraint (1). Ignoring the in integer constraint on array dimension K_1 and K_2, the effective beamforming gain of (3) is upper bounded as:

$$G(N, B_{ve}, B_{he}, \sigma_v, \sigma_h) \leq \frac{2}{\sigma_h \sigma_v + \frac{B_{ve} B_{he}}{N}} \qquad (4)$$

with equality if and only if the array geometry is given by:

$$K_1 = \sqrt{\frac{N B_{ve} \sigma_h}{B_{he} \sigma_e}}, K_2 = \sqrt{\frac{N B_{he} \sigma_v}{B_{ve} \sigma_h}} \qquad (5)$$

The nearest integer pair close to (K_1; K_2) as specified by (5) and satisfying the total elements constraint (1) gives the best analog beamforming gain.

Figs. 3 and 4 present antenna patterns in horizontal plane for LOS and NLOS/VLOS propagation conditions, respectively. Patterns have been obtained for antenna array with N=64 antenna elements per polarization, where for VLOS/NLOS the basic configuration of K_1xK_2=8x8 provides effective gain of around 20 dBi (the nominal maximum gain is 24 dBi). The optimal configuration, i.e. the one which allows to maximize the effective antenna gain in suburban environment characterized by angular spread from TABLE I, is K_1xK_2=32x2, obtained based on described procedure. However, the antenna array 32x2 has larger scanning loss in horizontal angle than 8x8 array (4.5 dB scanning loss of 32x2 as compare to 3 dB of loss in case of 8x8 array for +/- 60 degree of horizontal scanning angle range). Therefore, the K_1xK_2=16x4 antenna array was selected as the tradeoff. The 16x4 array has only 0.5 dB higher scanning loss as compare to 8x8 array and the effective gain is only 0.2 dB lower than gain of 32x2 array.

Especially in case of 8x8 antenna patterns in NLOS/VLOS presented in Fig. 4, the effect of beam widening and gain drop (around 4 dB) of the main effective beam in comparison to main nominal beam is visible, which corresponds to measurement results presented in Fig. 1. The most interesting observation is the 2 dB increase in effective antenna gain, when antenna array configuration is changed from 8x8 to 16x4. Next section presents impact on 5G FWA performance when effective antenna pattern is used during simulation study instead of nominal antenna pattern for suburban propagation environment, and how much this performance improves when optimal pattern is assumed.

III. System Level Simulations of 5G FWA in Suburban

A. Simulation Assumptions

In system level simulations we assumed a suburban area of approximate dimension 700 m x 600 m, which consists of 16 blocks. Each block contains 20 houses, 10 per each side of the same street, and is served by 2-sectoral BS. It was assumed that 10% of houses, which are the closest to BSs, have indoor Customer Premise Equipment (CPE), whereas for the remaining 90% of houses an outdoor CPEs were assumed. Fig. 5 illustrates detailed topology of FWA network used for the system level simulations.

For path loss calculation we used empirical models presented in [3] and disclosed in TABLE II. It needs be noted that the path loss model is for omnidirectional antennas, and any study with assumed directional antennas and analog beamforming should either utilize full 3D channel model with angular spread statistics embedded, or effective directional antenna pattern should be used on top of omnidirectional path loss model.

In system level simulations we assumed VLOS conditions for wanted signal links towards outdoor CPEs and for interfering links from other sectors but placed on the same street. LOS path loss model with additional Outdoor-to-Indoor (O2I) penetration loss [11] has been assumed for serving links towards indoor CPEs. That is, VLOS conditions apply for 90% of all simulated wanted signal links, whereas remaining 10% stays in LOS conditions with additional O2I loss. NLOS conditions have been assumed in case of interfering links from BSs placed on other street than the street where victim CPE is placed. All remaining simulation assumptions are included in TABLE III.

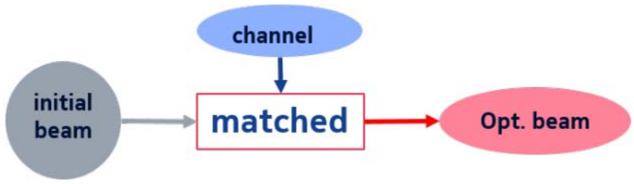

Fig. 2. The optimal beam pattern (and the underlining array geometry using uniform plenary array) should match the channel angular spread to maximize the effective antenna gain [4].

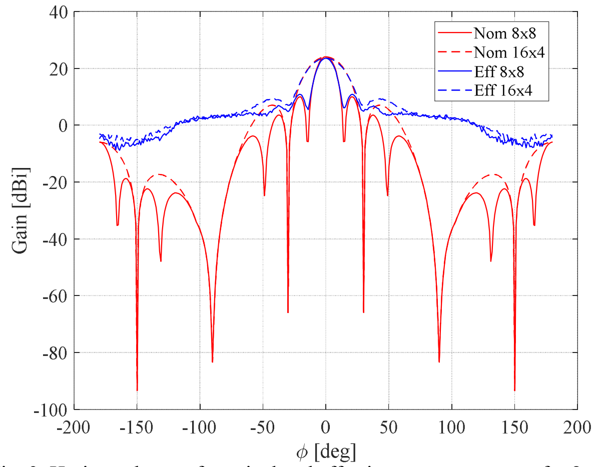

Fig. 3. Horizontal cuts of nominal and effective antenna patterns for 8x8 and 16x4 configurations in LOS.

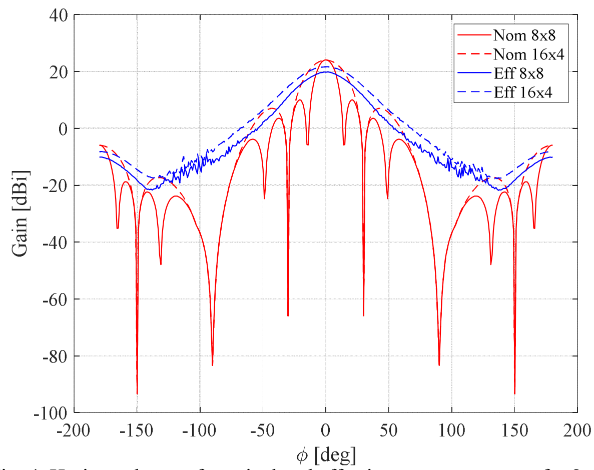

Fig. 4. Horizontal cuts of nominal and effective antenna patterns for 8x8 and 16x4 configurations in NLOS/VLOS.

TABLE II. Assumed Path Loss Model for Suburban Area [3]

Propagation conditions	Path loss [dB] (d [m]: 2D distance between BS and CPE)	Shadow fading [dB]
LOS	$61.4 + 24.0 \cdot \log_{10}(d)$	4.2
VLOS	$45.1 + 40.6 \cdot \log_{10}(d)$	6.4
NLOS	$80.3 + 31.3 \cdot \log_{10}(d)$	4.8
O2I loss	Mean 15.1 dB, standard deviation 2.5 dB [11]	

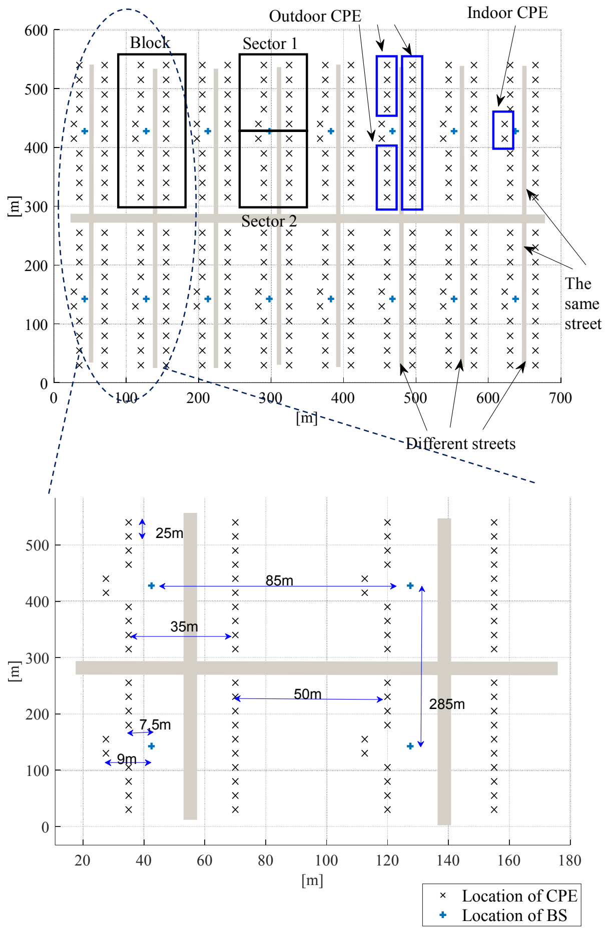

Fig. 5. Topology of assumed 5G FWA network in suburban area.

TABLE III. MAIN SIMULATION ASSUMPTIONS

BS	
Carrier frequency	28 GHz
Channel bandwidth	800 MHz
Antenna array pattern (nominal)	According to [9]
Gain of single antenna element	6 dBi
Antenna array configuration (V × H)	8x8 and 16x4
Tx power for antenna array per polarization (without losses)	28 dBm
Height of antenna array centre	8 m
CPE	
Number of simultaneously served CPEs	1 CPE / sector
Antenna array pattern (nominal)	According to [9]
Gain of single antenna element	6 dBi
Antenna array configuration (V × H)	1 antenna element
Height of antenna centre	1.5 m
Orientation in horizontal plane	Towards BS
Orientation in vertical plane	Towards BS
NF	9 dB

TABLE IV. PARAMETERS DESCRIBING BASELINE LINK LEVEL PERFORMANCE FOR DL

Parameter	**Value**	**Note**
α	0.6	Represents implementation losses
$SINR_{min}[dB]$	-10	Based on QPSK, 1/8 rate
$SINR_{max}[dB]$	30	Based on 256QAM 0.93

B. Simulation Results

Simulation scenario assumes analog beamforming, which in each sector allows to serve only single CPE at a time. It means that all available resources are assigned to single CPE only and therefore the throughput obtained by single CPE is equivalent to the capacity of the whole sector. Maximum Ratio Combining (MRC) type of precoding has been used for determination of beam pointing direction per polarization/stream for analog beamforming.

For calculation of cell capacity the model from 3GPP [10] has been used and is described below (6). This model is based on SINR values obtained from simulation results.

$$T(SINR)[bps/Hz] = $$

$$= \begin{cases} 0, for\ SINR < SINR_{min} \\ \alpha \cdot S(SINR), for\ SINR_{min} \leq SINR < SINR_{max} \\ \alpha \cdot S, for\ SINR \geq SINR_{max} \end{cases} \quad (6)$$

Where:
$S(SINR)[bps/Hz] = log_2(1 + SINR)$ – Shannon bound,
α - Attenuation factor, representing implementation losses,
$SINR_{min}[dB]$- Minimum SINR of the code set,
$SINR_{max}[dB]$- Minimum SINR of the code set.
TABLE IV includes values of α, $SINR_{min}$ and $SINR_{max}$ according to 3GPP assumptions from [10].

Simulations have been performed only for DL direction, and the power of interference has been calculated as the sum of DL power received from sectors other than the serving sector, i.e. we assumed only inter-cell interference.

Presented simulation results compare two approaches for system level modelling of propagation phenomena, especially angular spread, and directional antenna patterns for analog beamforming:

- *Nominal*: simulations assume nominal directional antenna pattern and omnidirectional statistical path loss model, without consideration of multipath propagation, especially angular spread. Such approach is allowed in case of link budget calculations for omnidirectional antennas but very often is wrongly assumed also for calculations with directional antennas.

- *Effective*: simulations assume full 3D channel model, where multipath propagation and associated angular spread is included and reflected in link budget calculations also for directional antennas. This approach is equivalent to the calculations with effective antenna pattern and omnidirectional path loss model.

Simulation results are presented in Figs. 6 – 10 and include both assumed antenna array configurations: basic 8x8 and optimized 16x4. For both antenna array configurations, the results for nominal and effective approach of modelling are presented.

Fig. 6 presents Cumulative Distribution Function (CDF) of DL received (Rx) power of wanted signal, i.e. for serving link from own BS. Red curves represent Rx power calculated according to nominal pattern approach, where maximum gains of nominal antennas on BS and CPE sides have been assumed. Due to that, in both cases of BS antenna array configurations, 8x8 and 16x4, the simulation results are the same, as nominal maximum gains of these configurations are identical. The difference between medians of CDF for nominal and effective approaches follow the difference between maximum antenna gains for VLOS presented in figure 4, as 90% of serving links are performed in VLOS conditions. In case of 8x8 configuration the difference is as high as 5.5 dB, but for optimal configuration it drops to 3.5 dB. Therefore, the effective Rx power of DL wanted signal increases by 2 dB, only due to change in BS antenna array configuration.

One can claim that optimal antenna, due to widened pattern in horizontal plane, would lead to higher interference and thus negligible benefits of antenna pattern optimization. However, this statement is not justified for noise limited environments, where power of interference between radio nodes is well below the power of noise. Indeed, in Fig. 7 we observe increase of DL interference power when antenna array configuration is changed from 8x8 to 16x4, but at the same time we can see in Fig. 8 that ratio of interference power to noise power (I/N) is below 0 dB for majority of simulated DL links. This proves that simulated FWA scenario is noise limited and improvement of system performance can be expected after antenna pattern optimization. It is also worth to mention the substantial increase of DL interference power when effective approach is used in place of nominal approach, which is caused directly by widening of main antenna beam and increase of side lobes levels, as illustrated in Fig. 4.

Fig. 9 illustrates CDFs of DL SINR, which due to limited interference, follow the shapes of CDFs of DL Rx power of wanted signal. Therefore, we can see that nominal approach leads to overestimation of DL SINR in comparison to effective approach. This can have negative impact on the first real deployments of 5G FWA networks in mmWave, as system performance evaluated wrongly by nominal approach would not be achievable in the field. Again, around 5.5 dB of SINR overestimation is obtained in case of 8x8 configuration, which drops to around 3.5 dB for 16x4 configuration. Looking at curves for effective approach, it can be concluded that optimization of BS antenna array, i.e. change of antenna array configuration from 8x8 to 16x4, allows to improve DL SINR in realistic network of 5G FWA in mmWave by 2 dB, for assumed deployment scenario. It has to be underlined that 2 dB of improvement has been achieved only by the change in antenna array configuration, without any change in Tx power of BS. Therefore, to obtain the same SINR as before antenna pattern optimization, the Tx power of BS can be decreased by 2 dB, e.g. for energy costs savings.

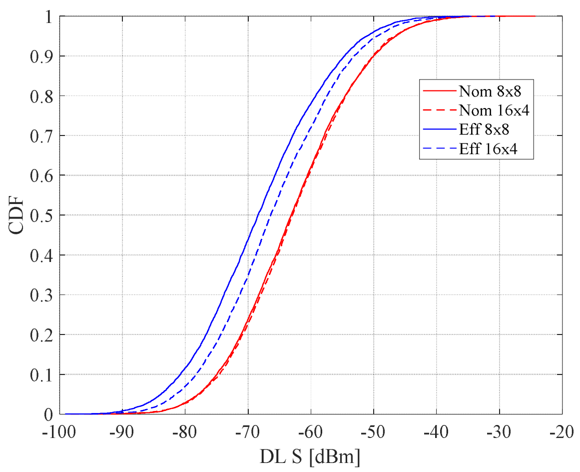

Fig. 6. CDF of DL Rx power of wanted signal.

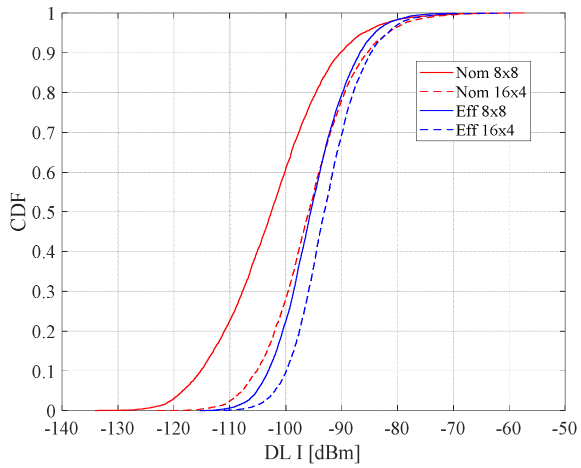

Fig. 7. CDF of DL Rx power of interference signal.

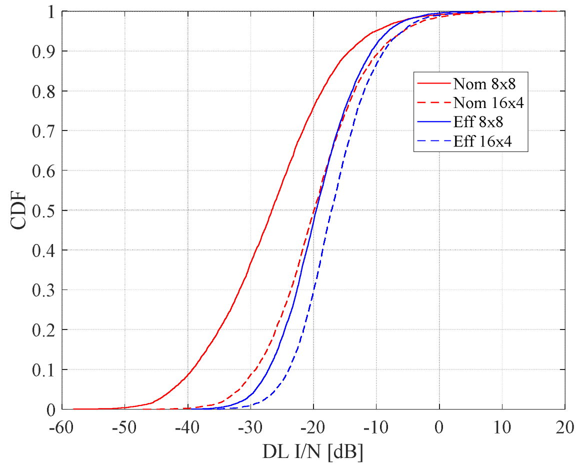

Fig. 8. CDF of DL I/N.

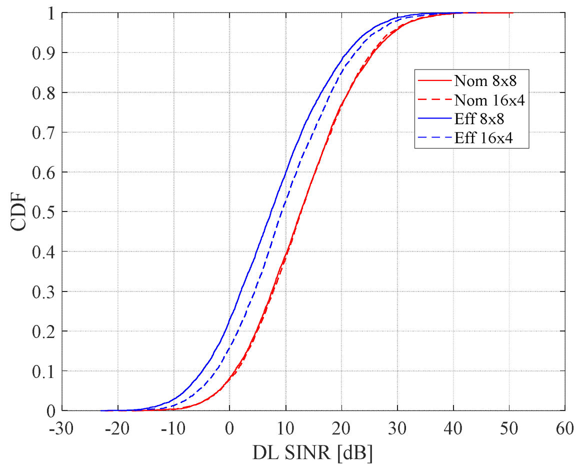

Fig. 9. CDF of DL SINR.

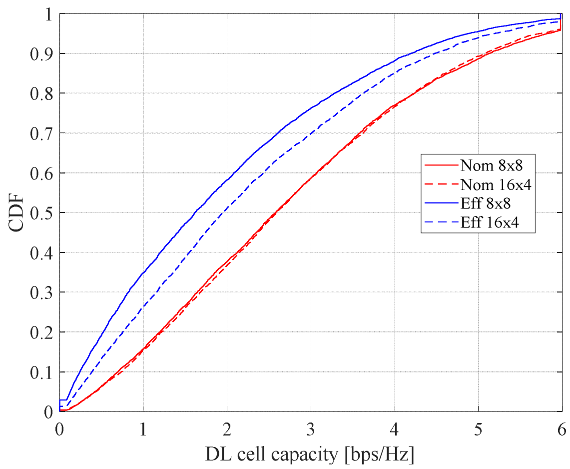

Fig. 10. CDF of DL cell capacity.

TABLE V. SUMMARY OF SIMULATION RESULTS FOR SINR AND CELL CAPACITY

Metric	Nom. 8x8	Eff. 8x8	Nom. 16x4	Eff. 16x4
Median of SINR [dB]	12.7	7.4	12.8	9.3
Median cell capacity [bps/Hz]	2.48	1.65	2.51	1.93
10%-tile of cell capacity [bps/Hz]	0.70	0.24	0.74	0.39

Using the link level performance model described by (6), the DL SINR from Fig. 9 has been translated into DL cell capacity presented in Fig. 10. The results show the spectral efficiency for single stream transmission from one polarization of antenna. In case of MIMO 2x2 the spectral efficiency can be doubled in most of the cases because the cross-polarization ratio (XPR) is quite high in most of the radio channels [8] and could guarantee low inter-stream interference even with open loop MIMO precoding schemes.

Again, the most noticeable are the overestimation of performance when nominal approach is used instead of effective approach and improvement of effective performance when optimal antenna pattern is assumed:

- Overestimation of median cell capacity is around 50% for 8x8 and around 30% for 16x4 antenna array configuration, and more than two times overestimation of cell edge throughput at 10%-tile. This illustrates how significant can be the difference between realistic 5G FWA system performance and simulation evaluations based on nominal approach, which could precede implementations in the field.

- Improvement of DL cell capacity due to antenna pattern optimization, is around 15% for the median and around 60% for 10%-tile of CDF, which can be understood as cell edge capacity.

Detailed comparison of SINR and cell capacity simulation results is included in TABLE V.

IV. CONCLUSION

We have demonstrated differences in the system level simulation results of mmWave 5G suburban FWA system performance, when so-called nominal and effective approaches are used. It has been shown that simplified and commonly used nominal approach can overestimate realistic cell edge capacity over two times. In a bigger context, such overestimation can lead to inaccurate picture of system performance, capacity and coverage as well as may lead to suboptimal deployments of first 5G networks, which in most cases will be adjustable only after initial filed measurements under real operation conditions. Not only intra-system performance of first 5G deployments can be impacted by inaccurately determined co-existence requirements but also performance of other systems working in the same or adjacent frequency bands can be impacted, as underestimated or overestimated power of interference signals originated in 5G network may lead to wrongly concluded co-existence conditions. Therefore, this paper suggests the effective antenna pattern approach for realistic study of 5G system performance, obtained by accurate modelling of relation between mmWave propagation conditions and directional antenna patterns for analog beamforming.

It has been also presented that with the usage of the method proposed in [4] the performance of mmWave 5G FWA system can be easily improved due to optimization of antenna pattern. For presented simulation scenario the improvement has been obtained by the change in antenna array configuration from 8x8 to 16x4, which allowed to improve the cell edge capacity by around 60%.

REFERENCES

[1] Research and Markets. 2019, “5G Fixed Wireless Access (FWA) Market by Offering (Hardware: Access Units & CPE, Services), Demography (Urban, Semi-Urban, Rural), Application (Residential, Commercial, Industrial, Government), and Region - Global Forecast to 2026”.

[2] D. Chizhik, J. Du, R. Feick, M. Rodriguez, G. Castro, R. A. Valenzuela, “Path loss, beamforming gain and time dynamics measurements at 28 GHz for 90% indoor coverage”, European Conference on Antennas and Propagation (EuCAP), 2018.

[3] J. Du, D. Chizhik, R. Feick, M. Rodriguez, G. Castro, R. A. Valenzuela, “Suburban Fixed Wireless Access Channel Measurements and Models at 28 GHz for 90% Outdoor Coverage”, arXiv: 1807:03763, 2018.

[4] J. Du, M. Rybakowski, K. Bechta and R. A. Valenzuela, “Matching in the Air: Optimal Analog Beamforming under Angular Spread”, preprint, submitted to IEEE for possible publication.

[5] O. N. Alrabadi, E. Tsakalaki, H. Huang and G. F. Pedersen, "Beamforming via Large and Dense Antenna Arrays Above a Clutter", IEEE Journal on Selected Areas in Communications, vol. 31, no. 2, pp. 314-325, February 2013.

[6] D. A. Zarbouti, G. V. Tsoulos, G. E. Athanasiadou, ”Effective radiation pattern concept for wireless systems analysis”, Electronics Letters, vol. 53, pp. 1160-1162, Aug. 2017.

[7] K. Bechta, M. Rybakowski, J. Du, “Impact of Effective Antenna Pattern on Millimeter Wave System Performance in Real Propagation Environment”, European Conference on Antennas and Propagation (EuCAP), 2019.

[8] 3GPP Radio Access Network Working Group, “Study on channel model for frequencies from 0.5 to 100 GHz (Release 15)”, 3GPP TR 38.901 V15.0.0.

[9] 3GPP Radio Access Network Working Group, “Radio Frequency (RF) requirement background for Active Antenna System (AAS) Base Station (BS) (Release 13)”, 3GPP TR 37.842 V13.0.0.

[10] 3GPP Radio Access Network Working Group, “Study on New Radio Access Technology; RF and co-existence aspects (Release 14)”, 3GPP TR 38.803 V14.0.0.

[11] J. Du, D. Chizhik, R. Feick, M. Rodriguez, G. Castro, R. A. Valenzuela, “Suburban Residential Building Penetration Loss at 28 GHz for Fixed Wireless Access," IEEE Wireless Communications Letters, vol. 7, pp. 890-893, Dec. 2018.

Matching in the Air: Optimal Analog Beamforming under Angular Spread

Jinfeng Du, *Member, IEEE*, Marcin Rybakowski, Kamil Bechta, and Reinaldo A. Valenzuela, *Fellow, IEEE*

***Abstract*—Gbps wireless transmission over long distance at high frequency bands has great potential for 5G and beyond, as long as high beamforming gain could be delivered at affordable cost to combat the severe path loss. With limited number of RF chains, the effective beamwidth of a high gain antenna will be "widened" by channel angular spread, resulting in gain reduction. In this paper, we formulate the analog beamforming as a constrained optimization problem and present closed form solution that maximizes the effective beamforming gain. The optimal beam pattern of antenna array turns out to "match" the channel angular spread, and the effectiveness of the theoretical results has been verified by numerical evaluation via exhaustive search and system level simulation using 3D channel models. Furthermore, we propose an efficient angular spread estimation method using as few as three power measurements and validate its accuracy by lab measurements using a 16×16 phased array at 28 GHz. The capability of estimating angular spread and matching the beam pattern on the fly enables high effective gain using low cost analog/hybrid beamforming implementation, and we demonstrate a few examples where substantial gain can be achieved by optimizing array beam pattern matching to the median angular spread.**

***Index Terms*—millimeter wave, analogy beamforming, angular spread, antenna pattern, array geometry, gain reduction**

I. Introduction

The fifth generation wireless communication systems (5G) will adopt millimeter wave (mmWave) frequency bands to meet the capacity demand for future mobile broadband applications and new use cases [1]–[3]. However, the high path loss and sensitivity to blockages [4]–[6], channel state information acquisition challenges [7], hardware limitation and other difficulties [8] make it challenging to provide high user rate at high frequencies without shrinking the traditional cell coverage range.

The critical part of high frequency links is the antenna and associated beamforming method. High beamforming gain is essential to combat the severe path loss such that Gbps throughput over long distance and coverage in non-line of sight (NLOS) areas can be realized. Full digital beamforming, capable of altering both amplitude and phase for each antenna element, is costly as it requires a dedicated RF chain for every antenna element and powerful baseband processing. Analog or hybrid beamforming with limited number of RF chains will be used in most of the products indented for mm-Wave frequency bands. However, owing to the channel angular spread and limited number of RF chains, the effective beamwidth of the antenna will be "widened" by the channel, as illustrated in Fig. 1, resulting in reduced effective beamforming gain. This can be intuitively understood by an analogy of lighthouse beacons being scattered and widened in fog, leading to shortened reach. A sample of measured beam pattern obtained by rotating a horn antenna in azimuth, presented in Fig. 1, shows 4.5 dB gain reduction as compared to its nominal gain of 14.5 dBi (as measured in anechoic chamber). Previous measurement campaigns have reported significant loss of directional gain in various deployment scenarios, including suburban fixed wireless access (FWA) [9], [10], indoor offices [11], and industrial factories [12], where up to 7 dB gain reduction (90th percentile) out of 14.5 dBi nominal gain was reported.

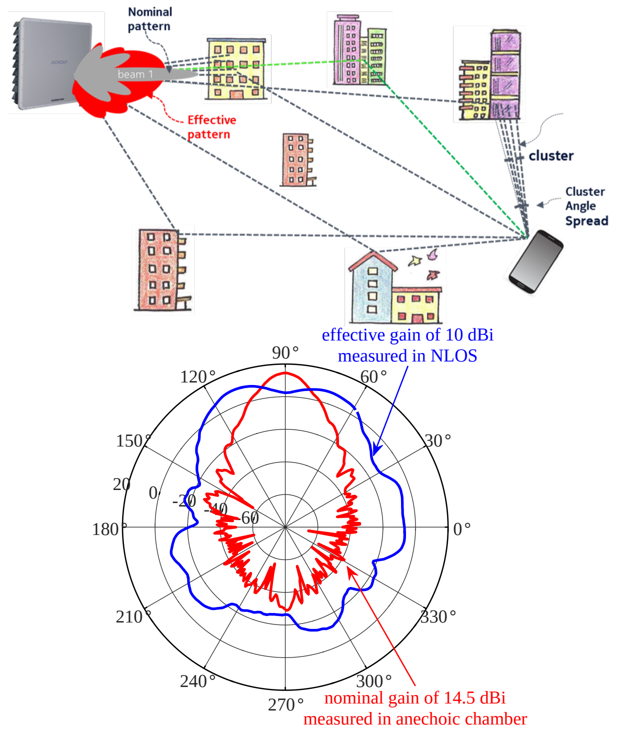

Figure 1. Illustration of angular spread in a NLOS multi-path propagation channel (upper) and the phenomenon of "widened" effective beamwidth from a NLOS measurement at 28 GHz (lower), where a 4.5 dB gain reduction has been observed compared to its nominal gain of 14.5 dBi.

Angular spread has been widely acknowledged and carefully modeled for wireless communications, for example, by the 3rd Generation Partnership Project (3GPP) [13]. It is different

Jinfeng Du and Reinaldo A. Valenzuela are with Nokia Bell Labs, Holmdel, NJ 07733, USA (e-mail: {jinfeng.du, reinaldo.valenzuela}@nokia-bell-labs.com).

Marcin Rybakowski and Kamil Bechta are with Nokia Mobile Networks, 54-130 Wroclaw, Poland (e-mail: {marcin.rybakowski, kamil.bechta}@nokia.com).

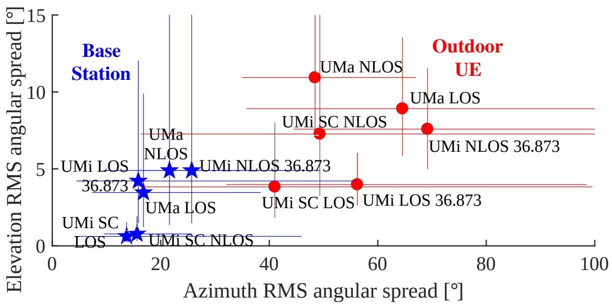

Figure 2. A chart of RMS angular spread (mean value and the corresponding range of 10% to 90%) for BS and for outdoor UE using 3GPP channel models [13] for 28 GHz with BS-UE distance of 100 m. Two instances from UMi 36.873 are also plotted for reference.

in azimuth and in elevation for most relevant deployment scenarios, and a chart of the root-mean-square (RMS) angular spread (its mean and associated 10% to 90% range) for base station (BS) and for outdoor user equipment (UE) is presented in Fig. 2, created based on 3GPP channel models [13] for 28 GHz with BS-UE distance of 100 m[1]. Such difference has also been observed in other channel models developed by mmMagic, METIS, and NYU Wireless [14].

However, the impact of channel angular spread on system design, planning and performance evaluation has not been well understood. The prevailing practice for link budget calcualtion, inter-site interference and co-existence studies is to use nominal antenna pattern rather than the effective pattern, leading to inaccurate received power and interference level estimation. Although high directional antennas have been used for backhaul links, they are usually installed at high heights with direct line-of-sight (LOS) path and close to zero angular spread. This is in contrast to mobile or fixed wireless access applications where the antennas might be below average clutter height and the impact of angular spread could be significant.

A. Our Contribution

Main contributions of this paper are:

- A method for the optimal analog beamforming matching beam pattern to channel angular spread, with closed form solution for uniform planar arrays;
- An efficient angular spread estimation method using as few as three power measurements;
- Examples of practical implementation that provides substantial gain.

In this paper, we focus on wireless access deployment scenarios where large antenna arrays are deployed to improve the link budget. We formulate the analog beamforming as a constrained optimization problem to maximize the effective beamforming gain for given channel angular spread, leading to a closed form solution of the optimal array geometry for uniform planar arrays. The optimal beam pattern turns out to match the given channel angular spread, and the potential gain of the optimal array over a squared array of the same size is demonstrated by system level simulations using 3GPP three-dimension (3D) channel models.

[1] Angular spreads are not sensitive to frequency or distance in [13].

We also propose a method of estimating channel angular spread in azimuth and in evaluation using as few as three power measurements, and validate its accuracy via lab measurements using a 16×16 phased array at 28 GHz. The capability of estimating angular spread and optimizing beam pattern on the fly enables dynamic directional beam configuration, and it helps to achieve high effective gain using low cost analog/hybrid beamforming implementation.

Furthermore, we take advantage of the difference in elevation and azimuth angular spread in most deployment scenarios and demonstrate via examples that, without per-UE beam optimization, substantial gain can be achieved by optimizing array geometry only with respect to the median angular spread.

To the best of our knowledge, this work is the first of its kind in matching antenna pattern with channel angular spread to improve effective beamforming gain, which is essential and critical to ensure sufficient link budget in mmWave deployment.

B. Related Work

Some recent work have provided preliminary investigations on the impact of channel angular spread for channel modeling, link budget analysis, and system performance evaluation. The mismatch between nominal antenna gain and received power level was observed in various channel measurements with directional antennas, and such antenna specific variation was embedded directly into "directional" path loss models [15]–[17], which leads to different path loss models for each different combination of transmit and receive directive antennas. This is in contrast to the "omni" path loss models widely adopted by industrial standards such as [13] where the propagation channel is characterized free from any antenna assumptions and the path loss is modeled as it would be observed with ideal omni antennas at both the transmitter and the receiver. For example, in [10]–[12] the effective gain reduction caused by angular spread is modeled separately from the "omni" path loss channel models. Reduction of directional gain and capacity by azimuth angular spread have been evaluated in [18] for single/multiple sector beams, and the impact of angular spread in azimuth and in elevation for mmWave squared arrays have been studied in [19] for Gbps coverage with wireless relayed backhaul.

System level simulations of mobile networks in [20] have demonstrated up to 40% deviation from realistic value of Long Term Evolution (LTE) downlink (DL) throughput when nominal antenna pattern is assumed instead of effective antenna pattern. Study for 5G scenario with analog beamforming in mm-Wave range was presented in [21] where the radio link budget for serving link and interfering links were evaluated for both nominal and effective antenna gains. The impact of 3GPP 3D channel models on effective antenna array patterns has been visualized in [22] and it was found that the downlink Signal to Interference and Noise Ratio (SINR) can be overestimated by 10 to 17 dB in NLOS scenario when using nominal beam pattern rather than effective pattern. The impact of angular spread on the efficiency of tapering method has been evaluated via simulations [23] which indicates that the first side-lobe suppression level (SSL) can decrease to 16 dB in LOS conditions, or even to 2 dB in NLOS, in comparison to SSL of 20 dB for the nominal antenna pattern.

C. Paper Organization

A brief description of system model is in Sec. II and array geometry optimization is presented in Sec. III. System level simulation and lab measurements are reported in Sec. IV. Several potential applications are discussed in Sec. V and conclusions are in Sec. VI.

II. System Models

To highlight the key idea and to simplify presentation, we focus exclusively on uniform planar array where elements are separated by half a wavelength. This configuration facilitates simple and direct representation of the nominal beam pattern by the underlining array size and array geometry via Fourier transform. Extension to other beamforming methods and array types will be discussed in Sec. III.

We consider the case of high gain antennas whose beam pattern can be approximately characterized by Gaussian functions[2] both in azimuth and in elevation [19]

$$g(\phi,\theta;B_h^2,B_v^2)=\frac{2}{B_hB_v}e^{-\frac{\phi^2}{2B_h^2}}e^{-\frac{\theta^2}{2B_v^2}}, \tag{1}$$

where B_h and B_v are the RMS beamwidth (in radius) in azimuth and in elevation, respectively. The directional gain, defined as the peak to average power ratio of the antenna pattern, is determined by the RMS beamwidths as [19]

$$G=\frac{2}{B_hB_v}, \tag{2}$$

In the absence of scattering, the RMS beamwidths of the antenna pattern are set, correspondingly, to their nominal value B_{h0} and B_{v0}, which can be determined from anechoic chamber measurement. From (2) we can obtain the corresponding nominal gain as $G_{norm}=2/(B_{h0}B_{v0})$.

In the presence of scattering, signals may come from multiple directions. The received signal along a certain direction is the circular convolution of the nominal antenna pattern and the channel angular response [11]. Assuming, for tractability, the channel angular response can also be modeled as Gaussian functions. That is, for a channel with RMS azimuthal angular spread (ASD[3]) σ_h and RMS elevation angular spread (ZSD) σ_v, we can write its normalized channel angular response as

$$h(\phi,\theta;\sigma_h^2,\sigma_v^2)=\frac{2}{\sigma_h\sigma_v}e^{-\frac{\phi^2}{2\sigma_h^2}}e^{-\frac{\theta^2}{2\sigma_v^2}}.$$

The effective antenna pattern is a circular convolution of two independent Gaussian signals with variance (B_{h0},B_{v0}) and (σ_h^2,σ_v^2), respectively. The resulting effective beam pattern still has the Gaussian form as (1) but with variance $(B_{h0}^2+\sigma_h^2,B_{v0}^2+\sigma_v^2)$. Therefore, the effective RMS beamwidth in azimuth and in elevation are given, respectively, by

$$B_h=\sqrt{B_{h0}^2+\sigma_h^2},\ B_v=\sqrt{B_{v0}^2+\sigma_v^2}. \tag{3}$$

Therefore, we can determine the effective beamforming gain from the nominal antenna pattern and channel angular spread

$$G_{eff}=\frac{2}{\sqrt{B_{h0}^2+\sigma_h^2}\sqrt{B_{v0}^2+\sigma_v^2}}.$$

When the number of antenna elements increases, the effective gain in scattering environment is always smaller than its nominal gain, and will saturate[4] at the limit $\frac{2}{\sigma_h\sigma_v}$ imposed by the channel angular spread.

III. Array Geometry Optimization and Angular Spread Estimation

A. Theoretical Derivation of Optimal Array Geometry

We focus on analog/RF beamforming where there are in total N antenna elements, arranged in rectangular/square shape to form a uniform planar array of size (K_1,K_2), with

$$K_1K_2\le N. \tag{4}$$

Array of (K_1,K_2)=$(1,N)$ corresponds to a horizontally deployed uniform linear array whereas K_2=1 indicates a vertically deployed uniform linear array.

We assume all antenna elements are identical and each has nominal beamwidth B_{he} in azimuth and B_{ve} in elevation, which could be measured from anechoic chamber. They can also be derived from its nominal gain by assuming identical beamwidth in elevation and in azimuth, i.e.,

$$B_{he}=B_{ve}=\sqrt{2/G_e},$$

where G_e is the element gain and the last step is from (2).

Since the effective beamforming gain depends on array geometry (K_1,K_2), element beamwidth B_{ve} and B_{he}, and channel angular spread σ_v and σ_h, we can optimize the array geometry (K_1,K_2) to maximize the effective beamforming gain subject to the size constraint (4).

Theorem 1. *Ignoring the integer constraint on array dimension K_1 and K_2, the effective beamforming gain of an antenna array with N elements is upper bounded as*

$$G(N,B_{ve},B_{he},\sigma_v,\sigma_h)\le\frac{2}{\sigma_h\sigma_v+\frac{B_{ve}B_{he}}{N}}, \tag{5}$$

with equality if and only if the array geometry is given by

$$K_1=\sqrt{\frac{NB_{ve}\sigma_h}{B_{he}\sigma_v}},\ K_2=\sqrt{\frac{NB_{he}\sigma_v}{B_{ve}\sigma_h}}. \tag{6}$$

Proof: See Appendix A. ■

The nearest integer pair close to (K_1,K_2) as specified by (6) and satisfying the total elements constraint (4) gives the best analog beamforming gain.

[2]Such approximation has been widely adopted in standard specifications such as 3GPP [13]. Empirical observation indicates that the main lobe can be well approximated by Gaussian function for antenna gain as low as 5 dBi.

[3]3GPP convention uses ASD/ZSD for angular spread at the base station and ASA/ZSA at the user terminal. We use ASD/ZSD throughput the paper for convenience and corresponding value of ASA/ZSA from [13] should be used when optimizing beam pattern for user terminal.

[4]When there are as many RF chains as the number of antenna elements, generalized beamforming has the potential to provide effective gain that grows linearly with the number of elements, providing that perfect channel state information is available.

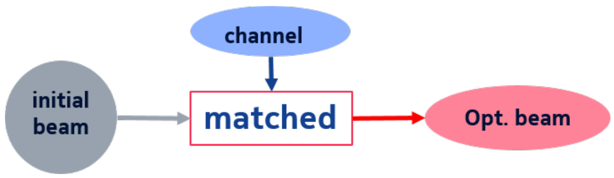

Figure 3. The optimal beam pattern (and the underlining array geometry using uniform plenary array) should match the channel angular spread as prescribed by (7) to maximize the effective analog beamforming gain.

Note that the ratio between the optimal RMS azimuth and elevation beamwidth equals the ratio of the channel RMS spread in azimuth and in elevation, i.e.,

$$\frac{B_{h0}}{B_{v0}} = \frac{B_{he}/K_2}{B_{ve}/K_1} = \frac{\sigma_h}{\sigma_v}. \tag{7}$$

Hence, the optimal beam pattern (generated by the optimal array geometry) matches the channel angular spread in both azimuth and elevation, as illustrated in Fig. 3.

Remark 1. *The optimal geometry that provides the maximal effective gain is determined for the given angular spread and number of elements. The actually implementation might not be exact as what suggested by the optimal solution due to implementation difficulties or cost constraints. For example, RF design would prefer symmetric circuits and antenna elements placement, and the use of splitters in the feed network may limit the granularity of array geometry options. Nevertheless, the beam pattern should match the angular spread as close as possible as prescribed in* (7) *after balancing all the tradeoffs.*

The same concept and methodology of array geometry optimization for uniform plenary arrays shall also apply to other types of directional antennas (like horn, reflector antennas, plasma antennas, etc.) or antenna arrays using non-directional elements (e.g., dipole, monopole). It is also applicable to other beam generating methods such as phase-only pattern synthesis [30], [31] which does not require relocation of array elements. In such applications, it is the azimuth and elevation beamwidth of generated beam patterns that should be subjected to optimization and the optimal beam pattern shall match channel angular spread as specified by (7).

B. Theoretical Derivation of Angular Spread Estimation

When channel angular spread (ASD σ_h and/or ZSD σ_v) is unknown or time varying, the effective gain of a rectangular-shaped sub-array can be determined in real time from measured signal strength using three or more different sub-array configurations, as detailed below. For a uniform planar array of size (N_1, N_2), i.e., there are N_1 rows and N_2 column, we can measure the signal strength of three sub-panels of size (n_1, k_1), (n_1, k_2), and (n_2, k_1), where $n_1, n_2 \le N_1$, and $k_1, k_2 \le N_2$. The effective gains of the corresponding sub-arrays, which depend on $(B_{ve}, B_{he}, \sigma_v, \sigma_h)$ but not shown explicitly to simplify notation, can be written as

$$G(n_1,k_1) = \frac{2}{\sqrt{(B_{ve}/n_1)^2+\sigma_v^2}\sqrt{(B_{he}/k_1)^2+\sigma_h^2}}, \tag{8}$$

$$G(n_1,k_2) = \frac{2}{\sqrt{(B_{ve}/n_1)^2+\sigma_v^2}\sqrt{(B_{he}/k_2)^2+\sigma_h^2}}, \tag{9}$$

$$G(n_2,k_1) = \frac{2}{\sqrt{(B_{ve}/n_2)^2+\sigma_v^2}\sqrt{(B_{he}/k_1)^2+\sigma_h^2}}. \tag{10}$$

By combining (8) and (9) we have,

$$\frac{G(n_1,k_1)}{G(n_1,k_2)} = \frac{\sqrt{(B_{he}/k_2)^2+\sigma_h^2}}{\sqrt{(B_{he}/k_1)^2+\sigma_h^2}}, \tag{11}$$

from which we can obtain

$$\left[\frac{G^2(n_1,k_2)}{G^2(n_1,k_1)} - 1\right]\left(\frac{\sigma_h}{B_{he}}\right)^2 = \frac{1}{k_1^2} - \frac{G^2(n_1,k_2)}{k_2^2 G^2(n_1,k_1)}, \tag{12}$$

leading to an estimate of normalized ASD, in its squared form,

$$\left(\frac{\sigma_h}{B_{he}}\right)^2 = \frac{1/k_1^2 - G^2(n_1,k_2)/(k_2^2 G^2(n_1,k_1))}{G^2(n_1,k_2)/G^2(n_1,k_1) - 1}. \tag{13}$$

Similarly, by combining (11) and (13) we obtain an estimate of the normalized ZSD, in its squared form,as

$$\left[\frac{G^2(n_2,k_1)}{G^2(n_1,k_1)} - 1\right]\left(\frac{\sigma_v}{B_{ve}}\right)^2 = \frac{1}{n_1^2} - \frac{G^2(n_2,k_1)}{n_2^2 G^2(n_1,k_1)}, \tag{14}$$

$$\left(\frac{\sigma_v}{B_{ve}}\right)^2 = \frac{1/n_1^2 - G^2(n_2,k_1)/(n_2^2 G^2(n_1,k_1))}{G^2(n_2,k_1)/G^2(n_1,k_1) - 1}. \tag{15}$$

If there are more measurements using different sub-arrays, each such pair would provide an estimate of the normalized ASD or ZSD, and such estimates should be combined together by treating each of such estimation as one realization of (12) and (14) for ASD and ZSD, respectively. Then all the equations formulated using (12) will be treated as an overdetermined linear system for ASD and all the equations formulated using (14) will be treated as an overdetermined linear system for ZSD.

Assume there are n independent estimates of ASD established by (12) and l independent estimates of ZSD (14). For i=1, . . . , n, let a_i and b_i represent the corresponding constants on the left-hand-side (LHS) and the right-hand-side (RHS), respectively, of the i^{th} ASD estimation established by (12). That is,

$$a_i = \left[\frac{G^2(n_1,k_2)}{G^2(n_1,k_1)} - 1\right]_i, \quad b_i = \left[\frac{1}{k_1^2} - \frac{G^2(n_1,k_2)}{k_2^2 G^2(n_1,k_1)}\right]_i,$$

where the subscript i is used to simply indicate the association to the i^{th} equation. Similarly, for j=1, . . . , l, we denote c_j and b_j as the LHS and RHS constants, respectively, of j^{th} ZSD estimation established by (14).

We can combine these independent estimates together as

$$\left(\frac{\sigma_h}{B_{he}}\right)^2 \bar{\boldsymbol{a}} = \bar{\boldsymbol{b}}, \ \left(\frac{\sigma_v}{B_{ve}}\right)^2 \bar{\boldsymbol{c}} = \bar{\boldsymbol{d}}, \tag{16}$$

where

$$\bar{\boldsymbol{a}} \triangleq [a_1,\ldots,a_n]^T, \ \bar{\boldsymbol{b}} \triangleq [b_1,\ldots,b_n]^T,$$
$$\bar{\boldsymbol{c}} \triangleq [c_1,\ldots,c_l]^T, \ \bar{\boldsymbol{d}} \triangleq [d_1,\ldots,d_l]^T.$$

Applying the classical Least Square estimator, we obtain the improved estimation of the normalized ASD and ZSD, in their squared form, as

$$\left(\frac{\sigma_h}{B_{he}}\right)^2 = \frac{\bar{\boldsymbol{a}}^T\bar{\boldsymbol{b}}}{\bar{\boldsymbol{a}}^T\bar{\boldsymbol{a}}},\ \left(\frac{\sigma_v}{B_{ve}}\right)^2 = \frac{\bar{\boldsymbol{c}}^T\bar{\boldsymbol{d}}}{\bar{\boldsymbol{c}}^T\bar{\boldsymbol{c}}}. \tag{17}$$

Estimators other than the Lease Square estimator used in (17) can also be applied here to seek tradeoff among accuracy, complexity and robustness.

Since angular spread is defined to quantify how wide the channel energy spreads in angular domain, it is non-negative by definition. However, the estimates of the squared value of ASD and ZSD obtained using (13), (15), or (17) might be negative because of estimation noise. Such negative valued estimate is therefore illegitimate, and its value should be replaced by zero.

With estimation from (13), (15), or (17), the effective gain of a sub-array of size (m_1, m_2) can be estimated as

$$G(m_1, m_2) = G(n_1, k_1)\frac{\sqrt{\frac{1}{n_1^2}+\frac{\sigma_v^2}{B_{ve}^2}}\sqrt{\frac{1}{k_1^2}+\frac{\sigma_h^2}{B_{he}^2}}}{\sqrt{\frac{1}{m_1^2}+\frac{\sigma_v^2}{B_{ve}^2}}\sqrt{\frac{1}{m_2^2}+\frac{\sigma_h^2}{B_{he}^2}}}. \tag{18}$$

IV. Numerical Evaluation, System Level Simulation and Lab Measurements

In this section we will demonstrate the benefits of array geometry optimization by numerical results, system level simulation and lab measurements using a 28 GHz phased array with 256 elements.

A. Numerical Evaluation

Effective beamforming gain for analog beamforming (i.e., one RF chain) using uniform planar arrays with 256 antenna elements at 28 GHz are shown in Fig. 4 for both the urban macro (UMa) NLOS scenario (blue line) and the urban micro (UMi) Street Canyon LOS scenario (red line), where the angular spreads of radio channels are from 3GPP models [13] assuing BS-UE distance of 100 m. The effective gain obtained using (20) for a set of different array geometry are highlighted by markers and connected by solid curves to illustrate the general trend of effective gain with respect to array geometry. The optimal array geometries for each channel, designed based on Theorem 1, are highlighted in the plot using black triangles.

With total of 256 elements, 5 dBi each, the ideal gain obtained by digital beamforming with full channel state information would be 29.1 dBi. In scenarios where angular spread is moderate, such as the 3GPP UMi Street Canyon LOS with median ASD of 14° and ZSD of 0.6°, a 64×4 tall array (very close to the optimal geometry 85×3) is 4 dB better than the 16×16 squared array, and 16 dB better than a 1×256 fat array. In a different environment such as the 3GPP UMa NLOS case which is characterized by larger angular spreads (median ASD of 22° and ZSD of 5°), a 32×8 tall array (optimal) is 0.5 dB better than a 16×16 squared array, 9 dB better than a 1×256 fat array. This shows the importance of matching antenna beam pattern to channel angular spread and highlights the benefit of antenna beam pattern to corresponding angular spread of radio channels.

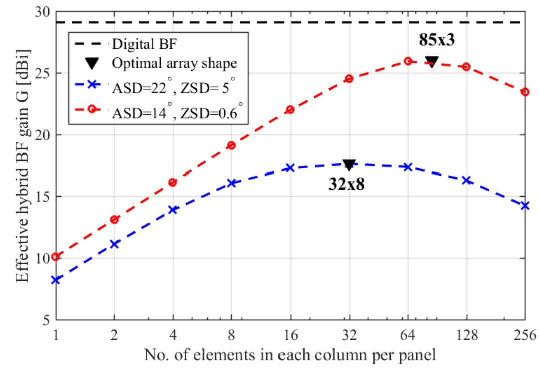

Figure 4. Effective beamforming gain of (20) for analog beamforming using uniform planar array with 256 elements at 28 GHz with BS-UE distance of 100 meters for both the UMa NLOS scenario (blue line) and the UMi Street Canyon LOS scenario (red line) using 3GPP models [13]. The optimal array geometries from Theorem 1 are highlighted as black triangles.

Table I
Summary of key parameters of the system level simulation.

Parameters	Values
Network layout	3-ring hexagon-grid with wrap around, 200 m ISD
Macro cell	19 sites, each has 3 “cell” (location anchor, no BS)
Micro BS	3 cluster circles per macro; each has 1 micro BS
BS drop	Random drop along the edge of cluster circles
BS antenna	Uniform planar array with 128 elements (8 dBi)
Antenna pattern	as per 3GPP TR 38.803 [27]
BS antenna height	10 m
UE height	1.5 to 22.5 m, each has a 2x2 array (5 dBi/element)
Number of UE	1 per micro BS
UE location	20% outdoor, 80% indoor
Penetration loss	50% high loss, 50% low loss
UE distribution	uniform
BS-UE distance	minimum 3 m (2D)
LOS probability	as per 3GPP TR 38.901 [13]
Channel model	3GPP TR 38.901 UMi Street Canyon
Correlation	0.5 between sites

B. System Level Simulation Using 3D Channel Models

The system level simulation was performed to examine the accuracy of the theoretical analysis presented in Sec. III with full 3D spatial statistical channel model, as specified in 3GPP TR 38.901 [13], and antenna array model with beamforming algorithm adopted from 3GPP 5G system evaluation described in 3GPP TR 38.803 [27]. Key parameters of our system level simulation are summarized in Table I. Note that in our simulation results, both the baseline and our scheme, we always assume that the BS already finds the best aiming direction (i.e., selection diversity gain is already included in both cases), and we show that optimizing the beam pattern can bring in additional gain.

First set of simulation results aim to verify correctness of analysis of effective antenna gain, for BS transmission in downlink, described above. For this purpose, we override some of the simulation parameters from Table I to remove some constraints normally seen in system level simulations. More specifically, we set all UEs at 10 m high (same height as the BS) and 60 m from its serving BS with both the BS and UE antennas aiming towards the strongest direction on its boresight. The median ASD is fixed to 16° and median

Table II
SIMULATION RESULTS MATCH THEORETICAL ANALYSIS OF EFFECTIVE BEAMFORMING GAIN OF RECTANGULAR ARRAYS WITH MAXIMUM OF 128 ELEMENTS (EACH OF 8 DBI GAIN).

BF gain [dBi]	Nominal	Theory	Simulation
8×16	29.07	19.91	19.58
42×3	29.00	24.31	24.35

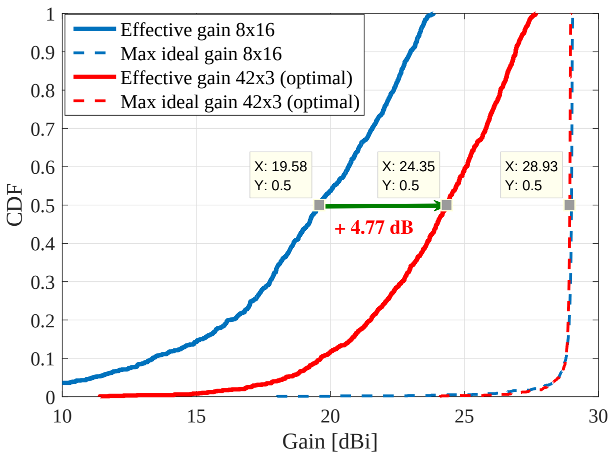

Figure 5. System level simulation results of the effective beamforming gain of rectangular arrays with maximum 128 elements using 3GPP 3D spatial channel model with median ASD of 16° and ZSD of 1° for both the default array geometry of 8×16 (blue lines) and the optimal geometry of 42×3 (red lines). The median of the gains obtained from system level simulation match the values predicted by theoretical analysis within 0.5 dB.

ZSD to 1° to facilitate direct comparison against theoretical analysis. Results of simulations are presented in Fig. 5 and Table II. It can be noticed, that median value of simulated antenna gain cumulative distribution function (CDF) matches the theoretical value within 0.5 dB.

Second set of simulation results are to demonstrate the benefits of optimizing antenna array geometry in realistic deployment scenarios as described in Table I. Ideally, one can maximize the gain by performing per-UE adaptive beam pattern optimization. Such per-UE beam pattern optimization might be implemented over a fixed array using advanced phase-only pattern synthesis [30], [31] without relocating array elements[5]. As UE moves, how frequent per-UE beam pattern optimization should be performed is an open problem. The optimal tradeoff among performance, overhead and complexity for per-UE beam optimization would be an interesting research direction.

To highlight the gain in practical implementations, we propose to use a fixed array geometry optimized with respect to the median channel angular spread in the deployment scenario and all UEs in the system are served by directional beams with the "same" beam pattern[6]. Two array geometries are used in simulation, i.e., the default 8×16 arrangement and the optimal 42×3 configuration as obtained using Theorem 1. Simulation results for the received DL serving signal power, DL interference power, and DL signal to interference plus noise power ratio (SINR) are presented in Fig. 6. As compared to the default 8×16 array configuration assumed by 3GPP, the optimized 42×3 array has demonstrated large increase in signal power (Fig. 6 left) thanks to its matching to the median channel angular spread, and modest reduction in interference power (Fig. 6 middle) thanks to its increased vertical resolution, leading to a combined gain of 6.6 dB on median SINR (Fig. 6 right). Should all users/devices distributed at the same height, widened azimuthal beam may lead to an increase in interference and therefore smaller SINR gain using optimized array geometry. Although the gain of using the optimized array differs from UE to UE, and some UE experience higher gain than others depending on how well the optimized beam pattern matches to its channel angular spread, substantial gain on the signal strength and SINR at system level has been observed. Therefore, the proposed array geometry optimization can be implemented to achieve substantial gain at system level without any per-UE beam pattern optimization.

C. Lab Measurements

To verify the effectiveness of the proposed techniques, we have carried out proof-of-concept measurements using a 28 GHz 16×16 array as the transmitter (Tx) and a 10 dBi horn as the receiver (Rx). Different antenna array geometry was configured by setting zero amplitude for selected antenna elements (AE). The "muted" antenna elements behaved like dummy elements which have marginal impact for antenna pattern due to EM coupling from active AEs. However, this small impact does not influence our general conclusion. The Rx horn antenna was connected to a Signal Analyzer. Tx signal with 100 MHz bandwidth was radiated from the antenna array and the received signal power was measured at Rx side. Since different Tx sub-array has different Tx power, the difference in beamforming gain is determined by the difference in Rx power subtracting the difference in Tx power. This operation also eliminates the common losses (such as cable loss, connector loss) experienced by all signals.

Calibration in anechoic chamber was done using different antenna array configurations with boresight alignment. The measured total array gain with the same number of antenna elements but different geometry (e.g. 8×8, 16×4, 4×16 for 64 elements) was almost the same, with difference around 0.5 dB which could be attributed to dummy elements coupling effect, beam alignment offset or other measurement noise.

Proof-of-concept measurements, as shown in Fig. 7, were carried out for both LOS and NLOS scenarios in an controlled lab environment. For LOS, two rows of reflective panels are used to create multipath-rich environment with larger angular spread in azimuth to verify the gain of optimal antenna arrays. For NLOS measurements, a metal rack and additional panels are used to increase angular spread. Reflective panels are used to intentionally create vastly different angular spread to demonstrate how well the proposed techniques work both in LOS and in NLOS environment. Note that in this experiment, it is the match between measurement and estimation rather than the absolute value of beamforming gain that matters.

[5]Relocating array elements after deployment might be challenging.

[6]Due to boundary effects, beams pointing away from boresight direction of the planar array may have slightly different beamwidth. Such effect is taken care by the simulator and is reflected in our results.

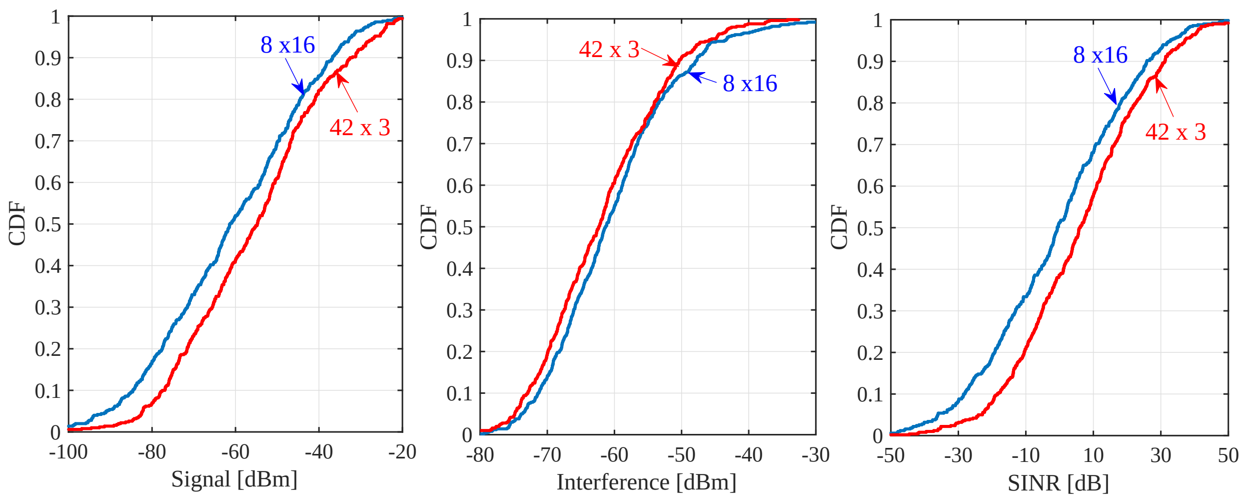

Figure 6. System level simulation results of the DL received signal power (left), interference power (middle), and the SINR (right) of rectangular arrays for both the default array geometry of 8 × 16 and the optimized geometry of 42 × 3. 3GPP 3D spatial channel model under UMi Street Canyon scenario with 33 dBm transmit power. The combined gain of signal power increase and interference power decrease leads to an increase of median SINR by 6.6 dB.

Figure 7. Lab measurement setup for both LOS (left) and NLOS (right) where a 28 GHz phased array of 16 × 16 was used as the transmitter and a 10 dBi horn as the receiver. Different subarrays were activated generate beams of different beamwidth.

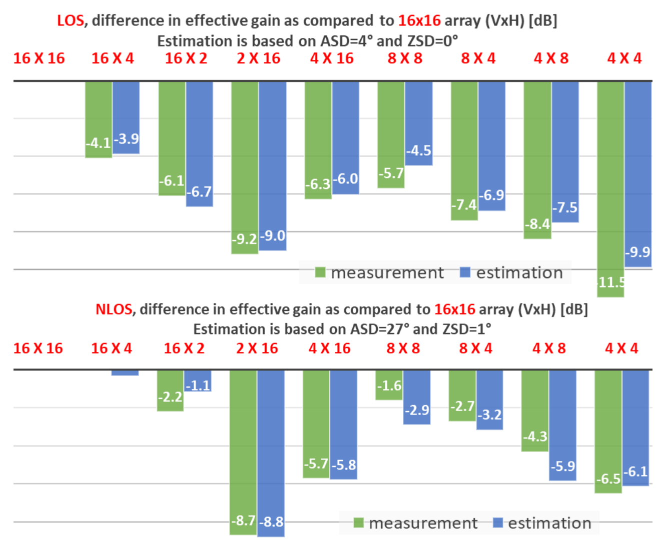

Figure 8. Lab measurement results and estimated effective beamforming gains for LOS (upper) and NLOS (lower).

The measured relative gain, using the full 16×16 array as baseline, as well as the estimated gain based on estimated angular spreads using the methods presented in Sec. III-B (rounded to integer value) are shown Fig. 8. The estimated angular spread in the controlled radio channel created using reflection panels was found to be 4° in ASD and 0° in ZSD for LOS, and 27° in ASD and 1° in ZSD for NLOS. Note that the large angular spread in azimuth and small angular spread in elevation are in line with what specified in standard channel models [13].

The results have verified the effective antenna gain for different antenna array geometry with different number of antenna elements for LOS and NLOS scenarios. For example, in LOS, the 16×2 sub-array has similar gain as the 8×8 by using 2 times less antenna elements. In NLOS, the effective antenna gain of 16×2 array is only 2.2 dB worse than 16×16, whereas the effective gain of 2×16 array is 8.7 dB worse, clearly demonstrated the need of array optimization. Furthermore, these measurement results match our estimated gain (based on estimated angular spread) with high accuracy. These examples clearly validate our analysis on antenna array optimization and angular spread estimation.

V. Potential Applications

We present here a few potential applications where optimizing array geometry can be applied to improve system performance.

A. Deployment Specific Array Optimization

For arrays with the same number of elements, the beam pattern of a tall array has wider beamwidth in azimuth than in elevation. In environments where azimuth angular spread is much larger than elevation angular spread, which is the case for deployment scenarios covered by 3GPP channel models, a tall array with the same number of elements (e.g., 16×4) has beam pattern that matches the channel angular spread better as compared to the beam pattern of the squared array (i.e., 8×8). Since the effective gain is maximized when the nominal beam pattern matches channel angular spread, optimizing the array

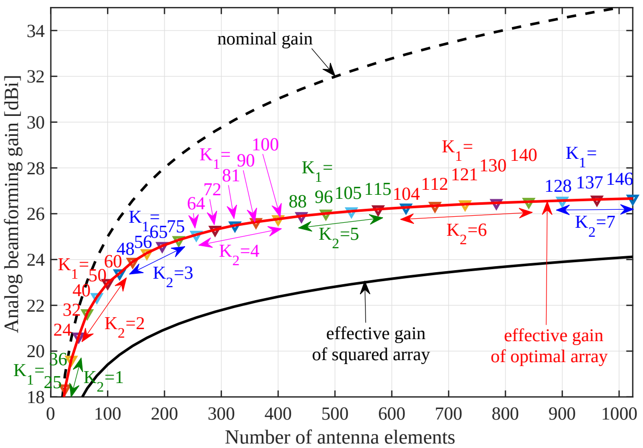

Figure 9. Example of optimal array geometry and the effective gain as function of array size. The ASD and ZSD are according to specifications in 3GPP UMi street canyon NLOS channel [13].

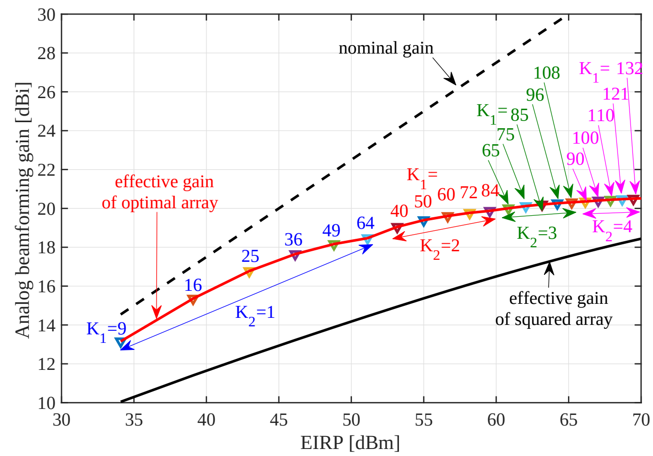

Figure 10. Example of optimal analog beamforming gain and array geometry as a function of EIRP limit for 3GPP indoor LOS channel [13].

geometry may improve the signal strength by a few dB and thus leading to better system performance.

Pre-design of arrays in different geometry can be targeted for each typical deployment scenarios, such as urban macro sites, urban micro small cells, suburban FWA, and indoor office. For each typical deployment scenario, one may design the array geometry based on the median value of angular spread in such cases and exploit the fact that the spreads in azimuth and in elevation are not the same. Such design strategy would provide similar gain on signal to noise power ratio (SNR) over the squared array for majority of the users, as verified by our system level simulations.

In Fig. 9 we compare the effective analog beamforming gain of the optimal array to the gain of traditional squared arrays in 3GPP UMi street canyon NLOS deployment scenarios. Optimal array geometry as labeled in the figure are obtained according to Theorem 1 and the corresponding effective beamforming gain is obtained using (20). For same number of antenna elements, 5 dBi each, the optimal array design can improve the effective beamforming gain (thus the signal strength) by 2 to 3 dB over squared arrays. Configuration for other radio propagation environments with different angular spreads or other values of element gain can be obtained in a similar way straightforwardly. Since the angular spreads at UE are much larger than those at BS, as shown in Fig. 2, using large antenna arrays at UE is inefficient in providing beamforming gain.

B. Optimizing Array Geometry under EIRP Constraint

For devices with strict equivalent isotropic radiated power (EIRP) limit, such as indoor terminals, the maximum allowable number of antenna elements N can be determined from the EIRP limit as:

$$N \leq 10^{(\mathrm{EIRP}-P_t-G_e)/20},$$

where EIRP is in dBm, P_t is the per-element transmit power in dBm and G_e is the per-element gain in dBi. For example, with per-element directional gain of 5 dBi and per-element transmit power of 10 dBm, a maximum of 25 elements is allowed for indoor mobile stations subject to the peak 43 dBm EIRP limit imposed in the United States [24]. At a higher peak EIRP limit of 55 dBm for indoor modems, up to 100 such antenna elements can be used. In Fig. 10 we plot the nominal gain, the effective gain of squared arrays, and the effective gain of optimal arrays with the same number of elements, as a function of EIRP limit, where the optimal configuration of antenna array, obtained by applying Theorem 1, is as indicated in the figure. Compared to squared arrays with the same EIRP limit, 3 to 4 dB improvement of effective beamforming gain (thus signal strength) can be achieved by array geometry optimization for 3GPP indoor LOS scenarios [13]. Configurations for other radio propagation environments with different angular spreads or other values of element gain and element power can be obtained straightforwardly following the same method.

On the other hand, the improved effective gain from array geometry optimization can also be leveraged to maintain the same link budget (thus throughput) but with fewer antenna elements as compared to conventional squared arrays. For example, as shown in Fig. 10, a 5×5 squared array with 43 dBm EIRP (including 24 dBm Tx power) would have effective gain of 13 dBi, whereas a 16×1 array would have 22 dBm Tx power but with effective gain of 15 dBi. Thus, using the 16×1 array would maintain the same link signal strength as the 5×5 squared array but with 2 dB less Tx power and 36% reduction in antenna elements, which translates to a combined 4 dB reduction of EIRP. Such reduction will not only leads to lower power consumption and reduced hardware cost, but also lower electric and magnetic fields (EMF) radiation, which could help 5G system to meet performance expectations under RF EMF compliance limits [25].

C. Array Optimization for FWA Cell Capacity Enhencement

High path loss and large signal bandwidth (in the order of 1000 MHz) at mmWave bands lead to low to median SNR for users in NLOS or at long distance. Since the throughput is close to linear of SNR level in noise limited systems, a

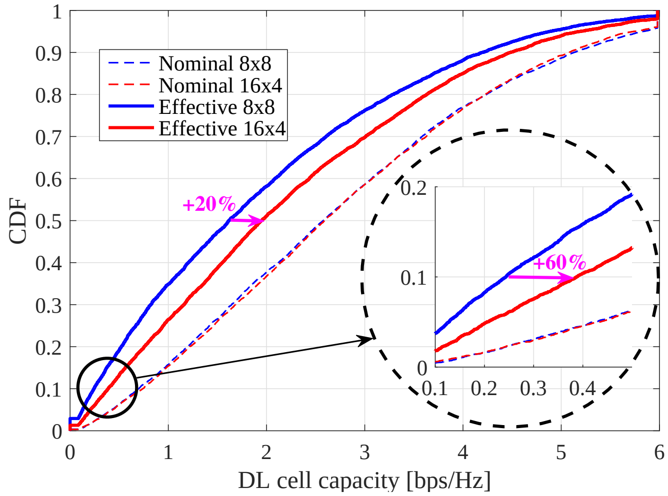

Figure 11. CDF of DL cell capacity (bps/Hz) for 5G FWA at 28 GHz in a suburban deployment scenario [26], where optimized array geometry of 16×4 is compared to the default 8×8 squared array.

modest gain in signal strength could lead to substantial gain in throughput, especially for cell edge users.

In Fig. 11 we plot the CDFs of the DL cell capacity (bps/Hz) for 5G FWA at 28 GHz in a suburban residential deployment scenario [26] where antenna arrays of 64 elements are used at lamppost-mounted access points. Detailed simulation setup can be found in [26]. With 800 MHz bandwidth and 285 m inter-site distance along the same street, the system is essentially noise limited for most of the Customer Premise Equipment (CPE). The optimized array of 16×4 achieves about 2 dB gain in median DL SINR as compared to the default 8×8 squared array. We map the DL SINR to DL cell capacity using the 3GPP configuration [27], and the plot the CDFs of cell capacity in Fig. 11. As compared to the default squared array, the optimized array provides a 20% increase of cell capacity at median and 60% increase at 10th percentile (i.e., cell edge).

VI. Conclusions and Discussions

In this paper we address the link budget challenge of high speed wireless access at high bands by focusing on the effective beamforming gain of antenna arrays under channel angular spread. We have presented closed form solution to match the antenna beam pattern with channel angular spread, which can be very useful in designing deployment specific antenna arrays for typical scenarios based on long-term historical data to improve link budget. We have also developed a method to estimate channel angular spread based on as few as three power measurements, which facilitate dynamic directional beam configuration in a per-transmission basis. This opens the door of a new operation regime for analog beamforming at high frequencies.

Although we made a few assumptions regarding the angular-power distribution to make analysis tractable, the feasibility and projected gains of our methods have been confirmed with impressive accuracy by our 3GPP compliant system level simulations using 3D channel models and by our lab measurement using a 16×16 phased array at 28 GHz. Furthermore, our proposed use cases for deployment-specific array geometry optimization only require the median value of RMS angular spread, which can be estimated based on historical data for each deployment scenarios.

Since the key ingredients of our solution is to match the beam pattern with channel angular spread, the proposed geometry optimization and angular spread estimation methods also apply to other array types and beamforming methods, despite that our description focused exclusively on beamforming over uniform planar array. For such applications, it is the RMS beamwidths in azimuth and in elevation that should be used in analysis rather than the dimension of arrays. The capability of real-time UE-specific optimal beam pattern optimization developed here is especially interesting for advanced beamforming techniques of phased arrays [28], [30], [31] and novel antenna technologies using metasurfaces [29].

Extension to panel-based hybrid beamforming is straightforward. Assuming there are in total N antenna elements evenly allocated to M sub-panels, each supported by one dedicated RF chain. Each sub-panel has N/M elements arranged in rectangular/square shape to form a uniform planar array, where the optimal array geometry (K_1, K_2) can be optimized as in Sec. III to maximize the effective analog beamforming gain $G(K_1, K_2)$ for each sub-panel. Assuming perfect channel state information is available for digital beamforming when combining M panels via maximum ratio combining/transmission, the effective beamforming gain of the N-element M-subpanel hybrid beamforming is therefore $MG(K_1, K_2)$. As the number of RF chains increase, hybrid beamforming has the potential to better combat gain degradation caused by angular spread, and the corresponding gain of beam pattern optimization may therefore be reduced.

When multiple UEs are served simultaneously by a fixed array via separate RF chains, our work enables a new dimension of resource allocation by optimizing the subarrays assigned for each UE based on the corresponding angular spread. Such subarray allocation problems require non-trivial combinatorial optimization and we leave it to future work.

Acknowledgment

The authors would like to thank Dmitry Chizhik for helpful discussions on channel angular spread, and Jakub Bartz for help during all the measurements in the laboratory.

Appendix A
Proof of Optimal Array Geometry

For a uniform planar array of size (K_1, K_2) where each of its antenna elements has nominal beamwidth B_{he} in azimuth and B_{ve} in elevation, the analog beamforming pattern could be generated by applying phase shift to each individual elements whose coefficient is given by a $K_1 \times K_2$ Fourier Transform matrix

$$\left[e^{-j2\pi k\frac{d_v}{\lambda}\sin(\theta-\theta_0)}e^{-j2\pi l\frac{d_h}{\lambda}\sin(\phi-\phi_0)}\right],$$

where $k{=}0,\ldots,K_1{-}1$, $l{=}0,\ldots,K_2{-}1$. The beam aiming direction (ϕ_0, θ_0) are relative to the boresight direction of the array. λ is the wavelength of the carrier frequency and d_h and d_v are antenna element separation distance in azimuth and in elevation, respectively.

In free space or anechoic chamber where there is no angular spread, the generated beam pattern of the uniform planar array of size (K_1, K_2) shall has K_1 times gain in elevation and K_2 times in azimuth, as compared to a single element. Assuming both the element beam pattern and the array beam pattern are in Gaussian shape as in (1), the nominal RMS beamwidth B_{v0} and B_{h0} of the (K_1, K_2) array shall be K_1 and K_2 times, respectively, smaller than the element beamwidth B_{ve} and B_{he}. That is,

$$B_{v0} = \frac{B_{ve}}{K_1},\ B_{h0} = \frac{B_{he}}{K_2}. \tag{19}$$

Given angular spread σ_v and σ_h, the effective analog beamforming gain can be determined by substituting (19) and (3) into (2), described as follows

$$\begin{aligned} G(K_1, K_2, B_{ve}, B_{he}, \sigma_v, \sigma_h) &= \frac{2}{B_v B_h} \\ &= \frac{2}{\sqrt{(\frac{B_{ve}}{K_1})^2+\sigma_v^2}\sqrt{(\frac{B_{he}}{K_2})^2+\sigma_h^2}}, \\ &= \frac{2}{\sqrt{\frac{B_{ve}^2 B_{he}^2}{K_1^2 K_2^2} + \sigma_v^2\sigma_h^2 + \sigma_h^2\frac{B_{ve}^2}{K_1^2} + \sigma_v^2\frac{B_{he}^2}{K_2^2}}}. \end{aligned} \tag{20}$$

Since $K_1K_2 \le N$, the effective beamforming gain (20) can be rewritten as

$$G = \frac{2}{\sqrt{\frac{B_{ve}^2 B_{he}^2}{N^2} + \sigma_v^2\sigma_h^2 + \sigma_h^2\frac{B_{ve}^2}{K_1^2} + \sigma_v^2\frac{B_{he}^2}{K_2^2}}} \tag{21}$$

$$\le \frac{2}{\sqrt{\frac{B_{ve}^2 B_{he}^2}{N^2} + \sigma_v^2\sigma_h^2 + 2\sigma_h\sigma_v\frac{B_{ve}B_{he}}{N}}} \tag{22}$$

$$= \frac{2}{\sigma_h\sigma_v + \frac{B_{ve}B_{he}}{N}}, \tag{23}$$

where (21) is by substitution of $K_1K_2{=}N$, and (22) is from the inequality of arithmetic and geometric means (i.e., the AM-GM inequality), with equality hold, thus achieving the maximal effective gain (23), if and only if

$$\frac{K_1}{K_2} = \frac{\sigma_h B_{ve}}{\sigma_v B_{he}} = \frac{\sigma_h/B_{he}}{\sigma_v/B_{ve}}. \tag{24}$$

Combine (24) with constraint $K_1K_2{=}N$ leads to the solution presented in (6).

References

[1] T. S. Rappaport et al., "Millimeter wave mobile communications for 5G cellular: it will work," *IEEE Access*, vol. 1, pp. 335–349, 2013.

[2] K. Haneda et al., "5G 3GPP-like channel models for outdoor urban microcellular and macrocellular environments," in *proc. IEEE Vehicular Technology Conference (VTC Spring)*, May 2016.

[3] T. S. Rappaport, Y. Xing, G. R. MacCartney, A. F. Molisch, E. Mellios and J. Zhang, "Overview of millimeter wave communications for fifth-generation (5G) wireless networks-with a focus on propagation models," *IEEE Transactions on Antennas and Propagation*, vol. 65, pp. 6213–6230, Dec. 2017.

[4] J. Ko, Y.-J. Cho, S. Hur, T. Kim, J. Park, A. F. Molisch, K. Haneda, M. Peter, D. Park and D.-H. Cho, "Millimeter-wave channel measurements and analysis for statistical spatial channel model in in-building and urban environments at 28 GHz," *IEEE Trans. Wireless Communications*, vol. 16, pp. 5853–5868, Sep. 2017.

[5] V. Raghavan, A. Partyka, L. Akhoondzadeh-Asl, M. A. Tassoudji, O. H. Koymen and J. Sanelli, "Millimeter wave channel measurement and implications for PHY layer design," *IEEE Transactions on Antennas and Propagation*, vol. 65, pp. 6521–6533, Dec. 2017.

[6] T. S. Rappaport, G. R. MacCartney, S. Sun, H. Yan and S. Deng, "Small-scale, local area, and transitional millimeter wave propagation for 5G communications," *IEEE Transactions on Antennas and Propagation*, vol. 65, pp. 6474–6490, Dec. 2017.

[7] J. Du and R. A. Valenzuela, "How much spectrum is too much in millimeter wave wireless access," *IEEE Journal on Selected Areas in Communications*, vol. 35, pp. 1444–1458, Jul. 2017.

[8] I. A. Hemadeh, K. Satyanarayana, M. El-Hajjar and L. Hanzo, "Millimeter-wave communications: physical channel models, design considerations, antenna constructions, and link-budget," *IEEE Communications Surveys & Tutorials*, vol. 20, pp. 870–913, May 2018.

[9] L. J. Greenstein and V. Erceg, "Gain reductions due to scatter on wireless paths with directional antennas," *IEEE Communications Letters*, vol. 3, pp. 169–171, Jun. 1999.

[10] J. Du, D. Chizhik, R. Feick, G. Castro, M. Rodríguez and R. A. Valenzuela, "Suburban fixed wireless access channel measurements and models at 28 GHz for 90% outdoor coverage," *IEEE Transactions on Antennas and Propagation*, vol. 68, pp. 411–420, Jan. 2020. (see also *arxiv: 1807.03763*)

[11] D. Chizhik, J. Du, R. Feick, G. Castro, M. Rodríguez and R. A. Valenzuela, "Path loss, beamforming gain and time dynamics measurements at 28 GHz for 90% indoor coverage," *IEEE Transactions on Antennas and Propagation*, accepted for publication. (see also *arxiv: 1712.06580*)

[12] D. Chizhik, J. Du, R. A. Valenzuela, J. Otterbach, R. Fuchs and J. Koppenborg, "Path loss and directional gain measurements at 28 GHz for factory automation," in *proc. IEEE International Symposium on Antennas and Propagation*, Jul. 2019.

[13] "Study on channel model for frequencies from 0.5 to 100 GHz," *3GPP Technical Report TR 38.901 V14.3.0*, Dec. 2017.

[14] "Comparison of mmWave channel models and measurements with TS 38.901," *3GPP TSG-RAN WG4 NR Ad hoc 2, R4-1706876*, May 2017.

[15] J. A. Azevedo, F. E. Santos, T. A. Sousa and J. M. Agrela, "Impact of the antenna directivity on path loss for different propagation environments," *IET Microwaves, Antennas & Propagation*, vol. 9, pp. 1392–1398, Oct. 2015

[16] T. S. Rappaport, G. R. MacCartney, M. K. Samimi and S. Sun, "Wideband millimeter-wave propagation measurements and channel models for future wireless communication system design," *IEEE Transactions on Communications*, vol. 63, pp. 3029–3056, Sept. 2015.

[17] G. R. MacCartney, T. S. Rappaport, S. Sun and S. Deng, "Indoor office wideband millimeter-wave propagation measurements and channel models at 28 and 73 GHz for ultra-dense 5G wireless networks," *IEEE Access*, vol. 3, pp. 2388–2424, Oct. 2015.

[18] O. N. Alrabadi, E. Tsakalaki, H. Huang and G. F. Pedersen, "Beamforming via large and dense antenna arrays above a clutter," *IEEE Journal on Selected Areas in Communications*, vol. 31, pp. 314–325, Feb. 2013.

[19] J. Du, E. Onaran, D. Chizhik, S. Venkatesan and R. A. Valenzuela, "Gbps user rates using mmWave relayed backhaul with high gain antennas," *IEEE Journal on Selected Areas in Communications*, vol. 35, pp.1363–1372, Jun. 2017.

[20] D. A. Zarbouti, G. V. Tsoulos and G. E. Athanasiadou, "Effective radiation pattern concept for wireless systems analysis," *Electronics Letters*, vol. 53, pp. 1160–1162, Aug. 2017.

[21] K. Bechta, M. Rybakowski, F. Hsieh and D. Chizhik, "Modeling of radio link budget with beamforming antennas for evaluation of 5G systems," in *proc. IEEE 5G World Forum*, Jul. 2018.

[22] K. Bechta, M. Rybakowski and J. Du, "Impact of effective antenna pattern on millimeter wave system performance in real propagation environment," in *proc. European Conference on Antennas and Propagation (EuCAP)*, Apr. 2019.

[23] K. Bechta, M. Rybakowski and J. Du, "Efficiency of antenna array tapering in real propagation environment of millimeter wave system," in *proc. European Conference on Antennas and Propagation (EuCAP)*, Apr. 2019.

[24] *Report and Order and Further Notice of Proposed Rulemaking*, Federal Communications Commission, FCC-16-89, Jul. 14, 2016.

[25] "Case studies supporting IEC 62232 - Determination of RF field strength, power density and SAR in the vicinity of radio communication base stations for the purpose of evaluating human exposure," *IEC TR 62669:2019*, Apr. 2019.

[26] K. Bechta, J. Du and M. Rybakowski, "Optimized antenna array for improving performance of 5G mmWave fixed wireless access in suburban environment," in *proc. IEEE 5G World Forum*, Sept. 2019.

[27] "Study on new radio access technology: Radio Frequency (RF) and co-existence aspects (Release 14)," *3GPP Technical Report TR 38.803 V14.2.0*, Sep. 2017.
[28] A. H. Naqvi and S. Lim, "Review of recent phased arrays for millimeter-wave wireless communication," *Sensors (Basel)*, 18(10):3194, Sep. 2018.
[29] H.-T. Chen, A. J. Taylor and N. Yu, "A review of metasurfaces: physics and applications," *Reports on Progress in Physics*, vol. 79, no. 7, Jun. 2016.
[30] A. F. Morabito, A. Massa, P. Rocca and T. Isernia, "An effective approach to the synthesis of phase-only reconfigurable linear arrays," *IEEE Transactions on Antennas and Propagation*, vol. 60, pp. 3622–3631, Aug. 2012.
[31] M. Khalaj-Amirhosseini, "Phase-only power pattern synthesis of linear arrays using autocorrelation matching method," *IEEE Antennas and Wireless Propagation Letters*, vol. 18, pp. 1487–1491, July 2019.

IEEE Access
Multidisciplinary : Rapid Review : Open Access Journal

Received October 18, 2020, accepted November 11, 2020, date of publication November 19, 2020, date of current version December 8, 2020.

Digital Object Identifier 10.1109/ACCESS.2020.3039423

Rework the Radio Link Budget for 5G and Beyond

KAMIL BECHTA[1], JINFENG DU[2], (Member, IEEE), AND MARCIN RYBAKOWSKI[1]
[1]Mobile Networks, Nokia, 54-130 Wrocław, Poland
[2]Bell Labs, Nokia, Holmdel, NJ 07733, USA

Corresponding author: Kamil Bechta (kamil.bechta@nokia.com)

ABSTRACT The 5^{th} generation of mobile communication system (5G) enables the use of millimeter wave frequency bands and beamforming with narrow-beam directional antennas for mobile communication. Accurate estimation of radio link budget which enables direct assessment of achievable cell range or maximum throughput and facilitates network parametrization before deployment is one of the most challenging problems in radio network planning. In contrast to traditional cellular systems, where omni-directional or sectoral antennas are deployed with half-power beam-width much larger than angular spread of the radio channel, the beam-width of antenna arrays assumed for 5G in sub-6GHz and millimeter wave bands can be comparable to or smaller than channel angular spread in scattering environment. Since the effective antenna pattern is determined jointly by the nominal antenna pattern and channel angular spread, it is no longer appropriate to use nominal pattern in radio link budget analysis or system level simulations. Simplified approach, where nominal pattern is assumed for all typical propagation conditions, results in overestimation of the signal power in serving links and underestimation of interference, which in consequence gives erroneous estimation of link budget and leads to unsatisfactory network design and deployment. To avoid inaccurate calculation of link budget while maintaining simplicity it is proposed to modify the simplified approach by using effective antenna patterns. On the other hand, effective antenna pattern can be further optimized by matching its half-power beam-width to the angular spread of the radio channel. It is demonstrated via simulations how to rework the radio link budget for accurate estimation of system performance in high bands for 5G and beyond, along with benefits of effective antenna pattern optimization.

INDEX TERMS 5G, angular spread, beamforming, directional antenna, effective antenna pattern, millimeter wave, radio link budget.

I. INTRODUCTION

The first wave of commercial deployment of the 5^{th} generation of mobile communication system (5G) started in early 2019. The 5G New Radio (NR) [1], which was named by 3^{rd} Generation Partnership Project (3GPP) - a standardization body - to emphasize its revolutionary nature, can deliver up to Gbps download data rate in selected locations, which is over ten times higher than what 4G (Long Term Evolution - LTE) [2] can provide. However, we have already learned that the performance of these first networks is not always as expected by the end users, and coverage has been a big challenge from day one. What are the most common reasons of the first 5G networks unsatisfactory performance?

One of the answers is overestimation of radio link budget. Overestimation in this case means that at the stage of network planning the assumed coverage of the cell and the level of downlink (DL) signal power from serving base station (BS) were higher than what was measured in the field. As a consequence, the DL signal to interference plus noise ratio (SINR), and therefore DL throughput, are lower than initially expected.

As different as reasons of SINR overestimation can be, the most probable one is too simplified method of link budget calculation, inherited from previous generations of cellular system analysis. In traditional cellular systems where omni-directional or sectoral antennas are deployed, the antenna half-power beam-widths (HPBW) are much larger than angular spread of the radio channels. Therefore, the impact of channel angular spread on link budget is negligible and the simplified method works. However, 5G NR is adapted to use - in both sub-6GHz and millimeter waves (mmWave) bands - antenna arrays whose beam-width is comparable to or smaller than channel angular spread. The complex relation

The associate editor coordinating the review of this manuscript and approving it for publication was Hassan Tariq Chattha.

between 5G narrow-beam directional antennas and channel angular spread should be carefully examined and properly accounted for in 5G radio link budget calculation. Inheriting the simplified radio link budget tool from previous generations would lead to noticeable difference in SINR as compared to detailed simulation results using three-dimensional (3D) channel modeling. Inaccurate estimation of SINR *"may lead to suboptimal deployments of first 5G networks"*, a direct quote from [3].

This article summarizes the authors' latest studies on proper modeling of 5G link budget with narrow-beam antennas and its impact on network performance estimation. Section II introduces definitions of nominal and effective antenna beam patterns. In Section III two different methods for simple link budget calculation are presented and their estimation of 5G network performance is compared. Section IV shows the efficiency of antenna tapering from the perspective of effective antenna beam pattern. A method for optimization of effective antenna beam pattern is provided in Section V, and system level simulation results are presented in Section VI. Section VII summarizes and concludes the article.

II. NOMINAL ANTENNA PATTERN VS. EFFECTIVE ANTENNA PATTERN

When designing an antenna, one of the main objectives is to obtain a specific radiation pattern. In case of antenna arrays, the expectations are mostly high maximum gain and low level of side lobes. Antenna pattern which has been determined by design and validated by measurements in an anechoic chamber is referred to hereinafter as *nominal antenna pattern* of the antenna.

With increasing number of antenna elements in the array, the maximum gain of the nominal antenna array pattern increases and its HPBW decreases. These relations are described by [4]:

$$g_{\max}^{Nom} = \frac{2}{B_{ho} \cdot B_{vo}} = N \cdot G_e, \tag{1}$$

where $g_{\max}^{Nom}$ is the maximum nominal antenna array gain, B_{ho} and B_{vo} are the nominal root mean square (RMS) beam-width in horizontal and vertical planes (in radians), respectively, N is the number of antenna elements in the array, and G_e is the gain of a single antenna element.

In practical channel scattering environment, which differs significantly from anechoic chamber propagation conditions, the maximum realizable gain and associated HPBW of an antenna array differ from their nominal values and are hereinafter referred to as effective. Therefore, the antenna pattern measured in a scattering environment is defined as *effective antenna pattern* for that channel.

Nominal antenna pattern and nominal gain are antenna specific, whereas effective antenna patterns and the corresponding effective gains change depending on a channel. The difference between nominal and effective antenna patterns depends on an angular spread in the scattering environment introduced by a real deployment scenario. Equations (2)-(4) describe how effective antenna patterns can be analytically obtained based on nominal antenna pattern and power angular spectrum (PAS) of the assumed propagation environment.

$$g^{Eff}(\phi_0,\theta_0) = \int_{-180^\circ}^{180^\circ}\int_{0^\circ}^{180^\circ} g^{Nom}(\phi,\theta) \cdot p(\phi-\phi_0,\theta-\theta_0)\,d\phi d\theta, \tag{2}$$

$$g_{Az}^{Eff}(\phi_0) = g^{Eff}\left(\phi_0,\theta_0=90^\circ\right) = \int_{-180^\circ}^{180^\circ} g^{Nom}\left(\phi,\theta=90^\circ\right)\cdot p_{Az}(\phi-\phi_0)d\phi, \tag{3}$$

$$g_{Ele}^{Eff}(\theta_0) = g^{Eff}\left(\phi_0=0^\circ,\theta_0\right) = \int_{0^\circ}^{180^\circ} g^{Nom}\left(\phi=0^\circ,\theta\right)\cdot p_{Ele}(\theta-\theta_0)d\theta. \tag{4}$$

In the above equations g^{Eff} is the 3D effective antenna pattern, whereas g^{Nom} is the 3D nominal antenna pattern. g_{Az}^{Eff} and g_{Ele}^{Eff} indicate azimuth and elevation cuts of effective antenna pattern, respectively. ϕ and θ define angular domain in azimuth and elevation, respectively, whereas ϕ_0 and θ_0 indicate boresight direction between transmitter (Tx) and receiver (Rx) in azimuth and elevation, respectively. p_{Az} and p_{Ele} represent realizations of PAS in azimuth and elevation, respectively.

The level of antenna gain degradation, defined as a difference between nominal and effective antenna gain, depends on propagation environment of antenna deployment. Series of measurement campaigns of effective antenna pattern in different deployment scenarios have been performed and published in [5]–[8]. For instance, Fig. 1 presents samples of measurement results performed in a factory propagation environment [7]. The polar plot presented indicates how effectively the shape of directional antenna pattern can vary between consecutive measurements, even in the line of sight (LOS) conditions. Despite of very strong direct path, the multipath propagation components impact the outcome effective pattern noticeably. As can be expected, nominal pattern is degraded even more significantly in case of non-line of sight (NLOS) conditions, where the direct path is not present, and outcome effective pattern is formed only by multipath components. It is visible that NLOS effective beam pattern is wider than in LOS case and its main direction in horizontal plane is less obvious as there are many clusters with similar strength in measured radio channel.

Fig. 2 presents a summary of statistically analyzed measurement results in different deployment scenarios, i.e. indoor office [5], suburban fixed wireless access (FWA) [6], factory automation [7] and urban Manhattan street canyons [8]. In all the scenarios a severe impact of angular spread on effective antenna gain is visible. In case of NLOS the reduction in

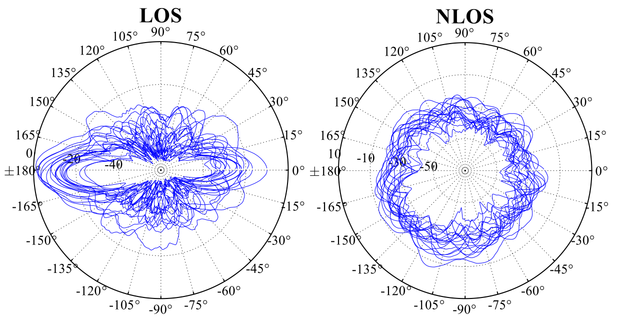

FIGURE 1. Horizontal angular spectra of effective directional antenna patterns measured in indoor factory environment [7].

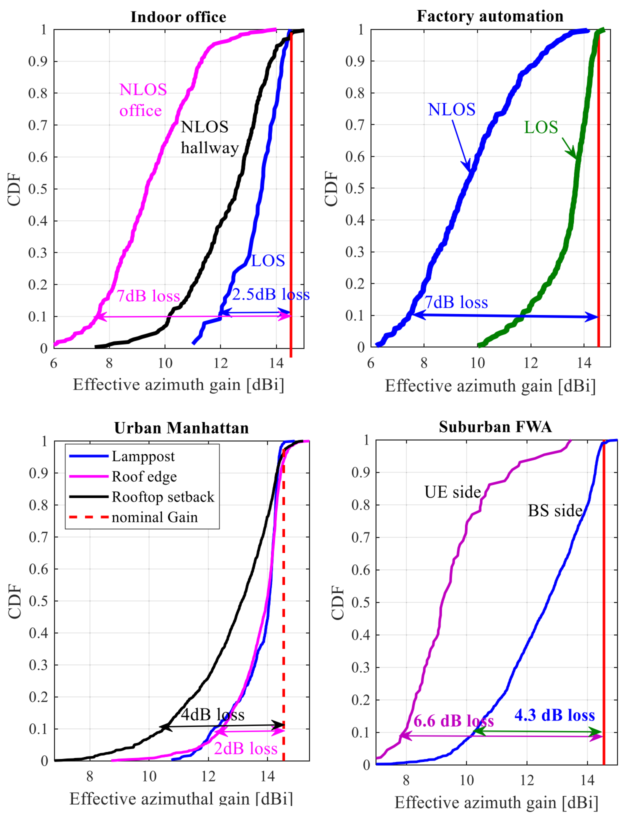

FIGURE 2. CDFs of effective antenna gains measured in indoor office [5], suburban FWA [6], factory automation [7] and urban Manhattan [8] environments presented in comparison with nominal antenna gain.

azimuth gain can be as high as 7 dB for 10% of measured radio links or 5 dB for 50% of measured radio links, in reference to maximum nominal gain of 14.5 dBi in azimuth.

Those measurement results demonstrate that nominal antenna patterns, as measured in an anechoic chamber, are valid only in free space propagation conditions. This conclusion is particularly important in the context of simulation campaigns which were aimed to estimate performance of 5G system before the commercial deployment began. Reliable simulation results should have ensured correctness of minimum requirements for 5G equipment and helped to better optimize the first 5G networks deployed in the field.

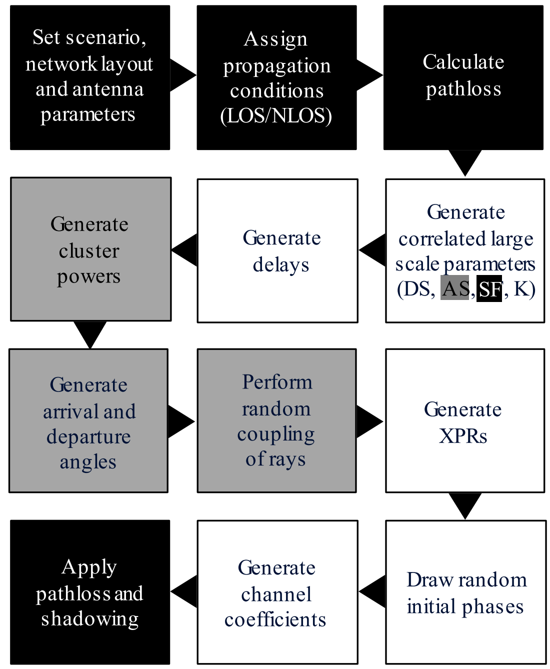

FIGURE 3. Block diagram of statistical channel model reconstruction according to 3GPP [9].

We already know that it was not always the case. Next section demonstrates how the performance estimated for typical deployment scenarios can deviate from realistic values if in link budget calculations the nominal antenna pattern is wrongly used instead of realistic effective pattern.

III. RADIO LINK BUDGET: HOW IT SHOULD BE DONE?

For link-level and detailed system-level simulations, 3GPP [9] has provided instruction on how to generate statistical 3D channel models, as shown in Fig. 3, which includes all the necessary radio propagation phenomena that must be taken into account during comprehensive simulation to provide estimation of radio link budget and performance.

However, such detailed simulation is very time- and resource-consuming, and could be prohibitively complex, especially for system level simulation with many radio links needed to be calculated for evaluation of useful and interference signals conditions. To meet a growing need for quick link budget estimation and system performance evaluation, a simplified method, which considers only the black blocks from Fig. 3, is commonly used, for example in [10] for coexistence studies.

According to section 5.2.5 of [10] the model of received power in DL and uplink (UL) should include only path loss and directional antenna gains, determined based on nominal antenna patterns taken from antenna datasheet. Such an approach considers only some of large-scale parameters of a radio channel model, i.e. path loss and shadowing, but neglects other relevant parameters, especially angular spread, which determines effective antenna pattern. Therefore, the real impact of angular spread on the effective antenna gain is lost in the link budget calculation, which leads to inaccurate estimation of received power.

The simplified method was popular in evaluations of previous generations wireless networks as the antenna beam-width is usually much larger than the channel angular spread, and the difference between nominal and effective antenna gain is small. 5G, however, adopts much narrower antenna beam-width and the gap between nominal and effective antenna gain is too large to be ignored, as evidenced by the measurement results presented in Section II (which clearly show that angular spread leads to a decrease of nominal antenna gain).

Therefore, to avoid inaccurate calculation of link budget while maintaining simplicity, it is proposed to use only black blocks from Fig. 3 but on top of that apply the effective antenna patterns defined by (2), instead of nominal antenna patterns, according to the following steps:

1. Determine the nominal antenna pattern applicable for a given radio link (as in the simplified approach).
2. Determine the PAS.
3. Calculate 3D effective antenna pattern according to (2) based on nominal antenna pattern and PAS as determined in Step 1 and Step 2.
4. Determine the effective antenna gain applicable for evaluated radio link based on the geometry determined by the positions of Tx and Rx and effective antenna pattern from Step 3.

The above method can be used in case of analog beamforming or panel-based hybrid beamforming where the beamforming vector can be drawn from Grid of Beams (GoB) codebook, conventional Fourier transform based beamforming, or other advanced beamforming techniques such as eigen beamforming and zero forcing beamforming.

PAS in Step 2 can be constructed either on a per-scenario basis, i.e. one PAS for all links in the same deployment scenario, or on a per-user equipment (UE) basis with one unique PAS for each UE. The former has negligibly increased complexity, and the per-scenario PAS can be derived based on the statistical channel model applicable for assumed propagation scenario (e.g. by realization of gray blocks from Fig. 3 for model [9]) or from the angular spread measurements performed in the analyzed environment (e.g. [6]). For illustration, Fig. 4 presents the nominal and effective antenna patterns of an 8 × 8 BS antenna array at 28 GHz with per-scenario PAS for the UMi SC deployment scenario [11]. Noticeable difference between nominal and effective patterns, especially in case of NLOS conditions and side lobes, would translate directly into DL SINR values.

The per-UE PAS generation can be done in the similar way as the per-scenario case but requires UE-specific angular spread and cluster realization. This will bring desired accuracy at the cost of slightly increased complexity.

In Fig. 5 a comparison is made of the CDFs of DL SINR for the UMi SC deployment scenario [11] using four methods: 1) a simplified approach with nominal patterns; 2) a simplified approach with effective patterns generated by per-scenario PAS; 3) a simplified approach with effective patterns generated by per-UE PAS; 4) a full-scale 3D simulation.

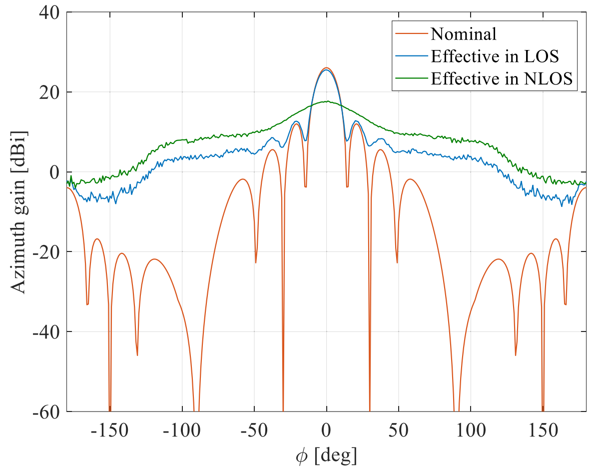

FIGURE 4. Nominal and effective Tx antenna pattern cuts in horizontal plane for 8 × 8 array in mmWave (28 GHz) 3GPP UMi SC deployment [11].

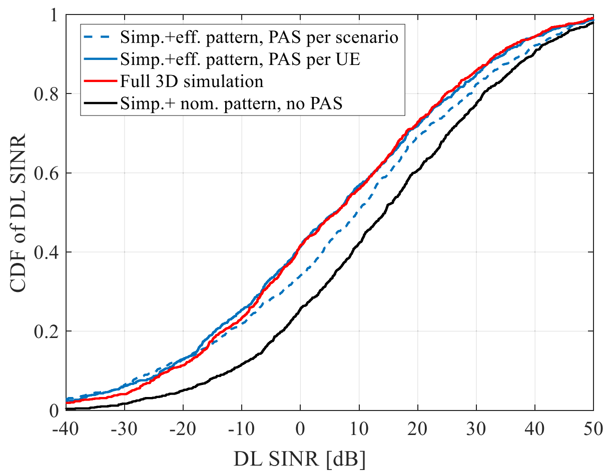

FIGURE 5. CDFs of DL SINR for mmWave 3GPP UMi SC deployment scenario [11] (combined LOS and NLOS links).

Compared to the complex and time-consuming full-scale 3D simulation (treated as ground truth for 3GPP related studies), the results obtained by simplified method with nominal pattern can be over 10 dB too optimistic at 10^{th} percentile and over 8 dB at median. The CDF of simplified approach with effective patterns generated by per-UE PAS is within 1 dB from the ground truth for a wide range of percentiles (from 10^{th} to 99^{th}). When per-scenario PAS is used, the accuracy decreases slightly (2 dB gap at 10^{th} percentile and 3 dB gap at median). Therefore, using effective patterns can provide significantly more accurate results - closer to full 3D simulation results - than those obtained for nominal pattern. In the rest of this paper per-UE PAS will be used when using effective patterns because of its excellent accuracy with marginal added complexity.

To demonstrate the significance of using effective antenna pattern in system level simulations of 5G networks a comparison is made of the results obtained using nominal antenna patterns as suggested in 3GPP [10] against the results obtained using effective antenna patterns (with per-UE PAS), for deployment scenarios of urban macro (UMa) and urban micro street canyon (UMi SC) [11] as well as suburban FWA [12]. The focus is put on the cumulative distribution function (CDF) curves for DL SINR obtained in system level simulations with Monte Carlo methodology for stochastic channel model [9] using the simplified method, for both nominal and effective antenna patterns.

DL Rx power from serving link (DL S) or from an inter-cell interfering link (DL I) are calculated as:

$$P_{Rx} = \frac{P_{Tx} \cdot G_{Tx} \cdot G_{Rx}}{PL}, \tag{5}$$

where P_{Rx} and P_{Tx} are Rx and Tx power respectively, whereas G_{Rx} and G_{Tx} are Rx and Tx antenna gains used for calculation of a given radio link. PL indicates path loss. For link i, either for a serving link or interfering link, the Tx (Rx) antenna gains were determined by Gn^i_{Tx} (Gn^i_{Rx}) or Ge^i_{Tx} (Ge^i_{Rx}) for nominal or effective antenna patterns, respectively. These gains are presented by (6)-(9).

$$Gn^i_{Tx} = g^{Nom}_{Tx}\left(\phi^{AoD}_{i,LOS} - \phi^{AoD}_{i,BF}, \theta^{ZoD}_{i,LOS} - \theta^{ZoD}_{i,BF}\right), \tag{6}$$

$$Gn^i_{Rx} = g^{Nom}_{Rx}\left(\phi^{AoA}_{i,LOS} - \phi^{AoA}_{i,BF}, \theta^{ZoA}_{i,LOS} - \theta^{ZoA}_{i,BF}\right), \tag{7}$$

$$\begin{aligned} Ge^i_{Tx} &= \sum_{j=1}^{N_i} Gn^{i,j}_{Tx} \cdot P_{i,j} \\ &= g^{Eff}_{Tx}\left(\phi^{AoD}_{i,LOS} - \phi^{AoD}_{i,BF}, \theta^{ZoD}_{i,LOS} - \theta^{ZoD}_{i,BF}\right), \end{aligned} \tag{8}$$

$$\begin{aligned} Ge^i_{Rx} &= \sum_{j=1}^{N_i} Gn^{i,j}_{Rx} \cdot P_{i,j} \\ &= g^{Eff}_{Rx}\left(\phi^{AoA}_{i,LOS} - \phi^{AoA}_{i,BF}, \theta^{ZoA}_{i,LOS} - \theta^{ZoA}_{i,BF}\right). \end{aligned} \tag{9}$$

In (6)-(9) $g_{Tx}(\phi^{AoD}, \theta^{ZoD})$ and $g_{Rx}(\phi^{AoA}, \theta^{ZoA})$ are the 3D nominal/effective patterns of Tx and Rx antennas, respectively. $\phi^{AoD}_{i,LOS}$, $\theta^{ZoD}_{i,LOS}$, $\phi^{AoA}_{i,LOS}$ and $\theta^{ZoA}_{i,LOS}$ represent angles of LOS direction between Tx and Rx in azimuth and elevation for radio link i. $\phi^{AoD}_{i,BF}$, $\theta^{ZoD}_{i,BF}$, $\phi^{AoA}_{i,BF}$ and $\theta^{ZoA}_{i,BF}$ represents directions in azimuth and elevation for which main beams of Tx and Rx antennas are pointed (beamformed). In (8) and (9), $Gn^{i,j}_{Tx}$ and $Gn^{i,j}_{Rx}$ indicate nominal gains of transmitting and receiving antennas respectively for multipath j of radio link i. $P_{i,j}$ is the power carried by multipath j ($j = 1, 2, \ldots, N_i$) of radio link i and $\sum_{j=1}^{N_i} P_{i,j} = 1$.

TABLE 1 summarizes differences in simulation results obtained by application of nominal and effective patterns. Due to the presence of a strong directive path in LOS condition, the effective antenna gain is close to nominal gain, whereas in NLOS conditions the effective gain is noticeably lower. This difference in the gains causes the overestimation of the DL S using the nominal pattern. On the other hand, angular spread of radiated energy in horizontal plane causes increased effective gain of side lobes as compared to the nominal values in both LOS and NLOS conditions. This is the reason of underestimation of DL I by calculations with nominal pattern, because the major part of interference is received by the side lobes. Therefore, the use of nominal pattern causes overestimation of DL S and underestimation of DL I, which leads to significantly overestimated DL SINR in all simulated deployment scenarios, as large as 14 dB for UMi SC. These results clearly show that a simplified method with nominal pattern for 5G network estimation can give an erroneous picture of performance metrics which cannot be met in real field deployments.

TABLE 1. Summary of 5G 28 GHz networks performance obtained from system level simulation results for different deployment scenarios [11], [12].

Deployment scenario	UMa [11]		UMi SC [11]		FWA [12]
	LOS	**NLOS**	**LOS**	**NLOS**	**Vegetation LOS**
Array size of BS	16x16		8x8		8x8
Nominal gain [dBi]	32.0		26.0		24.0
Effective gain [dBi]	31.5	21.0	25.5	17.5	20.0
Nominal median *DL S* [dBm]	-19.5	-31.0	-51.7	-61.3	-63.1
Effective median *DL S* [dBm]	-21.4	-45.6	-54.3	-74.7	-68.4
Nominal median *DL I* [dBm]	-57.6		-72.7		-102.6
Effective median *DL I* [dBm]	-53.2		-66.9		-95.5
Nominal median *DL SINR* [dB]	**30.2**		**14.2**		**12.7**
Effective median *DL SINR* [dB]	**16.4**		**4.4**		**7.4**

IV. EFFICIENCY OF ANTENNA ARRAY TAPERING IN REAL PROPAGATION ENVIRONMENT

Previous sections clearly demonstrated that effective antenna pattern may be significantly different from nominal antenna pattern, which has been proved by simulations and measurements. Impact on the main lobe is visible especially in NLOS conditions, whereas substantial increase in the level of side lobes is observed for both LOS and NLOS conditions. The difference between the main lobe gain and the first side lobe gain, commonly referred as the first sidelobe suppression level (SSL), is usually around 13 dB for square antenna arrays without amplitude tapering. In practice, this difference can be further increased by an application of tapering [13] (attenuation of amplitude of outer antenna elements in the array) at the cost of loss in nominal gain of the main lobe. Application of tapering, as one of the common approaches in 5G to suppress side lobe level, helps to decrease the energy

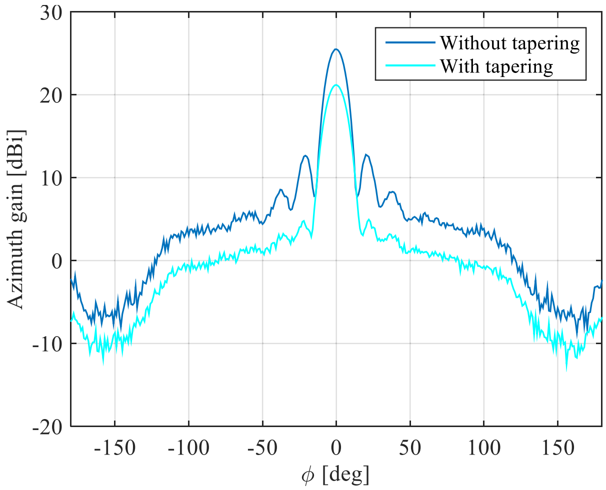

FIGURE 6. Effective Tx antenna pattern cut in horizontal plane for 8 × 8 array in mmWave 3GPP UMi SC deployment for LOS conditions [14].

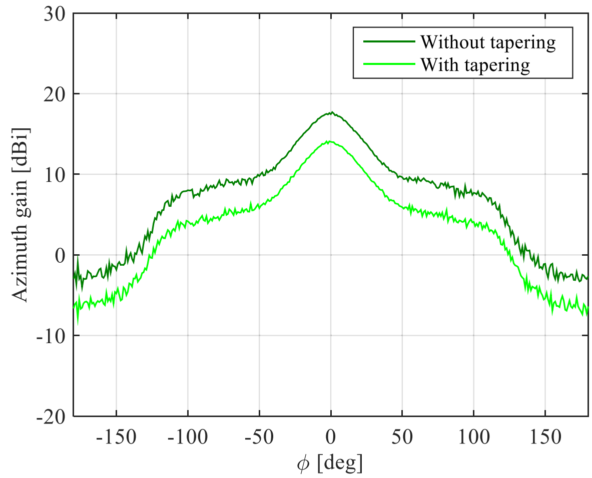

FIGURE 7. Effective Tx antenna pattern cut in horizontal plane for 8 × 8 array in mmWave 3GPP UMi SC deployment for NLOS conditions [14].

radiated/captured to/from undesired directions and therefore minimize the power of interference in the radio channel.

However, if angular spread in scattering environment impacts the shape of nominal antenna pattern, for which tapering is applied, what is the impact on tapering efficiency?

To address this question, a system level simulation was performed for UMa and UMi SC scenarios with 16×16 and 8×8 antenna arrays, respectively [14]. Tapering was applied by multiplication of uniform magnitudes of antenna array beam weight factors by coefficients obtained from Chebyshev function [15] to minimize the bandwidth or smearing while forcing all side lobes to be below a specified level, which in this study was set to 20 dB. For nominal pattern the obtained SSL is 20.6 dB for 16×16 array and 21.5 dB for 8×8 array, in line with the design of the Chebyshev tapering window.

In LOS conditions, as shown in Fig. 6 for UMi SC with 8×8 array, the drop in gain of the main lobe is lower than the drop in gain of the first side lobe, and therefore the tapering still helps to improve the system's SINR. However, the reduction of tapering effectiveness even in LOS, with effective SSL of 16.3 dB in contrast to the nominal 21.5 dB SSL without angular spread, should be considered during network deployment, where the interference from side lobes is crucial for performance evaluation.

In NLOS conditions, as shown in Fig. 7, the same level of gain drop is observed for the main lobe and side lobes, which suggests that tapering is not an efficient method in NLOS conditions with the effective SSL as low as 3.4 dB. Similar observations apply to the 16×16 array under UMa channels [14].

For 5G networks, where tapering is used, it is therefore important to verify whether the design of the antenna array with applied tapering is validated under realistic propagation conditions.

V. METHOD FOR ANTENNA ARRAY OPTIMIZATION

Directional antenna performs spatial filtering of electromagnetic energy from the space, and it is reasonable to match the antenna pattern to the PAS of the channel in given propagation conditions. In [16] a detailed solution was presented of how to maximize the energy radiated to or captured from the space for a given array size and channel angular spread constraints. It has been verified by laboratory and field measurements for determination of the optimal antenna array geometry for uniform planar arrays with analog beamforming. For convenience, the fundamentals of the solution from [16] are quoted below.

It was assumed that N antenna elements, arranged in rectangular/square shape, form a uniform planar array of size $(K_1; K_2)$, with:

$$K_1 K_2 \leq N. \tag{10}$$

The array of $(K_1; K_2) = (1; N)$ corresponds to a horizontally deployed uniform linear array, whereas $K_2 = 1$ indicates a vertically deployed uniform linear array. Let B_{ve} and B_{he} be the nominal beam-widths of the antenna elements whose gain is G_e. The nominal RMS beam-widths B_{v0} and B_{h0} of the analog beams formed by antenna array of size $(K_1; K_2)$ can be approximately described as:

$$B_{v0} = \frac{B_{ve}}{K_1}, \quad B_{h0} = \frac{B_{he}}{K_2}. \tag{11}$$

The effective beamforming gain can be determined based on nominal antenna pattern and channel angular spread [4] as:

$$G(N, B_{ve}, B_{he}, \sigma_v, \sigma_h) = \frac{2}{\sqrt{\left(\frac{B_{ve}}{K_1}\right)^2 + \sigma_v^2}\sqrt{\left(\frac{B_{he}}{K_2}\right)^2 + \sigma_h^2}}, \tag{12}$$

where σ_h and σ_v are the RMS azimuth spread of departure (ASD) and RMS zenith spread of departure (ZSD), respectively.

Since the effective gain (12) depends on the panel geometry $(K_1; K_2)$, and B_{ve} and B_{he} are determined by the antenna element via $G_e = 2/(B_{ve}B_{he})$, the array geometry (K_1; K_2) can be optimized to maximize the effective beamforming gain G stated in (12) subject to the size constraint (10). While ignoring the integer constraint on array dimension K_1 and K_2, the effective beamforming gain is maximized if and only if the array geometry is given by:

$$K_1 = \sqrt{\frac{NB_{ve}\sigma_h}{B_{he}\sigma_e}}, \quad K_2 = \sqrt{\frac{NB_{he}\sigma_v}{B_{ve}\sigma_h}}. \tag{13}$$

The nearest integer pair close to (K_1; K_2) as specified by (13) and satisfying the total elements constraint (10) gives the best analog beamforming gain and constitutes the *optimal antenna array pattern*. Next section demonstrates the efficiency of the method presented and its impact on improvement of performance in a 5G network.

VI. FROM ANTENNA ARRAY OPTIMIZATION TO IMPROVED LINK BUDGET

System level simulation results of improved single-user (SU) MIMO performance of mmWave 5G FWA small cells network deployed in a suburban area were presented in [12]. By optimizing antenna array configuration from 8 × 8 to 16 × 4 for a given channel angular spread, the DL SINR has been improved by 2 dB, which led to the increase of DL cell capacity by 60% at the cell edge.

However, some concerns may be raised regarding the impact of antenna pattern widening in horizontal plane (due to optimization) on interference in multi-user (MU) scenario. Therefore, this section includes new simulation results to quantify the impact of antenna array optimization on DL performance in MU-MIMO scenario. The focus is put on the DL signal strength S, interference to noise ratio (INR), SINR and throughput. For each of the above metrics the results for antenna arrays of size 64 and 144 elements are presented with 2 or 4 simultaneously served UE per cell.

A. SIMULATION ASSUMPTIONS

As 3GPP in [9] does not define channel model for suburban environment, the simulation study presented in this section is based on 3GPP UMi SC stochastic model improved by statistics obtained for suburban 28 GHz measurement campaign presented in [6]. No site-specific channel characteristic was assumed. TABLE 2 includes the main angular spread characteristics of channel model, which are used to estimate the effective beam patterns for link budget calculation.

For system level simulations a suburban area of approximate dimension 700 m × 600 m was assumed, which consisted of 16 blocks. Each block contained 20 houses, 10 per each side of the same street, and was served by 2-sectoral BS. Fig. 8 illustrates detailed topology of modelled FWA network. It was assumed that 10% of houses which are the closest to BSs have indoor Customer Premise Equipment (CPE), whereas for the remaining 90% of houses outdoor CPE was assumed. For path loss calculation the empirical models presented in [6], [17] and summarized in TABLE 3 were used.

TABLE 2. Angular spread model assumed for system study of 5G FWA in suburban area at 28 GHz (azimuth spread of departure, ASD; zenith spread of departure, ZSD; azimuth spread of arrival, ASA; zenith spread of arrival, ZSA).

Propagation condition	$\log_{10}$ (ASD/1°)	$\log_{10}$ (ZSD/1°)	$\log_{10}$ (ASA/1°)	$\log_{10}$ (ZSA/1°)
LOS	$\mu = 1.14$ $\sigma = 0.41$ [9]	$\mu = 0.15$ $\sigma = 0.35$ [9]	$\mu = 1.21$ $\sigma = 0.12$ [6]	$\mu = 0.58$ $\sigma = 0.28$ [9]
VLOS	$\mu = 0.82$ $\sigma = 0.24$ [6]	$\mu = 0.05$ $\sigma = 0.35$ [9]	$\mu = 1.21$ $\sigma = 0.12$ [6]	$\mu = 0.86$ $\sigma = 0.31$ [9]
NLOS	$\mu = 0.82$ $\sigma = 0.24$ [6]	$\mu = 0.05$ $\sigma = 0.35$ [9]	$\mu = 1.21$ $\sigma = 0.12$ [6]	$\mu = 0.86$ $\sigma = 0.31$ [9]

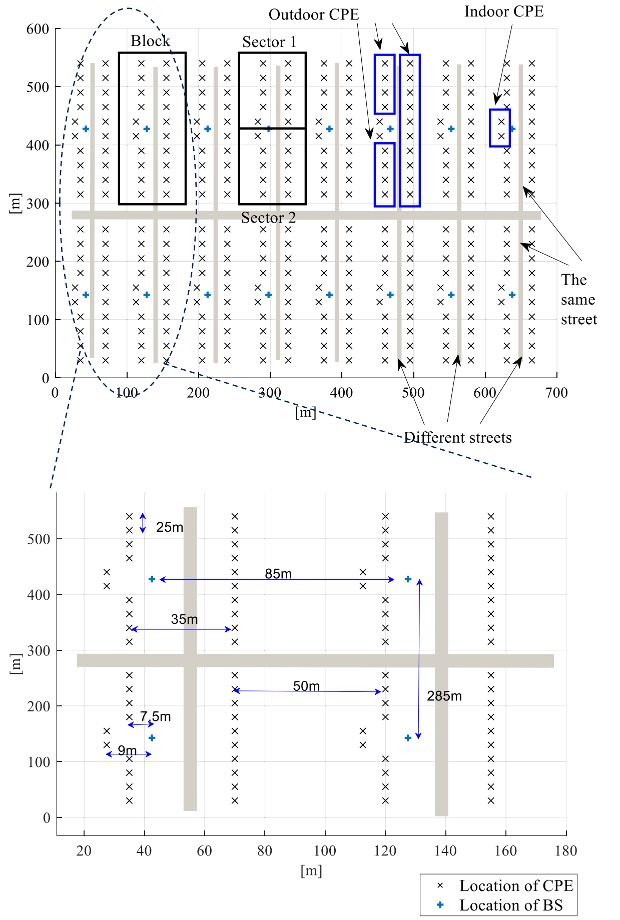

FIGURE 8. Topology of a mmWave FWA network in suburban area.

Vegetation LOS conditions (VLOS) were assumed for wanted signal links towards outdoor CPE and for interfering links from other sectors but placed on the same street. LOS path loss model with additional Outdoor-to-Indoor (O2I) penetration loss [17] was assumed for serving links towards indoor CPE. Thus, VLOS conditions applied to 90% of all simulated wanted signal links, whereas the remaining 10% stayed in LOS conditions with additional O2I loss. NLOS

TABLE 3. Assumed path loss model for suburban area [6].

Propagation conditions	Path loss [dB] (d [m]: 2D distance between BS and CPE)	Shadow fading [dB]
LOS	$61.4 + 24.0 \cdot \log_{10}(d)$	4.2
VLOS	$45.1 + 40.6 \cdot \log_{10}(d)$	6.4
NLOS	$80.3 + 31.3 \cdot \log_{10}(d)$	4.8
O2I loss	Mean 15.1 dB, standard deviation 2.5 dB [17]	

TABLE 4. Main assumptions of system level simulations for estimation of the performance in mmWave 5G FWA network in suburban environment.

BS	
Carrier frequency	28 GHz
Channel bandwidth per UE	800 MHz
Antenna array pattern (nominal)	According to [18]
Gain of single antenna element	6 dBi
Antenna array configuration (M * V × H)	For N=64: M*8x8 and M*16x4; For N=144: M*12x12 and M*24x6; M={2,4}
Max total Tx power per polarization (without losses)	28 dBm
Height of antenna array centre	8 m
CPE	
Number of simultaneously served CPEs	{2,4} / sector
Antenna array pattern (nominal)	According to [18]
Gain of single antenna element	6 dBi
Antenna array configuration (V × H)	1 antenna element
Height of antenna centre	1.5 m
Orientation in horizontal plane	Towards BS
Orientation in vertical plane	Towards BS
Rx NF	9 dB

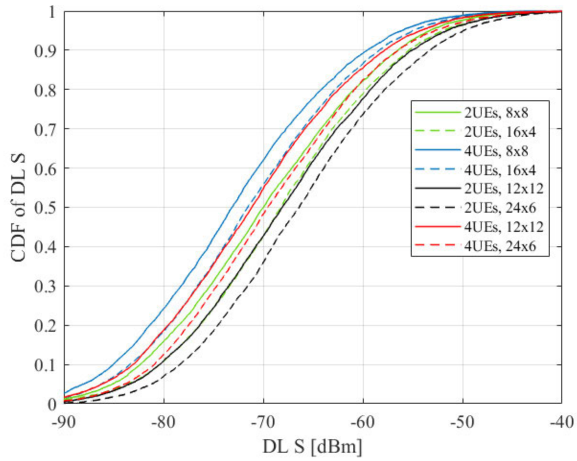

FIGURE 9. CDFs of DL S per UE for mmWave suburban FWA deployment with MU-MIMO (combined LOS and NLOS links).

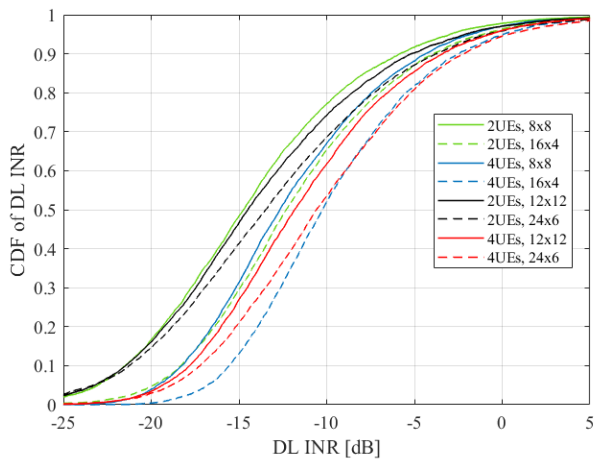

FIGURE 10. CDFs of DL INR per UE for mmWave suburban FWA deployment with MU-MIMO (combined LOS and NLOS links).

conditions were assumed in case of interfering links from BSs placed on a different street than the street where victim CPE was placed. Interfering link from the same cell (intra-cell interference) followed the same condition as wanted signal link. Other predefined suburban FWA deployment parameters, as shown in TABLE 4, are chosen judiciously to represent a realistic deployment scenario.

B. SIMULATION RESULTS

Simulation results have been obtained from system level simulations using Monte Carlo methodology, following the 3GPP stochastic channel model reconstruction as shown in the Fig. 3. Results have been collected in the form of CDFs of the most relevant performance metrics, which provides statistical performance assessment of the FWA network. This approach enables obtaining a broader picture of system performance in reference to deterministic site-specific evaluations. Deterministic channel models, such as clustered delay line (CDL) models of 3GPP [9], are more appropriate for link level simulations and are not in the scope of this work.

Simulation scenario assumes MU-MIMO with analog beamforming per antenna array, which in each sector allows to serve 2 or 4 users at a time. The Maximum Ratio Combining (MRC) precoding has been used for determination of beam pointing directions per polarization.

For the calculation of DL throughput, the model from section 5.2.7 of 3GPP [10] has been used with input SINR obtained from simulations. All the performance metrices are presented for a single stream transmission per user from one polarization of the antenna. In case of MIMO rank 2 the available throughput can be doubled due to high cross-polarization ratio (XPR) in most of the radio channels [9], which could guarantee low inter-stream interference, even with open loop MIMO precoding schemes.

CDFs of DL S, INR, and SINR are shown in Fig. 9, Fig. 10, and Fig. 11, respectively. Note that optimization of antenna pattern leads to the increase of DL interference by more than

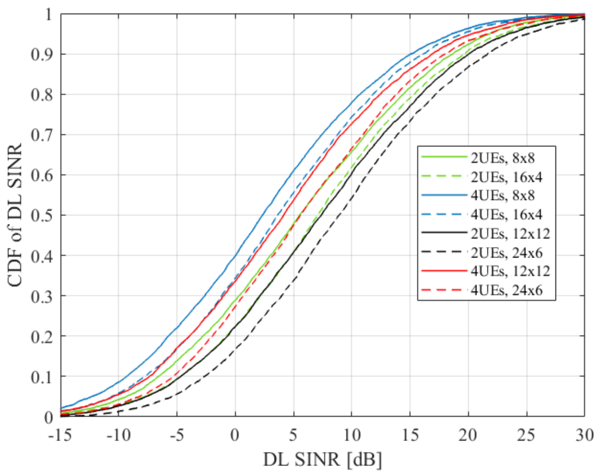

FIGURE 11. CDFs of DL SINR per UE for mmWave suburban FWA deployment with MU-MIMO (combined LOS and NLOS links).

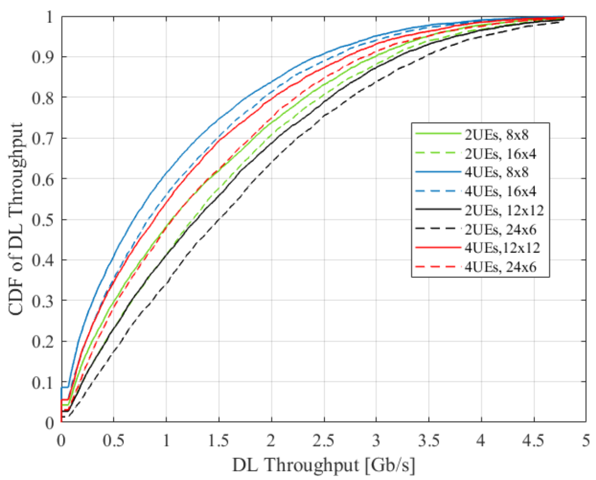

FIGURE 12. CDFs of DL throughput per UE for mmWave suburban FWA with MU-MIMO deployment (combined LOS and NLOS links).

2 dB in median, but due to low INR (95% of links feature interference below the noise level) this rise has negligible impact on DL SINR. The almost 2 dB gain in DL S by optimizing antenna pattern dominates the improvement of DL SINR and throughput (Fig. 12).

TABLE 5 and TABLE 6 contain comparisons of DL SINR and DL throughput for MU-MIMO with 2 and 4 users per cell, when antenna array configurations is optimized from 8×8 to 16×4 and from 12×12 to 24×6, respectively. Optimization of antenna pattern allows 12% to 17% improvement in the DL throughput in median and 39% to 52% improvement at the cell edge. The significant improvement of the cell edge performance is particularly important for mmWave deployments, due to challenging propagation conditions.

TABLE 5. Summary of system level simulation results of the performance in mmWave 5G FWA network in suburban environment for $N = 64$.

	2UEs, 8x8	2UEs, 16x4	4UEs, 8x8	4UEs, 16x4
	DL SINR per UE			
Median	5.5 dB	7.1 dB	2.4 dB	3.6 dB
	→ +1.6 dB →		→ +1.2 dB →	
Cell edge (10%-tile)	-6.6 dB	-4.7 dB	-9.3 dB	-7.8 dB
	→ +1.9 dB →		→ +1.5 dB →	
	DL Throughput per UE			
Median	1.1 Gbps	1.3 Gbps	0.8 Gbps	0.9 Gbps
	→ +17 % →		→ +12 % →	
Cell edge (10%-tile)	138 Mbps	200 Mbps	76 Mbps	106 Mbps
	→ +42 % →		→ +39 % →	

TABLE 6. Summary of system level simulation results of the performance in mmWave 5G FWA network in suburban environment for $N = 144$.

	2UEs, 12x12	2UEs, 24x6	4UEs, 12x12	4UEs, 24x6
	DL SINR per UE			
Median	7.4 dB	8.9 dB	4.2 dB	5.6 dB
	→ +1.5 dB →		→ +1.4 dB →	
Cell edge (10%-tile)	-4.7 dB	-2.7 dB	-7.4 dB	-5.4 dB
	→ +2.0 dB →		→ +2.0 dB →	
	DL Throughput per UE			
Median	1.3 Gbps	1.5 Gbps	0.95 Gbps	1.1 Gbps
	→ +15 % →		→ +16 % →	
Cell edge (10%-tile)	203 Mbps	300 Mbps	116 Mbps	177 Mbps
	→ +48 % →		→ +52 % →	

VII. CONCLUSION

The deployment of 5G and Beyond networks, which utilize beamforming and mmWave or terahertz (THz), requires careful preparations due to complex relations between narrow-beam directional antenna and challenging propagation conditions. When link budget of realistic network is estimated, it is not enough to rely only on nominal antenna pattern, as it occurred in case of omni-directional or sectoral antennas with HPBW much larger than angular spread in the radio channel. In particular, analog beamforming and GoB based hybrid beamforming require effective antenna pattern to be used during estimation of planned network performance and optimization of its parameters. The presented system level simulation results demonstrate that network performance can be overestimated significantly if simplified link budget calculation with nominal antenna pattern is used, which may lead to wrong decisions during network deployments. With a new radio link budget calculation method proposed herein, with slightly added complexity as compared to the simplified approach, the network performance can be estimated accurately and further maximized if optimization of antenna pattern could be done for a given angular spread, leading to about 50% increase of cell edge rate as demonstrated by the FWA example, which is particularly important in challenging propagation conditions of mmWave.

VIII. ACKNOWLEDGMENT

This article was presented in part at the European Conference on Antennas and Propagation 2019 and in part at the 2019 IEEE 5G World Forum.

REFERENCES

[1] *Work Item on New Radio (NR) Access Technology*, document RP-190213, 2019.
[2] *Revised LTE WI Description*, document RP-181726, 2008.
[3] K. Bechta, M. Rybakowski, F. Hsieh, and D. Chizhik, "Modeling of radio link budget with beamforming antennas for evaluation of 5G systems," in *Proc. IEEE 5G World Forum*, Jul. 2018, pp. 427–432.

[4] J. Du, E. Onaran, D. Chizhik, S. Venkatesan, and R. A. Valenzuela, ''Gbps user rates using mmWave relayed backhaul with high-gain antennas,'' *IEEE J. Sel. Areas Commun.*, vol. 35, no. 6, pp. 1363–1372, Jun. 2017.
[5] D. Chizhik, J. Du, R. Feick, M. Rodriguez, G. Castro, and R. A. Valenzuela, ''Path loss and directional gain measurements at 28 GHz for non-line-of-sight coverage of indoors with corridors,'' *IEEE Trans. Antennas Propag.*, vol. 68, no. 6, pp. 4820–4830, Jun. 2020.
[6] J. Du, D. Chizhik, R. Feick, M. Rodriguez, G. Castro, and R. A. Valenzuela, ''Suburban fixed wireless access channel measurements and models at 28 GHz for 90% outdoor coverage,'' *IEEE Trans. Antennas Propag.*, vol. 68, no. 1, pp. 411–420, Jan. 2020.
[7] D. Chizhik, J. Du, R. A. Valenzuela, J. Otterbach, R. Fuchs, and J. Koppenborg, ''Path loss and directional gain measurements at 28 GHz for factory automation,'' in *Proc. IEEE Int. Symp. Antennas Propag. USNC-URSI Radio Sci. Meeting*, Jul. 2019, pp. 2143–2144.
[8] J. Du, D. Chizhik, R. A. Valenzuela, R. Feick, M. Rodriguez, G. Castro, T. Chen, M. Khli, and G. Zussman, ''Directional measurements in urban street canyons from macro rooftop sites at 28 GHz for 90% outdoor coverage,'' *IEEE Trans. Antennas Propag.*, to be published.
[9] *Study on Channel Model for Frequencies From 0.5 to 100 GHz (Release 15)*, document TR 38.901 V15.0.0, 3GPP, 2018.
[10] *Study on New Radio Access Technology; RF and co-existence aspects (Release 14)*, document TR 38.803 V14.0.0, 3GPP, 2018.
[11] K. Bechta, M. Rybakowski, and J. Du, ''Impact of effective antenna pattern on millimeter wave system performance in real propagation environment,'' in *Proc. Eur. Conf. Antennas Propag. (EuCAP)*, 2019, pp. 1–5.
[12] K. Bechta, J. Du, and M. Rybakowski, ''Optimized antenna array for improving performance of 5G mmWave fixed wireless access in suburban environment,'' in *Proc. IEEE 2nd 5G World Forum (5GWF)*, Sep. 2019, pp. 376–381.
[13] C. A. Balanis, *Antenna Theory: Analysis and Design*. Hoboken, NJ, USA: Wiley, 2016.
[14] K. Bechta, M. Rybakowski, and J. Du, ''Efficiency of antenna array tapering in real propagation environment of millimeter wave system,'' in *Proc. Eur. Conf. Antennas Propag. (EuCAP)*, 2019, pp. 1–4.
[15] E. Oran Brigham, *The Fast Fourier Transform and its Applications*. Upper Saddle River, NJ, USA: Prentice-Hall, 1988.
[16] J. Du, M. Rybakowski, K. Bechta, and R. A. Valenzuela, ''Matching in the air: Optimal analog beamforming under angular spread,'' 2019, *arXiv:1910.11054*. [Online]. Available: http://arxiv.org/abs/1910.11054
[17] J. Du, D. Chizhik, R. Feick, G. Castro, M. Rodriguez, and R. A. Valenzuela, ''Suburban residential building penetration loss at 28 GHz for fixed wireless access,'' *IEEE Wireless Commun. Lett.*, vol. 7, no. 6, pp. 890–893, Dec. 2018.
[18] *Radio Frequency (RF) requirement background for Active Antenna System (AAS) Base Station (BS) (Release 13)*, document TR 37.842 V13.0.0, 3GPP, 2016.

KAMIL BECHTA received the M.Sc. degree in wireless communications from the Electronics Faculty, Military University of Technology, Warsaw, Poland, in 2010, where he is currently pursuing the Ph.D. degree in the area of extended modeling of performance and co-existence requirements for 5G and Beyond with massive MIMO antenna configurations.

After graduation, he worked as a Research Assistant with the Military University of Technology, Warsaw, and he joined Nokia Siemens Networks, in 2011, as a 3GPP RAN4 Standardization Specialist responsible for RF and RRM requirements of HSPA and LTE. Since 2015, he has been a 5G Senior Radio Research Engineer with Nokia Bell Labs, where he was leading a team responsible for spectrum and co-existence studies for 5G. In 2017, he was participating in the development of advanced baseband platform software for 5G network products of Nokia, whereas since July 2017, he has been responsible for specification and architecture of radio modules for 5G systems with the Mobile Networks Department, Nokia, Wroclaw. He is a coauthor of more than 15 articles and five patents in the area of wireless communications.

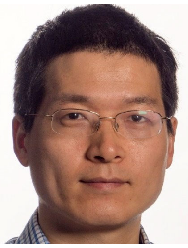

JINFENG DU (Member, IEEE) received the B.Eng. degree in electronic information engineering from the University of Science and Technology of China (USTC), Hefei, China, and the M.Sc., Tekn.Lic., and Ph.D. degrees from the Royal Institute of Technology (KTH), Stockholm, Sweden.

He was a Postdoctoral Researcher with the Massachusetts Institute of Technology (MIT), Cambridge, MA, USA, from 2013 to 2015. After that, he joined Bell Labs, Holmdel, NJ, USA, where he is currently a member of Technical Staff. His research interests include the general area of wireless communications, especially in communication theory, information theory, wireless networks, millimeter wave propagation, and channel modeling.

Dr. Du received the Best Paper Award from IC-WCSP, in October 2010, and his paper was elected as one of the ''Best 50 Papers'' in the IEEE GLOBECOM 2014. He received the prestigious ''Hans Werthen Grant'' from the Royal Swedish Academy of Engineering Science (IVA) in 2011, the ''Chinese Government Award for Outstanding Self-Financed Students Abroad,'' in 2012, and the International PostDoc Grant from the Swedish Research Council, in 2013. He also received three grants from the Ericsson Research Foundation.

MARCIN RYBAKOWSKI received the M.Sc. degree in electronics and telecommunication (wireless communication) from the Faculty of Electronics, Wrocław University of Science and Technology, Poland, in 2003, where he is currently pursuing the Ph.D. degree in electromagnetic field exposure for multiantenna systems.

He worked with Becker Avionics, Wroclaw, Poland, as an RF Engineer and Fujitsu, Tokyo, Japan, as an RFIC Engineer. He joined Siemens (then Nokia Siemens Networks), Wroclaw, in 2006, as an Integration and Verification Engineer for 3G and Wimax Base Stations. He has been a Senior Radio Research Engineer with Nokia Solutions and Networks (then Nokia Bell Labs) since 2012, where he was responsible for research on small cells networks for 3G HSPA systems and radio channel modeling for 5G systems. Since 2016, he has been a Senior Specialist at Nokia, and works with the Mobile Networks 5G & Small Cell Architecture Department, Wrocław, where he is responsible for specification and architecture of radio modules for 5G systems. He is the coauthor of more than 15 articles and holds more than ten patents in the area of wireless systems. His research interests include EMF exposure, multiantenna systems, radio wave channel modelling, and evaluation and modelling of wireless systems.

Mr. Rybakowski received the ''Young Scientist Award'' for the best paper presented at the 10th National Symposium of Radio Science (URSI), and the M.Sc. thesis on microwave, antenna and radar engineering ranked third in a competition organized by the IEEE Polish Section.

URSI GASS 2020, Rome, Italy, 29 August - 5 September 2020

Impact of Effective Antenna Pattern on Radio Frequency Exposure Evaluation for 5G Base Station with Directional Antennas

Kamil Bechta(1), Christophe Grangeat (2), and Jinfeng Du(3)
(1) Nokia, Mobile Networks, Wroclaw, Poland
(2) Nokia, Mobile Networks, Paris, France
(3) Nokia, Bell Labs, Holmdel, NJ, USA

Abstract

Together with introduction of 5th generation (5G) of mobile communication system the new challenge for radio frequency (RF) exposure evaluation for base stations (BS) arises, which is mainly caused by high gain directional antennas with beamforming and beam steering. To assess RF exposure due to narrow and high gain service/traffic beams the extrapolation methods have been defined on the basis of exposure for broadcast/signaling beams which easier for determination due to theirs lower directivity. This paper indicates what is the impact on extrapolation of RF exposure for service/traffic beam if antenna gains assumed during calculations are based on nominal patterns, as measured in anechoic, instead of effective patterns determined by realistic propagation conditions. Example calculations performed for representative commercially available antenna indicate that extrapolated RF exposure for service/traffic beam can be overestimated by 1.5 dB to 2.0 dB, when power of reflected waves is dominant, i.e. BS and point of investigation are in non line of sight (NLOS) conditions.

1 Introduction

5th generation (5G) of mobile communication systems introduces wide use of high gain directional antenna by base stations (BS). On top of that the beamformed antenna pattern can be steered towards different directions inside the cell to maximize the end user data rate. Therefore, the radio frequency (RF) exposure evaluation is complex because the electromagnetic field exposure parameters may change rapidly depending on traffic variations and beam directions. The International Electrotechnical Commission (IEC) has proposed guidelines to address the actual parameters of RF exposure for massive multiple input multiple output (mMIMO) and beamforming in [1] and [2]. This paper investigates how the accuracy of extrapolation method proposed in [1] can be improved by using the effective antenna pattern instead of the nominal antenna pattern when assessing the EMF exposure levels in one place.
Section 2 of this paper clarifies the difference between nominal and effective antenna patterns. Section 3 indicates how the level of extrapolation factor changes upon replacement of the nominal antenna pattern by effective antenna pattern in the example of commercial antenna. Section 4 proposes closed-form model for calculation of effective antenna gain according to angular spread statistics in given propagation conditions. Section 5 summarizes and concludes the paper.

2 Nominal and effective antenna patterns

With increasing number of antenna elements in the array the *nominal* gain of the antenna array, as measured in anechoic chamber, increases and the half-power beam-width (HPBW) decreases. In scattering environment, the maximum realizable antenna array gain, the *effective* beam pattern and its associated HPBW differ from nominal values. Difference between the nominal and the effective patterns in the radio channel with scattering depends on the angular spread introduced by the real deployment scenarios.
Nominal antenna array gain in the free space propagation conditions can be expressed by following equation [3]:

$$g_{\max}^{Nom} = \frac{2}{B_{ho} \cdot B_{vo}} = N \cdot G_e \tag{1}$$

where $g_{\max}^{Nom}$ is the maximum nominal antenna array gain, B_{ho} and B_{vo} are the nominal root mean square (RMS) beamwidth in horizontal and vertical planes (in radians), respectively, N is the number of antenna elements in the array, and G_e is the gain of single antenna element. Equations (2)-(4) give the overview how the effective antenna patterns can be analytically obtained based on nominal antenna pattern and power angular spectrum (PAS) for assumed propagation environment model.

$$g^{Eff}\left(\phi_0,\theta_0\right) = \int_{-180^\circ}^{180^\circ}\int_{0^\circ}^{180^\circ} g^{Nom}\left(\phi,\theta\right)\cdot p\left(\phi-\phi_0,\theta-\theta_0\right)d\phi d\theta \tag{2}$$

$$g_{Az}^{Eff}\left(\phi_0\right) = g^{Eff}\left(\phi_0,\theta_0=90^\circ\right) = \int_{-180^\circ}^{180^\circ} g^{Nom}\left(\phi,\theta=90^\circ\right)\cdot p_{Az}\left(\phi-\phi_0\right)d\phi \tag{3}$$

$$g_{Ele}^{Eff}\left(\theta_0\right) = g^{Eff}\left(\phi_0=0^\circ,\theta_0\right) = \int_{0^\circ}^{180^\circ} g^{Nom}\left(\phi=0^\circ,\theta\right)\cdot p_{Ele}\left(\theta-\theta_0\right)d\theta \tag{4}$$

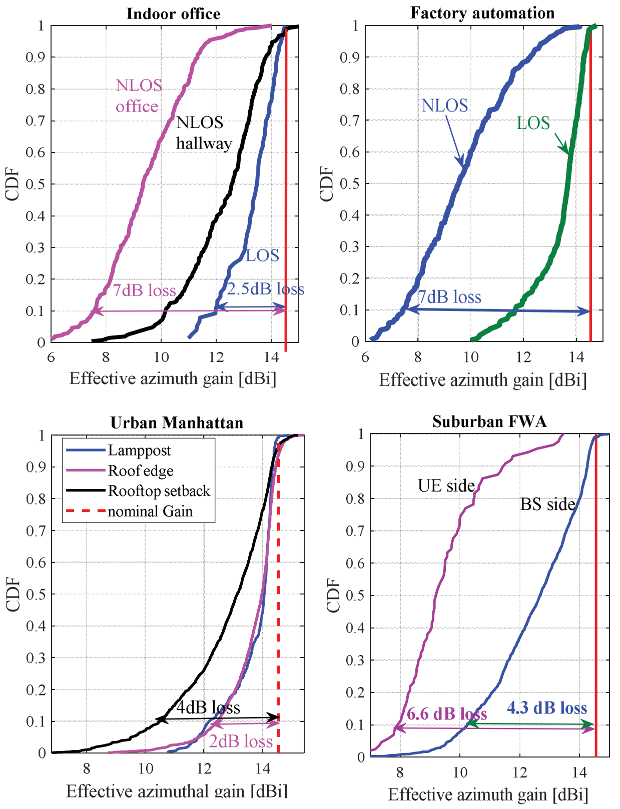

Figure 1. CDFs of effective antenna gains measured in indoor office, suburban FWA, factory automation and urban Manhattan environments presented in comparison with nominal antenna gain [4][5][6][7]

In above equations g^{Eff} indicates three-dimensional (3D) effective antenna pattern, whereas g^{Nom} indicates 3D nominal antenna pattern. g^{Eff}_{Az} and g^{Eff}_{Ele} indicate azimuth and elevation cuts of effective antenna pattern, ϕ and θ define angular domain in azimuth and elevation, respectively, whereas ϕ_0 and θ_0 indicate boresight direction between transmitter (Tx) and receiver (Rx) in azimuth and elevation, respectively. p_{Az} and p_{Ele} represent realizations of power angular spectrum (PAS) in azimuth and elevation.

Fig. 1 presents summary of statistically analyzed measurement result in different deployment scenarios, i.e. indoor office, suburban fixed wireless access (FWA), factory automation and urban Manhattan [4][5][6][7], in the form of cumulative distribution function (CDF) from measurement result samples. In all scenarios the severe impact of angular spread on effective antenna gain is visible. In case of NLOS the reduction in azimuth gain can be as high as 7 dB for 10% of measured radio links or 5 dB for 50% of measured radio links, in reference to maximum nominal gain of 14.5 dBi.

Measurement results demonstrate that nominal antenna patterns, as measured in anechoic chamber, are valid only in free space propagation conditions. This conclusion is particularly important in the context of calculations which are aimed to evaluate RF exposure from mMIMO antennas of 5G system.

3 Accuracy of extrapolation factor

To illustrate the impact of angular spread in real propagation conditions on antenna pattern and therefore on extrapolation factor defined in [1], the example of commercial antenna have been used [8]. Main parameters of antenna [8] are disclosed in Table 1. The effective antenna patterns for broadcast beams (also called signaling beams) and service beams (also called traffic beams) have been determined in statistical simulations according to (3) and (4). Simulations have been performed for 3.5 GHz frequency and the angular spread statistics from urban macro (UMa) channel model defined by 3rd generation partnership project (3GPP) standardization organization in [9]. Output effective beam patterns in horizontal plane are presented in Fig. 2, whereas Fig. 3 illustrates magnified view of main lobes. As can be noticed, the difference between maximum gains of nominal and effective beam patterns are small in case of line of sight (LOS) and for both broadcast/signaling and service/traffic beam are around 0.4 dB. However, this difference grows significantly in NLOS conditions, up to 4.8 dB and 6.3 dB for broadcast/signaling and service/service beams, respectively. Simulated values of maximum antenna gains are captured in Table 2.

According to definition made in [1] the extrapolation factor is the ratio of the equivalent isotropic radiated power (EIRP) envelope of all service/traffic beams to the EIRP envelope of the broadcast/signaling beam in the direction of the measurement location. Envelope of EIRP is determined by the maximum antenna gains in the full steering range of mMIMO antenna and the transmit power. Assuming the same transmit power is used for broadcast/signaling and service/traffic beams, the extrapolation factor in the boresight direction can be approximated based on maximum antenna gains of broadcast/signaling and service/traffic beams. Values of extrapolation factor calculated according to this approach for nominal and effective maximum antenna gains are captured in Table 2. Results indicate that for the analyzed example of commercial antenna and assumed propagation environment the extrapolation factor can be overestimated by 1.5 dB in NLOS conditions, which may lead to overly conservative compliance distance due to RF exposure.

Table 1. Main parameters of assumed antenna patterns [8]

Parameter	Beam
Broadcast/signaling	
Gain [dBi]	20.8
Horizontal HPBW [°]	58
Vertical HPBW [°]	6.6
Service/traffic	
Gain [dBi]	16.7
Horizontal HPBW [°]	24
Vertical HPBW [°]	6.6

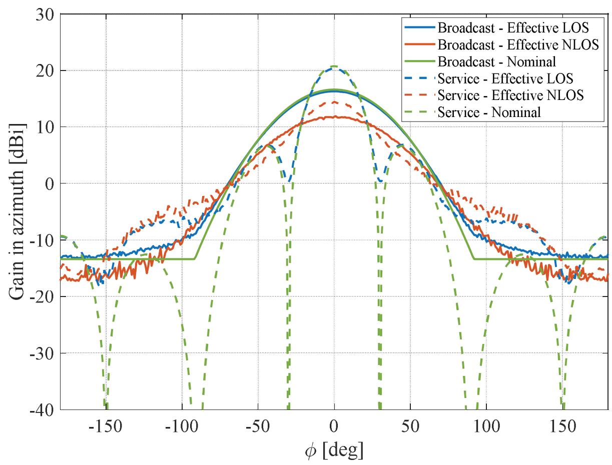

Figure 2. Nominal and effective antenna patterns of broadcast/signaling and service/traffice beams [8]

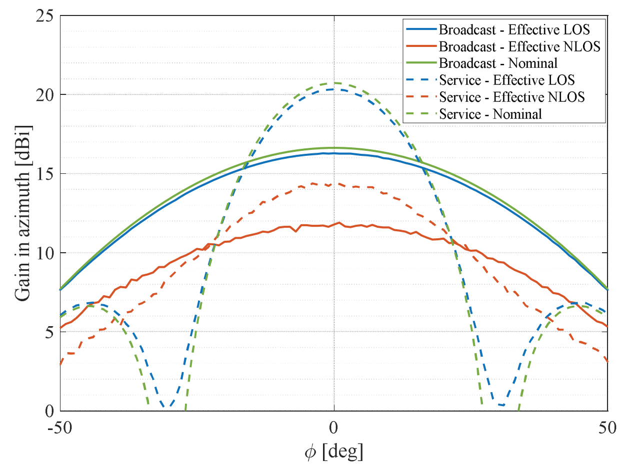

Figure 3. Nominal and effective antenna patterns of broadcast and service/traffice beams [8] – magnified view of main lobes

Table 2. Maximum antenna gains and approximated extrapolation factor according to statistical simulations

Beam type	Nominal max gain [dBi]	Simulated effective max gain [dBi]	
		LOS	*NLOS*
Broadcast/signaling	16.7	16.3	11.9
Service/traffic	20.8	20.4	14.5
Approximated extrapolation factor [dB]	4.1	4.1	2.6

Table 3. Maximum antenna gains and approximated extrapolation factor according to closed-form calculations

Beam type	Nominal max gain [dBi]	Calculated effective max gain [dBi]	
		LOS	*NLOS*
Broadcast/signaling	16.7	16.4	13.8
Service/traffic	20.8	19.5	15.9
Approximated extrapolation factor [dB]	4.1	3.1	2.1

4 Simplified calculation of effective maximum antenna gain

As presented by (2) the effective antenna pattern is assumed to be convolution of two gaussian signals, i.e. nominal antenna pattern with variance indicate by (B_{h0}^2, B_{v0}^2) and PAS with variance indicated by (σ_h^2, σ_v^2), where σ_h is RMS azimuthal angular spread and σ_v is RMS elevation angular spread, respectively, in given propagation environment. The resulting effective antenna pattern is also gaussian signal with variance indicated by $(B_{h0}^2 + \sigma_h^2, B_{v0}^2 + \sigma_v^2)$. Therefore, following (1) the maximum effective antenna gain can be determined by (5).

$$g_{\max}^{Eff} = \frac{2}{\sqrt{B_{h0}^2 + \sigma_h^2} \cdot \sqrt{B_{v0}^2 + \sigma_v^2}} \tag{5}$$

The RMS angular spread can be obtained from statistical channel models, like [8], measurements or ray tracing simulations and introduced into (5) to calculate the effective maximum antenna gain, as running of statistical simulations with (2) may not always be feasible. Afterwards, the calculation results can be used to improve accuracy of extrapolation factor introduced in [1].

Table 3 include results of calculations performed according to (5) for antenna beam patterns metrics from Table 1. As [8] does not include detailed information about antenna array layout, the parameters assumed in presented work have been selected to match metrics from Table 1, and used for calculations according to (5), which in more details is described in [3] and [10].

5 Conclusion

This paper discusses effective antenna pattern, especially maximum effective antenna gain, from the perspective of RF exposure evaluation for 5G with mMIMO and beamforming. It has been presented that the maximum effective antenna gain in realistic propagation environment is lower than maximum nominal antenna gain measured in anechoic chamber or ideal free space conditions. Difference between nominal and effective gains depends on the scattering intensity in the radio channel between transmitting antenna and the point of investigation and is noticeable especially in case of NLOS conditions The analysis has been performed using a representative commercially available antenna for which the ratio of service/traffic beam gain and broadcast beam gain has been calculated. Such approximation of extrapolation factor, as determined in [1], indicates that its value for analyzed antenna, working in 3.5 GHz frequency and deployed in UMa environment, can be overestimated by 1.5 dB to 2.0 dB for NLOS conditions if nominal antenna patterns are assumed instead of effective antenna pattern. Therefore, it is important to consider using the effective antenna gains in extrapolation factor to reduce overestimation of RF exposure.

7 References

[1] IEC TR 62669, “Case studies supporting IEC 62232 – Determination of RF field strength and SAR in the vicinity of radiocommunication base stations for the purpose of evaluating human exposure”.

[2] IEC 62232:2017, “Determination of RF field strength, power density and SAR in the vicinity of radiocommunication base stations for the purpose of evaluating human exposure”, September 2017.

[3] J. Du, E. Onaran, D. Chizhik, S. Venkatesan, R. A. Valenzuela, “Gbps User Rates Using mmWave Relayed Backhaul with High Gain Antennas”, IEEE Journal on Selected Areas in Communications, vol. 35, pp. 1363-1372, Jun. 2017.

[4] D. Chizhik, J. Du, R. Feick, M. Rodriguez, G. Castro, R. A. Valenzuela, “Path loss, beamforming gain and time dynamics measurements at 28 GHz for 90% indoor coverage”, submitted to IEEE for possible publication. (arXiv:1712.06580).

[5] J. Du, D. Chizhik, R. Feick, M. Rodriguez, G. Castro, R. A. Valenzuela, “Suburban Fixed Wireless Access Channel Measurements and Models at 28 GHz for 90% Outdoor Coverage”, IEEE Transactions on Antennas and Propagation, vol. 68, pp. 411-420, Jan. 2020.

[6] D. Chizhik, J. Du, R. A. Valenzuela, J. Otterbach, R. Fuchs, J. Koppenborg, “Path Loss and Directional Gain Measurements at 28 GHz for Factory Automation”, IEEE International Symposium on Antennas and Propagation and USNC-URSI Radio Science Meeting, Jul. 2019.

[7] J. Du, D. Chizhik, R. A. Valenzuela, R. Feick, M. Rodriguez, G. Castro, T. Chen, M. Khli, G. Zussman, “Directional Measurements in Urban Street Canyons from Macro Rooftop Sites at 28 GHz for 90% Outdoor Coverage,” submitted to IEEE for possible publication. (arxiv:1908.00512).

[8] Commscope, “RRZZHHTTS4-65B-R7”, Datasheet, Sep. 2019.

[9] 3GPP Radio Access Network Working Group, “Study on channel model for frequencies from 0.5 to 100 GHz (Release 15)”, 3GPP TR 38.901 V15.0.0.

[10] J. Du, M. Rybakowski, K. Bechta and R. A. Valenzuela, “Matching in the Air: Optimal Analog Beamforming under Angular Spread”, submitted to IEEE for possible publication. (arxiv:1910.11054).

IEEE Access
Multidisciplinary ⋮ Rapid Review ⋮ Open Access Journal

Date of publication xxxx 00, 0000, date of current version xxxx 00, 0000.

Digital Object Identifier 10.1109/ACCESS.2017.Doi Number

Analysis of 5G Base Station RF EMF Exposure Evaluation Methods in Scattering Environments

Kamil Bechta[1], Christophe Grangeat[2], Jinfeng Du[3], Member, IEEE and Marcin Rybakowski[1]

[1]Mobile Networks, Nokia, Wroclaw, Poland
[2]Mobile Networks, Nokia, Paris, France
[3]Bell Labs, Nokia, Murray Hill, NJ, USA

Corresponding author: Kamil Bechta (e-mail: kamil.bechta@nokia.com).

This article is corrected and extended version of conference paper presented during 2020 XXXIIIrd General Assembly and Scientific Symposium of the International Union of Radio Science (URSI GASS 2020).

ABSTRACT Together with the introduction of the 5th generation (5G) of mobile communication systems the methods for the assessment of radio frequency electromagnetic field (RF EMF) exposure are being updated to account for actual transmitting, beamforming and beam-steering performances. The International Electrotechnical Commission (IEC) develops and validates methods for assessing the RF EMF exposure due to base stations (BS). When the assessment is performed in-situ, it is recommended to extrapolate the maximum level of exposure from measurement of stable signals, such as broadcast signal with 5G BS (gNodeB). A comparative analysis of extrapolation method based on nominal antenna pattern (as measured in anechoic chamber) and effective antenna pattern (as measured in scattering environment) of gNodeB is proposed in this paper. This analysis shows that extrapolation method with nominal antenna pattern may lead to significant over-estimation of the maximum RF EMF exposure in case of scattering environment or non-line-of-sight (NLOS) conditions, up to several dB, depending on design of evaluated beam patterns. This over-estimation can be reduced by using effective antenna pattern in order to better represent the actual propagation conditions, such as those found in urban or dense urban areas. In such actual propagation conditions it is recommended to perform extrapolation of the maximum exposure using appropriate channel characteristics, especially accurate value of angular spread, due to the fact that the use of beamforming and spatial filtering is sensitive to time-variant radio channel conditions. A simplified calculation method to improve the accuracy of RF EMF exposure extrapolation from broadcast signal measurements in scattering environment or NLOS is presented in this paper, leveraging joint modeling of antenna beam pattern and angular spread The proposed simplified calculation method of the effective extrapolation factor provides an accurate evaluation of RF EMF exposure compared to complex channel model simulations and it reduces overestimation resulting from an extrapolation factor based on nominal antenna gains of broadcast and traffic beams.

INDEX TERMS 5G, angular spread, beamforming, effective antenna pattern, EMF, exposure extrapolation, scattering environment

I. INTRODUCTION

Starting from the early stage of radio frequency (RF) equipment deployments, the impact of RF electromagnetic field (EMF) on people has been a subject of extensive research. This continues since the beginning of the global systems for mobile communication (GSM) era. Results of biological, human and epidemiological research studies are the foundation of international recommendations and guidance about RF EMF exposure limits, such as those developed by the International Commission on Non-Ionizing Radiation Protection (ICNIRP) [1] or the IEEE Standards Association (IEEE SA) [2]. ICNIRP RF EMF Guidelines are referenced in many national and international regulations, such as the European Council Recommendation 1999/519/EC [3].

The role of international standardization bodies, such as the International Electrotechnical Commission (IEC) is to develop harmonized methods for the assessment of equipment compliance with these RF EMF exposure limits, sometimes in cooperation with the IEEE SA. For the

IEEE Access
Multidisciplinary : Rapid Review : Open Access Journal

assessment of compliance of mobile networks base station (BS), the most generally implemented standard is IEC 62232:2017 [4]. It is used by equipment manufacturers, mobile network operators and regulators at all stage of mobile network life, starting when placing equipment on the market, when putting them into operation and when surveying in-situ compliance during operation.

Implementation case studies have also been published in the IEC Technical Report (TR) 62669:2019 [5] to show good practice of [4]. The publication of this TR [5] coincides with the first commercial deployments of the 5th generation (5G) of mobile communication system and includes early stage analysis of the impact of the utilization of massive multiple-input-multiple-output (mMIMO) systems [6] using antennas with advanced beamforming and beam-steering capabilities. Such antennas have radiation patterns with high gain and small half power beam width (HPBW) varying in time and space, while traditional antennas deployed previously had constant gain and beam direction. The 5G beamforming patterns can change its gain, shape and spatial position in the cell several times within 1 ms, as in the New Radio (NR) standard [7] by the 3rd Generation Partnership Project (3GPP) for 5G system. These differences in beam pattern designs have significant impact on the methods for the assessment of RF EMF exposure from BS of 5G system (gNodeB).

Several studies [8], [9] have investigated the impact of time and spatial averaging on the actual exposure values. They have been analyzed in detail in [5], which also includes guidelines for considering the actual maximum exposure in compliance assessment. Another recommendation of [5] is to develop methods for the extrapolation of maximum exposure from in-situ measurements of broadcast beams, which are stable beams in terms of transmitted power and beam pattern. The extrapolation factor consists in the ratio of the envelope of the exposure resulting from all configured traffic beams and the exposure to broadcast beam in one direction. Determination of RF EMF exposure associated with traffic beam is particularly important as traffic signals carry majority of radio resources related to downlink (DL) transmission, which necessitates a reliable assessment of exposure associated with given gNodeB. Extrapolation techniques are described in [10] and [11] and have been introduced in the update of [4]. The extrapolation formula for exposure from traffic beams can be defined as below:

$$E_{asmt} = E_{broadcast} \times \sqrt{F_{extBeam} \times F_{BW} \times F_{PR} \times F_{TDC}} \quad (1),$$

where E_{asmt} and $E_{broadcast}$ are the extrapolated electric field strength of traffic signal in V/m and evaluated (measured) electric field strength of broadcast signal in V/m per given resource element, respectively. $F_{extBeam}$ is extrapolation factor corresponding to the ratio of the equivalent isotropic radiated power (EIRP) envelope of all traffic signals to the EIRP envelope of the broadcast signal in the direction of the measurement location. F_{BW}, F_{PR} and F_{TDC} are remaining extrapolation factors corresponding respectively to the ratio of the total carrier bandwidth and the subcarrier frequency spacing of the broadcast signal, the power reduction factor (if the actual maximum approach is used) and the maximum technology duty cycle of all signals [5].

Extrapolation of maximum RF EMF exposure associated with gNodeB has been investigated in multiple studies and publications. For example, [12] indicates the need for definition of accurate extrapolation method based on measurements of broadcast signal and factors such as new antenna radiation patterns, time division duplex (TDD) access to the medium, number of possible simultaneous beams and distribution of terminals associated with given BS causing movement of beams in the space. Detailed studies with comprehensive measurement campaigns have been presented in [11] and [13], where high accuracy of extrapolation procedures was demonstrated in comparison to corresponding measurement results of artificially forced maximum possible RF EMF exposure associated with traffic signals. However, in the majority of published studies the extrapolation of maximum exposure from gNodeB is investigated in good propagation conditions, where line-of-sight (LOS) visibility between examined gNodeB and measurement location is ensured. Such approach simplifies the evaluation and allows to neglect the impact of reflections and scattering, which reduce accuracy of extrapolation method. It has been already noticed in [14] that extrapolation in scattering environment or non-line-of-sight (NLOS) conditions is much more complex and ratio between gains of broadcast and traffic beams is difficult to be predicted in case of radio links based on scattering objects. Confirmation of these predictions can be found in [15] which presents results of exposure extrapolated for different evaluation points inside 5G cell with mMIMO antenna and compares these extrapolations with measurement of actual exposure associated with traffic signal. In case of measurement points placed in the middle of the cell and ensuring LOS visibility with gNodeB, the extrapolated exposure and the measured maximum exposure demonstrate good agreement, in similar way as it was presented in [11] and [13]. However, the measurement results for points placed in NLOS conditions, i.e. when direct visibility between measurement location and gNodeB is not ensured, show significantly lower maximum exposure than obtained from extrapolation method described in [5], [11] and [13], especially for the points placed on the cell edge. This overestimation of the maximum exposure in NLOS conditions confirms predictions made in [14] that, in the presence of reflections and scattering objects, the accuracy of extrapolation method is lower than in LOS conditions. Therefore, instead of assuming free space propagation conditions, on top of theoretical parameters of broadcast and traffic signals, the accurate extrapolation of the maximum exposure should be performed with appropriate radio channel characteristics due to the fact that the use of beamforming and spatial filtering is sensitive to time-variant radio channel conditions.

This paper presents an alternative approach to (1) for evaluating the $F_{extBeam}$ extrapolation factor associated with a gNodeB considering the actual propagation conditions. Section II of the paper introduces definitions of nominal and effective antenna patterns, which are crucial from the perspective of accurate extrapolation procedure. In Section III the simulation results of $F_{extBeam}$ extrapolation factors in LOS and NLOS conditions are presented, assuming broadcast and traffic beam patterns of commercially available 5G antenna [16] and three different propagation environments according to 3GPP channel model [17]. Section IV includes detailed description of calculation method for effective extrapolation factor, whereas Section V concludes the paper.

II. NOMINAL AND EFFECTIVE ANTENNA PATTERNS

When designing an antenna, one of the main objectives is to obtain a specific gain, HPBW and radiation pattern. In case of antenna arrays, the expectations are mostly high maximum gain and low level of side lobes. Antenna pattern which has been determined by design and validated by measurements in an anechoic chamber is referred to hereinafter as *nominal antenna pattern* of the antenna.

In practical channel scattering environment, which differs significantly from anechoic chamber propagation conditions, the maximum realizable gain and associated HPBW of an antenna array differ from their nominal values and are hereinafter referred to as effective. Therefore, the antenna pattern measured in a scattering environment is defined as *effective antenna pattern* for that channel.

Nominal antenna pattern and gain are antenna specific, whereas effective antenna patterns and the corresponding effective gains change depending on a radio channel in the actual conditions of propagation. The difference between nominal and effective antenna patterns depends on an angular spread (AS) in the scattering environment introduced by a real deployment scenario. Equations (2) to (4) describe how the effective antenna gains g^{Eff} can be analytically obtained from nominal antenna gains g^{Nom} and power angular spectrum (PAS) p of the assumed propagation environment, which in more details is described in the Appendix.

$$g^{Eff}\left(\phi_0,\theta_0\right)=\int_{-180^\circ}^{180^\circ}\int_{-90^\circ}^{90^\circ} g^{Nom}\left(\phi,\theta\right)p\left(\phi_0-\phi,\theta_0-\theta\right)d\phi d\theta\,, \quad (2)$$

$$g_{Az}^{Eff}\left(\phi_0\right)=g^{Eff}\left(\phi_0,\theta_0=0^\circ\right)=\int_{-180^\circ}^{180^\circ} g^{Nom}\left(\phi,\theta=0^\circ\right)p_{Az}\left(\phi_0-\phi\right)d\phi\,, \quad (3)$$

$$g_{Ele}^{Eff}\left(\theta_0\right)=g^{Eff}\left(\phi_0=0^\circ,\theta_0\right)=\int_{-90^\circ}^{90^\circ} g^{Nom}\left(\phi=0^\circ,\theta\right)p_{Ele}\left(\theta_0-\theta\right)d\theta\,. \quad (4)$$

In the above equations ϕ and θ define angular domain in azimuth and elevation, respectively, whereas ϕ_0 and θ_0 indicate the main beam orientation angles in azimuth and elevation, respectively. g_{Az}^{Eff} and g_{Ele}^{Eff} indicate effective antenna gains if only azimuth or elevation plane is considered, respectively, whereas p_{Az} and p_{Ele} represent realizations of PAS in azimuth and elevation, respectively. Effective antenna gains g^{Eff} when calculated for full ranges of beam orientation angles, i.e. $\phi_0 \in \left[-180^\circ;180^\circ\right)$ and $\theta_0 \in \left[-90^\circ;90^\circ\right]$, allows to obtain 3D effective antenna pattern in given propagation conditions specified by PAS p.

Figure 1 presents a summary of statistically analyzed measurement results in different deployment scenarios, i.e. indoor office [19], suburban fixed wireless access (FWA) [20], factory automation [21] and urban Manhattan street canyons [22]. In all the scenarios a severe impact of AS on effective antenna gain is visible. In case of NLOS the reduction in azimuth gain can be as high as 7 dB for 10% of measured radio links or 5 dB for 50% of measured radio

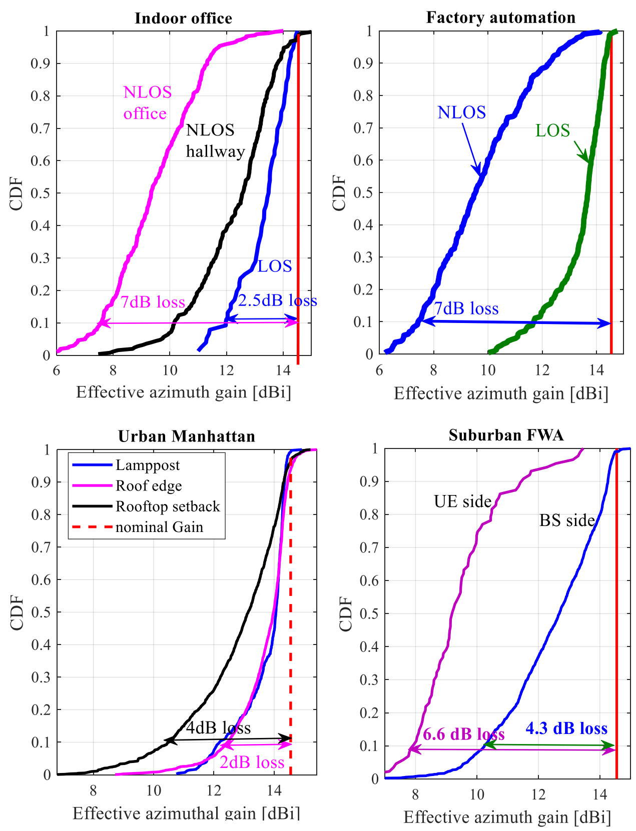

FIGURE 1. Cumulative distribution functions (CDF) of the effective antenna gains measured in indoor office [19], suburban FWA [20], factory automation [21] and urban Manhattan [22] environments presented in comparison with nominal antenna gain (14.5 dBi)

IEEE Access
Multidisciplinary ⁝ Rapid Review ⁝ Open Access Journal

links, in reference to maximum nominal gain of 14.5 dBi in azimuth. This effect is valid for all frequency bands used in the current and future mobile communication systems.

As presented by (2) to (4) the effective antenna pattern is obtained as mathematical convolution of functions describing nominal antenna pattern and PAS in angular domain. Therefore, the shape of effective antenna pattern and its gain are directly connected with the shape and the gain of nominal antenna pattern, as well as AS phenomenon in the given propagation environment. In general, the narrower the HPBW of nominal antenna pattern is and the higher the AS is, the bigger the difference between nominal and effective pattern is. When the nominal patterns of broadcast and traffic beams, used by given gNodeB, have different HPBW and gains, the resulting effective patterns of those beams are impacted differently by the same AS. In consequence the corresponding extrapolation factor $F_{extBeam}$ takes different values in free space propagation or LOS conditions and in NLOS conditions or scattering environment, and impacts the accuracy of maximum RF EMF exposure extrapolation, as described by (1).

Next section demonstrates how the value of $F_{extBeam}$, for the same pair of broadcast and traffic beam patterns, can vary between different scattering propagation conditions.

III. SIMULATION VERIFICATION OF THE EXTRAPOLATION FACTOR

To illustrate the impact of AS in NLOS or scattering environment on $F_{extBeam}$ extrapolation factor, the broadcast and traffic beam patterns of commercial 5G antenna of gNodeB [16] has been used. The effective antenna patterns for the broadcast beam and the traffic beam have been determined in statistical simulations according to (2). Simulations have been performed for 3.5 GHz carrier frequency and the AS statistics for three different propagation environments defined by 3GPP in channel model [17]:

- urban micro street canyon (UMi SC),
- urban macro (UMa),
- rural macro (RMa).

Main parameters of the antenna [16] and root mean square (RMS) values of AS characteristics of all assumed propagation environments are listed in Table I.

Example effective beam patterns in horizontal plane determined for UMa environment are presented in Fig. 2. As can be noticed, the difference between main beam gains of nominal and effective beam patterns are small in case of LOS, but this difference grows significantly in NLOS. On the other hand, the difference in the level of side lobes is noticeable in both LOS and NLOS.

Effective patterns in Fig. 2 were obtained from (2) as mean value from realization of 1000 Monte Carlo statistical simulation drops for parameters of nominal antenna pattern and AS as presented in Table I. AS statistical distributions from 3GPP channel model [17] are defined by inverse

TABLE I
MAIN PARAMETERS OF ASSUMED ANTENNA BEAM PATTERNS [16] AND PROPAGATION ENVIRONMENTS IN NLOS CONDITIONS [17] FOR 3.5 GHZ BAND

Parameter	Value	
Broadcast beam		
Nominal Gain	16.7 dBi	
Nominal Horizontal HPBW	58°	
Nominal Vertical HPBW	6.6°	
Traffic beam		
Nominal Gain	20.8 dBi	
Nominal Horizontal HPBW	24°	
Nominal Vertical HPBW	6.6°	
UMi SC NLOS		
RMS azimuthal AS (σ_h)	Mean	23.97°
	Mean – 2SD	3.77°
	Mean + 2SD	152.57°
RMS elevation AS (σ_v) (Tx-Rx distance of 100 m)	Mean	0.78°
	Mean – 2SD	0.15°
	Mean + 2SD	3.89°
UMa NLOS		
RMS azimuthal AS (σ_h)	Mean	27.40°
	Mean – 2SD	7.55°
	Mean + 2SD	99.48°
RMS elevation AS (σ_v) (Tx-Rx distance of 500 m)	Mean	0.58°
	Mean – 2SD	0.06°
	Mean + 2SD	5.56
RMa NLOS		
RMS azimuthal AS (σ_h)	Mean	8.91°
	Mean – 2SD	1.12°
	Mean + 2SD	70.79°
RMS elevation AS (σ_v) (Tx-Rx distance of 1000 m)	Mean	1.01°
	Mean – 2SD	0.25°
	Mean + 2SD	4.03°

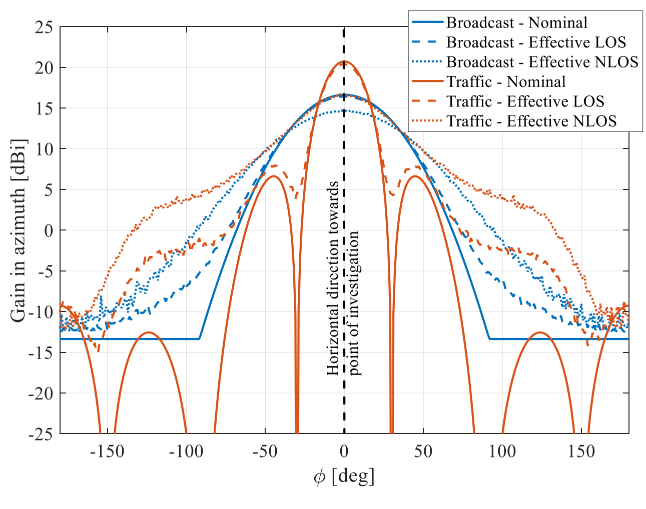

FIGURE 2. Nominal and mean effective antenna patterns of broadcast and traffic beams [16] in 3GPP UMa [17] scenario (boresight direction)

Gaussian and Laplacian functions for azimuth and zenith spreads, respectively. Therefore, Fig. 3 presents cumulative distribution functions (CDF) of main beam effective gains for broadcast and traffic antenna patterns to better illustrate how the effective gain, and $F_{extBeam}$ extrapolation factor, can change in given propagation environment depends on

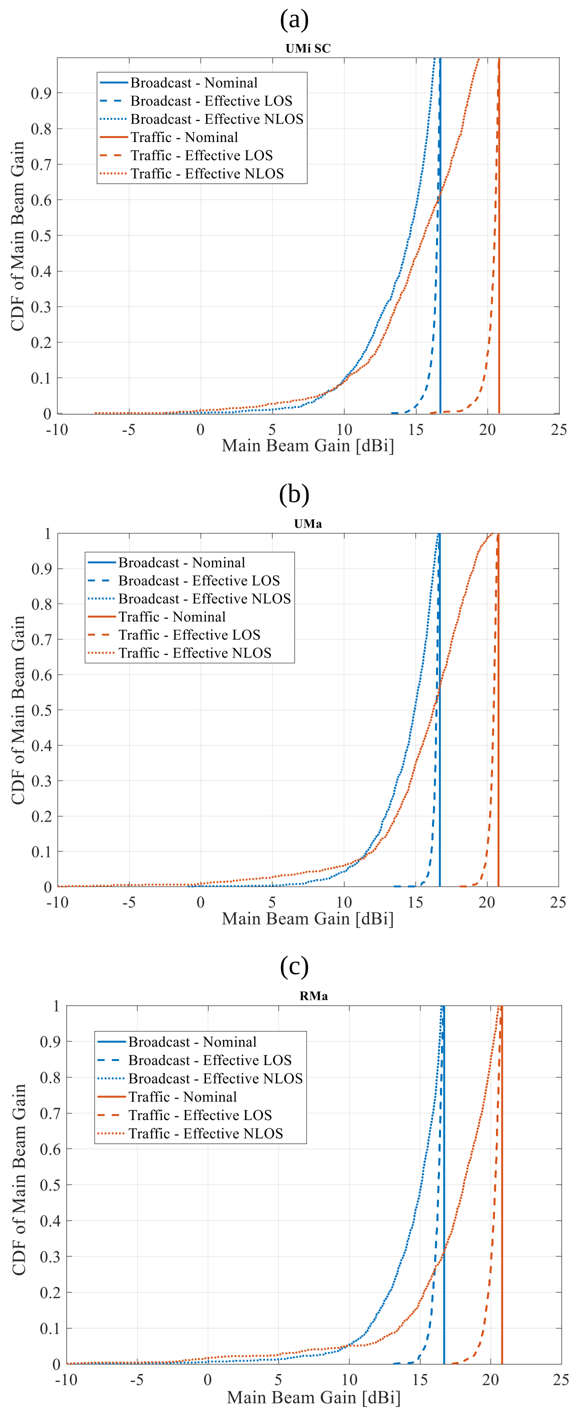

FIGURE 3. CDFs of nominal and effective main beam gains for broadcast and traffic patterns of antenna [16] and 3GPP propagation environments [17] of (a) UMi SC, (b) UMa and (c) RMa

intensity of scattering. Particularly interesting is the change in effective gains of broadcast and traffic beams in highly scattering NLOS conditions. For all three investigated propagation environments in more than 5% of obtained simulation results the effective gain of broadcast beam is higher than traffic beam. This phenomenon in highly scattering environments could be attributed to two factors: 1) the main beams are widened to similar level by the very

TABLE II
NOMINAL AND SIMULATED EFFECTIVE GAINS OF MAIN BEAMS FOR BROADCAST AND TRAFFIC ANTENNA PATTERNS [16] IN UMI SC, UMA AND RMA SCENARIOS [17]

Beam type		**Nominal gain of main beam**	**Simulated effective gain of main beam**	
			LOS	*NLOS*
UMi SC (Boresight)				
Broadcast	Median	16.7 dBi	16.5 dBi	14.6 dBi
	5%-tile		15.5 dBi	8.5 dBi
	95%-tile		16.7 dBi	16.2 dBi
Traffic	Median	20.8 dBi	20.5 dBi	15.6 dBi
	5%-tile		19.4 dBi	8.2 dBi
	95%-tile		20.7 dBi	19.0 dBi
UMa (Boresight)				
Broadcast	Median	16.7 dBi	16.5 dBi	14.9 dBi
	5%-tile		16.0 dBi	10.2 dBi
	95%-tile		16.6 dBi	16.4 dBi
Traffic	Median	20.8 dBi	20.5 dBi	16.2 dBi
	5%-tile		19.8 dBi	8.9 dBi
	95%-tile		20.7 dBi	19.4 dBi
UMa (Steered at -60°in azimuth)				
Broadcast	Mean	5.8 dBi	6.5 dBi	8.8 dBi
Traffic	Mean	16.4 dBi	16.0 dBi	12.2 dBi
RMa (Boresight)				
Broadcast	Median	16.7 dBi	16.3 dBi	15.1 dBi
	5%-tile		15.3 dBi	9.8 dBi
	95%-tile		16.6 dBi	16.4 dBi
Traffic	Median	20.8 dBi	20.3 dBi	18.1 dBi
	5%-tile		19.1 dBi	9.8 dBi
	95%-tile		20.7 dBi	20.4 dBi

large AS; and, 2) traffic beam has higher side lobes and thus higher power leakage than the broadcast beam.

Table II includes summary of statistical simulation results presented in Fig. 3. The difference between effective gains of broadcast and traffic beams can be then considered as $F_{extBeamEff}$ extrapolation factor used by (1) for extrapolation of maximum RF EMF exposure. Figure 4 presents values of the $F_{extBeamEff}$ obtained this way for the assumed antenna and propagation conditions. These values are compared with the nominal extrapolation factor $F_{extBeamNom}$ of 4.1 dB (delta between nominal gains of broadcast and traffic beams, which are 16.7 dBi and 20.8 dBi, respectively), and are estimated for 5%-tile, median and 95%-tile effective gains from Fig. 3 and Table II.

As can be expected, the value of $F_{extBeamEff}$ for LOS conditions is very close to the value of $F_{extBeamNom}$ and in all simulated propagation environments does not exceed 0.3 dB for estimations for the range of 5% to 95%-ile values of effective gain. This conclusion is aligned with findings published in [11], [13], [14] and [15]. However, comparison of the value of $F_{extBeamEff}$ in NLOS conditions to the $F_{extBeamNom}$ value reveals significant misalignment. This difference is particularly visible in Fig. 4a, where

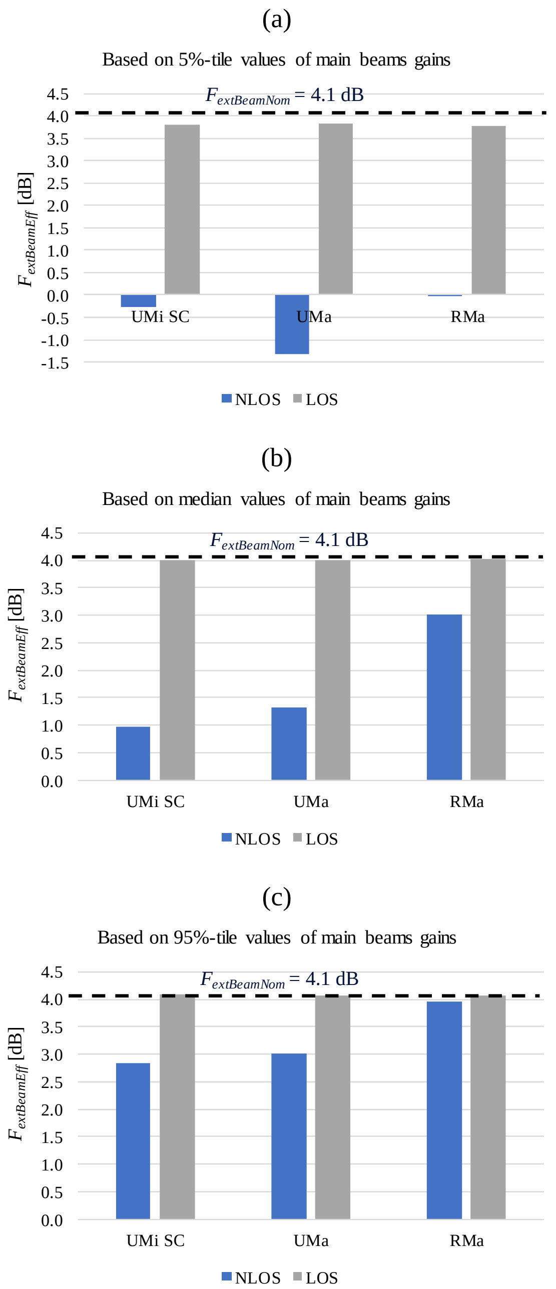

FIGURE 4. Comparison of nominal and effective values of extrapolation factor simulated for antenna [16] and 3GPP propagation environments of UMi SC, UMa and RMa [17], based on (a) ratio between 5%-tile values of broadcast and traffic main beams gains, (b) ratio between median values of broadcast and traffic main beams gains and (c) ratio between 95%-tile values of broadcast and traffic main beam gains

$F_{extBeamEff}$ was estimated based on the effective antenna gains corresponding to the 5%-tile of CDFs from Fig. 3. This case represents extrapolation of gains between broadcast and traffic beams in highly scattering environment, which leads to decrease of effective antenna gains and lower value of $F_{extBeamEff}$. On the other hand, if extrapolation is performed in more favorable NLOS propagation conditions the effective antenna gains is also higher and leads to higher value of $F_{extBeamEff}$ as illustrated in Fig. 4c, where extrapolation factor was estimated based on the 95%-tile of simulated effective antenna gains. This particular case illustrates that after exclusion of only 5% of the most favorable statistical NLOS conditions the difference between $F_{extBeamNom}$ and $F_{extBeamEff}$ is still higher than or equal to 1.3 dB, 1.1 dB and 0.1 dB in UMi SC, UMa and RMa environments, respectively. These differences increase respectively to 3.1 dB, 2.8 dB and 1.1 dB if 50% of the most favorable statistical NLOS conditions are excluded (Fig. 4b), and increase further to 4.4 dB, 5.4 dB and 4.1 dB, respectively, if only 5% of the less favorable statistical NLOS conditions are considered (Fig. 4a).

These findings are similar in measurement results presented in [15], where authors indicate that $F_{extBeamNom}$ leads to significant overestimation of extrapolated maximum RF EMF exposure in NLOS. However, studies presented in [15] do not include detailed description of broadcast and traffic beam patterns used during measurements and extrapolation, neither characteristic of assumed propagation scenarios.

Obtained results indicate that extrapolation factor in free space propagation and LOS conditions can be modeled by $F_{extBeamNom}$, where nominal antenna patters can be assumed with acceptable accuracy. However, in NLOS or scattering environment conditions, where effective antenna patterns apply, the extrapolation factor should be modelled by $F_{extBeamEff}$. Therefore, study presented in this section can be used as a basis for more accurate extrapolation of maximum RF EMF exposure associated with gNodeB when taking NLOS or scattering environment assumptions.

Simulation results presented above assume that calculation of extrapolation factor is based on the maximum gains (nominal or effective) of broadcast and traffic beams determined for the main lobes in the boresight directions, i.e. pointing to the center of the cell where the point of

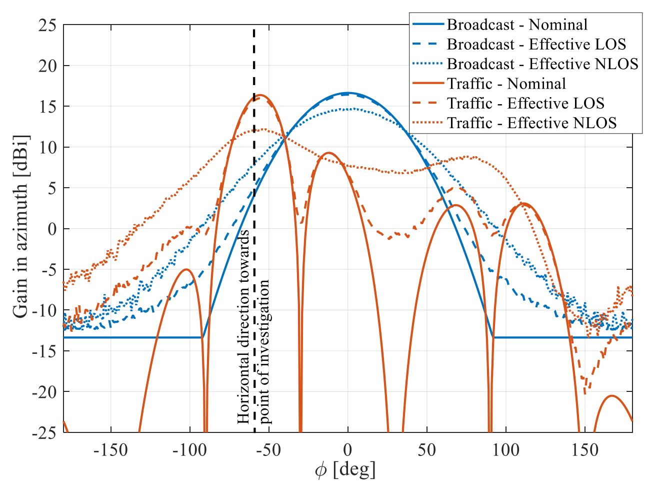

FIGURE 5. Nominal and mean effective antenna patterns of broadcast and traffic beams [16] in 3GPP UMa [17] scenario (pointing at -60° in azimuth)

IEEE Access
Multidisciplinary ⋮ Rapid Review ⋮ Open Access Journal

investigation (RF EMF exposure measurement or extrapolation) is placed. Similar assumption has been also made in [15], on top of which an additional measurement location, placed on the cell edge, were investigated. What was found during this study is that RF EMF exposure measured at the cell edges is overestimated even more than in the case of cell center, if $F_{extBeamNom}$ extrapolation factor is used. To verify these findings, additional simulation results are presented below. In this case it was assumed that the traffic beam is steered in horizontal plane and points at -60° from the boresight direction. Beam-steering is not applicable to the broadcast beam which is assumed to be stable in power and radiation pattern. Simulation study has been performed only for UMa scenario, as for other propagation conditions the similar conclusions are expected to be drawn. Figure 5 illustrates comparison of nominal and effective patterns at azimuthal angle of -60° from the boresight, whereas Table II includes the nominal and mean effective gains of broadcast and traffic beams obtained at this steering angle for UMa scenario. In this case the value of $F_{extBeamNom}$ extrapolation factor increases to 10.6 dB, in comparison to 4.1 dB obtained in the boresight direction. This behavior is followed by $F_{extBeamEff}$ in LOS conditions, which equals 9.5 dB, and still close to its nominal value. On the other hand, the value of $F_{extBeamEff}$ in NLOS is only 3.4 dB, which means that maximum RF EMF exposure in NLOS is overestimated by 7.2 dB, if $F_{extBeamNom}$ is used for extrapolation. This conclusion is consistent with findings from [15], where measurements performed on the cell edge indicate that extrapolated maximum exposure in NLOS or scattering environment is overestimated more than in the center of the cell.

Presented simulation results, obtained for commercial antenna used by gNodeB and practical propagation environment models of 3GPP, indicate that the concept of effective antenna pattern is important for accurate extrapolation of maximum RF EMF exposure associated with gNodeB, especially in NLOS conditions.

IV. SIMPLIFIED METHOD FOR CALCULATION OF EFFECTIVE EXTRAPOLATION FACTOR

As noticed in [14], extrapolation of maximum RF EMF exposure in NLOS conditions is complex and the ratio between gains of broadcast and traffic beams is difficult to be predicted in case of radio channels with rich scattering. Values of $F_{extBeamEff}$ extrapolation factor presented in the previous section was obtained from computationally power- and time-consuming statistical simulations with Monte Carlo methodology. Therefore, such method may not be always available or convenient during practical estimations of exposure associated with gNodeB under operation, even though it provides full range of results possible for given statistical channel model. Although extrapolation of maximum exposure in LOS conditions can be made with acceptable error using the value of $F_{extBeamNom}$, the same approach leads to significant overestimation of the maximum exposure in actual scattering environments or NLOS. For that reason, a simple and effective solution is needed to determine $F_{extBeamEff}$ with similar accuracy as using comprehensive statistical simulations with 3D antenna patterns and 3D channel model.

Below is proposed a method for calculating effective maximum gains of antenna beam patterns, using closed form formulas, which allows for estimation of $F_{extBeamEff}$ used for extrapolation of maximum exposure associated with given gNodeB. As an input to the method the following parameters are required:

- maximum nominal gain ($g_{\max}^{Nom}$) in linear scale,
- nominal HPBW of the main beam in horizontal plane (B_h) in radians,
- nominal HPBW of the main beam in vertical plane (B_v) in radians,
- RMS azimuth AS (σ_h) of assumed scattering environment in radians,
- RMS elevation AS (σ_v) of assumed scattering environment in radians.

The RMS azimuth and elevation AS of the channel can be obtained either from standard propagation models, like [17], or by performance AS estimation using the method prescribed in [23]. Other methods for RMS AS determination are not precluded, e.g. ray-racing simulations assuming realistic model of deployment scenario, but it has to be noted that the accuracy of selected method impacts directly the accuracy of $F_{extBeamEff}$ estimation, as RMS AS determines effective antenna gain which is required for calculation of $F_{extBeamEff}$. If statistical channel models are selected for determination of RMS AS it is important to consider also standard deviation and not only the mean value of AS for given propagation conditions and frequency band. Due to lack of single model which represents accurately all possible radio channels occurring in realistic propagation environments, this approach for RMS AS determination allows to obtain the range of $F_{extBeamEff}$ values which are expected to be the most representative. Having wider range of $F_{extBeamEff}$ values gives the freedom to select the one which is expected to provide the most accurate RF EMF exposure estimation or the one which gives the most conservative RF EMF exposure estimation, but still lower than estimated on the basis of nominal antenna gains.

Proposed method for $F_{extBeamEff}$ estimation requires the conversion of nominal HPBW, B_h^{Nom} and B_v^{Nom}, to the corresponding nominal RMS beam-widths, B_{h0}^{Nom} and B_{v0}^{Nom}, and corresponding nominal gain $g_{\max 0}^{Nom}$ [19]. This conversion is based on the assumption that RMS beam-width is approximated by standard deviation (SD) of Gaussian distribution functions which describes the antenna pattern. The simplified calculation method includes the following steps:

1. Convert nominal HPBW of broadcast and traffic beams, B_h^{Nom} and B_v^{Nom}, to RMS beam-widths, B_{h0}^{Nom} and B_{v0}^{Nom}, according to (5) and (6), respectively:

$$B_{h0}^{Nom} = \frac{B_h^{Nom}}{2\sqrt{\ln(4)}} , \quad (5)$$

$$B_{v0}^{Nom} = \frac{B_v^{Nom}}{2\sqrt{\ln(4)}} . \quad (6)$$

2. Calculate RMS nominal gains $g_{\max 0}^{Nom}$ of broadcast and traffic beams according to (7):

$$g_{\max 0}^{Nom} = \frac{2}{B_{h0}^{Nom} \cdot B_{v0}^{Nom}} . \quad (7)$$

3. Calculate RMS effective gain $g_{\max 0}^{Eff}$ of broadcast and traffic beams according to (8), using RMS azimuth AS of assumed scattering environment (σ_h) and RMS elevation AS of assumed scattering environment (σ_v):

$$g_{\max 0}^{Eff} = \frac{2}{\sqrt{\left(B_{h0}^{Nom}\right)^2 + \left(\sigma_h\right)^2} \cdot \sqrt{\left(B_{v0}^{Nom}\right)^2 + \left(\sigma_v\right)^2}} . \quad (8)$$

4. Calculate maximum effective gain $g_{\max}^{Eff}$ of broadcast and traffic beams according to (9):

$$g_{\max}^{Eff} = \frac{g_{\max}^{Nom} \cdot g_{\max 0}^{Eff}}{g_{\max 0}^{Nom}} . \quad (9)$$

5. Calculate effective extrapolation factor $F_{extBeamEff}$ as a ratio between maximum effective gains of traffic and broadcast beams.

The presented method is limited only to use cases when maximum exposure is investigated in parts of the 5G cell where the main lobes of broadcast and traffic beams are pointed to, as it allows only for approximation of maximum effective gain of given beam pattern. The method is valid for codebook-based beamforming, where patterns and gains of broadcast and traffic beams are predefined and known before implementation. It can be used for beamforming implementations such as beam sweeping or grid-of-beams (GoB), single user MIMO (SU-MIMO), multi-user MIMO (MU-MIMO) and mMIMO. In more advanced types of beamforming, such as eigen-based beamforming (EBB) and zero-forcing, where beam weight factors (BWF) are determined 'online' based on the actual channel state information (CSI), the general concept of maximum exposure extrapolation based on comparison of broadcast and traffic beams is not applicable, because patterns and gains of these beams are not known in advance.

Table III presents example approximation of $F_{extBeamEff}$ extrapolation factor for antenna [16] and NLOS conditions of UMa scenario [17] with RMS AS based on

TABLE III
EXAMPLE RESULTS OF EXTRAPOLATION FACTOR CALCULATION PERFORMED ACCORDING TO PROPOSED METHOD FOR NLOS CONDITIONS IN UMA SCENARIO [17]

Step	Calculations and results
1	*Broadcast*
	$B_{h0}^{Nom} = \frac{B_h^{Nom}}{2\sqrt{\ln(4)}} = \frac{58°}{2.3548} = \frac{1.0123 \text{ rad}}{2.3548} = 0.4299 \text{ rad}$
	$B_{v0}^{Nom} = \frac{B_v^{Nom}}{2\sqrt{\ln(4)}} = \frac{6.6°}{2.3548} = \frac{0.1152 \text{ rad}}{2.3548} = 0.0489 \text{ rad}$
	Traffic
	$B_{h0}^{Nom} = \frac{B_h^{Nom}}{2\sqrt{\ln(4)}} = \frac{24°}{2.3548} = \frac{0.4128 \text{ rad}}{2.3548} = 0.1779 \text{ rad}$
	$B_{v0}^{Nom} = \frac{B_v^{Nom}}{2\sqrt{\ln(4)}} = \frac{6.6°}{2.3548} = \frac{0.1152 \text{ rad}}{2.3548} = 0.0489 \text{ rad}$
2	*Broadcast*
	$g_{\max 0}^{Nom} = \frac{2}{B_{h0}^{Nom} \cdot B_{v0}^{Nom}} = \frac{2}{0.4299 \text{ rad} \cdot 0.0489 \text{ rad}} = 95.1379$
	Traffic
	$g_{\max 0}^{Nom} = \frac{2}{B_{h0}^{Nom} \cdot B_{v0}^{Nom}} = \frac{2}{0.1779 \text{ rad} \cdot 0.0489 \text{ rad}} = 229.9033$
3	*Broadcast*
	$g_{\max 0}^{Eff} = \frac{2}{\sqrt{\left(B_{h0}^{Nom}\right)^2 + \left(\sigma_h\right)^2} \cdot \sqrt{\left(B_{v0}^{Nom}\right)^2 + \left(\sigma_v\right)^2}}$ $= \frac{2}{\sqrt{(0.4299 \text{ rad})^2 + (27.40°)^2} \cdot \sqrt{(0.0489 \text{ rad})^2 + (0.58°)^2}}$ $= \frac{2}{\sqrt{(0.4299 \text{ rad})^2 + (0.4782 \text{ rad})^2} \cdot \sqrt{(0.0489 \text{ rad})^2 + (0.0101 \text{ rad})^2}}$ $= 62.2899$
	Traffic
	$g_{\max 0}^{Eff} = \frac{2}{\sqrt{\left(B_{h0}^{Nom}\right)^2 + \left(\sigma_h\right)^2} \cdot \sqrt{\left(B_{v0}^{Nom}\right)^2 + \left(\sigma_v\right)^2}}$ $= \frac{2}{\sqrt{(0.1779 \text{ rad})^2 + (27.40°)^2} \cdot \sqrt{(0.0489 \text{ rad})^2 + (0.58°)^2}}$ $= \frac{2}{\sqrt{(0.1779 \text{ rad})^2 + (0.4782 \text{ rad})^2} \cdot \sqrt{(0.0489 \text{ rad})^2 + (0.0101 \text{ rad})^2}}$ $= 78.5042$
4	*Broadcast*
	$g_{\max}^{Eff} = \frac{g_{\max}^{Nom} \cdot g_{\max 0}^{Eff}}{g_{\max 0}^{Nom}} = \frac{16.7 \text{ dBi} \cdot 62.2899}{95.1379} = \frac{46.7735 \cdot 62.2899}{95.1379}$ $= 30.6242 = 14.8 \text{ dBi}$
	Traffic
	$g_{\max}^{Eff} = \frac{g_{\max}^{Nom} \cdot g_{\max 0}^{Eff}}{g_{\max 0}^{Nom}} = \frac{20.8 \text{ dBi} \cdot 78.5042}{229.9033} = \frac{120.2264 \cdot 78.5042}{229.9033}$ $= 41.0533 = 16.1 \text{ dBi}$
5	$F_{extBeamEff} = \frac{41.0533}{30.6242} = 1.3406 = 1.3 \text{ dB}$

IEEE Access
Multidisciplinary ⋮ Rapid Review ⋮ Open Access Journal

mean AS value. Figure 6 compares the simulated values of $F_{extBeamEff}$ obtained by comprehensive statistical simulation with full 3D channel model for 5%-tile, median and 95%-tile of effective antenna gains (as already indicated in Fig. 4 for NLOS) and the calculated values of $F_{extBeamEff}$ obtained using the presented simplified method for mean AS, mean AS plus twice SD and mean AS minus twice SD, respectively. Calculations made for different values of RMS AS were aimed to prove capability of the presented method to estimate $F_{extBeamEff}$ in NLOS conditions with high, average and low AS. Following observations can be made from results in Fig. 6:

1. Simulated and calculated values of $F_{extBeamEff}$ are well aligned and in majority of cases differ by 0.5 dB or less.
2. Simulated results based on 5%-tile, median and 95%-tile of effective antenna gains of broadcast and traffic beams are represented well by calculations performed for RMS AS based on mean AS plus twice SD, mean AS and mean AS minus twice SD, respectively. Therefore, these 3 calculations are considered as statistically representative for the range of $F_{extBeamEff}$ values.
3. RF EMF exposure estimation based on the calculated $F_{extBeamEff}$ for mean AS minus twice SD still provides less overestimation than that determined by nominal antenna gains. Therefore, if used in estimation of RF EMF exposure, it would help to reduce overestimation induced by the $F_{extBeamNom}$ extrapolation factor for NLOS or scattering environments.

Based on the above observations it can be concluded that extrapolation methods used in RF exposure standards such as [4] can benefit from using the method presented in this section to calculate the effective extrapolation factor $F_{extBeamEff}$ corresponding to the actual scattering environment of the gNodeB, instead of the nominal extrapolation factor $F_{extBeamNom}$.

V. CONCLUSIONS

Specific design of beam patterns generated by the newly deployed antenna arrays of gNodeB challenges the methods used so far for the assessment of RF EMF exposure associated with DL transmissions from BS of cellular systems. Methods for extrapolation of the maximum exposure, considered in IEC 62232 updates and being verified by industry, academia and administrations, are based on LOS assumptions. However, when used in actual scattering environments or NLOS propagation conditions, these methods may lead to significant over-estimation of the maximum exposure which depends on AS and the HPBW of nominal antenna beam patterns. Consequences of this overestimation may be unnecessary limited DL EIRP of the gNodeB or overestimate of the RF

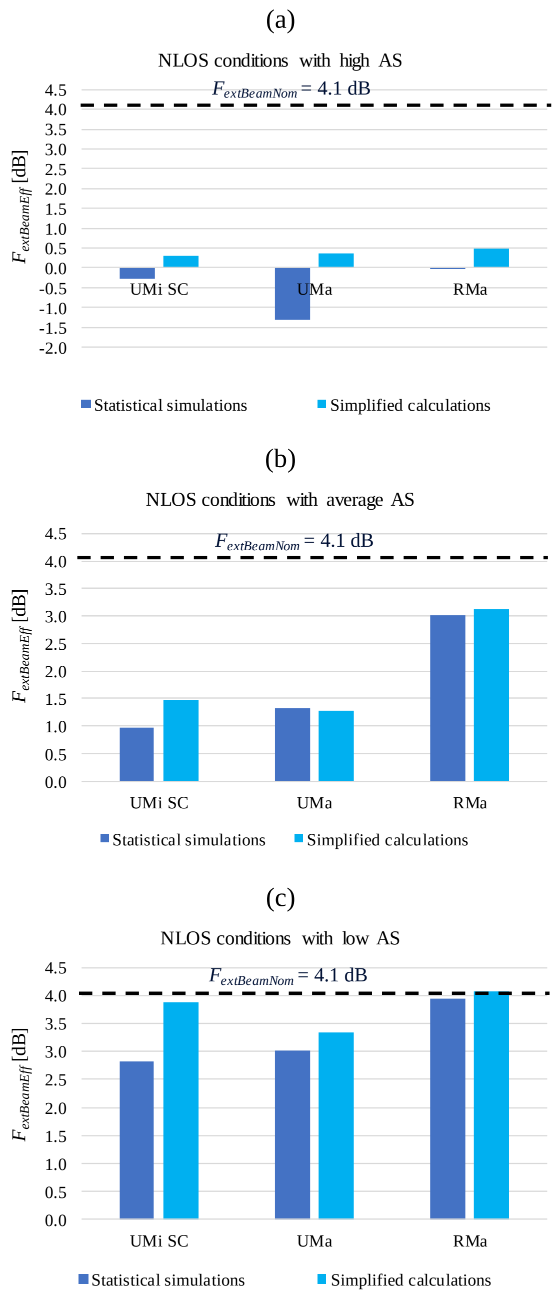

FIGURE 6. Comparison of simulated and calculated values of effective extrapolation factor in NLOS conditions for antenna [16] and 3GPP propagation environments of UMi SC, UMa and RMa [17]. Calculations based on (a) mean value of AS plus twice SD (NLOS conditions with high AS), (b) mean values of AS (NLOS conditions with average AS) and (c) mean value of AS minus twice SD (NLOS conditions with low AS)

EMF exposure compliance distances. Simulation results obtained for 3GPP 3D channel models indicate that maximum exposure may be overestimated even by 5.4 dB, if nominal antenna gains of broadcast and traffic beams are used for extrapolation in case of NLOS in UMa scenario with high AS. This overestimation decreases with smaller AS value and can be as low as 0.1 dB in RMa NLOS scenario with low AS. These values would change when using different broadcast and traffic beams than assumed in

IEEE Access
Multidisciplinary ⋮ Rapid Review ⋮ Open Access Journal

presented studies, but the general findings are found to be consistent with findings from the latest literature.

To facilitate extrapolation of maximum RF EMF exposure in realistic NLOS or scattering environment, this paper introduces an alternative extrapolation method leveraging the actual propagation conditions between the gNodeB and the measurement point. The proposed simplified calculation method of the effective extrapolation factor demonstrates good alignment with results of statistical simulations for 3GPP 3D channel model, if similar values of AS are used by both methods. It is also much more efficient than the computationally power- and time-consuming full statistical simulations while providing statistically representative range of extrapolation factor, if proper AS is selected for calculation. Even if the exact value of AS in the point of maximum RF EMF exposure estimation is not known, the range of calculated effective extrapolation factor allows to select the value which provides an accurate RF exposure estimation and at the same time reduces the unnecessary overestimation caused by extrapolation based on nominal antenna gains of broadcast and signal beams.

APPENDIX

Let $h(\phi,\theta)$ be the complex valued channel response in angular domain and $f(\phi,\theta)$ be the complex valued nominal antenna response which describes the variation of the fields with the direction of propagation (ϕ,θ), using coordinate system specified in [25]. The power of the nominal antenna response,

$$g^{Nom}(\phi,\theta)=\left|f(\phi,\theta)\right|^2 \tag{A0}$$

describes the power variation over direction in free space and thus represents the nominal radiation pattern of the antenna.

When acting as a receiver, the response of the receive antenna along direction (ϕ_0,θ_0) can be represented as,

$$r(\phi_0,\theta_0)=\int_{-180^\circ}^{180^\circ}\int_{-90^\circ}^{90^\circ} f(\phi,\theta)h(\phi_0-\phi,\theta_0-\theta)\,d\phi\,d\theta \tag{A1}$$

where the circular convolution between the channel and the antenna responses comes from the translation from spatial domain to angular domain via Fourier transform. The effective power angular spectrum of the receive antenna along direction (ϕ_0,θ_0) can therefore be represented as,

$$g^{Eff}(\phi_0,\theta_0)=E\left[\left|r(\phi_0,\theta_0)\right|^2\right]$$

$$\begin{aligned}&=\iint f(\phi,\theta)f^*(\phi',\theta')\cdot\\&\cdot\iint E\left[h(\phi_0-\phi,\theta_0-\theta)h^*(\phi_0-\phi',\theta_0-\theta')\right]d\phi\,d\theta\,d\phi'\,d\theta'\end{aligned} \tag{A2}$$

$$\begin{aligned}&=\iint f(\phi,\theta)f^*(\phi',\theta')\cdot\\&\cdot\iint p(\phi_0-\phi,\theta_0-\theta)\delta(\phi-\phi')\delta(\theta-\theta')\,d\phi\,d\theta\,d\phi'\,d\theta'\end{aligned} \tag{A3}$$

$$=\iint\left|f(\phi,\theta)\right|^2 p(\phi_0-\phi,\theta_0-\theta)\,d\phi\,d\theta \tag{A4}$$

where the expectation $E[*]$ is taken over randomness of channel realizations and (A3) comes from the assumption of uncorrelated scattering (e.g., rich scattering but finite angular resolution), with $p(\phi,\theta)$ as the channel power angular spectrum and $\delta(x)$ as the Dirac delta function. We can then obtain (2) directly from (A4) by substitution of $g^{Nom}(\phi,\theta)=\left|f(\phi,\theta)\right|^2$.

Similarly, when the same antenna acts as a transmitter, the same nominal antenna response $f(\phi,\theta)$ used for receiving will also apply for transmitting if we ignore potential hardware impairment. By keeping the antenna location unchanged and simply swapping its role from receiving to transmitting, the same channel response $h(\phi,\theta)$ shall apply as per channel reciprocity [24]. Therefore, the amount of energy dissipated along direction (ϕ_0,θ_0) will be proportional to the effective power angular spectrum as specified in (A4), from which we can obtain (2) for signal transmission as well.

REFERENCES

[1] *Guidelines for Limiting Exposure to Electromagnetic Fields (100 kHz to 300 GHz)*, document Health Phys 118(00):000-000; ICNIRP, 2020, doi: 10.1097/HP.0000000000001210.

[2] *IEEE Standard for Safety levels with Respect to Human Exposure to Radio Frequency Electromagnetic Fields, 3 kHz to 300 GHz*, IEEE Std C95.1-2019, 2019.

[3] *1999/519/EC Council Recommendation of 12 July 1999 on the limitation of exposure of the general public to electromagnetic fields (0 Hz to 300 GHz)*, European Council, 1999.

[4] *Determination of RF Field Strength, Power Density and SAR in the Vicinity of Radiocommunication Base Stations for the Purpose of Evaluating Human Exposure*, Standard IEC 62232:2017, 2017.

[5] *Case studies supporting IEC 62232 – Determination of RF field strength and SAR in the vicinity of radiocommunication base stations for the purpose of evaluating human exposure*, Technical Report IEC TR 62669:2019, 2019.

[6] E. Björnson, J. Hoydis, L. Sanguinetti, "Massive MIMO Networks: Spectral, Energy, and Hardware Efficiency,'' *Foundations and Trends® in Signal Processing*, Vol. 11, No. 3-4, pp 154–655, DOI: 10.1561/2000000093

[7] 3GPP RP-190213, "Work Item on New Radio (NR) Access Technology", Revision of RP-181726, 2019.

[8] P. Baracca, A. Weber, T. Wild, C. Grangeat, "A Statistical Approach for RF Exposure Compliance Boundary Assessment in Massive MIMO Systems,'' *International Workshop on Smart Antennas (WSA)*, Bochum (Germany), Mar. 2018.

[9] B. Thors, A. Furuskär, D. Colombi, C. Törnevik, "Time-averaged Realistic Maximum Power Levels for the Assessment of Radio Frequency Exposure for 5G Radio Base Stations Using Massive MIMO,'' *IEEE Access*, vol. 5, pp. 19711-19719, September 18th, 2017.

[10] H. Keller, "On the assessment of human exposure to electromagnetic fields transmitted by 5G NR base stations,'' *Health Physics*, 117(5):541–545, Nov. 2019.

[11] S. Aerts, L. Verloock, M. Van Den Bossche, D. Colombi, L. Martens, C. Tornevik, W. Joseph, ‘‘In-situ Measurement Methodology for the Assessment of 5G NR Massive MIMO Base Station Exposure at sub-6 GHz Frequencies,’’ *IEEE Access*, vol. 7, pp. 184658–184667, 2019.
[12] R. Pawlak, P. Krawiec, and J. Zurek, ‘‘On Measuring Electromagnetic Fields in 5G Technology,’’ *IEEE Access*, vol. 7, pp. 29826–29835, Mar. 2019.
[13] D. Franci, S. Coltellacci, E. Grillo, S. Pavoncello, T. Aureli, R. Cintoli, M. D. Migliore, ‘‘Experimental Procedure for Fifth Generation (5G) Electromagnetic Field (EMF) Measurement and Maximum Power Extrapolation for Human Exposure Assessment,’’ *Environments*, vol. 7, no. 3, p. 22, Mar. 2020.
[14] S. Adda, T. Aureli, S. D'Elia, D. Franci, E. Grillo, M. D. Migliore, S. Pavoncello, F. Schettino, R. Suman, "A Theoretical and Experimental Investigation on the Measurement of the Electromagnetic Field Level Radiated by 5G Base Stations," *IEEE Access*, vol. 8, pp. 101448 - 101463, May 2020.
[15] C. Bornkessel, T. Kopacz, D. Heberling, M. Hein, "Challenges to Assess Human Exposure to 5G Massive MIMO Base Stations: A Follow-Up Study," *BioEM 2020*.
[16] Commscope, "RRZZHHTTS4-65B-R7", Datasheet, Sep. 2019.
[17] 3GPP Radio Access Network Working Group, "Study on Channel Model for Frequencies from 0.5 to 100 GHz (Release 15)", 3GPP TR 38.901 V15.1.0.
[18] K. Bechta, J. Du, M. Rybakowski, "Rework the Radio Link Budget for 5G and Beyond," *IEEE Access*, vol. 8, 211585–211594, Nov. 2020.
[19] D. Chizhik, J. Du, R. Feick, M. Rodriguez, G. Castro, R. A. Valenzuela, "Path Loss, Beamforming Gain and Directional Gain Measurements at 28 GHz for Non-Line-of-Sight Coverage of Indoors with Corridors," *IEEE Transactions on Antennas and Propagation*, vol. 68, pp. 4820-4830, Jun. 2020.
[20] J. Du, D. Chizhik, R. Feick, M. Rodriguez, G. Castro, R. A. Valenzuela, "Suburban Fixed Wireless Access Channel Measurements and Models at 28 GHz for 90% Outdoor Coverage", *IEEE Transactions on Antennas and Propagation*, vol. 68, pp. 411-420, Jan. 2020.
[21] D. Chizhik, J. Du, R. A. Valenzuela, J. Otterbach, R. Fuchs, J. Koppenborg, "Path Loss and Directional Gain Measurements at 28 GHz for Factory Automation", *IEEE International Symposium on Antennas and Propagation and USNC-URSI Radio Science Meeting*, Jul. 2019.
[22] J. Du, D. Chizhik, R. A. Valenzuela, R. Feick, G. Castro, M. Rodriguez, T. Chen, M. Khli, G. Zussman, "Directional Measurements in Urban Street Canyons from Macro Rooftop Sites at 28 GHz for 90% Outdoor Coverage," *IEEE Transactions on Antennas and Propagation, 2020*. DOI: 10.1109/TAP.2020.3044398 (arxiv:1908.00512)
[23] J. Du, M. Rybakowski, K. Bechta and R. A. Valenzuela, "Matching in the Air: Optimal Analog Beamforming under Angular Spread," arXiv:1910.11054, Oct. 2019.
[24] H. L. Bertoni, *Radio Propagation for Modern Wireless Systems*, Prentice Hall, NJ, 2000.
[25] NGMN V1.0, *Recommendation on Base Station Active Antenna System Standards*, April 2020.

KAMIL BECHTA received the M.Sc. degree in wireless communications from the Electronics Faculty, Military University of Technology, Warsaw, Poland, in 2010, where he is currently pursuing the Ph.D. degree in the area of extended modeling of performance and co-existence requirements for 5G and Beyond with massive MIMO antenna configurations.

After graduation, he worked as a Research Assistant with the Military University of Technology, Warsaw, and he joined Nokia Siemens Networks, in 2011, as a 3GPP RAN4 Standardization Specialist responsible for RF and RRM requirements of HSPA and LTE. Since 2015, he has been a 5G Senior Radio Research Engineer with Nokia Bell Labs, where he was leading a team responsible for spectrum and co-existence studies for 5G. Since 2017, he has been responsible for specification and RF EMF exposure assessment of radio modules for 5G systems with the Mobile Networks Department, Nokia, Wroclaw.

Since 2020 Mr. Bechta represents Nokia in Polish Committee for Standardization and participates IEC Technical Committee MT3 for the RF EMF exposure assessment of base stations. In 2020 he received Nokia Technology Center Wroclaw Award. He is a coauthor of more than 20 articles and 7 patents in the area of wireless communications.

CHRISTOPHE GRANGEAT received the M.Sc. & Eng. degree in electronics and microwaves from IMT Atlantique and Université de Bretagne Occidentale, Brest, France, in 1989.

He joined Alcatel Research Center in 1990, where he developed and managed research activity on mobile phone antenna design and RF EMF dosimetry of mobile phones. Since 1990, successively with Alcatel, Alcatel-Lucent and Nokia, he developed technical expertise in the domain of green telecom, energy efficiency, alternative energies, antenna design, electromagnetic environment, RF exposure dosimetry and eco-sustainable development of mobile networks. Currently, he is Senior Specialist Energy Efficiency and RF Exposure Mitigation, and EMF manager within Nokia.

Mr. Grangeat received the Distinguished Members of Technical Staff (DMTS) Award in 2014. He has participated in multiple European and national research programs and has made significant contributions to international standard organizations such as IEC, CENELEC, ITU, ETSI and IEEE. Since 2018, he is co-convenor of IEC Technical Committee MT3 for the RF EMF exposure assessment of base stations. In 2019, he received the IEC 1907 Award for his contribution to the standardization of RF exposure assessment methods of 5G base stations.

JINFENG DU (S'07-M'13) received his B.Eng. degree in electronic information engineering from the University of Science and Technology of China (USTC), Hefei, China, and the M.Sc., Tekn. Lic., and Ph.D. degrees from the Royal Institute of Technology (KTH), Stockholm, Sweden.

He was a postdoctoral researcher at the Massachusetts Institute of Technology (MIT), Cambridge, MA, from 2013 to 2015, after which he joined Bell Labs in NJ, where he is currently a Member of Technical Staff. His research interests are in the general area of wireless communications, especially in communication theory, information theory, wireless networks, millimeter wave propagation and channel modeling.

Dr. Du received the Best Paper Award from IC-WCSP in October 2010, and his paper was elected as one of the "Best 50 Papers" in IEEE GLOBECOM 2014. He received the prestigious "Hans Werthen Grant" from the Royal Swedish Academy of Engineering Science (IVA) in 2011, the "Chinese Government Award for Outstanding Self-Financed Students Abroad" in 2012, and the International PostDoc" grant from the Swedish Research Council in 2013. He also received three grants from the Ericsson Research Foundation.

MARCIN RYBAKOWSKI received the M.Sc. degree in electronics and telecommunication (wireless communication) from the Faculty of Electronics, Wrocław University of Science and Technology, Poland, in 2003, where he is currently pursuing the Ph.D. degree in electromagnetic field exposure for multiantenna systems.

He worked with Becker Avionics, Wroclaw, Poland, as an RF Engineer and Fujitsu, Tokyo, Japan, as an RFIC Engineer. He joined Siemens (then Nokia Siemens Networks), Wroclaw, in 2006, as an Integration and Verification Engineer for 3G and Wimax Base Stations. He has been a Senior Radio Research Engineer with Nokia Solutions and Networks (then Nokia Bell Labs) since 2012, where he was responsible for research on small cells networks for 3G HSPA systems and radio channel modeling for 5G systems. Since 2016, he has been a Senior Specialist at Nokia, and works with the Mobile Networks 5G & Small Cell Architecture Department, Wrocław, where he is responsible for specification and architecture of radio modules for 5G systems. He is the coauthor of more than 15 articles and holds more than ten patents in the area of wireless systems. His research interests include EMF exposure, multiantenna systems, radio wave channel modelling, and evaluation and modelling of wireless systems.

Mr. Rybakowski received the "Young Scientist Award" for the best paper presented at the 10th National Symposium of Radio Science (URSI), and the M.Sc. thesis on microwave, antenna and radar engineering ranked third in a competition organized by the IEEE Polish Section.

jet INTL JOURNAL OF ELECTRONICS AND TELECOMMUNICATIONS, 2021, VOL. 67, NO. 2, PP. 301-308
Manuscript received September 21, 2020; revised April, 2021 DOI: 10.24425/ijet.2021.135980

Centralized Spectrum Sharing and Coordination Between Terrestrial and Aerial Base Stations of 3GPP-Based 5G Networks

Kamil Bechta

Abstract**—The objective of this paper is to estimate performance of a new approach for spectrum sharing and coordination between terrestrial base stations (BS) and On-board radio access nodes (UxNB) carried by Unmanned Aerial Vehicles (UAV). This approach employs an artificial intelligence (AI) based algorithm implemented in a centralized controller. According to the assessment based on the latest specifications of 3rd Generation Partnership Project (3GPP) the newly defined Unmanned Aerial System Traffic Management (UTM) is feasible to implement and utilize an algorithm for dynamic and efficient distribution of available radio resources between all radio nodes involved in process of optimization. An example of proprietary algorithm has been described, which is based on the principles of Kohonen neural networks. The algorithm has been used in simulation scenario to illustrate the performance of the novel approach of centralized radio channels allocation between terrestrial BSs and UxNBs deployed in 3GPP-defined rural macro (RMa) environment. Simulation results indicate that at least 85% of simulated downlink (DL) transmissions are gaining additional channel bandwidth if presented algorithm is used for spectrum distribution between terrestrial BSs and UxNBs instead of baseline soft frequency re-use (SFR) approach.**

Keywords**—5G, spectrum sharing, Unmanned Aerial Vehicle**

I. INTRODUCTION

FROM several years the Unmanned Aerial Vehicles (UAV) are gaining attention of telecom industry and therefore are subjects of academic studies and research projects. All this activity is focused on theoretical and practical issues in the most typical paradigms of UAV-related wireless communication. This quickly maturing sector has been recognized and addressed also by the 3rd Generation Partnership Project (3GPP) – the joint venture for development of global standards for cellular networks. 3GPP in the latest releases of its standards for the 4th Generation – Long Term Evolution (4G LTE) and the 5th Generation – New Radio (5G NR) systems has included a wide range of requirements, which allow UAV-related wireless communication to co-exist with the cellular 4G and 5G networks. As summarized in [1], recently the following areas have been addressed by 3GPP:

1. Enhanced LTE Support for Aerial Vehicles (Release 15) [2],
2. Remote Identification of Unmanned Aerial Systems (UAS) (Release 16) [3],
3. Study on application layer support for UAS and 5G Enhancement for UAVs (Release 17) [4].

From the perspective of two typical paradigms of UAV-related wireless communication, the co-existence between UAV and cellular 4G/5G networks brings advantages to both sides. The foundation for this co-operation is connectivity between UAV and its controller via 4G/5G networks, usage of licensed spectrum and standardized network protocols. This way the new practical use cases of UAV and cellular networks are enabled and lead to two typical paradigms, as shown in Fig. 1 [5,6]:

1. <u>UAV-Assisted Cellular Communication</u> - In this case the cellular network gains from the presence of UAV, which are deployed as aerial base stations (BS), called by 3GPP as On-board radio access nodes (UxNB). Main purpose of UxNBs is to complement the coverage of terrestrial BS or temporally increase the cellular network capacity.
2. <u>Cellular-Assisted UAV Communication</u> – By the usage of licensed spectrum and standardized communication protocols originated from cellular networks the UAVs are gaining more efficient control and traffic data flow in comparison to operation in unlicensed frequency bands.

This paper is focusing on the first of the abovementioned paradigms, i.e. UAV-Assisted Cellular Communication. One of the main challenges faced here is efficient spectrum sharing between cells served by terrestrial BSs and those served by UxNBs. Deployment of every UxNB inside the coverage area of 4G or 5G networks implicates allocation of spectrum resources to given UxNB. If UxNB is supposed to serve ground user equipment (UE) with the same quality of service (QoS) as UEs served by terrestrial BSs, the spectrum resources must be distributed in optimal way between all cells in given coverage area. Due to the mobile character of UxNBs it is also foreseen that spectrum resources will be allocated in dynamic way, which creates a new area for UAV related studies, i.e. cognitive UAV networks [6]. Main subject of these studies is spectrum allocation for UxNBs by dynamic utilization of the existing frequency bands used by terrestrial BSs. Several different approaches for spectrum sharing between UxNBs and terrestrial BSs can be found in the literature. For example, Sboui *et al.* [7] and Huang *et al.* [8] propose methods for dynamic control of power transmitted by lower priority UxNBs under constraints of limited interference towards higher priority terrestrial BSs. In both cases the power control algorithms aim to maximize the energy efficiency or data rate of UAV connections, which are optimized jointly with three-dimensional (3D) trajectory or altitude of UxNBs. Similar approach has been used by Hattab and Cabric [9], however here the transmit power of ground UEs connected to UxNBs is subject of control algorithm to minimize

Author is with Mobile Networks Business Division of Nokia
(e-mail: kamil.bechta@nokia.com)

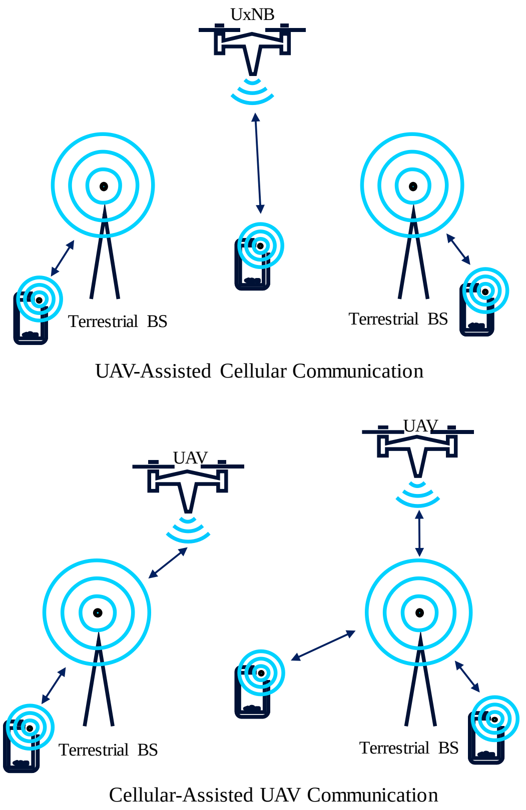

Fig. 1. Typical paradigms for UAV integration into cellular network [5,6]

interference received by terrestrial UEs. In this case the optimization process is performed by adaptation of time-division duplexing (TDD) protocol using stochastic geometry and comparison to the standard spectrum sharing and orthogonal allocation protocols. Zhang and Zhang [10] on the other hand propose a method for finding the optimal density of UxNBs based on the 3-D Poisson point process. Optimal density of UxNB network is found while maximizing its throughput and satisfying the terrestrial cells interference constraints.

According to the prepared review of literature, none of the abovementioned approaches is based on centrally implemented algorithm, which utilizes artificial intelligence (AI) or machine learning (ML). Therefore, the motivation of this paper is to describe and assess an example implementation of approach for centrally controlled spectrum sharing between UxNBs and terrestrial BSs, which is based on a neural networks algorithm.

Algorithm presented in the following parts of this paper is assumed to be implemented as one of the functions performed by Unmanned Aerial System Traffic Management (UTM), which according to 3GPP specification [4] is used to provide a number of services to support UAS (UAV and a UAV controller) in 4G and 5G networks. Therefore, Section II describes in more details the functions of UTM and UAS, as defined by 3GPP, and points to the enablers which allow for implementation of centralized algorithm for radio channels distribution. Section III presents description of the example algorithm for radio channels distribution between terrestrial and UxNB-served cells, which is based on the Kohonen neural networks theory [12]. This section includes also example simulation results of radio resource distribution obtained by the implementation of the proposed algorithm in terrestrial network with centralized controller, as well as indicates how the algorithm can improve the efficiency of radio channels distribution in comparison to soft frequency re-use (SFR) scheme. Section IV demonstrates the capability of the algorithm to distribute radio channels between 3GPP-defined Rural Macro (RMa) cells and UxNB-served cells for different densities of UxNBs. Conclusion and summary of the paper are included in Section V.

II. 3GPP-Based Control and Traffic Management for UAV

In December 2019, 3GPP approved the first version of Release 17 specification for support of UAS in 5G cellular networks [4]. It has been identified that 3GPP system can provide control plane and user plane communication services for UAS, i.e. UAV and its controller. Examples of services which can be offered to the UAS ecosystem includes data services for command and control (C2), telematics, UAS-generated data, remote identification, and authorization, enforcement, and regulation of UAS operation. Important role in this information flow via 3GPP network is performed by UTM management unit, which is used to provide a number of services to support UAS and their operations by following C2 communication [4]:

1. Network-Assisted C2 communication – the UAV controller and UAV register and establish respective unicast C2 communication links to the 3GPP network and communicate with each other via 5G network. Also, both the UAV controller and UAV may be registered to the 3GPP network via different radio access nodes. The 3GPP network needs to support mechanism to handle the reliable routing of C2 communication.
2. UTM-Navigated C2 communication – the UAV has been provided a pre-scheduled flight plan, e.g. array of 4D polygons, for autonomous flying, however UTM still maintains a C2 communication link with the UAV in order to regularly monitor the flight status of the UAV, verify the flight status with up-to-date dynamic restrictions, provide route updates, and navigate the UAV whenever necessary.

Figure 2 illustrates the above C2 communication flows in 3GPP ecosystem [4]. From the point of view of a centralized algorithm for radio resources allocation the more appropriate is UTM-Navigated C2 communication type – it allows for autonomous and dynamic operations with limited input from human-operated UAV controller. Requirements specified by 3GPP for remote identification of UAS assume flow of data between UAS, 3GPP network and UTM, which makes a centralized algorithm implementable inside UTM. Especially the following requirements allow to consider this implementation as feasible [4]:

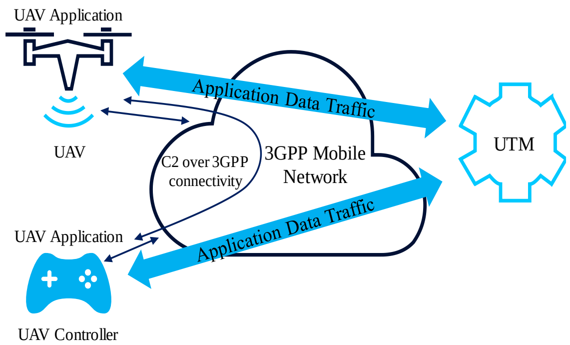

Fig. 2. UAS model in 3GPP ecosystem [4]

[9]

- R-5.1-003: The 3GPP system shall enable a UAS to send UTM the UAV data which can contain: unique identity (this may be a 3GPP identity), UE capability of the UAV, make & model, serial number, take-off weight, position, owner identity, owner address, owner contact details, owner certification, take-off location, mission type, route data, operating status.
- R-5.1-006: The 3GPP system shall support capability to extend UAS data being sent to UTM with the evolution of UTM and its support applications in future.
- R-5.1-009: The 3GPP system should enable a mobile network operator (MNO) to augment the data sent to a UTM with the following: network-based positioning information of UAV and UAV controller.
- R-5.1-012: The 3GPP system shall enable a UAS to update a UTM with the live location information of a UAV and its UAV controller.
- R-5.1-013: The 3GPP network should be able to provide supplement location information of UAV and its controller to a UTM.
- R-5.1-015: The 3GPP system shall provide the capability for network to obtain the UAS information regarding its support of 3GPP communication capabilities designed for UAS operation.

In particular, the requirement R-5.1-006 allows for future enhancements in UTM implementations and requests support of necessary data flow between UAS and UTM. Therefore, it can be assumed that any data needed by the algorithm will be available. However, very important data necessary for calculation of mutual interference between all radio nodes is the position of these nodes, and this information is already available e.g. by the requirement R-5.1-012. Other data required by an algorithm, like transmit power, antenna gain and receiver's acceptable interference, can be considered either as *make & model* or *operating status* data of the requirement R-5.1-003, or future defined data of the requirement R-5.1-006.

To conclude: 3GPP-defined UAS system and UTM manager can be considered as a feasible environment for implementation of a centralized algorithm for radio resources distribution between UxNB-served cells and terrestrial cells of 3GPP-based 4G or 5G networks. Next section describes example of such algorithm, based on the Kohonen neural networks theory.

III. Description of the Algorithm

In the presented study the Kohonen neural network [12] is used to map a layer of input data (i.e. parameters of UxNB-served cells and terrestrial cells) into a layer of output data (i.e. optimal distribution of radio channels) during the process of self-learning and mapping, which takes place inside a layer between the input and the output. Self-learning and mapping ensure that output data is optimal from the point of view of accepted criterion. In this study the criterion is minimal interference between UxNB-served cells and terrestrial cells. Therefore, the algorithm learns possible mutual interference between all cells in the network and map the same radio channel only to cells which are not interferers to each other, e.g. those which have sufficient separation distance.

Algorithm presented in this paper utilizes Kohonen neural network in the variant of competitive learning [12], where the input data layer includes additional weights which impact the processing inside the layer of self-learning and mapping, called here as 'competitive layer'.

The algorithm has been developed for dynamic and efficient distribution of radio channels between BSs of all involved cells (hereafter refereed as access points - APs). On top of the main part of the algorithm, two additional levels of optimization have been introduced to meet basic requirements for efficient spectrum utilization. Therefore, the algorithm consists of three general stages:

1. <u>Single channel allocation</u>,
2. <u>Multiple channels allocation</u>,
3. <u>Common Primary Channel (CPC) reallocation</u>.

The high-level description of the algorithm can be as follow: Stage 1 aims to allocate one channel to each AP, reusing channel as much as possible when the APs are not interfering with other APs too much. Inside Stage 1 the Outer Optimization Loop and the First Inner Optimization Loop exclude APs that cause interference to other APs, until the remaining APs do not interfere with each other and can use a single channel. Then the Second Inner Optimization Loop tries to add some excluded APs back, if possible, i.e. APs that were excluded for causing interference to other APs (which were also excluded) but can be included again as they cause no interference to the remaining APs. Stage 2 tries to give additional channels to APs that are not interfering with the group of APs the channels were assigned to before. Finally, Stage 3 tries to rearrange the channel assignments to give to all APs of the same MNO the single common channel.

Figure 3 illustrates general block diagram of the algorithm, whereas more detailed descriptions of all stages are presented in the following subsections.

A. *Stage 1: Single Channel Allocation*

Only this stage utilizes adapted Kohonen neural network in the variant of competitive learning [12]. Further stages include enhancements which perform optimization of outcomes from Stage 1.

The aim of adapted Kohonen neural network in the variant of competitive learning is to identify the function of costs, which is represented by the following vector:

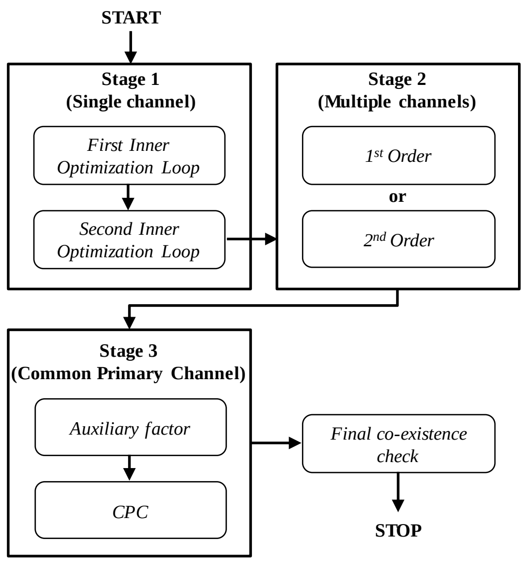

Fig. 3. General block diagram of the algorithm

$$\mathbf{V}=\left\{V_m=\sum_{n}^{M} w_{m,n}\cdot k_{m,n},\right\}_{M\times 1},m,n\in M\ , \qquad (1)$$

where V_m is equal to the sum of interference which given AP m causes to all other APs, whereas M is the number of APs from all cells in the scenario analyzed by the algorithm. Before determination of the vector **V** it is required to obtain the matrix of weights $\mathbf{W}=\{w_{m,n}\}_{M\times M},m,n\in M$, where $w_{m,n}$ is equal to the interference caused by particular AP m towards any other AP n. These interference values can be modified further, if the matrix of comparisons **K** is determined as below:

$$\mathbf{K}=\left\{k_{m,n}=\begin{cases}[0;1] \text{ if } \mathrm{ID}_m=\mathrm{ID}_n\\ 1 \text{ if } \mathrm{ID}_m\neq \mathrm{ID}_n\end{cases}\right\}_{M\times M},m,n\in M\ . \qquad (2)$$

General purpose of the matrix **K** is adaptation of the algorithm according to occurred interference case between AP m and AP n. First general case relates to the identification index (ID) of the MNO. If AP m and AP n belong to the same MNO, i.e. $\mathrm{ID}_m=\mathrm{ID}_n$, it can be assumed that, up to some extent, the MNO can manage interference between its own APs. In that case the value of multiplier $k_{m,n}$ is equal to 0 (interference between APs of the same MNO are fully manageable) or is between 0 and 1 (interference between APs of the same MNO are partially manageable or not manageable). If APs belong to different MNOs, i.e. $\mathrm{ID}_m\neq\mathrm{ID}_n$, multiplier $k_{m,n}$ is equal to 1. Second general case is connected with the priority of APs. If priorities of analyzed APs are different, the multipliers $k_{m,n}$ and $k_{n,m}$ should be equal to 1, which ensures that co-channel allocation will not occur, if at least one AP from the analyzed pair causes harmful interference to the other.

When the vector of costs **V** is determined, the obtained individual interference values can be compared with the vector of conditions $\mathbf{Y}=\{y_n\}_{M\times 1},n\in M$, where y_n represents the maximum interference limit acceptable by AP n. AP m, which has the highest cost among all APs, i.e. $V_m=\max(\mathbf{V})$, and does not fill all conditions of interference limit from the vector **Y**, i.e. $\forall n\in M: y_n<w_{m,n}\cdot k_{m,n}$, is excluded from further optimization. Positions of this AP in the auxiliary vector $\mathbf{x}=\{x_m\}_{M\times 1},m\in M$ is zeroed, assuming that at the beginning of the algorithm all values in the vector **x** are equal to 1.

Detailed description of processing in Stage 1 is as follows:

1. The algorithm goes through the matrix of interferences **W** and for each AP with non-zeroed value in the vector **x** calculates the total interference V_m which this AP causes to all other APs.
2. The algorithm sorts APs (new order) according to descending value of total interference in vector **V** caused by each AP.
3. According to the new order the algorithm checks if given AP causes harmful interference (above the threshold y_n) to any of its neighbors.
4. If harmful interference is caused at least to one of the neighbors, such AP is marked (value of this AP in the vector **x** is zeroed).
5. The algorithm M times repeats steps 3-4, but without APs already marked (First Inner Optimization Loop).
6. The algorithm M times repeats steps 1-5 (because in each repetition the number of APs with non-zeroed value in the vector **x** may be different).
7. The algorithm checks marked APs (with zeroed values in the vector **x**) one by one, if any of these APs can co-exist with all remaining APs (with non-zeroed values in the vector **x**). Marked APs are checked one by one according to descending value of total interference in vector **V**, i.e. during the check of given marked AP, other marked APs are not considered in calculation of total interference.
8. If any of marked APs can co-exist with all remaining unmarked APs, it also becomes unmarked and its value in the vector **x** is equal to 1 again.
9. The algorithm M times repeats steps 7-8 (Second Inner Optimization Loop).
10. The algorithm allocates the same channel to all APs which remain unmarked (have non-zeroed values in the vector **x**) after step 9.
11. The algorithm repeats steps 1-10 until all APs receive channels.

Stage 1 includes additional improvements on top of the basic Kohonen neural network [12], which are marked as the First Inner Optimization Loop and the Second Inner Optimization Loop.

The aim of the first loop is to ensure that each AP is examined not only against the total interference caused to all other APs but also against the interference caused towards individual neighbor. This prevents to stop the basic Kohonen algorithm when the AP, which causes the highest total interference towards all other APs, does not cause the significant interference to any individual AP, but the other AP with lower total interference causes significant interference to some individual APs. This step allows to identify APs which do not cause the highest total interference but are harmful interferers for individual neighbors.

The aim of the second loop is to additionally examine the APs excluded earlier as the strongest interferers. At the input of the second loop the interferers which cause harmful interference towards neighboring APs have zeroed value in the input vector **x** (x_m=0). During the second loop, each AP with x_m=0 is examined, according to descending order of the vector **V**, against all APs which remain with non-zeroed value in the vector **x** (x_m=1). If the harmful interferer meets the conditions in the second loop, it receives the channel allocation already before the start of the next optimization cycle for the next channel. The second loop allows then to allocate a channel to the strongest interferers, even though they did not meet the conditions in the main part of Stage 1, because the number of APs/neighbors in the second loop is different than in the main part of Stage 1. Therefore, the procedure of the Second Inner Optimization Loop helps to minimize the number of separate channels needed to ensure co-existence between all APs in the given area and shorten the algorithm's processing time.

As the result of Stage 1 all APs, which were under optimization process, receive a single channel which meets the main condition, i.e. interference in this channel are not higher than the acceptable level in vector **Y**. After this stage the algorithm identifies how many separated radio channels are needed to ensure co-existence between all considered APs. Detailed flow chart of Stage 1 can be found in [13].

B. Stage 2: Multiple Channels Allocation

During this stage all APs are checked for the capability of partial re-using of channels assigned to other APs during Stage

1, and therefore to obtain more radio resources for better spectrum utilization. There are two orders according to which all APs in the area can be examined:

- 1st Order: According to ascending values in the vector **V**. First are examined these APs which have the lowest total interference caused to all other APs. This approach favors APs which are causing low interference and allows them to get more additional channels than APs which cause higher interference, because APs which are examined earlier have higher probability to be allocated additional channel than APs which are examined later during Stage 2. According to this procedure, more channels are allocated to APs of denser network, i.e. belonging to MNO who deploys more APs in the given area than other MNOs. This is under assumption that MNO can minimize interference between own APs and therefore APs of denser network are aggressors to fewer neighbors than APs of less dense network.
- 2nd Order: According to descending values in the vector **V**. First are examined these APs which have the highest total interference caused to all other APs. This approach increases the probability that APs which cause high interference will be allocated more additional channels than in the case of the 1st Order approach. According to this procedure, more channels are allocated to APs of less dense network, i.e. belonging to MNO who deploys less APs in the given area than other MNOs. This is again under assumption that MNO can minimize interference between own APs and therefore APs of less dense network are aggressors to higher number of neighbors than APs of denser network.

Considering the above descriptions of the 1st Order and the 2nd Order, it is up to the central controller policy which approach should be used, as each of them leads to different outcomes. Once the order of APs' examination is chosen, main part of Stage 2 starts. The general rule of Stage 2, which leads to allocation of additional channels, is as follow: Depending on the chosen examination order, AP m is examined against all other APs, from AP 1 up to AP M, and receives additional channel l only when all other APs, which have already allocated channel l, are not interfered by AP m above the acceptable interference level. In the next cycle, AP m+1 must be examined also against additional channel(s) allocated to AP m in the previous cycle, and so forth. As the outcome of Stage 2 some APs can reuse additional channel(s) for better utilization of the available spectrum. These channels are then re-optimized during Stage 3. Detailed flow chart of Stage 2 can be found in [13].

C. Stage 3: CPC Reallocation

During Stage 3 some channels allocated to APs during Stage 1 and Stage 2 are re-allocated in a way which allows to allocate the same CPC to all APs with the same ID, i.e. belonging to the same MNO. Such functionality of the algorithm can be well seen by MNOs – CPC allows for easier mobility and handover of UEs between APs of the same MNO, and at the same time gives to the MNO the confidence that at least one part of the spectrum in the band is available constantly for its operation. During the first step of Stage 3 the algorithm analyses channels allocated during Stage 1 and Stage 2 to determine which particular channel would be the most suitable as the CPC for a given MNO. For that purpose, the auxiliary factor F_j is calculated in the following way:

- For j=1,…,J, where J is the number of MNOs, for each MNO find the channel l_j^{max} which has the highest number of allocations x_j^{max} . If more than one channel got the highest number of allocations, select the channel with lower ID. For each MNO calculate the difference Δ_j between x_j^{max} and the number M_j of all APs of given MNO. For each MNO calculate auxiliary factor F_j as a multiplication of Δ_j and M_j. Value of F_j determines the order according to which MNOs are re-optimized. This order has to be determined as re-allocation of channels for one MNO influences re-allocation in the network of other MNO and therefore it has to be started from the optimal point, i.e. re-allocation of channels starts from the MNO with the highest value of F_j factor and continues according to descending value of Fj. If more than one MNO have the same value of F_j, select the one with lower ID. Factor F_j helps also to determine which channel is the optimal CPC.
- Once the order of channels re-allocation and CPC for each MNO are determined, procedure of channels re-allocation starts. Stage 3 is the most complicated part of the algorithm, as it must ensure maintenance of the optimal co-existence between APs and at the same time shuffle the channels in a way which allocates CPC to all APs. Main part of Stage 3 runs according to the determined order of channels re-allocation - first are re-allocated channels of APs which belong to the MNO with the highest values of F_j factor. According to this order, each MNO is checked whether it has CPC allocated in all APs. If not, each AP which does not have CPC is evaluated against all other APs in the area, including also APs of other MNOs. This evaluation determines whether evaluated AP m causes interference to any other AP n. If yes, then that other AP n is checked whether it has channel which is the CPC for AP m being under evaluation. If yes, then the evaluated AP m is checked whether it has the channel which is the CPC for AP n. Depends of these checks, AP m and AP n exchange given channels between them. The evaluation cycle of AP m is repeated against next AP n+1. After that, AP m+1 of given MNO is evaluated. The same procedure is repeated for other MNOs. As the outcome of this procedure, all APs of all MNOs have allocated CPCs.

The last step of Stage 3 is called Final Coexistence Check. The aim of this step is to verify if any pair of interfering APs did not receive the same channel(s) during the re-allocation process (Stage 3). If such situation is detected the algorithm removes channel(s), which are the same for interfering APs, from the list of channels of one of the interfering APs. In the result of Final Co-existence Check some APs can have partially reduced number of channels, in comparison to the outcome of Stage 2, however this is the cost of re-allocation and allocation of CPC to all APs. Detailed flow charts of Stage 3 and Final Coexistence Check can be found in [13].

D. Verification of the 3-stage Algorithm by Simulations

Based on the above description of the algorithm a simple simulation scenario has been developed to verify the algorithm's effectiveness, i.e. whether outcomes of the consecutive stages follow agreed assumptions. It has been assumed that the algorithm is used by a central controller to allocate channels between APs of different MNOs. Main simulation parameters used for evaluation of the algorithm are included in Table I. Figure 4 presents example outcome of the full algorithm according to both the 1st and the 2nd Order of Stage 2. Results of each stage of the algorithm are marked by

[9]

TABLE I
MAIN SIMULATION PARAMETERS USED FOR EVALUATION OF THE 3-STAGE ALGORITHM

Parameter	Value
Area size	5 km x 5 km
No. of MNOs	3
No. of APs	20 (randomly positioned in the area and assigned to MNOs)
Carrier frequency	3500 MHz
Max EIRP	30 dBm
Interference threshold of AP	-75 dBm
Channel model	Free space
Other	*k*=0 for APs of the same MNO

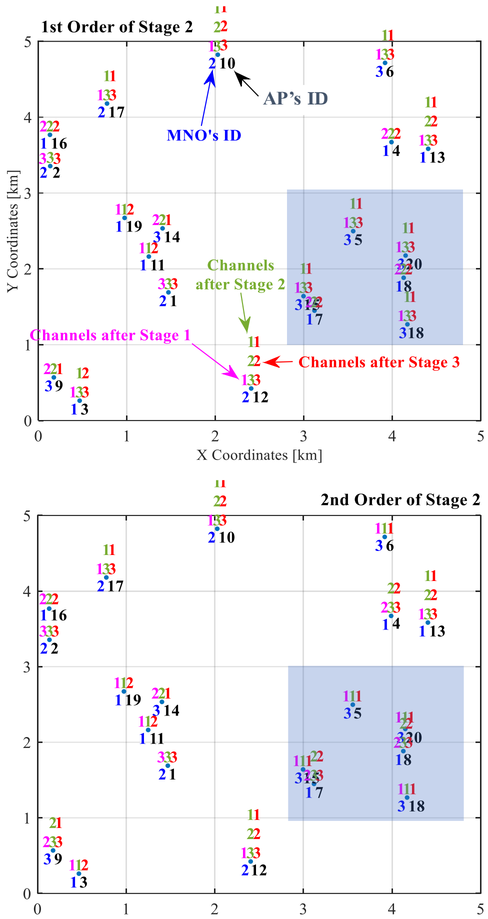

Fig. 4. Results of simulation verification of the consecutive stages of the algorithm

different colors (magenta, green and red respectively for consecutive stages), whereas positions of APs are marked by dark blue points. It can be noticed that three separate radio channels are needed to ensure co-existence in assumed simulation scenario, as '3' is the highest number obtained after Stage 1 (magenta color). As the result of Stage 2 some of APs have received additional one or two channels (green color), which means that better spectrum utilization has been obtained. Difference in the outcome of Stage 2 according to the 1st and the 2nd Order are visible inside the shaded area - in case of the 1st Order more channels are allocated to APs of the MNO 3, which in given area deploys more stations than the MNO 1. Opposite situation occurs in the case of the 2nd Order, when more channels are allocated to APs of the MNO 1. These allocations follow the reasoning described in subsection B. Finally, Stage 3 reshuffled channels allocated during previous stages and ensured that each MNO has CPC allocated to all of its APs (red color), i.e. the MNO 1 received CPC=2, the MNO 2 received CPC=3 and the MNO 3 received CPC=1.

Source code of the described algorithm in MATLAB modelling environment, with implemented the above simulation example, can be found in [13].

E. Efficiency of the Algorithm in Realistic Propagation Conditions

To illustrate capability of the algorithm for efficient channels distribution between BSs of realistic cellular network, a simple simulation scenario has been developed. It has been investigated if the algorithm can improve the spectrum utilization in a cellular network with SFR scheme [14]. As illustrated in Fig. 5, SFR allocates different frequencies for downlink (DL) transmission to UEs allocated at the cell edges, to avoid intercell interference. In assumed implementation, 3 radio channels are needed for SFR between 7 cells. This implementation allocates channel according to predetermined order, even if the actual propagation conditions in the place of network deployment allow to avoid intercell interference only due to the path loss. In that deployment scenario the SFR may lead to locally sub-optimal spectrum utilization, but at the same time is simple and does not require additional processing. Therefore, it has been investigated if the algorithm proposed in this paper is able to distribute radio channels between 7 cells in more efficient way than SFR does. The aim of this study was to illustrate the algorithm's efficiency in comparison to baseline SFR scheme. Main simulation assumptions used for this study are presented in Table II.

It has been assumed that DL intercell interference is calculated, i.e. BS is the aggressor for UEs of all neighboring cells. Due to that, the interference threshold for UE's receiver has been determined. Therefore, results of simulation indicate how the available radio channel can be distributed between 7 cells to avoid intercell interference and maximize spectrum utilization in RMa propagation environment. Figure 6 illustrates the geometry of assumed simulation scenario and includes example outcome of the algorithm's calculations. Only Stage 1 and Stage 2 of the algorithm, as described in subsections A and B, respectively, have been used. As can be noticed in the example results of Fig. 6, the algorithm was able to re-use channels 2 and 3 and allocate them to cells 2, 4 and 7 without generation of intercell interference. To obtain the full statistical picture of the algorithm's effectiveness the Monte Carlo simulation method has been used with 1000 drops of algorithm's realizations for assumed scenario. In case of SFR scheme for 100% of scenario realizations the 3 channels are

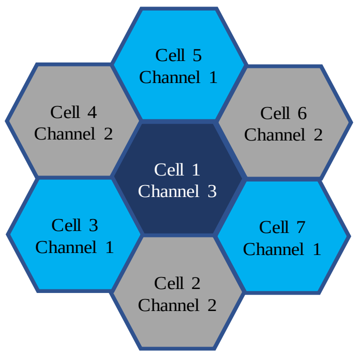

Fig.5. The frequency planning and power allocation for the SFR scheme [14]

TABLE II
MAIN SIMULATION PARAMETERS USED FOR ESTIMATION OF THE ALGORITHM'S PERFORMANCE IN REFERENCE TO SFR SCHEME

Parameter	Value
Propagation environment	3GPP RMa [15]
Height of the BS antenna	50 m
Height of the UE antenna	2 m
Inter-site distance	15000 m
Carrier frequency	1800 MHz
Available bandwidth	60 MHz
No. of MNOs	1
No. of BSs	7
Max EIRP of single BS	43 dBm
Interference threshold of UE	-104 dBm

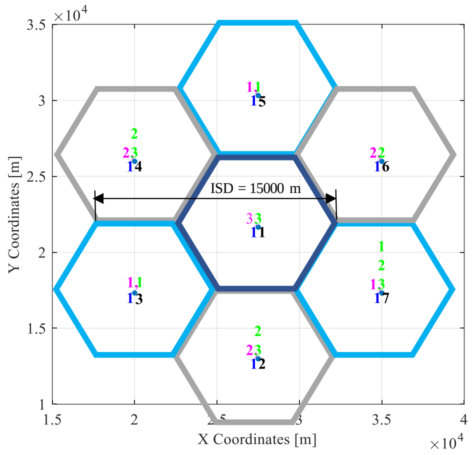

Fig. 6. Geometry of the assumed simulation scenario and example outcome of the algorithm's calculations

needed to avoid intercell interference, whereas according to obtained simulation results the presented algorithm required only 2 channels in 24% of simulated cases and 3 channels for 68% of cases. In remaining 8% of simulated cases the algorithm required 4 channels. Assuming that 60 MHz of the available bandwidth can be distributed between 2, 3 or 4 radio channels, thanks to Stage 2 of the algorithm, almost 60% of DL transmissions can utilize more than 20 MHz of bandwidth, which includes more than 10% of DL transmissions with 60 MHz bandwidth. Only for 5% of all DL transmissions the available bandwidth is less than 20 MHz. Therefore, 20 MHz of the bandwidth is allocated for remaining 35% of DL transmissions. It should be clarified at this point that 20 MHz is the amount of the spectrum which is available for each cell in case of SFR scheme. Presented algorithm allows then to maximize utilization of the available spectrum by the increase of channel bandwidth in 60% of DL transmissions.

Next section presents outcome of the algorithm in case of radio channels distribution between UxNBs and terrestrial BSs deployed in 3GPP-defined network of 5G system.

IV. SPECTRUM SHARING AND COORDINATION BETWEEN UXNBS AND TERRESTRIAL BSS

Similar simulation scenario as in subsection E of Section III has been used to illustrate capability of the algorithm to distribute radio channels between cells served by UxNBs and cells of terrestrial BSs, deployed in the same network and coverage area. Therefore, UxNBs have been assumed to provide additional coverage or network capacity (e.g. due to emergency situations) in the rural area, where the deployment of terrestrial BSs is not dense and may lead to local coverage or capacity shortage. Simulation parameters for this deployment case are presented in Table III.

Also, in this simulation scenario it has been assumed that DL interference is calculated between all cells, including cells served by terrestrial BSs and UxNBs. Assumption was made that the algorithm can be implemented as new functionality of UTM manager. According to requirements made by 3GPP [4] and listed in Section II, it was assumed that the UTM can obtain from 3GPP mobile network all data required for calculation of interference conditions by the algorithm, like equivalent isotropic radiated power (EIRP) and coordinates of all transmitters, interference threshold of receivers and type of propagation environment. Other necessary information can be subject of individual implementation of UTM and the used algorithm.

Three sub-scenarios have been studied, where the number of randomly distributed UxNBs was 1, 3 and 9, respectively. In all cases the algorithm was trying to find the minimal number of channels required to ensure co-existence between all cells and then re-use those channels in the most efficient way. It has been assumed that without the algorithm the number of channels required on top of 3 channels of SFR scheme would be equal to the number of UxNBs in the analyzed coverage area. Therefore, introduction of 1, 3 and 9 UxNBs in the area served by 7 terrestrial cells would respectively require 4, 6 and 12 separate channels to ensure co-existence between all cells. Figure 7 compares cumulative distribution functions (CDF) of minimal number of channels required in the abovementioned sub-scenarios as an outcome from Stage 1 of the algorithm. In sub-scenario with 1 UxNB the algorithm required less than 4 channels for 65% of statistical realizations and more than 4 channels only for 2% of cases. This means that in majority of simulated realizations the algorithm outperformed the simplified SFR-based scheme. Performance of the algorithm was even higher in remaining two sub-scenario – in case of 3 UxNBs for 99% of statistical realizations the algorithm required less than 6 channels and much less than 12 channels for 100% of realizations in case of sub-scenario with 9 UxNBs. During Stage 2 the algorithm was able to re-use channels pre-allocated during Stage 1 and due to that further increase the efficiency of spectrum utilization, which can be observed in Fig. 8. For at least 85% of DL transmissions in all simulated sub-scenarios the allocated channel bandwidth was higher than obtainable by SFR-based approach, i.e. 15 MHz, 10 MHz and 5 MHz for sub-

TABLE III
MAIN SIMULATION PARAMETERS USED FOR ILLUSTRATION OF THE ALGORITHM'S CAPABILITY TO DISTRIBUTE CHANNELS BETWEEN TERRESTRIAL BS AND UXNBS

Parameter	Value
Propagation environment	3GPP RMa [15]
Height of the terrestrial BS antenna	50 m
Altitude of UxNB	150 m
Height of the UE antenna	2 m
Inter-site distance	15000 m
2D position of UxNBs	Random
Carrier frequency	1800 MHz
Available bandwidth	60 MHz
No. of MNOs	1
No. of terrestrial BSs	7
No. of UxNBs	1, 3, 9
Max EIRP of terrestrial BS	43 dBm
Max EIRP of UxNB	23 dBm
Interference threshold of UE	-104 dBm

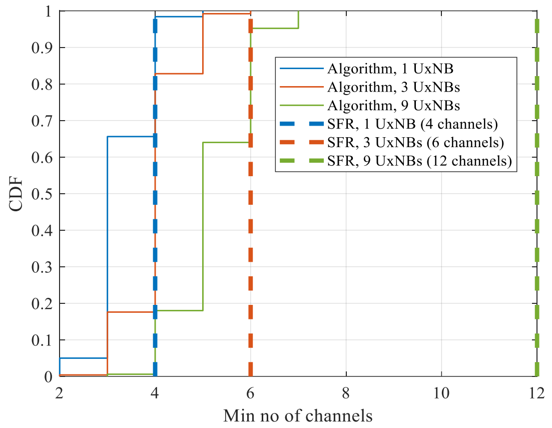

Fig. 7. Simulation results of minimal number of channels obtained for the algorithm and SFR scheme in terrestrial and aerial 3GPP RMa deployment

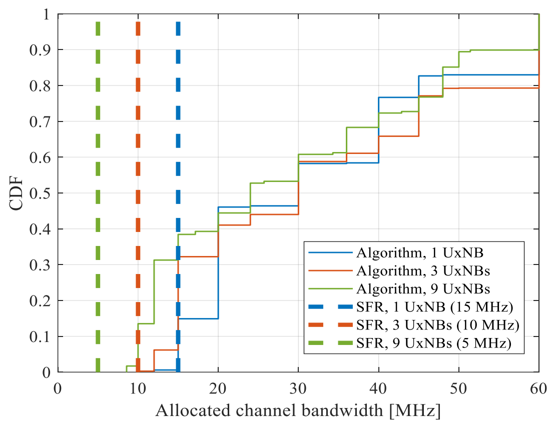

Fig. 8. Simulation results of allocated channel bandwidth obtained for the algorithm and SFR scheme in terrestrial and aerial 3GPP RMa deployment

scenarios with 1 UxNB, 3 UxNBs and 9 UxNBs, respectively. Only for less than 1% of realizations in sub-scenario with 1 UxNBs the algorithm allocated less than 15 MHz. It can be also noticed that with the increasing number of deployed UxNBs, the algorithm is able to outperform the SFR-based approach better. This is due to the limited number of transmitters in the analyzed deployment area, which allows to re-use radio channels between cells and still avoid intercell interferences. However, further increase of the number of UxNBs will lead to severe intercell interference and will decrease performance of the algorithm, which at some point may be similar to the performance of the SFR-based approach.

V. Conclusion

This paper includes high level feasibility study for implementation of a centralized algorithm for dynamic and efficient spectrum sharing between UxNBs and terrestrial BSs deployed in 3GPP-based cellular network of 4G or 5G systems. It has been presented that the latest releases of 3GPP specifications include definition of UTM manager and its functionalities. According to these requirements the UTM is able to monitor and control activities of UxNBs through 3GPP systems and at the same time can share relevant data about 4G or 5G networks, inside which the UxBNs are deployed. Based on the information from 3GPP specifications, it has been assumed that UTM manager is feasible to implement centralized algorithm as part of its functionalities. Proposal of the algorithm has been made, which is based on the principles of Kohonen neural networks theory. It has been shown that the algorithm is able to allocate minimum required radio resources to all radio nodes participating in optimization process and at the same time it helps to maximize spectrum utilization. By simple simulation scenarios it has been presented that spectrum available for transmissions inside 4G or 5G networks can be efficiently distributed between UxNBs and terrestrial BSs. In comparison to basic SFR scheme the centralized algorithm can allocate radio channels more efficiently. For assumed RMa deployment scenarios it has been observed that at least 85% of simulated DL transmissions are gaining more channel bandwidth if the presented algorithm is used instead of SFR-based approach. These preliminary results allow to consider the concept of centralized spectrum sharing between UxNBs and terrestrial BS inside 3GPP network as a valuable direction in studies on cognitive UAV networks, especially in the context of growing interest in UAV communication and work progress of 3GPP.

References

[1] 3GPP, “UAS-UAV”, https://www.3gpp.org/uas-uav, accessed 18 November 2019.
[2] 3GPP TR 36.777, “Release 15. Enhanced LTE support for aerial vehicles”, January 2018.
[3] 3GPP TS 22.125, “Release 16. Unmanned Aerial System (UAS) support in 3GPP. Stage 1”, September 2019.
[4] 3GPP TS 22.125, “Release 17. Unmanned Aerial System (UAS) support in 3GPP. Stage 1”, December 2019.
[5] S. Zhang, Y. Zeng, R. Zhang, “Cellular-Enabled UAV Communication: A Connectivity-Constrained Trajectory Optimization Perspective”, *IEEE Transactions on Communications*, Vol. 67, No. 3, March 2019. DOI: 10.1109/TCOMM.2018.2880468.
[6] B. Li, Z. Fei, Y. Zhang, “UAV Communications for 5G and Beyond: Recent Advances and Future Trends”, *IEEE Internet of Things Journal*, Vol. 6, No. 2, April 2019. DOI: 10.1109/JIOT.2018.2887086.
[7] L. Sboui, H. Ghazzai, Z. Rezki, M.-S. Alouini, “Energy-Efficient Power Allocation for UAV Cognitive Radio Systems”, 2017 IEEE 86th Vehicular Technology Conference (VTC-Fall). DOI: 10.1109/VTCFall.2017.8287971.
[8] J. Huang, W. Mei, J. Xu, Q. Ling, Z. Rui, “Cognitive UAV Communication via Joint Maneuver and Power Control”, *IEEE Transactions on Communications*, Vol. 67, No. 11, November 2019. DOI: 10.1109/TCOMM.2019.2931322.
[9] G. Hattab, D. Cabric, “Energy-Efficient Massive IoT Shared Spectrum Access over UAV-enabled Cellular Networks”, Accepted for publication in *IEEE Transactions on Communications*, 2020. DOI: 10.1109/TCOMM.2020.2998547.
[10] C. Zhang, W. Zhang, “Spectrum Sharing for Drone Networks”, *IEEE Journal on Selected Areas in Communications*, Vol. 35, No. 1, January 2017. DOI: 10.1109/JSAC.2016.2633040.
[11] X. Ying, M.M. Buddhikot, S. Roy, “SAS-Assisted Coexistence-Aware Dynamic Channel Assignment in CBRS Band”, *IEEE Transactions on Wireless Communications*, Vol. 17, No. 9, September 2018. DOI: 10.1109/TWC.2018.2858261.
[12] T. Kohonen, “Self-Organizing Maps”, Series in Information Sciences, Vol. 30, Springer-Verlag Berlin Heidelberg, Third ed., 2001.
[13] K. Bechta, “Radio resource allocation”, International Application No.: PCT/FI2017/050149.
[14] Y. Yu, E. Dutkiewicz, X. Huang, M. Mueck, G. Fang, “Performance Analysis of Soft Frequency Reuse for Inter-cell Interference Coordination in LTE Networks”, 2010 10th International Symposium on Communications and Information Technologies. DOI: 10.1109/ISCIT.2010.5665044.
[15] 3GPP TS 38.901, “Release 16. Study on channel model for frequencies from 0.5 to 100 GHz”, January 2020.

Impact of Effective Antenna Pattern on Estimation of Interference in Citizens Broadband Radio Service

Kamil Bechta, Marcin Rybakowski
Mobile Networks
Nokia
Wroclaw, Poland
kamil.bechta@nokia.com
marcin.rybakowski@nokia.com

Jinfeng Du
Bell Labs
Nokia
Murray Hill, NJ, USA
jinfeng.du@nokia-bell-labs.com

Abstract—**This paper investigates the impact of antenna pattern modeling accuracy on performance evaluation in realistic Citizens Broadband Radio Service (CBRS) cellular networks. The current practice of using nominal antenna pattern of CBRS device (CBSD), as measured in anechoic chamber, for estimation of interference conditions between CBSDs does not address the antenna gain degradation and antenna pattern reshaping caused by angular spread in scattering propagation environment. System level simulations have been conducted using a model of commercially available antenna of CBSD in urban macro deployment scenario with full 3D channel model and proprietary algorithm for resources distribution. The result reveals that the value of interference between each pair of investigated CBSDs can be underestimated by 6 dB if nominal antenna pattern is assumed in link budget calculation instead of effective antenna pattern. This underestimation may lead to suboptimal channels distribution in real spectrum sharing environment of CBRS network and severe co-existence issues between CBSDs. Therefore, effective antenna pattern of CBSD, as determined for given scattering propagation conditions, should be used for more accurate modeling of interference during CBRS network planning, optimization, as well as network operation in spectrum sharing environment.**

Keywords—angular spread; CBRS; effective antenna pattern; GAA; nominal antenna pattern; power angular spectrum

I. Introduction

Increasing demands of data throughput in mobile communication systems have been pushing mobile network operators (MNOs), equipment vendors and regulators to search for better utilization of radio frequency (RF) resources. Spectrum in classical cellular bands (such as those below 2.5 GHz) is increasingly crowded and expensive, and new spectrums in high bands above 6 GHz, such as the millimeter wave bands adopted in the 5th generation of mobile communication system (5G), have tens of GHz bandwidth (BW) available but suffer from worse radio propagation conditions and higher penetration/scattering loss in cluttered environments. Therefore, the challenge of providing adequate coverage of mobile communication systems without significant growth of cells density has driven the search of better utilization of frequency bands. One of such attempts is to the Citizens Broadband Radio Service (CBRS) system being specified in USA by Wireless Innovation Forum (WInnForum) standardization body.

CBRS is a three-tier architecture system for spectrum sharing in the 3550-3700 MHz frequency band [1], [2]. The first tier of CBRS is composed of incumbent services, basically military Radiolocation Service (RLS), Fixed Satellite Service (FSS) and for a finite period, grandfathered terrestrial wireless broadband service. As the highest tier in this framework, incumbents will receive full protection against interference from any other users. The second and the third tiers consist of CBRS Devices (CBSD), intended to provide wireless broadband access through authorized channel access in any location and frequency, and includes two groups of users called Primary Access License (PAL) and General Authorized Access (GAA) [3]. Due to the variety of radio access technologies which can be used as CBSD (e.g. 5G NR – New Radio, 4G LTE – Long Term Evolution, WLAN – Wireless Local Access Network, etc.), assurance of co-existence between CBSDs becomes challenging without external coordination. Such coordination is provided by Spectrum Access System (SAS) controller which is responsible for channels assignment to CBSDs through SAS-CBSD protocol [4]. In particular, the group of GAA users requires the guidance from SAS as GAA channels are unlicensed type.

SAS is specified to monitor interference conditions between CBSDs, as well as between CBSDs and incumbents of the first tier, to ensure that radio channels are distributed in an efficient way. Interference conditions between particular radio nodes are determined based on radio parameters of CBSDs declared by manufacturers or MNOs (users of CBSDs). One of the most important parameters of CBSD is antenna radiation pattern. However, according to the latest specifications of CBRS standard, developed by WInnForum [5]-[8], only a very general information about radiation patterns are required for reporting to SAS. The most detailed description is specified as an optional requirement and referred to as “Enhanced Antenna Pattern” [7]. According to [7] this pattern is equivalent to *nominal pattern* as determined by theoretical model, eventually measured in anechoic chamber and specified in technical datasheet of the antenna. However, when deployed in realistic radio wave scattered environment (which is significantly different from free space propagation of anechoic chamber) the *effective pattern* and gain of the antenna can deviate noticeably from nominal values [9].

Due to phenomenon of angular spread of radiated energy in scattering environment, the maximum effective gain of antenna pattern can be lower and its half power beam-width (HPBW) can be wider in comparison to nominal values. Additionally, the side lobes levels are increasing which is especially important for estimation of interference conditions. These deviations can be experienced even in line-of-sight (LOS) conditions but are visible especially in the case of non-line-of-sight (NLOS). Figures 1 and 2 present results of effective antenna pattern measurements performed in urban Manhattan environment [10]. As can be noticed on Fig. 1 the effective maximum gain in azimuth plane can be more than 4 dB below the nominal maximum gain in 10% of measured cases. Figure 2, on the other hand, illustrates impact of scattering environment on widening of antenna pattern and increase of side-lobes levels.

The aim of this paper it to demonstrate the difference in performance of CBRS system evaluated in the three-dimensional (3D) statistical system level simulations which consider nominal and effective antenna patterns. It is shown that in realistic simulation scenarios such as urban macro the values of interference between CBSDs can be significantly underestimated if nominal antenna pattern is used for estimation instead of effective antenna pattern. Consequence of this underestimation is suboptimal distribution of radio resources by SAS, which may lead to co-existence issues between CBSDs and unsatisfactory performance in CBRS network.

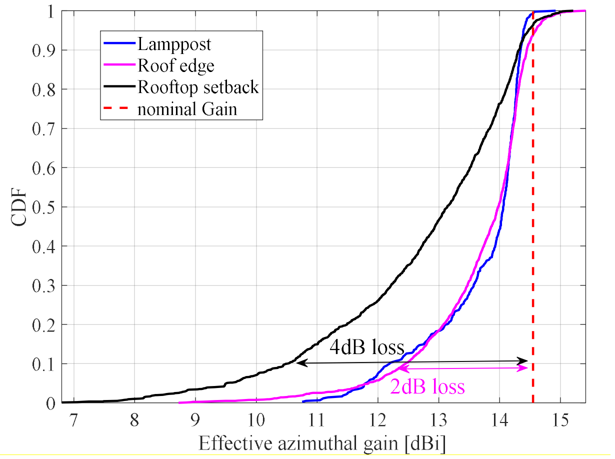

Fig. 1. CDFs of effective antenna gains measured in urban Manhattan environment [10] presented in comparison with nominal antenna gain

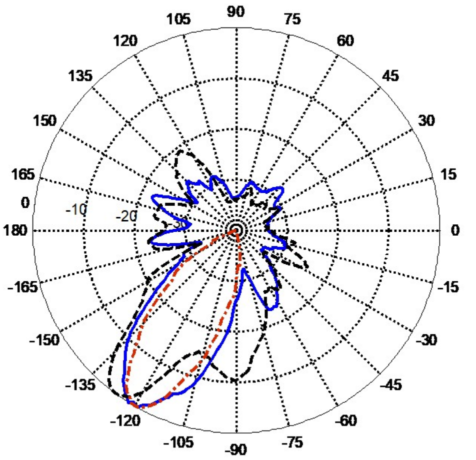

Fig. 2. Horizontal angular spectra of effective directional antenna patterns measured in urban Manhattan environment [10], where red dash-dot is the nominal pattern measured in anechoic chamber, and blue solid and black dashes lines are pattens from urban street canyon measurement

The rest of this paper is organized as follows. Section II introduces system modelling and Section III contains simulation scenario and results, whereas Section IV concludes and summarizes the paper.

II. System Modelling

Considering the abovementioned modifications in antenna pattern and gain, as introduced by scattering environment, it can be easily concluded that neglecting of those may have significant impact on correct evaluation of interference between radio nodes of CBRS system, i.e. CBSDs or CBSD and incumbent, which in consequence may lead to suboptimal spectrum allocation by SAS, if only nominal antenna pattern is assumed during evaluation.

Equations (1)-(3) describe how the effective antenna pattern can be analytically obtained based on nominal antenna pattern and power angular spectrum (PAS) of the assumed propagation environment [9].

$$g^{Eff}(\phi_0,\theta_0) = \int_{-180^\circ}^{180^\circ}\int_{0^\circ}^{180^\circ} g^{Nom}(\phi,\theta)\cdot p(\phi-\phi_0,\theta-\theta_0)\,d\phi\, d\theta, \quad (1)$$

$$\begin{aligned} g^{Eff}_{Az}(\phi_0) &= g^{Eff}(\phi_0,\theta_0=90^\circ) = \\ &= \int_{-180^\circ}^{180^\circ} g^{Nom}(\phi,\theta=90^\circ)\cdot p_{Az}(\phi-\phi_0)\,d\phi \end{aligned}, \quad (2)$$

$$\begin{aligned} g^{Eff}_{Ele}(\theta_0) &= g^{Eff}(\phi_0=0^\circ,\theta_0) = \\ &= \int_{0^\circ}^{180^\circ} g^{Nom}(\phi=0^\circ,\theta)\cdot p_{Ele}(\theta-\theta_0)\,d\theta \end{aligned}. \quad (3)$$

In above equations g^{Eff} indicates 3D effective antenna pattern, whereas g^{Nom} indicates 3D nominal antenna pattern. g^{Eff}_{Az} and g^{Eff}_{Ele} indicate azimuth and elevation cuts of effective antenna pattern, ϕ and θ define angular domain in azimuth and elevation, respectively, whereas ϕ_0 and θ_0 indicate boresight direction between Tx and Rx in azimuth and elevation, respectively. p_{Az} and p_{Ele} represent realizations of PAS in azimuth and elevation.

Accurate modeling of antenna pattern of CBSD is important during CBRS network deployment and operation. If at the stage of radio network planning (RNP) the impact of scattering environment will not be properly reflected in link budget calculations for serving and interfering links, i.e. nominal antenna pattern is considered instead of effective antenna pattern, the coverage and capacity of CBSD cells after deployment in the field may be significantly worse than estimated during RNP. This may lead to time consuming and expensive optimization of deployed cells, which could be avoided if accurate modeling of antenna pattern is assumed already at the early stage of RNP. Additionally, the effective antenna patterns of CBSDs should be determined, maintained and used also during operation of CBRS network, already after deployment. This relates to SAS functions, especially distribution of radio channels between GAA according to link budget calculations for interfering links, where antenna pattern model is particularly important. Therefore, if accurate antenna pattern of GAA, i.e. effective pattern in the place of GAA deployment, is not available to SAS the distribution of radio channels to all GAA cells in the network may be suboptimal and lead to locally increased interference or underutilized spectrum resources.

III. Simulation Scenario and Results

To emphasize the impact of accuracy in antenna pattern modeling on estimation of performance in realistic CBRS network, a commercially available antenna model used by CBSD [11] was assumed in simulation study, with deployment scenario parameters from practical network [12].

The purpose of simulation studies presented in this section was evaluation of impact on CBRS network performance if nominal antenna pattern is used by SAS to determine interference conditions between GAA access points deployed in realistic scattering environment, where effective antenna pattern applies. Simulation results obtained using both nominal and effective antenna patterns are presented, to illustrate the difference between effective (realistic) performance obtainable in the field and the one estimated inaccurately based on nominal antenna pattern. Such comparison of quantitative metrics allows to easily assess the importance of effective antenna pattern for optimal CBRS network operation.

A. *Effective pattern of practical antenna model for CBSD*

Simulation scenario assumed deployment of GAA access points in the urban macro (UMa) propagation environment at 3.5 GHz carrier frequency with available bandwidth of 10 MHz. For accurate modeling of angular spread phenomenon of realistic UMa environment, a full 3D statistical channel model determined by the 3rd Generation Partnership Project (3GPP) [13] was used. Based on angular spread statistical distributions, which in section 7.5 of [13] are defined by inverse Gaussian and Laplacian functions for azimuth and zenith spreads, respectively, the representative 3D PAS for UMa environment in LOS and NLOS conditions have been determined. Obtained 3D PAS have been then used to calculated 3D effective patterns of antenna model [11] according to (1). Table I includes main nominal parameters of antenna model [11], whereas Figs. 3 and 4 illustrate comparison of its nominal and

TABLE I. Main Nominal Parameters of Antenna Model [11]

Parameter	Value
Antenna Gain	10.5 ± 1.5 dBi
Horizontal Beam Width	65 ± 10°
Vertical Beam Width	35 ± 10°

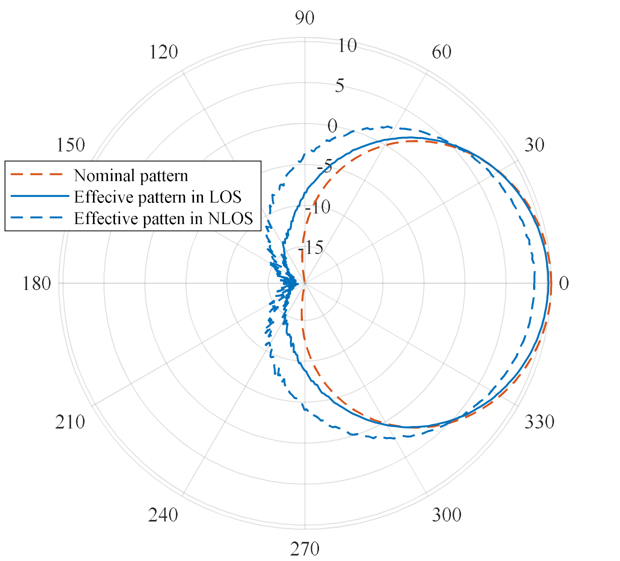

Fig. 3. Comparison of horizontal cuts of nominal and effective patterns of assumed antenna model in 3GPP UMa environment

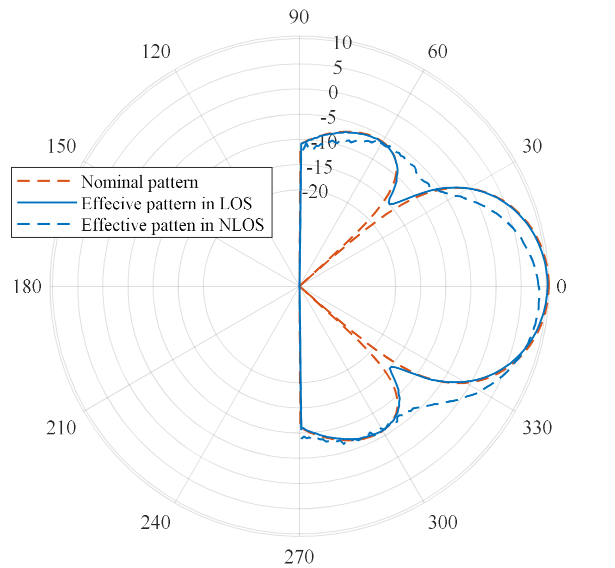

Fig. 4. Comparison of vertical cuts of nominal and effective patterns of assumed antenna model in 3GPP UMa environment

calculated effective pattern cuts in horizontal and vertical planes, respectively. As can be noticed on these figures, the maximum gain of antenna pattern drops between nominal and effective pattern by around 0.5 dB in case of LOS conditions, and almost 2 dB in case of NLOS conditions. However, in case of angles far from pattern's boresight, e.g. +/- 50° in horizontal plane, the effective gain is significantly higher than nominal in both LOS and NLOS conditions. These phenomena are caused by spatial filtering of multipath components (arose due to propagation by scatterings) by nominal antenna pattern, which in (1)-(3) is modeled by convolution function. The shape of simulated effective patterns is also aligned with measurement results presented in Figs. 1 and 2 for urban Manhattan scenario, as well as measurement results obtained for other environments in [14]-[16], where drop in maximum gain and increase of side lobe levels are observed.

In radio cellular networks most of interference is transmitted and received by side lobes (or other angles than boresight) of antenna pattern. From the antenna patterns of Figs. 3 and 4 it is clear that during interference calculations the effective antenna pattern should be used instead of nominal pattern. In other case, the value of estimated interference can be noticeably lower than the actual value experienced in real propagation conditions with scatterings, which may lead to suboptimal allocation of radio channels, leading to lower than expected performance or even receiver's blockage due to high interference.

B. Modeling of interference between CBSDs in UMa scattering environment and its impact on channels distribution

To evaluate the impact of nominal and effective antenna patterns on interference evaluation between GAA access points of the same network, and therefore on distribution of radio channels by SAS inside the CBRS network, the system level simulations with Monte Carlo methodology have been performed. It was assumed that SAS is distributing radio channels, of 10 MHz each, between GAA access points according to proprietary algorithm based on Kohonen neural networks. Details of the algorithm are described in [17] and [18]. Simulation parameters follow assumptions made for practical CBRS network in [12] and are summarized in Table II.

Figure 5 illustrates the cumulative distribution function (CDF) of point-to-point (p2p) interference between each pair of GAA access points obtained from conducted system level simulations. These values of interference have been used by Kohonen algorithm to decide about channels allocation between GAA access point in simulated deployment area of CBRS network. For instance, if interference caused by access point A to access point B and by access point B to access point A are both lower than -96 dBm per 10MHz, it is possible to allocate the same radio channel to both access points. Otherwise, the same channel cannot be allocated to access point A and access point B. Therefore, it is important to ensure that SAS accurately calculates interference between GAA access points. As can be noticed on Fig. 5, the effective interference for real propagation conditions can be more than 6 dB higher (in median) than estimation based on nominal antenna pattern. In consequence, the number of separate radio channels required to ensure co-existence between GAA access points is also different, as obtained from assumed Kohonen algorithm. According to CDFs on Fig. 6, the minimal number of channels are 8 and 10 for nominal and effective patterns (in median), respectively. In other words – when nominal pattern is used by SAS for determination of interference conditions between GAA access points in UMa propagation environment,

TABLE II. MAIN PARAMETERS OF SIMULATION SCENARIO

Parameter	**Value**
EIRP of GAA	From 40 dBm per 10MHz to 47 dBm per 10MHz (Cat B)
Interference protection criteria	-96 dBm per 10MHz
Antenna height above ground	6 m to 30 m
Down tilt	From 2° to 10°
Density of GAA	30 per km^2
Channel bandwidth	10 MHz
Simulated area	4 km^2
Position of GAA	Uniform random distribution inside simulated area

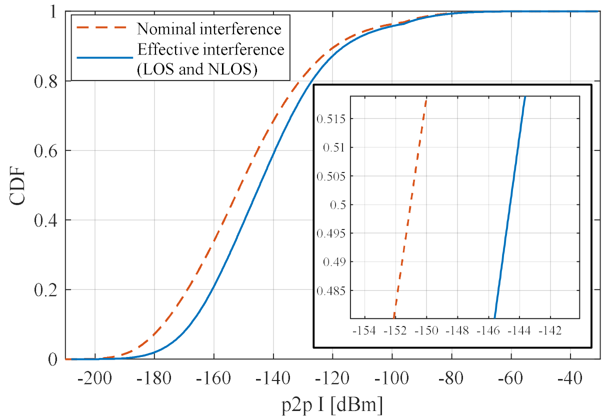

Fig. 5. CDF of point-to-point interference between each pair of GAA estimated with nominal and effective antenna patterns

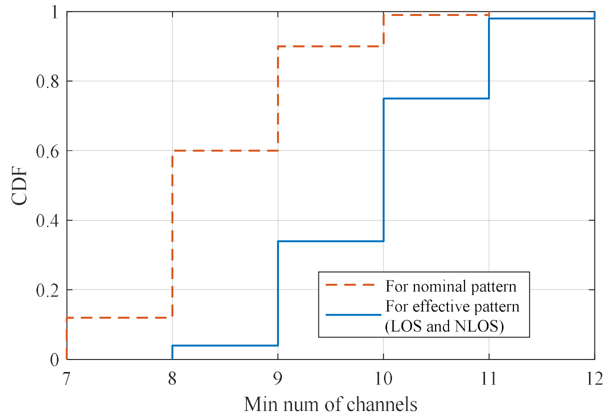

Fig. 6. Comparison of vertical cuts of nominal and effective patterns of assumed antenna model in 3GPP UMa environment

some of access points suffer interference originated from other access points, because 2 additional channels are missing to ensure sufficient co-existence conditions.

Presented evaluation has been performed for the 4G LTE type of GAA access points and associated antenna model. In case of 5G NR standard, which is adapted to utilize antenna arrays for shaping high gain narrow-beam antenna patterns via different beamforming techniques, the impact of scattering environments on effective antenna pattern is more visible, as demonstrated in [9]. Considering that at the beginning of 2020 the CBRS Alliance, an industry organization focused on developments of CBRS, together with Federal Communication Commission (FCC) enabled support for 5G NR deployments using shared spectrum in the 3.5 GHz band, the first CBSD implementations based on 5G NR standards are expected in 2021. Therefore, extension of study presented in this paper is planned to cover evaluation of CBRS performance with nominal and effective directional patterns of GAA based on 5G NR antenna arrays. However, results of already conducted studies suggest that enhancements of applicable requirements of WInnForum, especially [7] and [8], should be introduced to consider effective antenna pattern for improvement of performance in future CBRS network with 5G NR implementations.

IV. Conclusion

System level simulation study of performance in GAA type of cells in CBRS network with centralized SAS controller was performed. Simulation study assumed model of commercially available antenna of CBSD, as well as realistic deployment scenario, full 3D channel model and proprietary algorithm for resources distribution, to emphasize practical meaning of obtained results. The aim of the study was to clarify if nominal antenna pattern of CBSD (as measured in anechoic chamber) is appropriate for estimation of interference conditions between CBSDs in scattering propagation environment. It has been shown that effective antenna pattern of CBSD (as determined for given scattering propagation conditions) is needed for accurate modeling of interference during CBRS network planning and optimization, as well as during CBRS network operation in spectrum sharing environment. In assumed simulation scenario the value of interference between each pair of GAA cells can be underestimated even by 6 dB if nominal antenna pattern is assumed in link budget calculation instead of effective antenna pattern. This underestimation may lead to suboptimal channels distribution by SAS and in consequence to severe co-existence issues between GAA access points. Therefore, it is suggested that relevant requirements of CBRS standard should be enhanced to consider effective antenna patterns, especially in case of implementations based on 5G NR with high gain narrow-beam antenna patterns.

References

[1] “Report and Order and Second Further Notice of Proposed Rulemaking, Amendment of the Commission’s Rules with Regard to Commercial Operations in the 3550-3650 MHz Band”, GN Docket No. 12-354, Federal Communications Commission, 21 April 2015.

[2] “Order on Reconsideration and Second Report and Order, Amendment of the Commission’s Rules with Regard to Commercial Operations in the 3550-3650 MHz Band”, GN Docket No. 12-354, Federal Communications Commission, 2 May 2016.

[3] M. M. Sohul, M. Yao, T. Yang and J. H. Reed, “Spectrum Access System for the Citizen Broadband Radio Service”, IEEE Communications Magazine, vol. 53, Issue: 7, pp. 18 – 25, July 2015.

[4] “SAS to CBSD Protocol Technical Report-B”, WINNFORUM, WINNF-15-P-0062-V1.0.0, Version V1.0.0, 30 March 2016.

[5] “Requirements for Commercial Operation in the U.S. 3550-3700 MHz Citizens Broadband Radio Service Band”, Document WINNF-TS-0112, Version V1.9.1, 11 March 2020.

[6] “CBRS Operational and Functional Requirements (Release 2)”, Document WINNF-TS-1001, Version V1.2.0, 19 November 2020.

[7] “Signalling Protocols and Procedures for Citizens Broadband Radio Service (CBRS): Extensions to Spectrum Access System (SAS) - Citizens Broadband Radio Service Device (CBSD) Interface Technical Specification (Release 2)”, Document WINNF-TS-3002, Version V1.1.0, 30 September 2020.

[8] “CBSD Antenna Pattern Database Technical Specification”, Document WINNF-TS-5006, Version V1.0.0, 29 September 2020.

[9] K. Bechta, J. Du, M. Rybakowski, “Rework the Radio Link Budget for 5G and Beyond”, IEEE Access, vol. 8, pp. 211585–211594, November 2020.

[10] J. Du, D. Chizhik, R. A. Valenzuela, R. Feick, G. Castro, M. Rodriguez, T. Chen, M. Khli, G. Zussman, “Directional Measurements in Urban Street Canyons from Macro Rooftop Sites at 28 GHz for 90% Outdoor Coverage,” IEEE Transactions on Antennas and Propagation, in press. (arxiv:1908.00512).

[11] “AirScale Micro Remote Radio Head. Integrated Directional Antenna-AAQA for AZQC”, Nokia, 2018. (https://fccid.io/2AD8UAZQCRH1/Letter/Antenna-List-4446834)

[12] W. Gao, A. Sahoo, “Performance Impact of Coexistence Groups in a GAA-GAA Coexistence Scheme in the CBRS Band”, IEEE Transactions on Cognitive Communications and Networking (Early Access), 17 June 2020.

[13] 3GPP Radio Access Network Working Group, “Study on channel model for frequencies from 0.5 to 100 GHz (Release 15)”, 3GPP TR 38.901 V15.0.0.

[14] D. Chizhik, J. Du, R. Feick, M. Rodriguez, G. Castro, R. A. Valenzuela, “Path loss, beamforming gain and Directional Gain Measurements at 28 GHz for Non-Line-of-Sight Coverage of Indoors With Corridors,” IEEE Transactions on Antennas and Propagation, vol. 68, pp. 4820-4830, Jun. 2020.

[15] J. Du, D. Chizhik, R. Feick, M. Rodriguez, G. Castro, R. A. Valenzuela, “Suburban Fixed Wireless Access Channel Measurements and Models at 28 GHz for 90% Outdoor Coverage”, IEEE Transactions on Antennas and Propagation, vol. 68, pp. 411-420, Jan. 2020.

[16] D. Chizhik, J. Du, R. A. Valenzuela, J. Otterbach, R. Fuchs, J. Koppenborg, “Path Loss and Directional Gain Measurements at 28 GHz for Factory Automation”, IEEE International Symposium on Antennas and Propagation and USNC-URSI Radio Science Meeting, Jul. 2019.

[17] K. Bechta, “Radio resource allocation”, International Application No.: PCT/FI2017/050149.

[18] K. Bechta, “Centralized Spectrum Sharing and Coordination Between Terrestrial and Aerial Base Stations of 3GPP-Based 5G Networks”, International Journal of Electronics and Telecommunications, 2021, in press.

Downlink Interference in Multi-Beam 5G Macro-Cell

Kamil Bechta
NOKIA, Mobile Networks
Wroclaw, Poland
kamil.bechta@nokia.com
ORCID: 0000-0003-2379-0722

Cezary Ziółkowski
Institute of Communications Systems
Faculty of Electronics
Military University of Technology
Warsaw, Poland
cezary.ziolkowski@wat.edu.pl
ORCID: 0000-0003-0750-0705

Jan M. Kelner
Institute of Communications Systems
Faculty of Electronics
Military University of Technology
Warsaw, Poland
jan.kelner@wat.edu.pl
ORCID: 0000-0002-3902-0784

Leszek Nowosielski
Institute of Communications Systems
Faculty of Electronics
Military University of Technology
Warsaw, Poland
leszek.nowosielski@wat.edu.pl
ORCID: 0000-0002-4230-4905

Abstract—**Multi-beam antenna systems are the basic technology that is used in developed fifth-generation systems. This article is devoted to assessing the impact of a multi-beam antenna system on the interference level in the downlink. These interference are generated by neighboring base station antenna beams. The presented analysis is based on simulation studies in which the multi-elliptic propagation model is used. Transmission characteristics of propagation environments such as power delay profile and antenna beam patterns that define the geometric structure of the model were adopted on the basis of the 3GPP standard. The obtained results show the possibility of using the presented method to assess the separation angle between co-channel beams. It is the basis for minimizing spectral resources in the system.**

Keywords—5G, downlink, interference, multi-beam antenna system, multi-elliptical propagation model, signal-to-interference ratio (SIR), 3GPP standard

I. Introduction

Achieving greater transmission capacity for wireless links is the main goal of currently developed fifth-generation (5G) networks. The use of new spectral resources that cover frequency ranges exceeding 3 GHz provides an increase in the performance and capacity of these networks. However, propagation phenomena that occur in the millimeter-wave range cause numerous problems in the practical implementation of radio transmission equipment solutions. The increase in propagation environment attenuation at higher frequencies makes it necessary to reduce the size of cells and sectors served by individual network base stations. Hence, obtaining full coverage forces increasing the density of network access nodes (base stations) in a given area. The dominant number of mobile users of wireless networks occurs in urban areas, where the phenomenon of multi-path propagation significantly limits the transmission capabilities of radio links. As a result of this phenomenon in combination with the Doppler effect, which arises as a result of user motions, the signal undergoes a dispersion phenomenon both in time, frequency, and reception angle domains.

A multi-antenna system is one of the basic solutions used in the currently implemented 5G systems that minimize the impact of adverse propagation phenomena. A massive multiple-input-multiple-output (massive-MIMO) technology plays a special role. It uses a beamforming technique, which gives the possibility of practical implementation of spatial multiplexing for radio resources. This multiplexing allows minimizing spectral resources by using the same frequency sub-bands in angularly separated beams. In urban areas, the occurrence of multipath propagation is the cause of the angular dispersion of the received signals. This is the reason for receiving signal components from unwanted beams that significantly interfere with the signal from a useful beam (i.e., a reference beam). In this paper, we present a methodology for assessing the interference level in a downlink that arises as a result of using a multi-beam antenna system in the 5G base station (i.e., 5G gNodeB). In simulation studies, the use of a multi-elliptical propagation model (MPM) [1] and real beam patterns of the massive-MIMO antenna systems [2] determines the originality of the obtained results and the method of determining the interference level from undesirable beams (i.e., interfering beams) of the antenna system.

The rest of the paper is organized as follows. Section II describes the practical ways of using multi-beam antenna systems. Section III presents the basis for assessing the interference level in the downlink, which is based on the use of the MPM. Assumptions, obtained results, and conclusions from the carried out simulation tests are presented in Sections IV and V, respectively.

This work was developed within a framework of the research grants "Basic research in sensor technology field using innovative data processing methods" no. GBMON/13-996/2018/WAT sponsored by the Polish Ministry of Defense, and "Impact of various propagation conditions on effectiveness of wireless communication and electronic warfare systems" no. UGB/22-730/2020/WAT.

II. Multi-Beam Antenna System – Practical Aspects

One of the key differentiators of 5G is the ability to utilize the benefits of the massive-MIMO technique, especially the simplification of multiple-user access. Because of a large number of antenna elements connected to multiple transmission-reception radio chains, the fast fading was seen by the base station gradually disappears and the radio channel becomes flat in the frequency domain. This effect, called channel hardening, causes that in orthogonal frequency division multiplexing (OFDM) access, each subcarrier has similar channel gain and therefore different user equipment (UE) of the same cell can be allocated to the whole available frequency bandwidth [3].

On top of that massive-MIMO allows to significantly increase the cell capacity in reference to conventional MIMO. Due to spatial multiplexing of available resources, obtained by the ability of energy focusing by large antenna arrays, i.e., beamforming, massive-MIMO allows reusing the same frequency bandwidth by multiple UEs at the same time. However, such a multi-user scenario is possible only in the case of favorable propagation conditions, i.e., when the propagation channel responses from the base station to simultaneously served UEs are sufficiently different (UEs are considered to be spatially orthogonal). From that viewpoint, the number of available resources in the cell is multiplied by the number of UEs. In less favorable propagation conditions, i.e., when the spatial orthogonality between UEs is not sufficient, the available radio resources have to be distributed properly. Usually, if different UEs are served by different beams they can be allocated with full available bandwidth but in different time slots, to avoid intra-cell interference. In case when the same beam serves multiple UEs the available bandwidth is split between these UEs accordingly. It can be also possible that only single UE will be under the coverage of two neighboring beams, which would result in doubling of resources available from a single beam, i.e., such UE can be served in two consecutive time slots.

Even though that due to beamforming the massive-MIMO significantly limits the inter-cell interference in reference to legacy MIMO, the problem of unavoidable re-use of training sequences, i.e., pilot contamination, by UEs in different cells still exists and the inter-cell interference grows along with the number of base stations in the network [4]. Therefore, it is particularly important that inter-cell interference is accurately modeled at the stage of network planning and optimization as well as accurately estimated and limited during network operation by sufficient precoding.

III. Fundamentals of Interference Evaluation in Downlink

Dispersion in the reception angle domain is characteristic for areas, where multipath propagation occurs, e.g., urbanized areas with non-line-of-sight (NLOS) conditions. In such a propagation environment, the basis for power assessment is power angular spectrum, $p(\theta,\phi,d)$, where θ and ϕ are the angles in the elevation and azimuth planes, respectively, and d is the distance between a transmitter (Tx) and receiver (Rx). This function allows determining the received power $P_R(d)$ according to the relationship [5]

$$P_R(d)=\iint_{\Omega} p(\theta,\phi,d)\,d\theta d\phi \tag{1}$$

where $\Omega=\left\{(\theta,\phi):\theta\in\left[0°,90°\right),\phi\in\left[-180°,180°\right)\right\}$.

Thus, under NLOS conditions, knowing the angular power spectra for signals from the useful (i.e., reference) and unwanted (i.e., interfering) beams allows an assessment of the energy relationship between these signals. In this paper, we analyze the transmission of signals in the frequency range from 3 to 4 GHz and the receiving point distance exceeding 100 m. For these conditions, we can assume that the dispersion phenomenon of the received power dominates in the azimuth plane. This fact is shown in [1][5]. In this case, the signal-to-interference ratio (SIR) between the useful signal strength $P_{R0}(d)$ and the power of the interfering signal $P_{RI}(d)$ that comes from the unwanted beam has the form [6]

$$SIR=10\log_{10}\frac{P_{R0}(d)}{P_{RI}(d)}=10\log_{10}\frac{\int_{-180°}^{180°} p_0(\phi,d)\,d\phi}{\int_{-180°}^{180°} p_I(\phi,d)\,d\phi} \tag{2}$$

where $p_0(\phi,d)$ and $p_I(\phi,d)$ represent the angular power distributions of the useful and interfering signals in the azimuth plane, respectively.

Equation (2) reduces the SIR evaluation to determine $p_0(\phi,d)$ and $p_I(\phi,d)$. In this paper, we use the MPM to determine these channel characteristics. The geometry of this model describes the most probable locations of scatterers. Its structure consists of a set of confocal ellipses whose foci determine the position of the Tx (i.e., gNodeB) and Rx (i.e., UE). For the nth ellipse, the major, a_{xn}, and minor, b_{xn}, axes are defined based on a power delay profile (PDP) according to the following relationships [1][7]

$$a_{xn}=\frac{1}{2}(c\tau_n+d) \tag{3}$$

$$b_{xn}=\frac{1}{2}\sqrt{c\tau_n(c\tau_n+2d)} \tag{4}$$

where c denotes the speed of light, d is the distance between the Tx and Rx, and τ_n is a delay for which the PDP takes the nth local extreme.

The adopted way of creating the geometric structure of the MPM provides a mapping of transmission properties of propagation environments. Detailed descriptions of this structure are provided in [1][5][7][8]. In a simulation testing procedure, the mapping of directional antennas is obtained by using their normalized radiation pattern. Because these characteristics meet the definition properties of probability density [9], in the simulation procedure the directions of departure of propagation paths are generated on their basis. A detailed description of determining the radiation angle distribution is given in [8]. Radiated propagation paths are transformed in the MPM geometric structure. At the final stage of the simulation procedure, considering the receiving antenna pattern enables the determination of angular power spectra that come from individual beams and are seen on the antenna output [5].

IV. Simulation Studies

A. Assumptions

In the simulation studies, we consider a scenario illustrated in Fig. 1. In this case, the macro-cell gNode-B base station (Tx) with the massive-MIMO antenna array generates two beams in the selected sector, i.e., reference and interfering beams presented in green and red color, respectively. Their directions determined the angle of beam separation, $\Delta\alpha$. The UE (Rx) is in an area of the reference beam at the distance d. Directions of the UE (purple color) and reference gNodeB beams provide their alignment. We assess the SIR versus $\Delta\alpha$ between two analyzed transmitting beams for various d in the downlink.

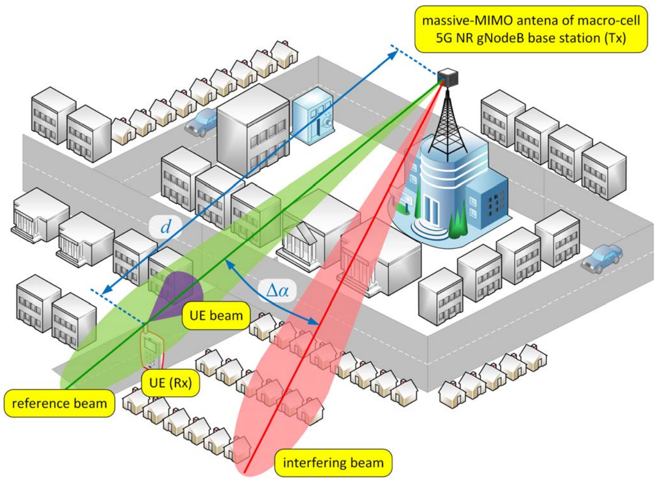

Fig. 1. Spatial scenario of simulation studies.

For more realistic simulation results, we use real patterns for the UE and gNodeB beams. For this purpose, we base on [2]. In the selected sector, the gNodeB is equipped with two vertical patches with 12×8 of antenna elements that generate two analyzed beams. The UE beam with a half-power beamwidth (HPBW) equal to 90° is generated by a single antenna element. Figure 2 depicts the three-dimensional pattern of the reference beam. The patterns of the UE (purple dashed line), reference (green line), and interference (red dotted line) beams in the azimuth plane are shown in Fig. 3. In this case, the interfering beam is presented for example $\Delta\alpha = 30°$.

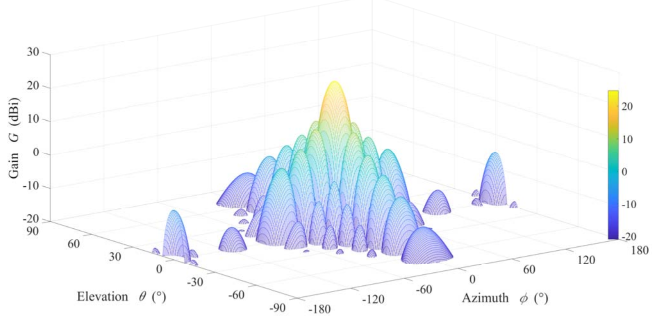

Fig. 2. Three-dimensional pattern of reference beam.

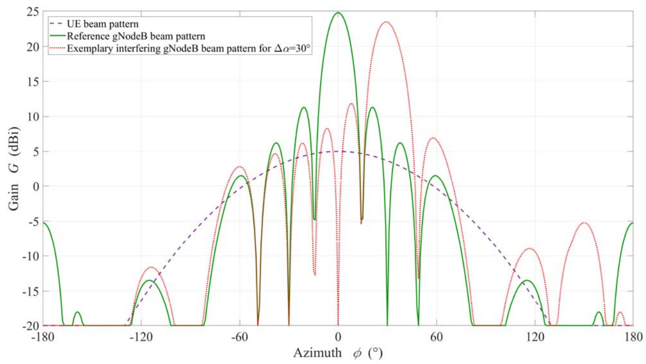

Fig. 3. Patterns of UE, reference and exemplary interfering beams in azimuth plane.

For the MPM, we additionally consider the following assumptions:

- carrier frequency of the transmitted signal is $f_0 = 3.5$ GHz,
- PDP is based on TLD-B, i.e., tapped-delay line (TDL) model of the 3GPP standard [10] for NLOS conditions; this TDL correspond an urban macro (UMa) scenario and normal-delay profile, i.e., rms delay spread is equal to $\sigma_\tau = 363$ ns [10],
- Rician factor is $\kappa = 0$ [10],
- intensity coefficient of the local scattering is $\gamma = 0$,
- analyzed distances between the gNodeB (Tx) and UE (Rx) are $d = \{100, 200, 500\}$ m,
- range of changes in the angle of beam separation is [0°, 60°].

B. Maintaining the Integrity of the Specifications

For the above assumptions, we carried out simulation studies. The obtained results are depicted in Fig. 4. In this case, graphs present the SIR versus angle of beam separation, $\Delta\alpha$, for various distances d between the UE and gNodeB.

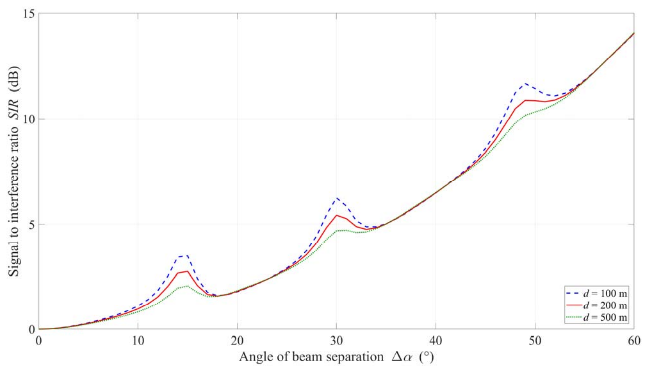

Fig. 4. SIR versus angle of beam separation for NLOS conditions, and different distances between UE and gNodeB.

The increase in $\Delta\alpha$ reduces the downlink interference between the reference beam providing services to the UE and the interference beam. However, the nature of the SIR graphs is not uniform. For $\Delta\alpha = 15°$, 30°, and 48°, there are local maxima. They result from considering side lobes in the realistic patterns of the base station beams. As the distance d increases, these maxima are less and less significant.

On the other hand, the obtained results differ significantly from those presented in [6], where some stabilization may be seen in the SIR graphs. In [6], two simplifications are assumed. Firstly, the beams are modeling only using the Gaussian main lobe pattern without side lobes. Secondly, the beam gain is constant regardless of its radiation direction. Whereas, in the real massive-MIMO antenna array, the beam gain depends on its direction. This second fact influences importantly on the differences in the presented results.

V. Conclusions

This paper focuses on assessing the interference in radio downlinks arising in multi-beam antenna systems. The presented method of the SIR evaluation is based on simulation studies, where the MPM and real beam patterns are used. The obtained results show the effectiveness of the developed solution in determining the angular separation in the multi-beam antenna arrays that provides an acceptable interference level. Unlike methods of inter-beam interference assessment used so far, the solution proposed in this paper considers the phenomenon of angular dispersion of received power, with particular regard to NLOS conditions. An ability to adapt the MPM geometric structure to the actual transmission conditions of a given propagation environment minimizes SIR evaluation errors. In that, the presented method of assessing the interference level at the receiving point can be used to determine the separation angle between co-channel beams, which allow minimizing the spectral resources in the system.

References

[1] J. M. Kelner and C. Ziółkowski, "Multi-elliptical geometry of scatterers in modeling propagation effect at receiver," in *Antennas and wave propagation*, P. Pinho, Ed. London, UK: InTech, 2018, pp. 115–141.

[2] 3GPP, "Evolved Universal Terrestrial Radio Access (E-UTRA) and Universal Terrestrial Radio Access (UTRA; Radio Frequency (RF) requirement background for Active Antenna System (AAS) Base Station (BS)," 3rd Generation Partnership Project (3GPP), Valbonne, France, Tech. Rep. 3GPP TR 37.842 V13.3.0 (2019-12), Release 13, Dec. 2019.

[3] E. G. Larsson, O. Edfors, F. Tufvesson, and T. L. Marzetta, "Massive MIMO for next generation wireless systems," *IEEE Commun. Mag.*, vol. 52, no. 2, pp. 186–195, Feb. 2014, doi: 10.1109/MCOM.2014.6736761.

[4] F. Fernandes, A. Ashikhmin, and T. L. Marzetta, "Inter-cell interference in noncooperative TDD large scale antenna systems," *IEEE J. Sel. Areas Commun.*, vol. 31, no. 2, pp. 192–201, Feb. 2013, doi: 10.1109/JSAC.2013.130208.

[5] C. Ziółkowski and J. M. Kelner, "Statistical evaluation of the azimuth and elevation angles seen at the output of the receiving antenna," *IEEE Trans. Antennas Propag.*, vol. 66, no. 4, pp. 2165–2169, Apr. 2018, doi: 10.1109/TAP.2018.2796719.

[6] J. M. Kelner and C. Ziółkowski, "Interference in multi-beam antenna system of 5G network," *Int. J. Electron. Telecommun.*, vol. 66, no. 1, pp. 17–23, Feb. 2020.

[7] C. Ziółkowski and J. M. Kelner, "Geometry-based statistical model for the temporal, spectral, and spatial characteristics of the land mobile channel," *Wirel. Pers. Commun.*, vol. 83, no. 1, pp. 631–652, Jul. 2015, doi: 10.1007/s11277-015-2413-3.

[8] C. Ziółkowski and J. M. Kelner, "Antenna pattern in three-dimensional modelling of the arrival angle in simulation studies of wireless channels," *IET Microw. Antennas Propag.*, vol. 11, no. 6, pp. 898–906, May 2017, doi: 10.1049/iet-map.2016.0591.

[9] R. Vaughan and J. Bach Andersen, *Channels, propagation and antennas for mobile communications*. London, UK: Institution of Engineering and Technology, 2003.

[10] 3GPP, "Study on channel model for frequencies from 0.5 to 100 GHz," 3rd Generation Partnership Project (3GPP), Technical Specification Group Radio Access Network, Valbonne, France, Tech. Rep. 3GPP TR 38.901 V16.1.0 (2019-12), Release 16, Dec. 2019

sensors

MDPI

Article

Modeling of Downlink Interference in Massive MIMO 5G Macro-Cell †

Kamil Bechta [1], Cezary Ziółkowski [2], Jan M. Kelner [2,*] and Leszek Nowosielski [2]

[1] Nokia Solutions and Networks, 54-130 Wrocław, Poland; kamil.bechta@nokia.com
[2] Institute of Communications Systems, Faculty of Electronics, Military University of Technology, 00-908 Warsaw, Poland; cezary.ziolkowski@wat.edu.pl (C.Z.); leszek.nowosielski@wat.edu.pl (L.N.)
* Correspondence: jan.kelner@wat.edu.pl; Tel.: +48-261-839-517

† The paper is an extended version of our paper published in Bechta, K.; Ziółkowski, C.; Kelner J.M.; Nowosielski, L. Downlink interference in multi-beam 5G macro-cell. In Proceedings of the 2020 23rd International Microwave and Radar Conference (MIKON), Warsaw, Poland, 5–8 October 2020; pp. 140–143, doi:10.23919/MIKON48703.2020.9253919.

Citation: Bechta, K.; Ziółkowski, C.; Kelner, J.M.; Nowosielski, L. Modeling of Downlink Interference in Massive MIMO 5G Macro-Cell. *Sensors* **2021**, *21*, 597. https://doi.org/10.3390/s21020597

Received: 12 December 2020
Accepted: 12 January 2021
Published: 16 January 2021

Abstract: Multi-beam antenna systems are the basic technology used in developing fifth-generation (5G) mobile communication systems. In practical implementations of 5G networks, different approaches are used to enable a massive multiple-input-multiple-output (mMIMO) technique, including a grid of beams, zero-forcing, or eigen-based beamforming. All of these methods aim to ensure sufficient angular separation between multiple beams that serve different users. Therefore, ensuring the accurate performance evaluation of a realistic 5G network is essential. It is particularly crucial from the perspective of mMIMO implementation feasibility in given radio channel conditions at the stage of network planning and optimization before commercial deployment begins. This paper presents a novel approach to assessing the impact of a multi-beam antenna system on an intra-cell interference level in a downlink, which is important for the accurate modeling and efficient usage of mMIMO in 5G cells. The presented analysis is based on geometric channel models that allow the trajectories of propagation paths to be mapped and, as a result, the angular power distribution of received signals. A multi-elliptical propagation model (MPM) is used and compared with simulation results obtained for a statistical channel model developed by the 3rd Generation Partnership Project (3GPP). Transmission characteristics of propagation environments such as power delay profile and antenna beam patterns define the geometric structure of the MPM. These characteristics were adopted based on the 3GPP standard. The obtained results show the possibility of using the presented novel MPM-based approach to model the required minimum separation angle between co-channel beams under line-of-sight (LOS) and non-LOS conditions, which allows mMIMO performance in 5G cells to be assessed. This statement is justified because for 80% of simulated samples of intra-cell signal-to-interference ratio (SIR), the difference between results obtained by the MPM and commonly used 3GPP channel model was within 2 dB or less for LOS conditions. Additionally, the MPM only needs a single instance of simulation, whereas the 3GPP channel model requires a time-consuming and computational power-consuming Monte Carlo simulation method. Simulation results of intra-cell SIR obtained this way by the MPM approach can be the basis for spectral efficiency maximization in mMIMO cells in 5G systems.

Keywords: 5G; downlink; interference; signal-to-interference ratio (SIR); massive MIMO; multi-beam antenna system; multi-elliptical propagation model; 3GPP standard

1. Introduction

Achieving greater transmission capacity for wireless links is the main goal of the currently developed fifth-generation (5G) mobile communication system [1,2]. The use of new spectral resources that cover frequency ranges exceeding 3 GHz provides an increase in the performance and capacity of next generation networks. However, propagation phenomena that occur in the centimeter-wave (cmWave) and millimeter-wave (mmWave) ranges cause numerous problems in the practical implementation of radio transmission equipment solutions [3,4]. The increase in propagation environment attenuation at higher frequencies makes it necessary to reduce the size of cells and sectors served by individual network base stations (BS). Hence, obtaining full coverage forces increased density of BSs in a given deployment area. The dominant amount of mobile users' equipment (UEs) of wireless networks occurs in urban areas, where the phenomenon of multipath propagation significantly limits the transmission capabilities of radio links. In combination with the Doppler effect, resulting from user motions, this phenomenon leads to signal dispersion in time, frequency, and reception angle domains [5].

A multi-antenna system is one of the basic solutions used in the currently implemented 5G systems that minimize adverse propagation phenomena. A massive multiple-input-multiple-output (mMIMO) technique plays a special role [6,7]. It uses a beamforming technique [8,9], which allows for the possibility of practical implementation of spatial multiplexing for radio resources. This multiplexing improves spectral efficiency by using the same frequency sub-bands in angularly separated beams (spatially orthogonal beams). In urban areas, multipath propagation is the cause of the angular dispersion of the received signals [10]. It is the reason for receiving signal components from unwanted beams that significantly interfere with the signal from the serving (i.e., useful, reference) beam. A level of this interference is directly connected with spatial orthogonality between reference and interfering beams. If a signal-to-interference ratio (SIR), i.e., the ratio between received powers of reference and interfering signals, is higher, then the spatial orthogonality between these beams is better. Therefore, at the mMIMO 5G network planning and optimization stages, it is important to assess spatial orthogonality in realistic propagation conditions accurately. This allows achievable performance for a given deployment scenario to be estimated. One of the metrics that can help estimate mMIMO cell performance is the relation between the SIR and angular separation between the reference and interfering beams. Since UEs are distributed mostly on a horizontal plane, rather than a vertical one, in the typical cells of a mobile network, in the majority of cases is enough to consider angular separation only on a horizontal plane to make an accurate estimation of the SIR. In other words, accurate modeling of the relation between the angular separation of reference and interfering beams on a horizontal plane and the SIR helps to estimate many parameters of mMIMO cells. For example, we may determine a minimum distance between UEs that can be served by simultaneous mMIMO beams with an assumed interference level or maximum number of uniformly distributed UEs, which can be served by simultaneous mMIMO beams with the assumed level of the SIR.

In the literature, an interference subject concerns interfering signals in a wide-sense. The nature of their formation may be diverse. In most cases, when we talk about interferences, we mean so-called non-intentional interferences, i.e., those arising from the operation of radio, electronic, or mechatronic devices, networks, or whole systems during their work. The second group is the so-called intentional interference (i.e., jamming) mainly used in the military or security to disrupt enemy communication systems or counteract radio systems in a protected area (i.e., electromagnetic curtain [11]), e.g., in airports, buildings, and infrastructure of strategic importance. Examples of jamming 5G systems are presented in [12,13]. The remainder of the paper focuses on non-intentional interferences.

The interference subject in communication systems, in particular in 5G systems, is widely represented in the literature. Works in this area focus on the three following topics:

- interference cancelation, mitigation, awareness, and management methods,
- interference modeling and assessment methods,
- interference estimation and measurement methods.

Software-based algorithms and hardware solutions that are implemented in BS and UE belong to the first method group. Papers focusing on this topic present novel solutions, usually based on simulation analysis, e.g., [14–19]. The purpose of these methods is to increase the efficiency of devices and networks and make better use of radio resources.

Various modeling methods are used in interference evaluation. They are usually based on energetic assessment of the received signals. However, interference level analysis may take different aspects into account. In this case, the important aspects influencing the received signal form have a crucial value in the faithful reflection of the modeled issue in relation to the real situation. These aspects include, first of all, the channel model, as well as the parameters and characteristics of antenna systems. The possibility of considering environment nature and propagation conditions, as well as the appropriate reflection of angular dispersions affecting the received signal powers, should be taken into account when choosing a channel model. On the other hand, considering the parameters and patterns of antenna systems is of crucial importance, especially in the analysis of 5G spatially multiplexing systems, including those ensuring beamforming (e.g., with the mMIMO system).

Modeling methods are used to evaluate existing systems or new solutions (e.g., new mitigation algorithm) and, in particular, to evaluate inter- and intra-system electromagnetic compatibility, coexistence of 5G with other systems (e.g., fixed satellite services (FSS) [20,21], radars [22], long term evolution (LTE) [23], etc.) or to assess 5G network/system efficiency under occurring interference [24]. For 5G systems, intra-system interference (also called self-interference) analysis concerns, i.e., inter-cell [16–19] or inter-beam (or intra-cell) [17,24] interferences. In this case, we would like to note that most of the works available in the literature focus on inter-cell rather than inter-beam interference analysis. These methods are usually used in the network design and planning stages. This paper focuses on this group method for modeling and evaluating inter-beam interference in 5G massive-MIMO systems.

The last group of research and scientific works focuses on interference measurements in real environments for existing systems and networks, e.g., [23,25,26].

In this paper, we present a novel approach for assessing the interference level in a downlink (DL) that arises as a result of using a multi-beam antenna system in 5G BS (gNodeB), which is based on a multi-elliptical propagation model (MPM) [27]. Simulation results of the DL SIR obtained with the use of the MPM were compared with simulation results of the commonly used 3rd Generation Partnership Project (3GPP) channel model [28]. Simulations have been performed for realistic beam patterns of mMIMO antenna systems [29] and parameters of 5G networks determined by the 3GPP and International Telecommunication Union (ITU) [30]. These assumptions indicate the originality of the obtained results and the MPM approach for determining the interference level from undesirable beams, i.e., interfering beams of the antenna system.

Joint modeling of beamforming and angular spread is required to obtain an accurate estimation of realistic interference levels. Used spatial filtering of multipath components by the antenna pattern is sensitive to time-variant radio channel conditions. Such an approach to the modeling of 5G systems performance is gaining more attention. For example, in [31], the results of link budget calculations in the real propagation environment of the mmWave system can be found, whereas the corresponding impact on the efficiency of antenna array tapering is described in [32]. The study presented in this article follows the same modeling principles. Therefore, it can be considered as valuable input to the current state of the art.

The rest of the paper is organized as follows. Section 2 describes practical ways of using multi-beam antenna systems. Section 3 presents the basis for assessing the interference level in the DL based on the use of the MPM and 3GPP channel model. Assumptions, obtained results, and conclusions from the performed simulations are presented in Sections 4 and 5, respectively.

2. Multi-Beam Antenna System—Practical Aspects

One of the key differentiators of 5G is the ability to utilize the benefits of the mMIMO technique, especially the simplification of multiple-user access [1,2]. Due to a large number of antenna elements connected to multiple transmission-reception radio chains, fast fading, as seen by the gNodeB, gradually disappears, and the radio channel becomes flat in the frequency domain. This effect, called channel hardening, causes that in orthogonal frequency division multiplexing (OFDM) access each subcarrier has a similar channel gain. Therefore, different UEs from the same cell can be allocated to the whole available frequency bandwidth [6,7].

On top of this, mMIMO allows cell capacity in reference to conventional MIMO to increase significantly. Due to the spatial multiplexing of available resources obtained through energy focusing using large antenna arrays, i.e., beamforming, mMIMO allows the same frequency bandwidth to be reused by multiple UEs at the same time. However, such a multi-user scenario is only possible in the case of favorable propagation conditions, i.e., when propagation channel responses from the gNodeB are sufficiently different to simultaneously serve UEs (UEs are considered to be spatially orthogonal). From this viewpoint, the number of available resources in the cell are multiplied by the number of UEs. In less favorable propagation conditions, i.e., when the spatial orthogonality between UEs is not sufficient, the available radio resources have to be appropriately distributed. Usually, if different UEs are served by other beams, they can be allocated with full available bandwidth in different time slots to avoid intra-cell interference. In cases where the same beam serves multiple UEs, the available bandwidth is split between these UEs accordingly. It may also be possible that only a single UE will be under the coverage of two neighboring beams. This would result in a doubling of the resources available from a single beam, i.e., UE can be served in two consecutive time slots.

Even though, due to beamforming, mMIMO significantly limits inter-cell interference in reference to legacy MIMO, the problem of unavoidable re-use of training sequences, i.e., pilot contamination, by UEs in different cells still exists, and the inter-cell interference grows along with the number of base stations in the network [19]. Therefore, it is crucial that inter-cell interference, on top of intra-cell interference, is accurately modeled in the network planning and optimization stages, as well as accurately estimated and limited during network operation through sufficient precoding.

3. Interference Evaluation in Downlink

3.1. Fundamentals of the Multi-Elliptical Propagation Model

Dispersion in the angular domain is characteristic of areas where multipath propagation occurs, e.g., urbanized areas with non-line-of-sight (NLOS) or even line-of-sight (LOS) conditions [10]. In such propagation environments, the basis for power assessment is a power angular spectrum (PAS), $p(\theta, \phi, D)$, where θ and ϕ are the angles of arrival (AOA) in the elevation and azimuth planes, respectively, and D is the distance between a transmitter (Tx) and receiver (Rx). This function allows the received power $P_R(D)$ to be determined according to the relationship [33]

$$P_R(D) = \iint_{\Omega} p(\theta, \phi, D) d\theta d\phi. \tag{1}$$

where $\Omega = \{(\theta, \phi) : \theta \in [0°, 90°), \phi \in [-180°, 180°)\}$.

Thus, knowing the PAS for signals for useful (i.e., reference, serving) and unwanted (i.e., interfering) beams allows the energy relation between them to be assessed. In this paper, we analyze the transmission of signals in a frequency range from 3 to 4 GHz and with receiving point distances at 100, 200, and 500 m. For these conditions, we can assume that the dispersion phenomenon of the received power dominates in the azimuth plane. This fact is shown in [27,33]. In this case, the SIR between the useful signal strength $P_{R0}(D)$

[12]

and the power of the interfering signal $P_{RI}(D)$ that comes from the unwanted beam has the following form [5]:

$$SIR(D)(\mathrm{dB}) = 10\log_{10}\frac{P_{R0}(D)}{P_{RI}(D)} = 10\log_{10}\frac{\int_{-180^\circ}^{180^\circ} p_0(\phi, D)d\phi}{\int_{-180^\circ}^{180^\circ} p_I(\phi, D)d\phi}, \tag{2}$$

where $p_0(\phi, D) = \int_0^{90^\circ} p_0(\theta, \phi, D)d\theta$ and $p_I(\phi, D) = \int_0^{90^\circ} p_I(\theta, \phi, D)d\theta$ represent the PASs of the serving and interfering signals in the azimuth plane, respectively.

Equation (2) reduces the SIR evaluation to determine $p_0(\phi, D)$ and $p_I(\phi, D)$ in the case when the MPM is used. The geometry of this model describes the most probable locations of scatterers. Its structure consists of a set of confocal ellipses whose foci determine the positions of the Tx and Rx, i.e., the gNodeB and UE for the DL scenario, respectively. The scattering geometry of the MPM in the azimuth plane is illustrated in Figure 1 [27], whereas Figure 2 depicts the simplified MPM simulation procedure.

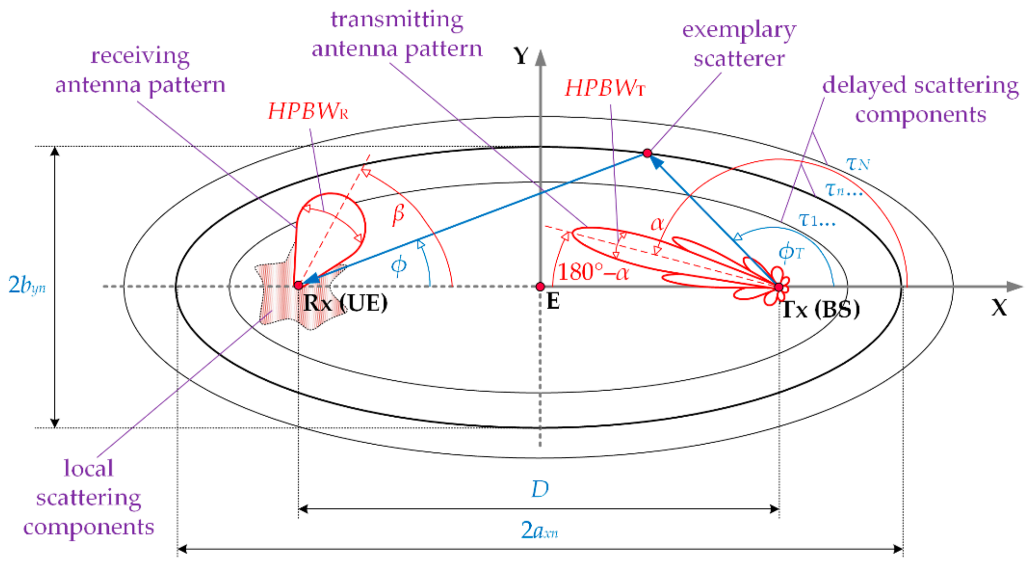

Figure 1. Scattering geometry of the multi-elliptical propagation model (MPM) in the azimuth plane.

Based on considered assumptions, i.e., the Tx-Rx distance—spatial scenario (step 1) and a chosen power delay profile (PDP) for LOS/NLOS conditions (step 2), in step 3, we calculate parameters of scattering geometry structure. For the nth ellipse (time-cluster), the major, a_{xn}, and minor, b_{yn}, axes are defined based on the PDP according to the following relationships [27,34]:

$$a_{xn} = \frac{1}{2}(c\tau_n + D), \tag{3}$$

$$b_{yn} = \frac{1}{2}\sqrt{c\tau_n(c\tau_n + 2D)}, \tag{4}$$

where c denotes the speed of light, τ_n is a delay for which the PDP takes the nth local extreme, $n = 1, 2, \ldots, N$, and N is the number of time-clusters (i.e., the local extremes) in the PDP.

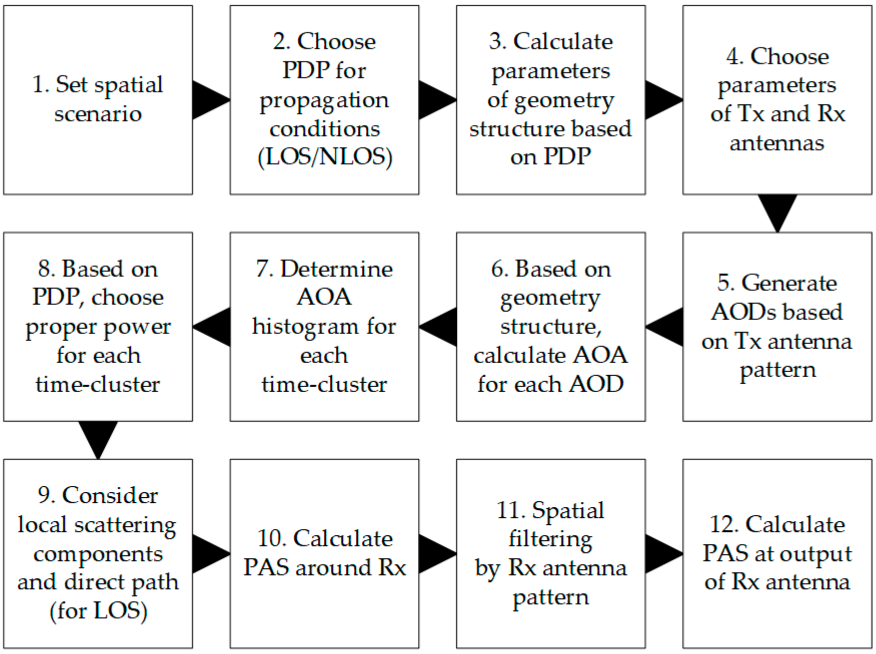

Figure 2. Simplified simulation procedure of the MPM.

The adopted way of creating the MPM geometric structure enables mapping of the transmission properties of propagation environments. Detailed descriptions of this structure are provided in [27,33–35].

In step 4, we choose the Tx and Rx antenna parameters, i.e., their pattern shapes, gains, directions of maximum radiation/reception, and half-power-beamwidths (HPBWs). In the simulation testing procedure, the mapping of directional antennas is obtained using their normalized radiation pattern [35], which is realized in step 5. Since these characteristics meet the definition properties of probability density [36], in the simulation procedure, the directions of departure of propagation paths are generated on their basis. A detailed description of determining the radiation angle distribution is given in [35]. In step 6, based on the MPM geometry structure, AOAs are calculated for each angle of departure (AOD). The sets of the obtained AOAs for each time-cluster are the basis for determining the histograms in step 7. For each time-cluster, we choose appropriate powers defined in the analyzed PDP (step 8). Next, in step 10, we multiply the AOA histograms with the proper powers to obtain the PAS seen around the Rx [33,35]. At this stage, the local scattering components and direct path for LOS conditions are also considered (step 9). Using spatial filtering by the Rx antenna pattern, we calculate the PAS seen on this antenna output (steps 11 and 12) [33]. During interference analysis, we launch the MPM simulation procedure twice for the serving and interference Tx beams, respectively.

3.2. Fundamentals of 3GPP Channel Model

For link-level and detailed system-level simulations, the 3GPP has provided instructions on how to generate statistical three-dimensional (3D) channel models, as shown in Figure 3 [28]. It includes all the necessary radio propagation phenomena that must be considered during a comprehensive simulation to provide an estimation of the radio link budget (including interference) and performance.

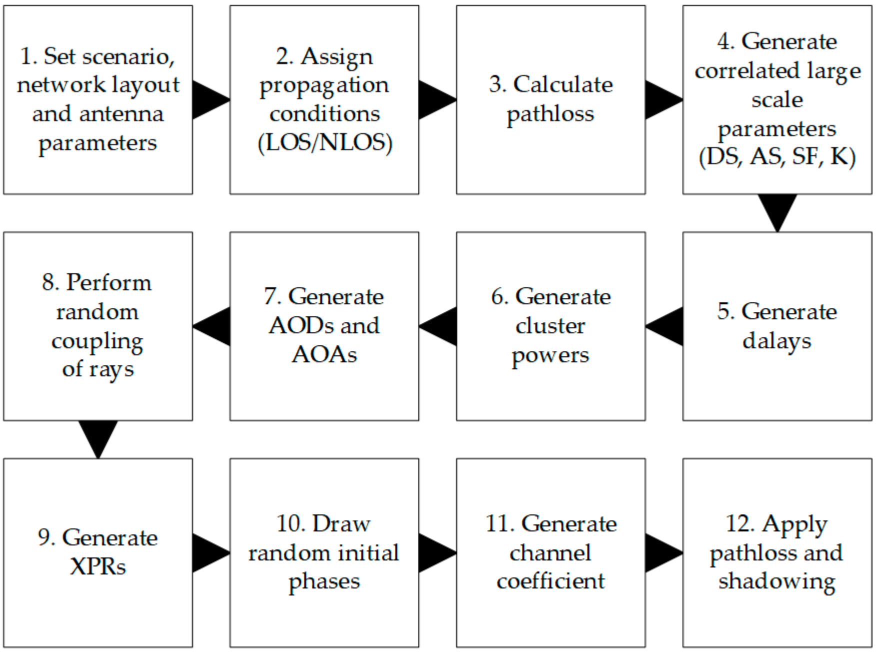

Figure 3. Block diagram of statistical channel model reconstruction according to 3GPP.

It should be noted that according to [28], dispersion in the angular domain is modeled in steps 4, 6, 7, and 8 of Figure 3. In step 4, when the angular spread (AS) for a given scenario and network layout is generated, i.e., based on the assumed statistical model, the following parameters are generated:

- azimuth spread of departure (ASD),
- zenith (i.e., elevation) spread of departure (ZSD),
- azimuth spread of arrival (ASA),
- zenith spread of arrival (ZSA).

In step 6, the power for all rays of all clusters (which arise due to multipath propagation) is generated, whereas in step 7, the angles of departure and arrival are determined for all these rays. Finally, in step 8, random coupling is performed between departure and arrival angles for rays inside a given cluster, in both azimuth and elevation. As can be noticed, according to the 3GPP channel model [28], the PAS, $p(\theta,\phi,D)$, obtained at the end of step 8 does not depend on the assumed antenna pattern. It is considered only in step 11, where channel coefficients for each cluster and each Tx and Rx element of antenna arrays are generated. Only at the end of step 11 are results of the spatial filtering of multipath components (clusters and rays) by the Tx and Rx nominal antenna patterns known. Therefore, to correctly calculate the received power of either reference or interfering signal, it is required to determine the effective antenna gains for the Tx and Rx. These effective antenna gains are defined as an integral part of the multiplied nominal antenna pattern (for the Tx or Rx) and PAS, which is equivalent to spatial filtering, as shown below [37]:

$$G^{Eff}(D) = \iint_{\Omega} g^{Nom}(\theta,\phi)p(\theta,\phi,D)d\theta d\phi, \tag{5}$$

where $g^{Nom}(\theta,\phi)$ indicates nominal 3D antenna pattern, either for the Tx or Rx, in either the reference or interfering link. Similarly, $G^{Eff}(D)$ indicates the effective gain of the Tx or Rx in either the reference or interfering link. Following the notation of Equation (2), the SIR calculated according to the 3GPP channel model [28] may be presented as follows:

$$SIR(D)(\mathrm{dB}) = 10\log_{10}\frac{P_{R0}(D)}{P_{RI}(D)} = 10\log_{10}\frac{G_{T0}^{Eff}(D)\cdot G_{R0}^{Eff}(D)}{G_{TI}^{Eff}(D)\cdot G_{RI}^{Eff}(D)}, \tag{6}$$

where $G_{T0}^{Eff}(D)$, $G_{R0}^{Eff}(D)$, $G_{TI}^{Eff}(D)$, and $G_{RI}^{Eff}(D)$ indicate the effective gains of the Tx and Rx in reference and interfering links, respectively.

4. Simulation Studies

4.1. Assumptions

In the simulation studies, we considered a scenario illustrated in Figure 4 [38]. In this case, the macro-cell gNodeB (Tx) with the mMIMO antenna array generates two beams in the selected sector, i.e., reference and interfering beams marked in green and red colors, respectively. Their directions determined the angle of beam separation, $\Delta\alpha$. The UE (Rx) is in an area of the reference beam at distance D. Directions of the UE (purple color) and reference gNodeB beams provide their alignment. We assessed the DL SIR versus $\Delta\alpha$ between the serving and unwanted beams for various distances D in an urban macro (UMa) deployment scenario.

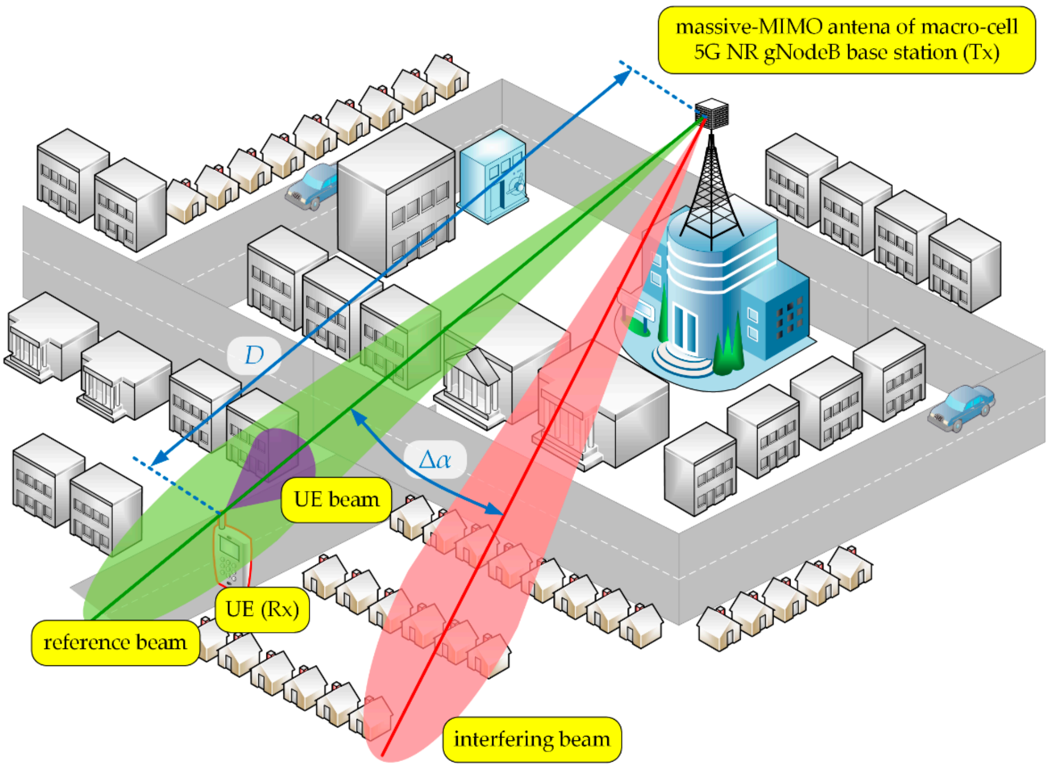

Figure 4. Spatial scenario of simulation studies [38].

For more realistic results, we used practical patterns for the UE and gNodeB beams, and simulation assumptions developed by the 3GPP and ITU in [29,30]. The gNodeB was equipped with an antenna array of 8 × 8 elements that generate two analyzed beams in the selected sector. The UE beam with HPBWs equal to 90° and 65° on the horizontal and vertical planes, respectively, is generated by a single antenna element. Figure 5 depicts the 3D pattern of the reference beam [38]. The patterns of the UE (purple dashed line), reference (green line), and interference (red dotted line) beams in the azimuth plane are shown in Figure 6 [38]. In this case, the exemplary interfering beam is presented for $\Delta\alpha = 30°$.

[12]

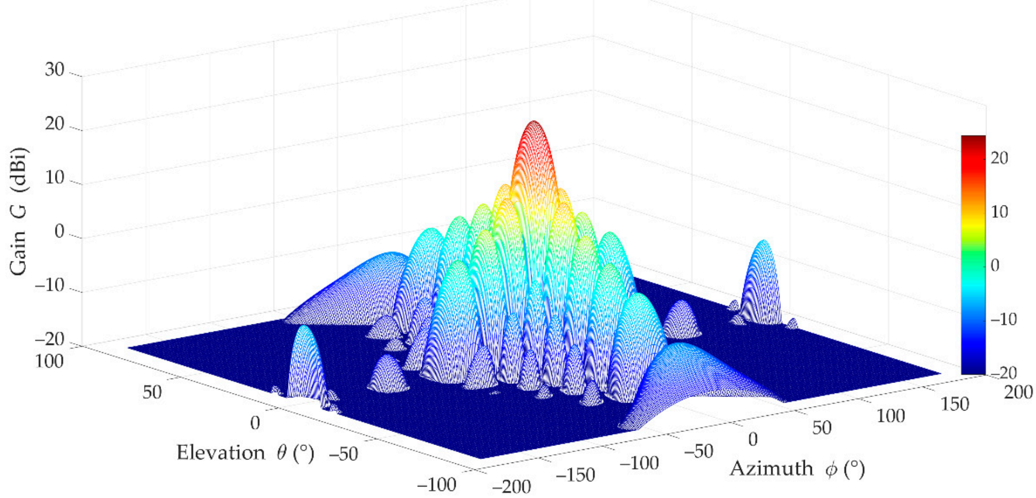

Figure 5. 3D pattern of reference beam [38].

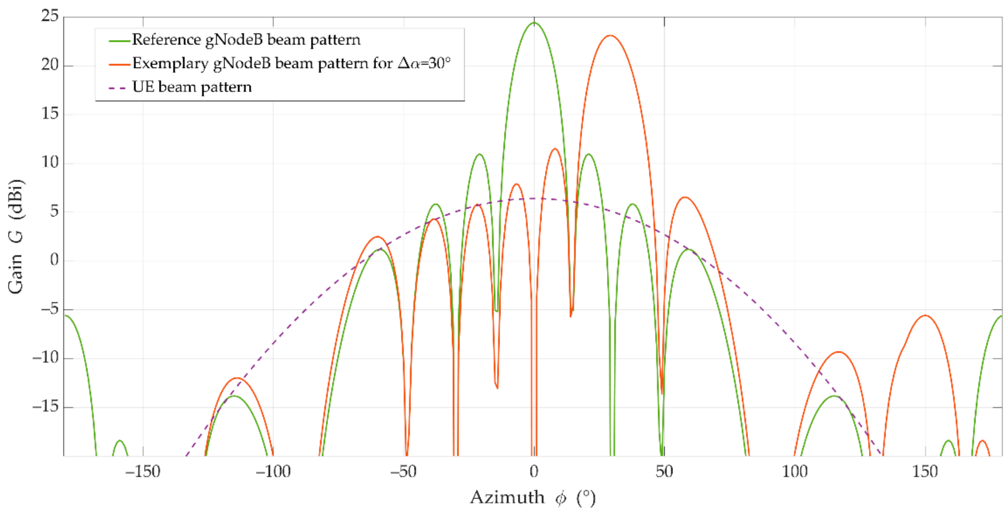

Figure 6. Patterns of users' equipment (UE), reference, and exemplary interfering beams in the azimuth plane [38].

The main simulation parameters are summarized in Table 1, whereas details of assumed channel models are as follows:

- in case of the MPM:
    - o PDPs are based on tapped-delay line (TDL) models from the 3GPP standard [28] (pp. 77–78, Tables 7.7.2-2, 7.7.2-4), i.e., TDL-D and TDL-B for LOS and NLOS conditions, respectively;
    - o these TDLs correspond an UMa scenario and normal-delay profile, i.e., rms delay spread (DS) is equal to $\sigma_\tau = 363$ ns [28] (pp. 80, Table 7.7.3-2);
    - o in the TDL-D for LOS conditions, the Rician factor is defined as $\kappa = 13.3$ dB [28] (pp. 78, Table 7.7.2-4);
    - o local scattering described by the von Mises distribution [39] with an intensity coefficient equal to $\gamma = 60$;
- in case of the 3GPP model:
    - o New Radio (NR) UMa LOS and NLOS statistical channel models with parameters from [28] (Section 7.5);
    - o Monte Carlo simulation methodology with 1000 repetitions of statistical channel model realizations.

Table 1. Main simulation parameters.

Parameter	Value
carrier frequency	3.5 GHz
distance D between gNodeB (Tx) and UE (Rx)	{100, 200, 500} m
height of gNodeB (Tx) antenna	25 m
height of UE (Rx) antenna	1.5 m
gain of single antenna element	6.4 dBi
HPBW of single antenna element	90° for H, 65° for V
spacing between antenna elements	0.5 of wavelength for H, 0.7 of wavelength for V
front to back ratio	30 dB
antenna array of gNodeB (Tx)	8 × 8
antenna array for UE (Rx)	1 × 1
range of angular separation $\Delta\alpha$ in horizontal plane between reference and interfering beams	from 0° to 60°, with step of 1°

The angular spread characteristics for the UMa channel are determined by the 3GPP [28] using the inverse Gaussian and Laplacian functions for the azimuth and zenith spreads, respectively. The mean and standard deviation values for these distributions are given in [28] (pp. 42–44, Table 7.5-6 Part-1). Therefore, the Monte Carlo simulation methodology is required to obtain a statistically representative set of results.

Two separate simulation tools have been used to obtain results for the MPM and 3GPP model. In the MPM's case, we use our own simulator developed in a MATLAB environment. It is based on analysis of propagation paths between the Tx and Rx, scattered on the multi-elliptical geometry, according to the block diagram depicted in Figure 2. Since 2015, the MPM and its simulator are developing [27,34]. In the first version, isotropic/omnidirectional pattern antennas were considered [34]. Next, we introduced the Gaussian pattern for the transmitting [35] and then for the receiving antennas [33]. In this case, the transmitting pattern is used to determine the path direction probability. In contrast, the receiving pattern is using for spatial filtering of the paths reaching to the Rx, similarly to the 3GPP model. In the last version of the simulator used in this research, we replaced the Gaussian patterns with realistic patterns based on3GPP recommendation [30]. In this case, we use the same approach as in the second simulator for the 3GPP model. The MPM simulator was validated at every stage of its evolution. In many of our papers, we showed its verification based on measurement data and comparison with other propagation models, e.g., [34,35,40]. Generating a huge number of propagation paths, we obtained an average result for the MPM based on only one simulation run. In this case, analysis of the confidence intervals of the obtained results is not possible. To achieve this aim, we have to follow an approach similar to that used in the 3GPP simulator, i.e., we must run multiple simulations for a small number of random propagation paths in accordance with the Monte Carlo process. We want to highlight that the calculation time for the Monte Carlo approach is definitely shorter for the MPM than the 3GPP simulator.

Simulation results for the 3GPP channel model have been obtained by a proprietary system-level simulator, also implemented in a MATLAB environment according to the block diagram depicted in Figure 3. A crucial part of this simulator is the implementation of the full 3D statistical channel model, as defined by the 3GPP in [28]. From the perspective of the results presented in this paper, the essential parts of the simulator used are the antenna model and fast fading models, based on Sections 7.3 and 7.5 of [28], respectively. As a UMa scenario has been assumed in this study, the most important statistical parameters of angular spread can be found in Table 7.5-6 Part-1 of [28]. This simulator is maintained and used to provide system-level simulation results as contributions to current 3GPP standardization works, as well as research studies, e.g., [37].

[12]

4.2. Results for LOS Conditions

For the above assumptions, we carried out simulation studies. Results obtained for LOS conditions are depicted in Figures 7 and 8. Graphs in Figure 7 present the SIRs versus the angle of beam separation for the various distances between the UE and gNodeB, obtained for the MPM and 3GPP model. Figure 8 shows the corresponding cumulative distribution functions (CDFs) of SIR.

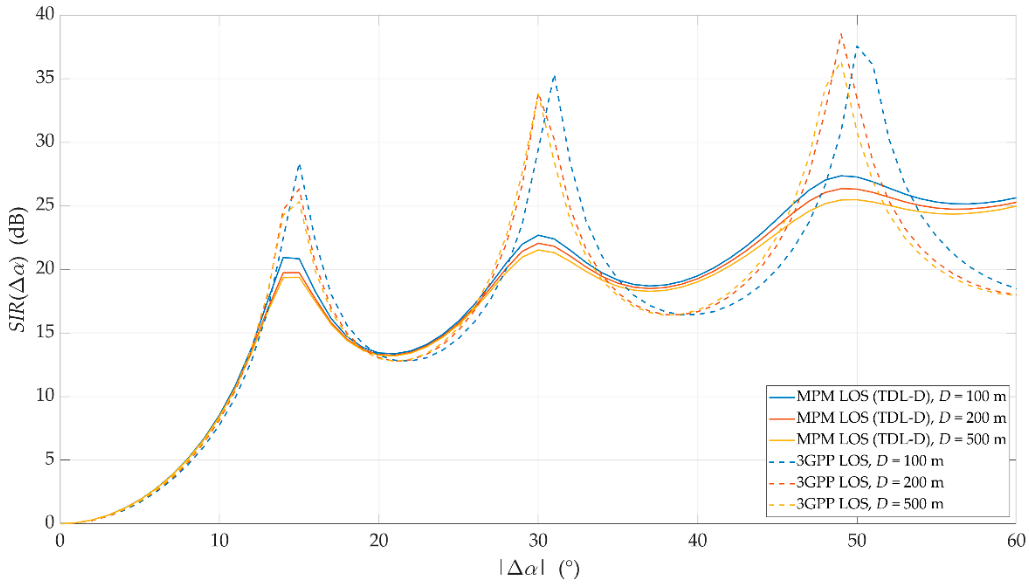

Figure 7. Signal-to-interference ratios (SIRs) versus angle of beam separation for line-of-sight (LOS) conditions and different UE–gNodeB distances obtained for the multi-elliptical propagation model (MPM) and 3GPP model.

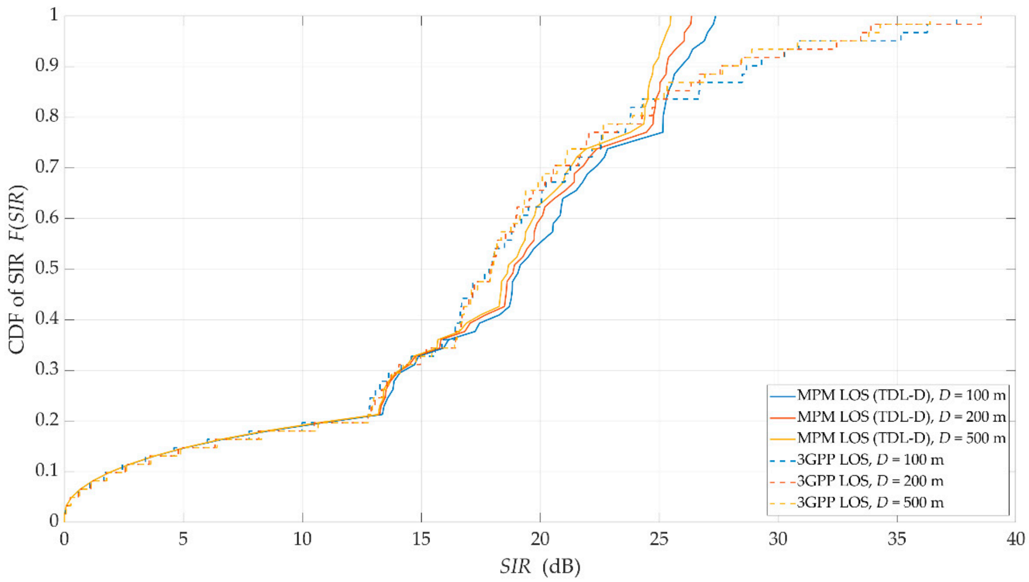

Figure 8. Cumulative distribution functions (CDFs) of SIR for LOS conditions and selected distances obtained for the MPM and 3GPP model.

As can be expected, an increase in $\Delta\alpha$ reduces the DL interference between the reference beam (providing services to the UE) and the interference beam. However, the nature of the SIR graphs is not uniform. For $\Delta\alpha \cong 15^\circ$, 30°, and 48°, there are local maxima. They are visible for both assumed channel models and result from considering side lobes in the realistic patterns of gNodeB beams. For the 3GPP channel model, the magnitudes of local maxima are noticeably higher than in the MPM. High maxima in the 3GPP model are caused by the significant difference between powers of direct and reflected multipath components, which is typical for the 3GPP LOS channel models. However, for the remaining ranges of angular separation $\Delta\alpha$, where local maxima are not present, the results obtained for the MPM and 3GPP model are comparable. The CDFs of SIR (see Figure 8) illustrate that for 80% of the analyzed range of angular separation, the results obtained by both models are within 2 dB, with half of these results within 1 dB of difference. This comparison of the LOS scenario clearly indicates that estimation of intra-cell interference and SIR with the use of the MPM demonstrates accuracy comparable with the 3GPP channel model.

To estimate intra-cell interference and SIR, the MPM only needs a single simulation instance. In contrast, the 3GPP statistical channel model requires computational power- and time-consuming Monte Carlo simulations. Taking the above facts into account, the MPM seems to be a reasonable alternative to the commonly used channel model of the 3GPP, especially if obtained simulation results are comparable.

4.3. Results for NLOS Conditions

Due to modeling of the transmission properties of the propagation environment, the 3GPP simulation test procedure is strictly statistical. On the other hand, the procedure used in the MPM is based on the PDP, which provides the creation of a geometric structure for the determined analysis of propagation paths. The DS ($\sigma_\tau = 363$ ns) is the only joint parameter that describes the transmission properties of the environment. Under LOS conditions, the signal arriving at the Rx via the direct path is the dominant component of the received signal. Hence, according to 3GPP and MPM procedures, simulation tests give us results with a similar set of values and the nature of changes. Under NLOS conditions, the 3GPP approach gives a statistical estimate of the SIR as a function of the beam separation angle and the distance from the gNodeB. In contrast, the MPM procedure is associated with specific transmission properties of the propagation environment, which define the PDP and constitute one random set of parameters in the 3GPP procedure.

For NLOS conditions, we carried out the simulation tests based on the assumptions described in Section 4.1. The obtained results are shown in Figures 9 and 10. Charts in Figure 9 depict the SIRs versus $\Delta\alpha$ for various D obtained for (a) the MPM and (b) the 3GPP model, respectively. The corresponding CDFs of SIR are illustrated in Figure 10.

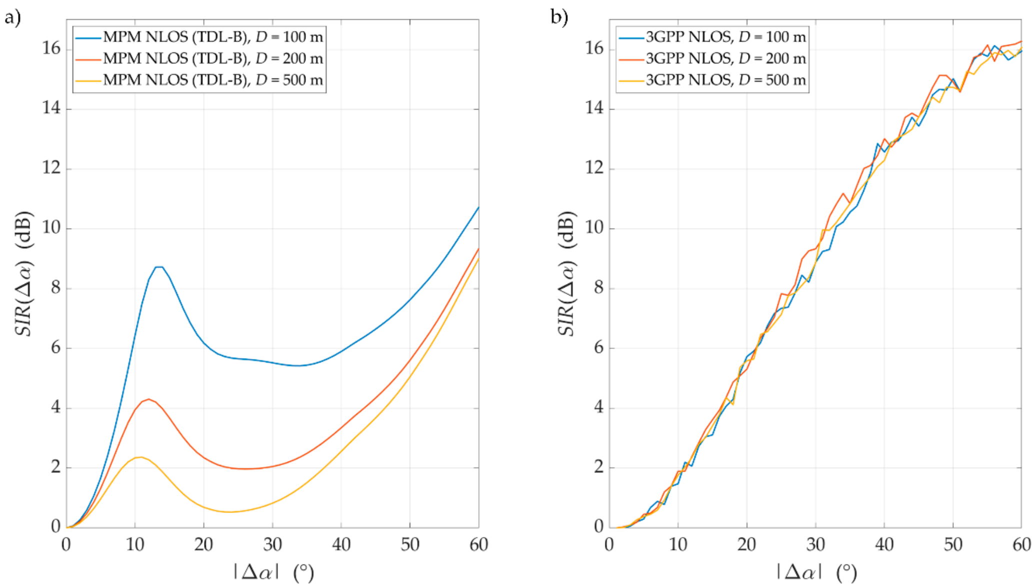

Figure 9. SIRs versus angle of beam separation for non-line-of-sight (NLOS) conditions and different distances between UE and gNodeB obtained for the (**a**) MPM and (**b**) 3GPP model.

[12]

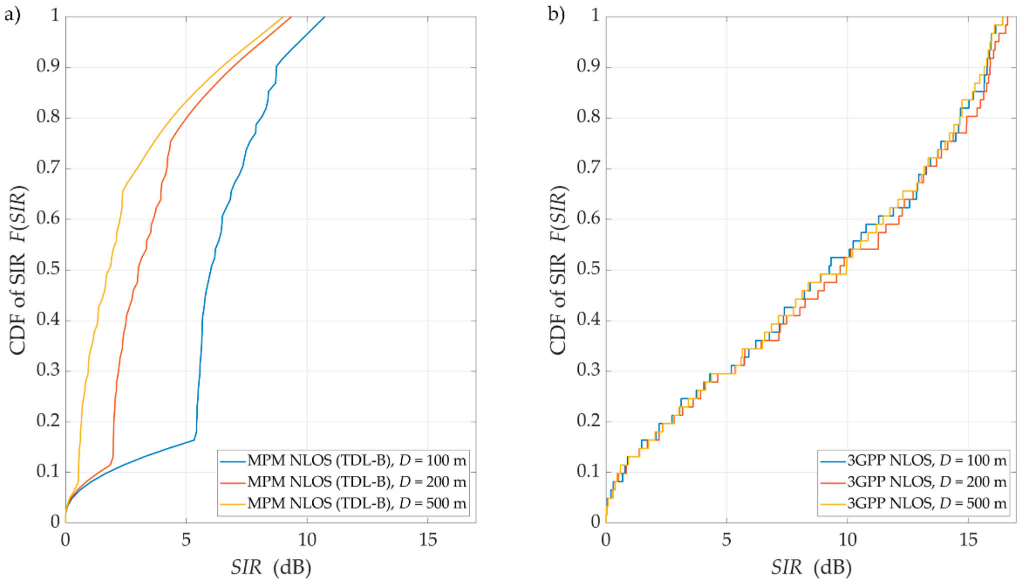

Figure 10. CDFs of SIR for NLOS conditions and selected distances obtained for (**a**) the MPM and (**b**) the 3GPP model.

As can be expected, an increase in $\Delta\alpha$ reduces the DL interference between the reference beam (providing services to the UE) and the interference beam. However, the spreading effect of the propagation environment causes significant angular dispersion in the power of the received signals. This is the reason for an increase in the level of co-channel inter-beam interference, i.e., a decrease in the SIR by about 15 dB in reference to corresponding LOS results. The results obtained in the 3GPP simulation test process show little differentiation in relation to the EU position. This effect is due to the multiple uses of averaging in the 3GPP procedure. It consists of a random selection of the transmission parameters of the propagation environment in the next simulation step. The selection randomness of these parameters is limited only by the condition of ensuring a constant the DS value.

On the other hand, use of the MPM makes it possible to assess the impact of the UE position on SIR changes. In this case, the PDP unambiguously defines the transmission environment parameters that are the basis for determining the MPM spatial structure. Thanks to this, it is possible to map the Rx position in relation to scattering element locations, which determines the individual propagation path trajectories. The simulation test results clearly indicate that estimation of the intra-cell interference and SIR with MPM use demonstrates greater detail in comparison to the 3GPP channel model [27]. Therefore, the MPM seems to be a reasonable alternative to the commonly used 3GPP channel model, especially if we want to obtain an assessment for strictly determined PDP.

It should be highlighted that the 3GPP model is currently considered a standard in the analysis of 5G systems and beyond. However, this does not mean that the results obtained by this model always faithfully reflect the simulated scenario. This may be due to differences between the modeling approaches, i.e., statistical, stochastic, geometric, or deterministic. Many models in the literature also show divergence from the 3GPP model, e.g., [41–44]. The authors of [41,42] propose models based on empirical measurements carried out in Vienna and New York, respectively, whereas ray-tracing approaches are described in [43,44]. In the last, differences in the CDFs of the received interference power are shown.

4.4. Analysis of SIR Confidence Intervals

To analyze simulation result variability, we determined the confidence intervals against the average SIRs, SIR_{avg}, presented in Sections 4.2 and 4.3. The obtained confidence intervals are depicted in Figures 11 and 12 for LOS and NLOS conditions, respectively. In

[12]

this case, considering the similarity of the results for various distances, we show the results only for $D = 100$ m.

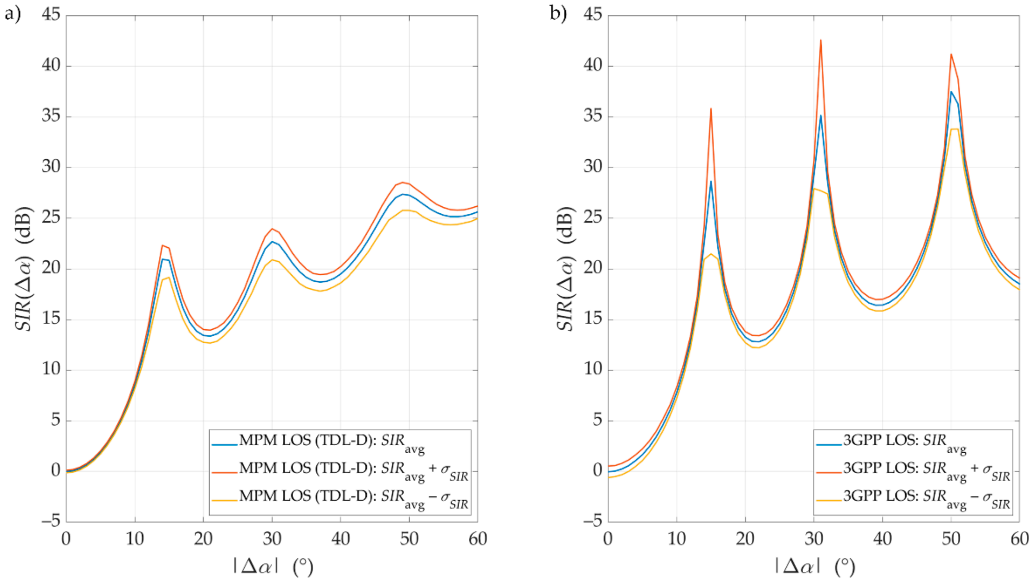

Figure 11. Exemplary SIRs with confidence intervals versus angle of beam separation for LOS conditions, *D* = 100 m, obtained for (**a**) the MPM and (**b**) the 3GPP model.

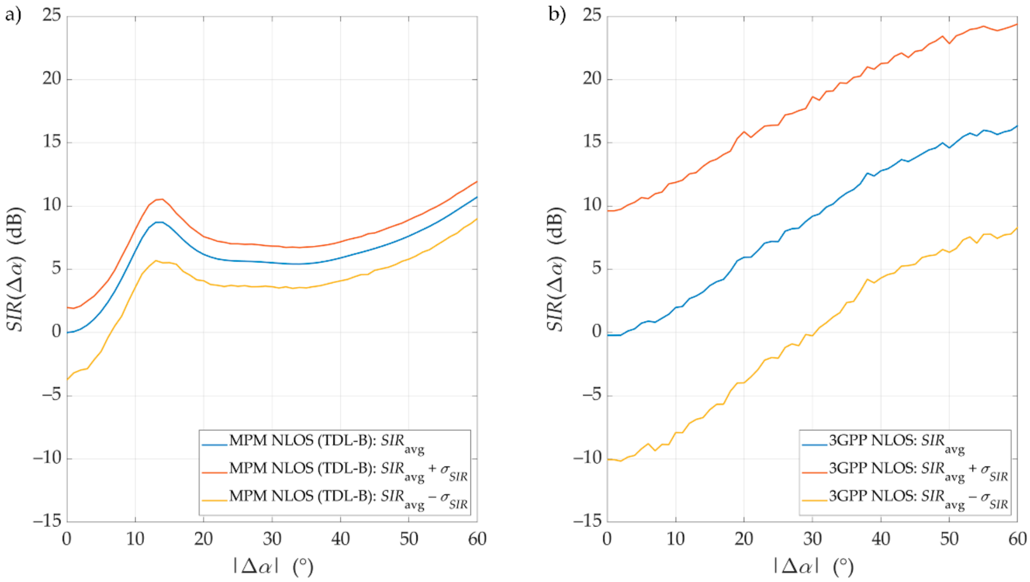

Figure 12. Exemplary SIRs with confidence intervals versus angle of beam separation for NLOS conditions, *D* = 100 m, obtained for (**a**) the MPM and (**b**) the 3GPP model.

The confidence intervals of the SIR graphs were illustrated as $SIR_{\text{avg}}(\Delta\alpha) \pm \sigma_{SIR}(\Delta\alpha)$, where $\sigma_{SIR}(\Delta\alpha)$ is a standard deviation for the selected separation angle, calculated based on 1000 values of the SIR set obtained during each Monte Carlo run. Using the Monte Carlo approach in the 3GPP simulator allows these confidential intervals to be obtained simultaneously. Average results for the MPM simulator, illustrated in previous sections, were obtained based on the so-called single-simulation mode. In this case, we used a huge number of propagation paths. To analyze the confidence intervals for these average results, we also had to run the MPM simulator in Monte Carlo mode with a small number of random propagation paths.

Generally, we may see that the MPM results fall within the ambit of the 3GPP confidence intervals. Under LOS conditions, both models' results are very convergent, as described in detail in Section 4.2. The obtained results of the confidence intervals further increase their similarity. In this case, a characteristic feature is a slight increase in the deviation with the increase in $\Delta\alpha$. Under NLOS conditions, the SIR results for the MPM fall wholly within the ambit of the confidence intervals obtained for the 3GPP model. For these propagation conditions, it is characteristic to keep the constant σ_{SIR} regardless of the separation angle.

To compare error distribution of the simulation results, we calculated the mean standard deviation, $\overline{\sigma}$, for the MPM: $\overline{\sigma}_{LOS}^{MPM} = 0.84$ dB and $\overline{\sigma}_{NLOS}^{MPM} = 1.83$ dB, and 3GPP: $\overline{\sigma}_{LOS}^{3GPP} = 0.94$ dB and $\overline{\sigma}_{NLOS}^{3GPP} = 8.91$ dB, under LOS and NLOS conditions, respectively. In this case, SIR variability may be modeled as a Gaussian random variable with a standard deviation determined by the appropriate $\overline{\sigma}$. Conversely, the average value of this random variable should be modeled using the averaged SIR described in Section 4.2 or Section 4.3. On the other hand, we can see the similarity of both simulators in their $\overline{\sigma}$ values for LOS conditions. Under NLOS conditions, the values of $\overline{\sigma}$ are definitely different. This may result from the fact that in the MPM, the scatterer locations are limited to the defined multi-elliptical structure related to the PDP. However, in the statistical 3GPP channel model, the potential positions of the scatterers are characterized by more spatial variation.

5. Conclusions

This paper focused on modeling the interference of radio DLs arising in multi-beam antenna systems, which helps to assess the performance of the mMIMO in 5G cells at network planning and optimization stages. Furthermore, we presented the comparison of two modeling methodologies that allow the DL intra-cell interference and SIR to be estimated. The presented methods of SIR evaluation were based on simulation studies. In this case, the MPM and 3GPP channel model, combined with realistic beam patterns and simulation parameters of the 3GPP/ITU, were used. The obtained results shown the effectiveness of the novel approach using the MPM in determining the minimum angular separation in multi-beam antenna arrays that provided an acceptable interference level compared with the simulation results obtained by the 3GPP channel model. Unlike the methods of inter-beam interference assessment used so far, the MPM solution proposed in this paper considers the phenomenon of the angular dispersion of received power. The ability to adapt the MPM geometric structure to actual transmission conditions minimizes SIR evaluation errors. In this, the presented novel MPM approach's utilization for assessing the interference level at the receiving point could be considered as an efficient method for the determination of the required minimum angular separation between co-channel beams of mMIMO cells. Therefore, the MPM approach might help maximize spectral efficiency in 5G networks under deployment. This statement is justified as for 80% of simulated samples of the intra-cell SIR the difference between results obtained by the MPM and commonly used 3GPP model was within 2 dB or less for LOS conditions of the UMa network operating in a 3.5 GHz band. In the case of NLOS, the difference between both channel models is more visible. This may result from the fact that in the MPM, the scatterer locations are limited to the defined multi-elliptical structure related to the PDP. Conversely, in the statistical 3GPP channel model, the potential positions of the scatterers are characterized by more spatial variation. Further studies are being conducted in which the MPM effectiveness is assessed in mmWave simulation scenarios with both DL and uplink.

Author Contributions: Conceptualization, K.B., J.M.K. and C.Z.; methodology, K.B., J.M.K. and C.Z.; software, K.B. and J.M.K.; validation, K.B. and J.M.K.; formal analysis, C.Z.; investigation, K.B. and J.M.K.; resources, K.B. and J.M.K.; data curation, K.B. and J.M.K.; writing—original draft preparation, K.B., J.M.K., C.Z. and L.N.; writing—review and editing, K.B., J.M.K., C.Z. and L.N.; visualization, J.M.K.; supervision, C.Z.; project administration, J.M.K. and C.Z.; funding acquisition, J.M.K. All authors have read and agreed to the published version of the manuscript.

Funding: This research was funded by the POLISH MINISTRY OF DEFENSE, grant number GBMON/13-996/2018/WAT on "Basic research in sensor technology field using innovative data processing methods" and grant number UGB/22-730/2020/WAT on "Impact of various propagation conditions on effectiveness of wireless communication and electronic warfare systems".

Institutional Review Board Statement: Not applicable.

Informed Consent Statement: Not applicable.

Data Availability Statement: The data presented in this study are available on request from the corresponding author. The data are not publicly available due to project restrictions.

Acknowledgments: The authors would like to express their great appreciation to the Remote Sensing Editors and anonymous Reviewers for their valuable suggestions, which have improved the quality of the paper.

Conflicts of Interest: The authors declare no conflict of interest.

References

1. Agiwal, M.; Roy, A.; Saxena, N. Next generation 5G wireless networks: A comprehensive survey. *IEEE Commun. Surv. Tutor.* **2016**, *18*, 1617–1655. [CrossRef]
2. Gupta, A.; Jha, R.K. A Survey of 5G network: Architecture and emerging technologies. *IEEE Access* **2015**, *3*, 1206–1232. [CrossRef]
3. Hemadeh, I.A.; Satyanarayana, K.; El-Hajjar, M.; Hanzo, L. Millimeter-wave communications: Physical channel models, design considerations, antenna constructions, and link-budget. *IEEE Commun. Surv. Tutor.* **2018**, *20*, 870–913. [CrossRef]
4. Geng, S.; Kivinen, J.; Zhao, X.; Vainikainen, P. Millimeter-wave propagation channel characterization for short-range wireless communications. *IEEE Trans. Veh. Technol.* **2009**, *58*, 3–13. [CrossRef]
5. Kelner, J.M.; Ziółkowski, C. Interference in multi-beam antenna system of 5G network. *Int. J. Electron. Telecommun.* **2020**, *66*, 17–23. [CrossRef]
6. Larsson, E.G.; Edfors, O.; Tufvesson, F.; Marzetta, T.L. Massive MIMO for next generation wireless systems. *IEEE Commun. Mag.* **2014**, *52*, 186–195. [CrossRef]
7. Araújo, D.C.; Maksymyuk, T.; de Almeida, A.L.F.; Maciel, T.; Mota, J.C.M.; Jo, M. Massive MIMO: Survey and future research topics. *IET Commun.* **2016**, *10*, 1938–1946. [CrossRef]
8. Ahmed, I.; Khammari, H.; Shahid, A.; Musa, A.; Kim, K.S.; Poorter, E.D.; Moerman, I. A Survey on Hybrid Beamforming Techniques in 5G: Architecture and System Model Perspectives. *IEEE Commun. Surv. Tutor.* **2018**, *20*, 3060–3097. [CrossRef]
9. Liu, W.; Weiss, S. *Wideband Beamforming: Concepts and Techniques*; Wiley: Chichester, UK, 2010; ISBN 978-0-470-71392-1.
10. Kelner, J.M.; Ziółkowski, C. Evaluation of angle spread and power balance for design of radio links with directional antennas in multipath environment. *Phys. Commun.* **2019**, *32*, 242–251. [CrossRef]
11. Rajchowski, P.; Cwalina, K.K.; Magiera, J.; Olejniczak, A.; Kosz, P.; Czapiewska, A.; Burczyk, R.; Kowalewski, K.; Sadowski, J.; Ambroziak, S. AEGIS—Mobile device for generating electromagnetic curtain for special applications and countering the threats of RCIED. *Int. J. Electron. Telecommun.* **2020**, *66*, 187–192. [CrossRef]
12. Lichtman, M.; Rao, R.; Marojevic, V.; Reed, J.; Jover, R.P. 5G NR jamming, spoofing, and sniffing: Threat assessment and mitigation. In Proceedings of the 2018 IEEE International Conference on Communications Workshops (ICC Workshops), Kansas City, MO, USA, 20–24 May 2018; pp. 1–6. [CrossRef]
13. Arjoune, Y.; Faruque, S. Smart jamming attacks in 5G New Radio: A review. In Proceedings of the 2020 10th Annual Computing and Communication Workshop and Conference (CCWC), Las Vegas, NV, USA, 6–8 January 2020; pp. 1010–1015. [CrossRef]
14. Kilzi, A.; Farah, J.; Nour, C.A.; Douillard, C. Mutual successive interference cancellation strategies in NOMA for enhancing the spectral efficiency of CoMP systems. *IEEE Trans. Commun.* **2020**, *68*, 1213–1226. [CrossRef]
15. Ali, K.S.; Elsawy, H.; Chaaban, A.; Alouini, M. Non-orthogonal multiple access for large-scale 5G networks: Interference aware design. *IEEE Access* **2017**, *5*, 21204–21216. [CrossRef]
16. Lee, H.; Park, Y.; Hong, D. Resource split full duplex to mitigate inter-cell interference in ultra-dense small cell networks. *IEEE Access* **2018**, *6*, 37653–37664. [CrossRef]
17. Elsayed, M.; Shimotakahara, K.; Erol-Kantarci, M. Machine learning-based inter-beam inter-cell interference mitigation in mmWave. In Proceedings of the ICC 2020—2020 IEEE International Conference on Communications (ICC), Dublin, Ireland, 7–11 June 2020; pp. 1–6. [CrossRef]
18. Mahmood, N.H.; Pedersen, K.I.; Mogensen, P. Interference aware inter-cell rank coordination for 5G systems. *IEEE Access* **2017**, *5*, 2339–2350. [CrossRef]
19. Fernandes, F.; Ashikhmin, A.; Marzetta, T.L. Inter-cell interference in noncooperative TDD large scale antenna systems. *IEEE J. Sel. Areas Commun.* **2013**, *31*, 192–201. [CrossRef]
20. Kim, S.; Visotsky, E.; Moorut, P.; Bechta, K.; Ghosh, A.; Dietrich, C. Coexistence of 5G with the incumbents in the 28 and 70 GHz bands. *IEEE J. Sel. Areas Commun.* **2017**, *35*, 1254–1268. [CrossRef]

[12]

21. Cho, Y.; Kim, H.-K.; Nekovee, M.; Jo, H.-S. Coexistence of 5G with satellite services in the millimeter-wave band. *IEEE Access* **2020**, *8*, 163618–163636. [CrossRef]
22. D'Andrea, C.; Buzzi, S.; Lops, M. Communications and radar coexistence in the massive MIMO regime: Uplink analysis. *IEEE Trans. Wirel. Commun.* **2020**, *19*, 19–33. [CrossRef]
23. Xu, S.; Li, Y.; Gao, Y.; Liu, Y.; Gačanin, H. Opportunistic coexistence of LTE and WiFi for future 5G system: Experimental performance evaluation and analysis. *IEEE Access* **2018**, *6*, 8725–8741. [CrossRef]
24. Xue, Q.; Li, B.; Zuo, X.; Yan, Z.; Yang, M. Cell capacity for 5G cellular network with inter-beam interference. In Proceedings of the 2016 IEEE International Conference on Signal Processing, Communications and Computing (ICSPCC), Hong Kong, China, 5–8 August 2016; pp. 1–5. [CrossRef]
25. Hong, H.; Choi, S.W.; Kim, C.S.; Chong, Y.J. Interference measurement between 3.5 GHz 5G system and radar. In Proceedings of the 2018 International Conference on Information and Communication Technology Convergence (ICTC), Jeju, Korea, 17–19 October 2018; pp. 1539–1541. [CrossRef]
26. Elgendi, H.; Mäenpää, M.; Levanen, T.; Ihalainen, T.; Nielsen, S.; Valkama, M. Interference measurement methods in 5G NR: Principles and performance. In Proceedings of the 2019 16th International Symposium on Wireless Communication Systems (ISWCS), Oulu, Finland, 27–30 August 2019; pp. 233–238. [CrossRef]
27. Kelner, J.M.; Ziółkowski, C. Multi-elliptical geometry of scatterers in modeling propagation effect at receiver. In *Antennas and Wave Propagation*; Pinho, P., Ed.; IntechOpen: London, UK, 2018; pp. 115–141, ISBN 978-953-51-6014-4.
28. *Study on Channel Model for Frequencies from 0.5 to 100 GHz*; Tech. Rep. 3GPP TR 38.901 V16.1.0 (2019-12), Release 16; 3rd Generation Partnership Project (3GPP); Technical Specification Group Radio Access Network: Valbonne, France, 2019.
29. *Evolved Universal Terrestrial Radio Access (E-UTRA) and Universal Terrestrial Radio Access (UTRA); Radio Frequency (RF) Requirement Background for Active Antenna System (AAS) Base Station (BS)*; Tech. Rep. 3GPP TR 37.842 V13.3.0 (2019-12), Release 13; 3rd Generation Partnership Project (3GPP): Valbonne, France, 2019.
30. SWG Sharing Studies. In *Working Document on Characteristics of Terrestrial Component of IMT for Sharing and Compatibility Studies in Preparation for WRC-23*; Document 5D/TEMP/228-E; International Telecommunication Union (ITU), Radiocommunication Study Groups: Geneva, Switzerland, 2020.
31. Bechta, K.; Rybakowski, M.; Du, J. Impact of effective antenna pattern on millimeter wave system performance in real propagation environment. In Proceedings of the 2019 13th European Conference on Antennas and Propagation (EuCAP), Krakow, Poland, 31 March–5 April 2019; pp. 1–5.
32. Bechta, K.; Rybakowski, M.; Du, J. Efficiency of antenna array tapering in real propagation environment of millimeter wave system. In Proceedings of the 2019 13th European Conference on Antennas and Propagation (EuCAP), Krakow, Poland, 31 March–5 April 2019; pp. 1–4.
33. Ziółkowski, C.; Kelner, J.M. Statistical evaluation of the azimuth and elevation angles seen at the output of the receiving antenna. *IEEE Trans. Antennas Propag.* **2018**, *66*, 2165–2169. [CrossRef]
34. Ziółkowski, C.; Kelner, J.M. Geometry-based statistical model for the temporal, spectral, and spatial characteristics of the land mobile channel. *Wirel. Pers. Commun.* **2015**, *83*, 631–652. [CrossRef]
35. Ziółkowski, C.; Kelner, J.M. Antenna pattern in three-dimensional modelling of the arrival angle in simulation studies of wireless channels. *IET Microw. Antennas Propag.* **2017**, *11*, 898–906. [CrossRef]
36. Vaughan, R.; Bach Andersen, J. *Channels, Propagation and Antennas for Mobile Communications*; IET Electromagnetic Waves Series; Institution of Engineering and Technology: London, UK, 2003; ISBN 978-0-86341-254-7.
37. Bechta, K.; Du, J.; Rybakowski, M. Rework the radio link budget for 5G and beyond. *IEEE Access* **2020**, *8*, 211585–211594. [CrossRef]
38. Bechta, K.; Ziółkowski, C.; Kelner, J.M.; Nowosielski, L. Downlink interference in multi-beam 5G macro-cell. In Proceedings of the 2020 23rd International Microwave and Radar Conference (MIKON), Warsaw, Poland, 5–8 October 2020; pp. 140–143. [CrossRef]
39. Abdi, A.; Barger, J.A.; Kaveh, M. A Parametric model for the distribution of the angle of arrival and the associated correlation function and power spectrum at the mobile station. *IEEE Trans. Veh. Technol.* **2002**, *51*, 425–434. [CrossRef]
40. Ziółkowski, C.; Kelner, J.M. Estimation of the reception angle distribution based on the power delay spectrum or profile. *Int. J. Antennas Propag.* **2015**, *2015*, e936406. [CrossRef]
41. Ademaj, F.; Taranetz, M.; Rupp, M. 3GPP 3D MIMO channel model: A holistic implementation guideline for open source simulation tools. *EURASIP J. Wirel. Commun. Netw.* **2016**, *2016*, 55. [CrossRef]
42. Rappaport, T.S.; Sun, S.; Shafi, M. Investigation and comparison of 3GPP and NYUSIM channel models for 5G wireless communications. In Proceedings of the 2017 IEEE 86th Vehicular Technology Conference (VTC-Fall), Toronto, ON, Canada, 24–27 September 2017; pp. 1–5. [CrossRef]
43. Almesaeed, R.; Ameen, A.S.; Mellios, E.; Doufexi, A.; Nix, A.R. A proposed 3D extension to the 3GPP/ITU channel model for 800 MHz and 2.6 GHz bands. In Proceedings of the 2014 8th European Conference on Antennas and Propagation (EuCAP), Hague, The Netherlands, 6–11 April 2014; pp. 3039–3043. [CrossRef]
44. Sheikh, M.U.; Jäntti, R.; Hämäläinen, J. Performance comparison of ray tracing and 3GPP street canyon model in microcellular environment. In Proceedings of the 2020 27th International Conference on Telecommunications (ICT), Bali, Indonesia, 5–7 October 2020; pp. 1–5. [CrossRef]

sensors

MDPI

Article

Inter-Beam Co-Channel Downlink and Uplink Interference for 5G New Radio in mm-Wave Bands †

Kamil Bechta [1], Jan M. Kelner [2,*], Cezary Ziółkowski [2] and Leszek Nowosielski [2]

[1] Nokia Solutions and Networks, 54-130 Wrocław, Poland; kamil.bechta@nokia.com
[2] Institute of Communications Systems, Faculty of Electronics, Military University of Technology, 00-908 Warsaw, Poland; cezary.ziolkowski@wat.edu.pl (C.Z.); leszek.nowosielski@wat.edu.pl (L.N.)
* Correspondence: jan.kelner@wat.edu.pl; Tel.: +48-261-839-517

† The paper is an extended version of our paper published in Bechta, K.; Ziółkowski, C.; Kelner J.M.; Nowosielski, L. Downlink interference in multi-beam 5G macro-cell. In Proceedings of the 2020 23rd International Microwave and Radar Conference (MIKON), Warsaw, Poland, 5–8 October 2020; pp. 140–143, doi:10.23919/MIKON48703.2020.9253919.

Abstract: This paper presents a methodology for assessing co-channel interference that arises in multi-beam transmitting and receiving antennas used in fifth-generation (5G) systems. This evaluation is essential for minimizing spectral resources, which allows for using the same frequency bands in angularly separated antenna beams of a 5G-based station (gNodeB). In the developed methodology, a multi-ellipsoidal propagation model (MPM) provides a mapping of the multipath propagation phenomenon and considers the directivity of antenna beams. To demonstrate the designation procedure of interference level we use simulation tests. For exemplary scenarios in downlink and uplink, we showed changes in a signal-to-interference ratio versus a separation angle between the serving (useful) and interfering beams and the distance between the gNodeB and user equipment. This evaluation is the basis for determining the minimum separation angle for which an acceptable interference level is ensured. The analysis was carried out for the lower millimeter-wave band, which is planned to use in 5G micro-cells base stations.

Keywords: wireless mobile communications; 5G; millimeter-wave; multi-beam antenna system; wireless downlink and uplink; co-channel interference; signal-to-interference ratio; multi-ellipsoidal propagation model; simulation studies

Citation: Bechta, K.; Kelner, J.M.; Ziółkowski, C.; Nowosielski, L. Inter-Beam Co-Channel Downlink and Uplink Interference for 5G New Radio in mm-Wave Bands. *Sensors* **2021**, *21*, 793. https://doi.org/10.3390/s21030793

Academic Editors: Waqas Khalid, Heejung Yu, Rehmat Ullah and Rashid Ali

Received: 19 December 2020
Accepted: 20 January 2021
Published: 25 January 2021

1. Introduction

This paper focuses on a methodology for assessing co-channel interference occurring in fifth-generation (5G) networks, in which a directional wireless link is one of the key techniques [1,2]. To this aim, especially in frequency bands below 6 GHz, 5G new radio (NR) base stations (gNodeBs) use multi-beam antenna systems based on massive multiple-input-multiple-output (massive-MIMO) technology, which is enabled by digital beamforming [3,4]. This solution reduces the energy expenditure due to the high gain and narrow width of the beams. The needed increase in the radio link capacity is obtained thanks to an energy balance improvement. On the other hand, massive-MIMO ensures the efficient use of spectral resources. An appropriate angular separation between individual beams makes it possible to use the same frequency channels. However, the minimization of spectral resources offered by this technology is associated with the need to assess the interplay of signals received by individual beams. In the millimeter-waves (mmWaves) frequency range, where early implementations of 5G are based on analog beamforming, the multi-beam transmissions inside a single cell sector are obtained by multiple sub-arrays, which constitute the full antenna array. Each of these sub-arrays is connected to individual transmission–reception chain and enables the simultaneous generation of multiple beams. Hitherto, evaluation methodologies of co-channel interference mainly concerned omnidirectional and sectoral antennas and homogeneous environments, e.g., [5–7]. From the viewpoint of 5G systems that use mmWaves, massive-MIMO, and beamforming, such analysis should consider narrow beams of antenna systems. Examples of such studies are presented in [8–11]. On the other hand, the analysis of co-channel interference is essential to assessing the coexistence and compatible functioning of different radio systems. The importance of this problem is presented in [9]. Besides, many new procedures in massive-MIMO and beamforming systems that increase the efficiency of 5G require assessing the level of interference between the antenna beams to and from individual users. The partial-nulling based statistical beamforming is an example of such a procedure, the use of which is based on the division of all users into two groups with a significantly different degree of spatial correlation [12]. The solution presented in [13] is another example that increases the spectral efficiency in massive-MIMO systems. These selected examples show the importance of assessing the level of interference between the beams of the antenna system from other users in developing and implementing new solutions.

The utilization of narrow beams and the dominance of the multipath propagation phenomenon in urban areas significantly change interference analysis methods. In this case, the practical used method of the interference assessment is based on simulation tests. Parameters of transmitted and received signals as well as their statistical properties for various types of propagation environments are input for these studies. The 3rd Generation Partnership Project (3GPP) standard [14] is commonly used for this aim. This approach recommends using deterministic cluster delay lines (CDLs) for link-level simulations, where average angles of departure (AODs) and arrival (AOAs), in addition to tapped delay line (TDL), are defined. For system-level simulations, where a statistical approach is more appropriate, the 3GPP standard [14] recommends the full three-dimensional (3D) modeling of a radio channel.

The interference topic is widely represented in the literature. On the one hand, there are works on counteracting interference in the emerging and future systems. Examples include software algorithms and hardware solutions aimed at interference cancellation [15], mitigation [16], or awareness [17,18]. In this case, the currently proposed solutions are mainly dedicated to multi-antenna systems. On the other hand, papers focusing on the interference evaluation and measurement [19] methodologies are presented. In general, the interference analysis can be performed at any distance from the signal source antenna. In the case of a near-field, the influence between the individual elements of the multi-antenna system can be investigated [20–24]. In the case of a far-field, inter-beam [25,26], inter-cell [18,26,27], or inter-system interferences, i.e., the coexistence of different systems and networks [9,11,28], might be studied. In the literature, the vast majority of scientific works concern coexistence topic and the inter-cell interference assessment, rather than inter-beam interference.

In this paper, we present a methodology for assessing co-channel interference that is resulting from the utilization of the same frequency channels in different beams of the gNodeB antenna system. To evaluate the signal-to-interference ratio (SIR), we use simulation tests that are based on a 3D multi-ellipsoidal propagation model (MPM) [29–31]. However, the proposed methodology differs from the simulation approach recommended by the 3GPP standard for link-level evaluations. In our methodology, using the MPM as a geometry-based model (GBM) provides a statistical SIR metric in contrast to the 3GPP approach with the pre-determined AODs and AOAs. In our solution, the knowledge of spatial parameters such as the average AODs and AOAs of propagation paths is not required to obtain results and the use of any power delay profile (PDP) or the TDL makes it possible to adapt this model to any propagation scenarios. The use of the MPM and antenna radiation patterns allow determining a power angular spectrum (PAS) of the received signals. The obtained PASs are the basis for the SIR assessment in the multi-beam antenna system. The MPM geometry is constructed based on the PDP or TDL, which describe the transmission properties of a propagation environment. This original way of mapping the effects of propagation phenomena enables obtaining a fully statistical

[13]

SIR evaluation. It ensures a relationship of simulation results with the analyzed type of propagation environment. The presented analysis is an extension of the paper [32], which focused only on the downlink (DL) interference in multi-beam 5G macro-cell for 3.5 GHz band and under non-line-of-sight (NLOS) conditions. In that case, we used a two-dimensional multi-elliptical model [31]. In this study, based on the 3D MPM, we discuss the inter-beam co-channel interference in DL and additionally uplink (UL) for 28 GHz band, under line-of-sight (LOS) and NLOS conditions. Using the 3D MPM to modeling the inter-beam interference level testifies to the novelty of the presented approach. In this case, an original approach to the UL interference assessment was proposed, taking path loss corrections into account, compared to the DL scenario [32] shown previously.

The mutual configuration of the transmitting and receiving antenna beams is not only the factor considered in our methodology. The presented solution of the SIR determination also provides a mapping of the propagation environment influence on the PAS of the received signals. The 3GPP methodology also takes this impact into account. However, it is limited to well-defined types of environments that are defined based on the determined channel characteristics and distributions of channel parameters. In the case of the MPM methodology presented in this paper, we have the option to assess the SIR for any type of propagation environment, whose transmission properties are defined by an appropriate PDP. This fact significantly distinguishes the developed method and proves its originality.

The remainder of the paper is organized as follows: Section 2 shows the construction way of the MPM geometry based on the transmission properties of the propagation environment, i.e., the TDL. The essence of the PAS determination procedure and then the SIR assessment is presented in Section 3. In Sections 4 and 5, the description of the analyzed scenarios for the DL and UL transmissions and the results of simulation studies are drawn. Section 6 contains conclusions.

2. Multi-Ellipsoidal Propagation Model

In 5G networks, designing wireless links with narrow beams and beamforming technology enforces the use of GBMs. It is particularly important in relation to urbanized areas. In this case, there is a large directional variation in the received powers. The use of GBMs ensures the spatial power distribution in the vicinity of the receiving antenna. In combination with the narrow beam patterns, this approach gives the possibility of a statistical evaluation of the transmission properties of the wireless link. The MPM is one of the GBMs. The set of confocal ellipsoids forms its geometrical structure representing the potential locations of the scattering elements for an emitted radio wave. In the foci of the ellipsoids, a transmitter (Tx) and receiver (Rx) are located. In propagation scenarios, where the Tx and Rx are on the Earth's surface, the MPM structure is represented by a set of semi-ellipsoids, as shown in Figure 1 [31].

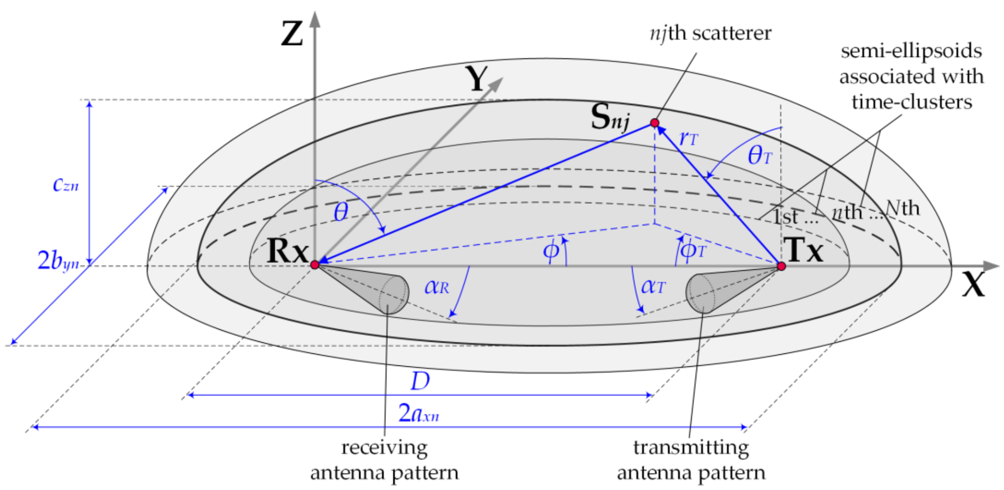

Figure 1. MPM geometrical structure considering Earth surface.

The MPM geometrical structure is closely related to the transmission properties of the propagation environment, which may be described by the PDP or TDL. In multipath environments, we can observe the occurrence of several or a dozen taps or local extremes in the TDLs or PDPs, respectively. It means that as a result of scattering on terrain obstacles, the electromagnetic wave reaches the Rx by different propagation paths but with the same delays τ_n for $n = 1, 2, \ldots, N$ [33]. Thus, based on the properties of geometrical figures, the most probable locations of the scattering elements form an ellipsoid. Of course, the number of ellipsoids is equal to the number N of time-clusters representing the taps or local extremes in the TDL or PDP, respectively. If the distance between the Tx and Rx is equal to D, then the parameters of individual ellipsoids such as a major, a_{xn}, and minor semi-axes b_{yn}, c_{zn} describe the following relationships:

$$a_{xn} = \frac{1}{2}(c\tau_n + D), \tag{1}$$

$$b_{yn} = c_{zn} = \frac{1}{2}\sqrt{c\tau_n(c\tau_n + 2D)}, \tag{2}$$

where c denotes the speed of light.

The geometrical structure of the MPM is described in detail in [29–31]. The 3D MPM may be reduced to the 2D multi-elliptical model, where propagation phenomena in the azimuth plane are dominant [31]. For this modeling procedure in relation to other GBMs, minimizing the estimation error of the PAS is shown in [34]. In the MPM, the phenomenon of local scattering around the transmitting and receiving antennas is also included. In this case, the AOAs of propagation paths are generated based on the 2D von Mises distribution [29,35]:

$$\begin{array}{c} f_0(\theta,\phi) = C_0 \frac{\exp(\gamma_\theta \cos(90^\circ - \theta))}{2\pi \mathrm{I}_0(\gamma_\theta)} \cdot \frac{\exp(\gamma_\phi \cos\phi)}{2\pi \mathrm{I}_0(\gamma_\phi)} \\ \text{for } \theta \in \langle 0, 90^\circ) \text{ and } \phi \in \langle -180^\circ, 180^\circ), \end{array} \tag{3}$$

where (θ, ϕ) is AOA in the elevation and azimuth planes, respectively, γ_θ and γ_ϕ define the angular dispersion of the components in the elevation and azimuth planes, respectively, $\mathrm{I}_0(\cdot)$ is the zero-order modified Bessel function of the imaginary argument, and C_0 represents the normalizing constant such that $\frac{C_0}{2\pi \mathrm{I}_0(\gamma_\theta)} \int_0^{90^\circ} \exp(\gamma_\theta \cos(90^\circ - \theta)) d\theta = 1$.

3. Evaluation of Co-Channel Interference in Multi-Beam Antenna

The co-channel interference assessment is based on the SIR measure defined as:

$$SIR = \frac{P_S}{P_I}\left(\frac{\mathrm{W}}{\mathrm{W}}\right) \quad \leftrightarrow \quad SIR(\mathrm{dB}) = P_S(\mathrm{dBm}) - P_I \ (\mathrm{dBm}), \tag{4}$$

where P_S and P_I are the powers of the serving and interfering signal, respectively, which occur at the output of the receiving antenna. In the multi-beam receiving antenna, the interference signal is from a wireless link whose receiving antenna beam is formed in the same frequency band as the serving beam. From the SIR definition, it follows that the main problem of assessing this measure relies on determining P_S and P_I. Note that these powers can be calculated based on the appropriate PASs, $p_{S,I}(\theta, \phi)$, which are seen at the output of the receiving antenna, namely:

$$P_{S,I} = \iint_{(\theta,\phi)} p_{S,I}(\theta, \phi) d\theta d\phi. \tag{5}$$

However, these distributions depend on the power pattern of the serving beam [30]:

$$p_{S,I}(\theta, f) = \widetilde{p}_{S,I}(\theta, f) |g(\theta, f)|^2, \tag{6}$$

where $\widetilde{p}_{S,I}(\theta,\phi)$ represent the PASs in the vicinity of the receiving antenna and $|g(\theta,\phi)|^2$ is the normalized power pattern of the receiving antenna.

Hence, it follows that the problem of the SIR assessment boils down to determining $\widetilde{p}_{S,I}(\theta,\phi)$. The developed methodology uses simulation tests to determine these PASs. The input data for simulation procedures that condition the estimation of $\widetilde{p}_{S,I}(\theta,\phi)$ is a set of the following parameters and characteristics:

- normalized power patterns $|g_S(\theta_T,\phi_T)|^2$, $|g_I(\theta_T,\phi_T)|^2$, and $|g(\theta,\phi)|^2$, of the serving and interfering transmitting and receiving beams, respectively, where (θ_T,ϕ_T) denotes AOD in the elevation and azimuth planes, respectively;
- gains G_S, G_I, and G of the serving and interfering transmitting and receiving beams, respectively;
- the Tx-Rx distances, i.e., D_S and D_I between the serving and interfering mobile stations (user equipment, i.e., UE-S and UE-I) and gNodeB for the UL scenario, respectively, or $D_S = D_I = D$ for the DL scenario;
- the type of propagation environment defined by the TDL or PDP and rms delay spread.
- Estimation of $\widetilde{p}_{S,I}(\theta,\phi)$ consists in the generation of a set of propagation paths departing from the transmitting antennas of the serving and interfering links and their transformation in a system composed of the semi-ellipsoid set. The generation procedure of AODs, (θ_T,ϕ_T), uses the properties of the normalized power radiation patterns [36]:

$$\frac{1}{4\pi}\iint\limits_{(\theta_T,\phi_T)} |g_{S,I}(\theta_T,\phi_T)|^2 \sin\theta_T d\theta_T d\phi_T = 1. \tag{7}$$

The function under integral is non-negative. Therefore, the normalized power radiation patterns meet the axioms of a probability density function. Hence, we can express the distribution of AOD as [36]:

$$f_{S,I}(\theta_T,\phi_T) = \frac{1}{4\pi}|g_{S,I}(\theta_T,\phi_T)|^2 \sin\theta_T. \tag{8}$$

The geometry structure of the MPM represents the statistical locations of the scattering elements. Thus, the intersection of the radiated path with individual semi-ellipses indicates the scattering places of this path. Knowing the AODs, (θ_T,ϕ_T), of radiated propagation paths, we can determine for each of them the radial coordinate r_T in a spherical system with an origin in the Tx (UE-S or UE-I). For the selected time-cluster (ellipsoid), this coordinate is described by [29]:

$$r_T = -\frac{1}{2a}b_y^2 D\sin\theta_T\cos\phi_T + \frac{1}{2a}\sqrt{\left(b_y^2 D\sin\theta_T\cos\phi_T\right)^2 + 4ab_y^2\left(a_x^2 - \frac{D^2}{4}\right)}, \tag{9}$$

where $a = \left(b_y\sin\theta_T\cos\phi_T\right)^2 + a_x^2\left(\cos^2\theta_T + (\sin\theta_T\sin\phi_T)^2\right)$.

Appropriate coordinate transformation resulting from translation the system origin to the Rx allows determining AOA, (θ,ϕ), for propagation paths reaching the Rx [29]:

$$\theta = \arctan\frac{\sqrt{(r_T\sin\theta_T\cos\phi_T + D)^2 + (r_T\sin\theta_T\sin\phi_T)^2}}{r_T\cos\theta_T}, \tag{10}$$

$$\phi = \arctan\frac{r_T\sin\theta_T\sin\phi_T}{r_T\sin\theta_T\cos\phi_T + D}. \tag{11}$$

In addition to the AOAs of propagation paths reaching the Rx with delays, the local scattering paths are also included. In this case, the AOAs are generated using the von Mises distribution described by Equation (3).

Powers $\widetilde{p}$ of individual paths are determined based on the PDP or TDL. To generate these powers, we use exponential distributions, $f(\widetilde{p})$, whose parameters (i.e., mean values p_n for $n = 1, 2, \ldots, N$) are equal to powers of the taps or local extremes occurring in the TDL or PDP, respectively:

$$f(\widetilde{p}) = \begin{cases} \frac{1}{p_n} \exp\left(\frac{\widetilde{p}}{p_n}\right) & \text{for} \quad \widetilde{p} \geq 0, \\ 0 & \text{for} \quad \widetilde{p} < 0, \end{cases} \tag{12}$$

where p_n is the nth local extreme of the PDP (or nth tap value of the TDL), which corresponds to the propagation paths reaching from the nth semi-ellipsoid, i.e., with the delay τ_n.

As a simulation result, we get the set of $\{(\theta, \phi, \widetilde{p})\}$ that enables estimating $\widetilde{p}_{S,I}(\theta, \phi)$ [29]. Additional multiplication of each $\widetilde{p}$ value by the appropriate value of $|g(\theta, \phi)|^2$ gives us the set of $\{(\theta, \phi, p)\}$, which is the basis for estimating $p_{S,I}(\theta, \phi)$. A detailed description of the practical implementation of the estimation procedure is provided in [30]. As a result, we can determine P_S and P_I based on Equation (5).

For the DL scenario, the SIR may be calculated based on Equation (4), because the serving and interfering beams are generated by the same gNodeB, i.e., $D_S = D_I = D$. However, for the UL scenario, the SIR assessment requires additional consideration of attenuation resulted from a difference in the distances between the gNodeB and UE-S or UE-I. Considering this fact, we have:

$$SIR = \frac{P_S}{P_I} \Delta PL \quad \leftrightarrow \quad SIR(\mathrm{dB}) = P_S(\mathrm{dBm}) - P_I \ (\mathrm{dBm}) + \Delta PL(\mathrm{dB}) \tag{13}$$

where:

$$\Delta PL = \frac{PL(D_S)}{PL(D_I)} \quad \leftrightarrow \quad \Delta PL(\mathrm{dB}) = PL(D_S)(\mathrm{dB}) - PL(D_I) \ (\mathrm{dB}) \tag{14}$$

represents the relationship between attenuation of propagation environment for different distances, $PL(D_S)$ and $PL(D_I)$ are path losses for the wireless links between the UE-S or UE-I and gNodeB, respectively. For assessing ΔPL, we use a close-in free space reference distance path loss model presented in [37]. To take the influence of variable weather conditions into account that are related to atmospheric precipitation, the used path loss model should be corrected based on ITU-R recommendations [38,39] or other approaches proposed in the literature, e.g., [40,41].

Generally, the proposed methodology of the interference evaluation consists of the following stages:

- defining the scenario parameters,
- determining the MPM parameters,
- determining the PASs for the serving and interfering links based on simulation studies,
- calculating the powers for the determined PASs,
- calculating the SIR finally.

4. Assumptions and Scenarios of Simulation Studies

The aim of the simulation tests is to present a method of modeling and assessing the co-channel interference that arises in the radio link with a multi-beam antenna system. The studies focused on determining the SIR relationship on the separation angle $\Delta\alpha$ and changes in the distance D (or distances D_S and D_I) between the UEs and gNodeB. The simulations were carried out for carrier frequency of 28 GHz, typical for the 5G micro- and pico-cells, where multiple sub-arrays and beamforming technologies are planned for implementation. Besides, we considered two scenarios for the DL and UL, which are illustrated in Figures 2 and 3, respectively.

[13]

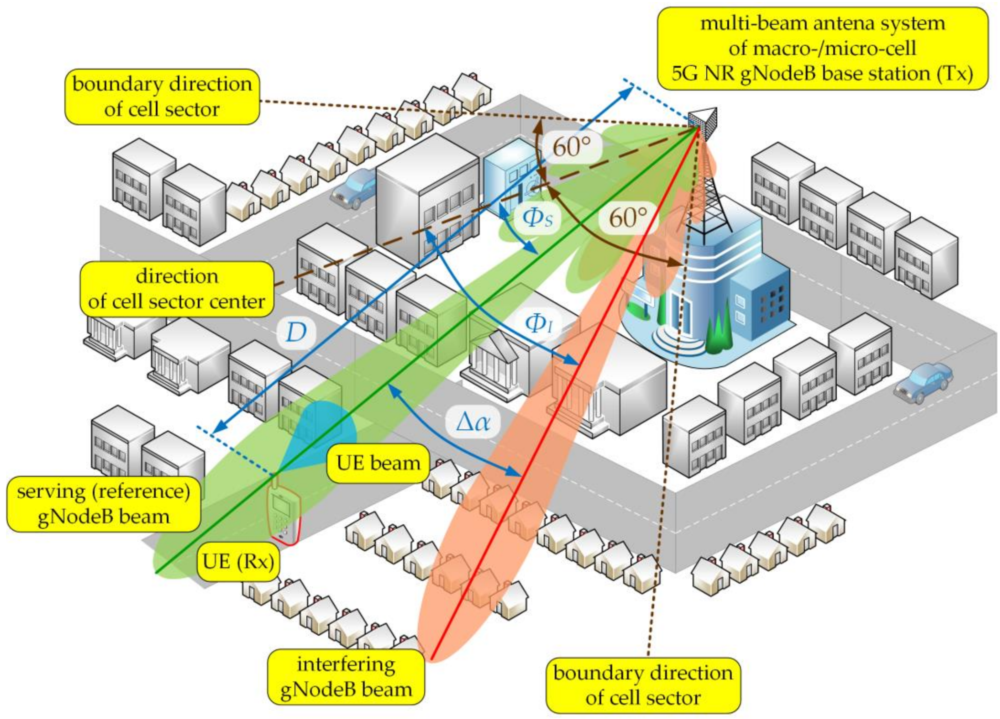

Figure 2. DL spatial scenario of simulation studies [32].

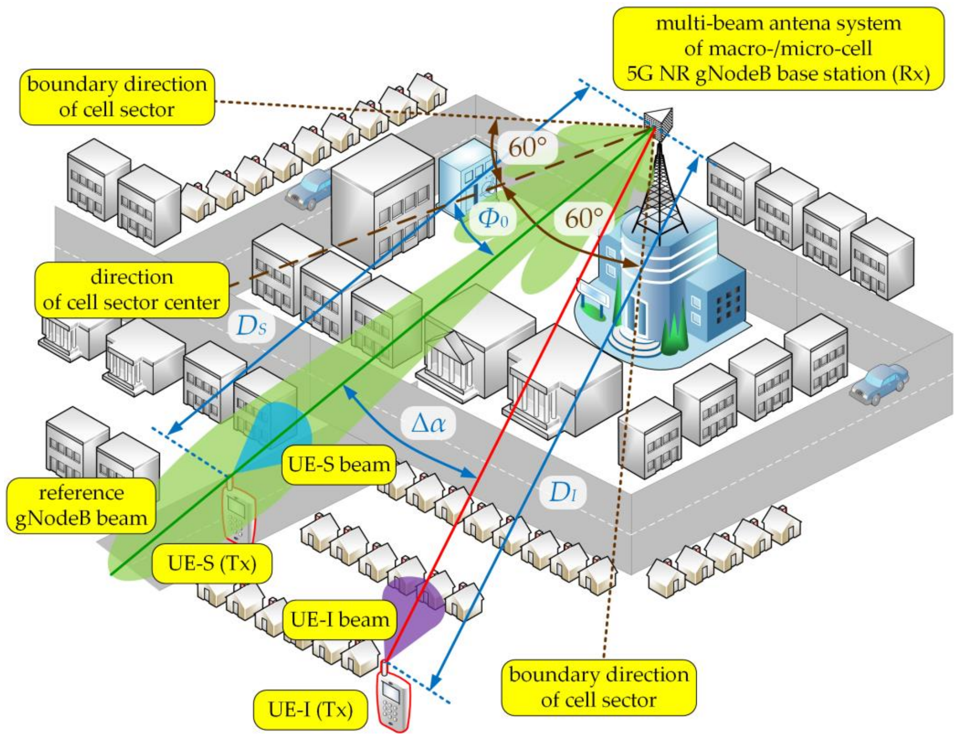

Figure 3. UL spatial scenario of simulation studies.

In the DL scenario, we assumed that the gNodeB was generating two beams (serving and interfering) in the selected sector that were operating in the same sub-band (frequency channel). Thus, the SIR assessment came down to determining P_S and P_I powers induced in the UE antenna that come from the signals generated by the serving and interfering beams of the gNodeB, respectively. The distances between the gNodeB (Tx) and UE (Rx) was equal to D. Besides, the serving (reference) gNodeB and UE beams were aligned, i.e., directed to each other ($\alpha_{TS} = 0$ and $\alpha_R = 0$, see Figure 1). In relation to the direction of the cell sector center, the reference and interfering gNodeB beams are oriented in Φ_S and Φ_I directions, respectively (see Figure 2). Thus, the separation angle of the beams is defined as:

$$\Delta\alpha = \Phi_S - \Phi_I, \tag{15}$$

Then the interfering beam orientation in relation to the Tx-Rx direction was equal to $\alpha_{TI} = \Delta\alpha$.

A similar scenario was taken into account for the UL transmission depicted in Figure 3. In this case, the analyzed gNodeB beam served one subscriber (UE-S) in its area, while another subscriber (UE-I) generated interferences towards this gNodeB beam. The UE-S and UE-I beams (Tx) were oriented to the gNodeB (Rx), i.e., $\alpha_{TS} = \alpha_{TI} = 0$ (see Figure 1). Whereas the gNodeB beam directions to the UE-S and UE-I were equal to $\alpha_{RS} = 0$ and $\alpha_{RI} = \Delta\alpha$, respectively. So, in both scenarios, the separation angle, $\Delta\alpha$, was always related with the direction of the gNodeB beam for the interfering link. In relation to the direction of the cell sector center, the gNodeB beam direction was equal to Φ_0 (see Figure 3). The distances between the gNodeB (Rx) and UE-S or UE-I (Tx) were equal to D_S or D_I, respectively.

In our tests, the direction of the reference gNodeB beam overlapped with the cell sector center, i.e., $\Phi_0 = \Phi_S = 0$. Hence, we considered the change in separation angle in the ranges of $0° \div 60°$. When analyzing the SIR changes in relation to the beam separation angle, we considered discrete distance values between the gNodeB and UE (or UE-I in the UL scenario), i.e., $D_S = 100$ m and $D = D_I \in \{50, 100, 150\}$ (m). In this case, $\Delta\alpha$ was changed from 0 to 60°, which corresponds to half of a 120° sector. Analyzing the SIR versus D or D_I (for the DL or UL scenarios, respectively), we considered a continuous change of the distance in the ranges of $10 \div 250$ m, whereas the separation angle has discrete values 15°, 20°, and 30°. For the UL scenario, we additionally used the close-in free space reference distance propagation models with path loss exponents equal to 1.9 and 4.5 for LOS and NLOS conditions, respectively [37].

To model the antenna power radiation patterns, we adopted 3GPP recommendations [42]. Half-power beamwidths of main-lobes of the antenna beams were 90° for the UE and about 12° for the gNodeB, respectively. Single antenna beam patterns of the UE and gNodeB for direction $\Phi_0 = 0°$ and $\Phi_0 = 30°$ are illustrated in Figure 4 [32]. In the gNodeB, we used a vertical patch as an antenna array with a size 12×8 of elements, whereas the UE antenna consists of a single element.

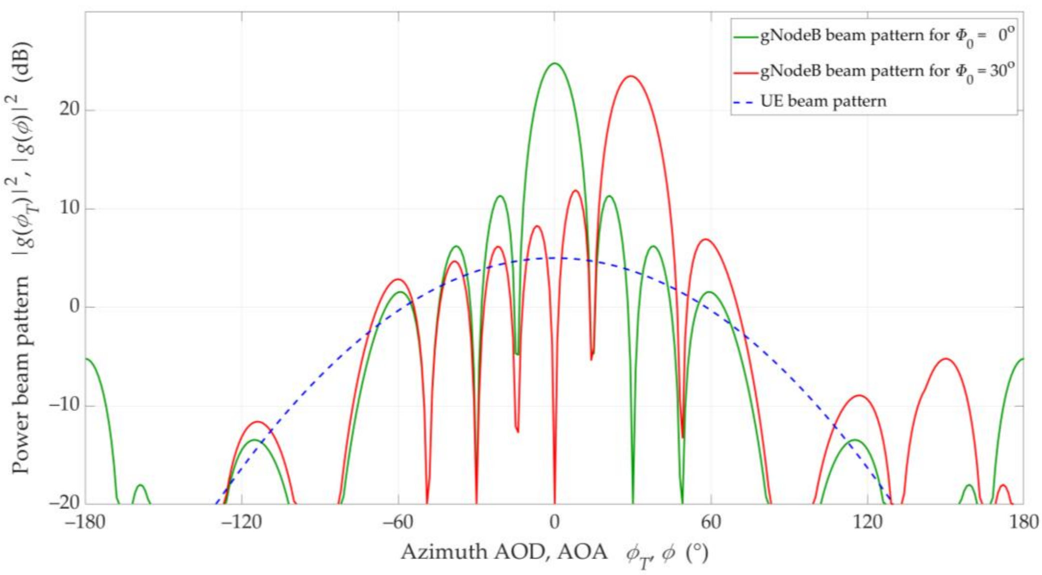

Figure 4. Antenna beam patterns of 1×1 UE and 12×8 gNodeB for Φ_0 = 0° and Φ_0 = 30° [32].

[13]

The simulations were carried out for an urban macro (UMa) environment that is characterized by a normal delay profile with the rms delay spread equal to 266 ns [14]. To model the channel transmission properties, we adopted the TDLs with the 3GPP standard [14], i.e., TDL-D and TDL-B for LOS and NLOS conditions, respectively. To estimate $p_{S,I}(\theta,\phi)$, we used the averaging PASs obtained in 3600 Monte-Carlo simulations. In each Monte-Carlo run, the PAS was obtained based on the generation of 10 random propagation paths for each time-cluster (ellipsoid). Figure 5 presents averaged PAS examples of the UE-S and UE-I in the azimuth plane for the UL scenario, $D_S = D_I = 100$ m, $\Delta\alpha = 30°$, LOS and NLOS conditions.

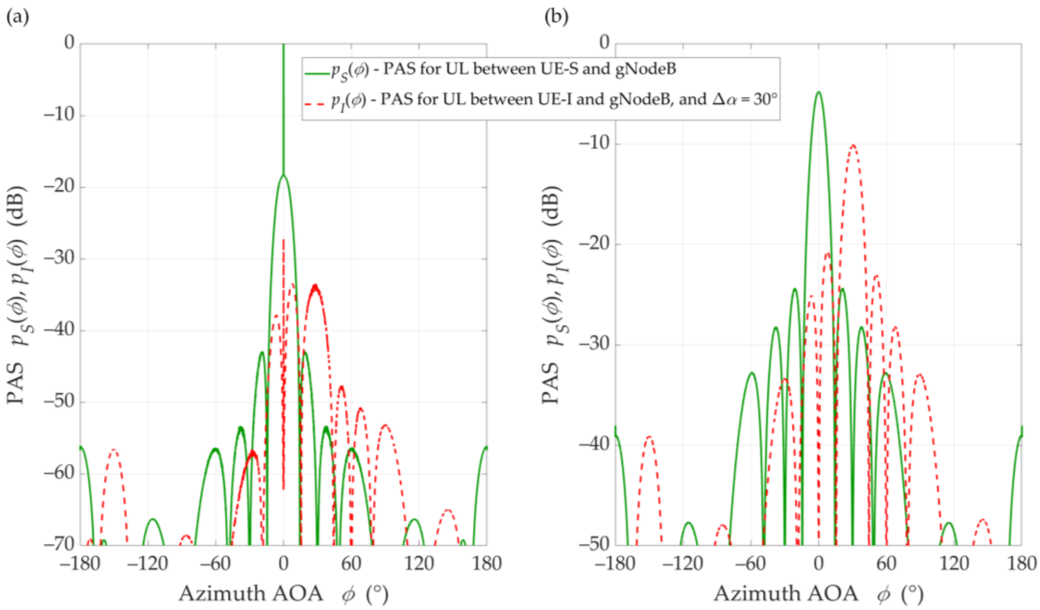

Figure 5. PASs of UE-S and UE-I in azimuth plane for $\Delta\alpha = 30°$, $D_S = D_I = 100$ m, under (**a**) LOS (TDL-D) and (**b**) NLOS (TDL-B) conditions.

The presented results show the diversity of $p_S(\theta,\phi)$ and $p_I(\theta,\phi)$ both due to the relationship between the beam lobes and surface areas under the graphs that correspond to the received powers, P_S and P_I, respectively. This fact indicates the dependence of the received power on the main lobe orientation of the gNodeB beam pattern in relation to the UE-I. This directly influences the determined SIR value. We observe the same situation in the DL scenario. A detailed analysis of the simulation test results is described in the next section.

5. Simulation Results

For the assumptions described in Section 4, we carried out simulation studies using the MATLAB environment. The results for the DL and UL scenarios are discussed in Section 5.1 and Section 5.2, respectively. Section 5.3 contains the comparison of inter-beam interference evaluation obtained based on the MPM and 3GPP statistical model [14]. In this case, we chose the DL scenario to present exemplary results.

5.1. DL Scenario

The simulation results for the DL scenario are presented in Figures 6–10. Figures 6 and 7 show the SIR graphs versus separation angles for selected distances between the gNodeB and UE, under LOS and NLOS conditions, respectively. Based on these charts, we also determined cumulative distribution functions (CDFs) of SIR, $F(SIR)$, presented in Figure 8.

[13]

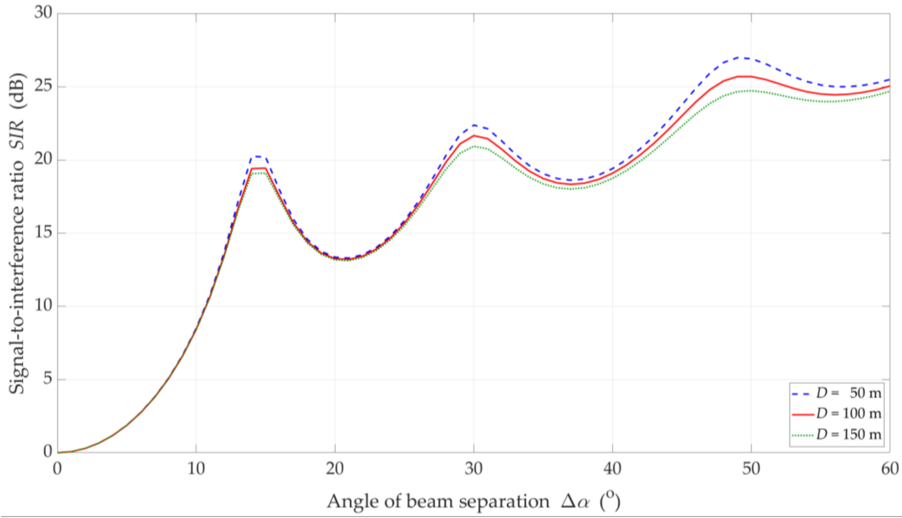

Figure 6. SIR versus separation angle for DL scenario, selected D = {50, 100, 150} m, and LOS (TDL-D) conditions.

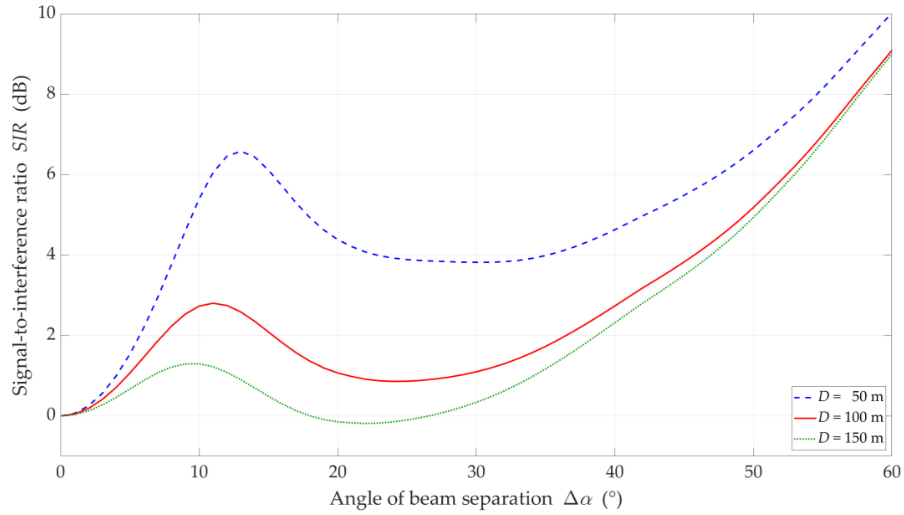

Figure 7. SIR versus separation angle for DL scenario, selected D = {50, 100, 150} m, and NLOS (TDL-B) conditions.

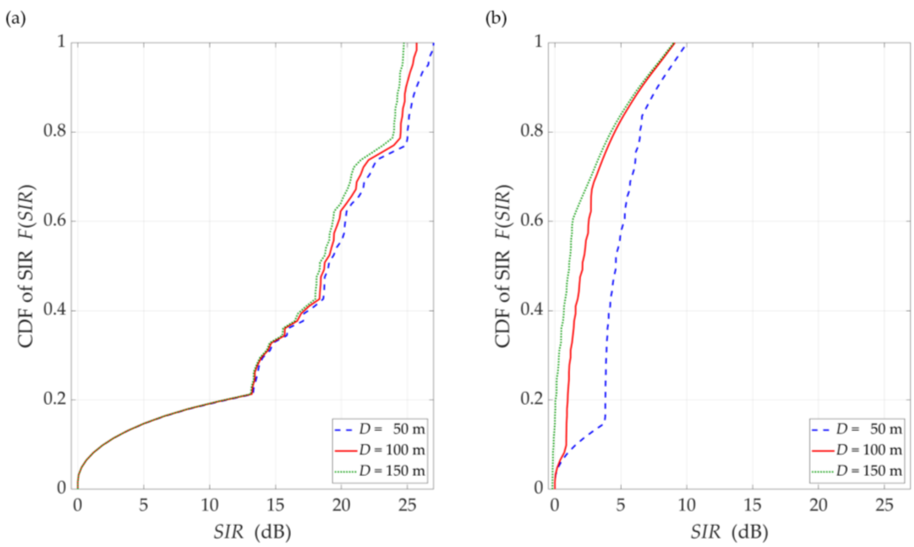

Figure 8. CDFs of SIR for DL scenario, selected D = {50, 100, 150} m, under (**a**) LOS (TDL-D) and (**b**) NLOS (TDL-B) conditions.

[13]

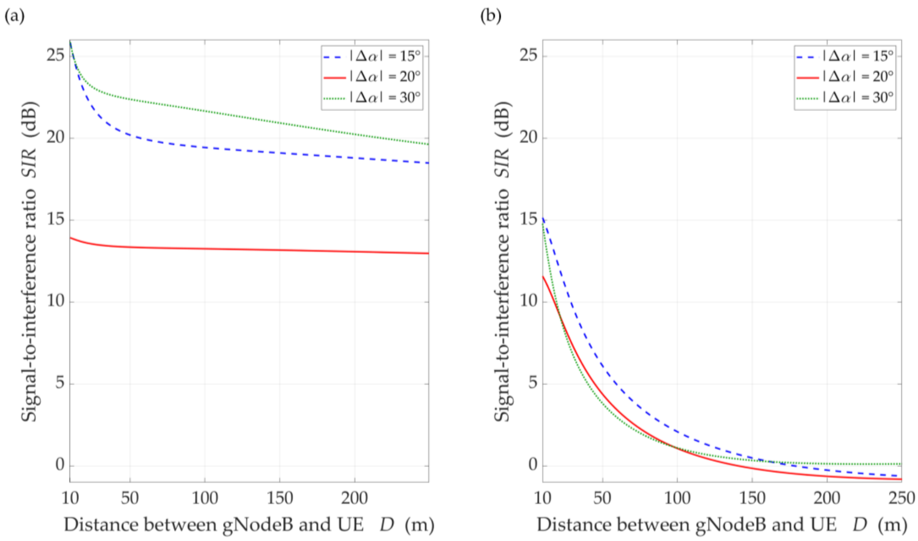

Figure 9. SIR versus distance for DL scenario, selected $\Delta\alpha$ = {15°, 20°, 30°}, under (**a**) LOS (TDL-D) and (**b**) NLOS (TDL-B) conditions.

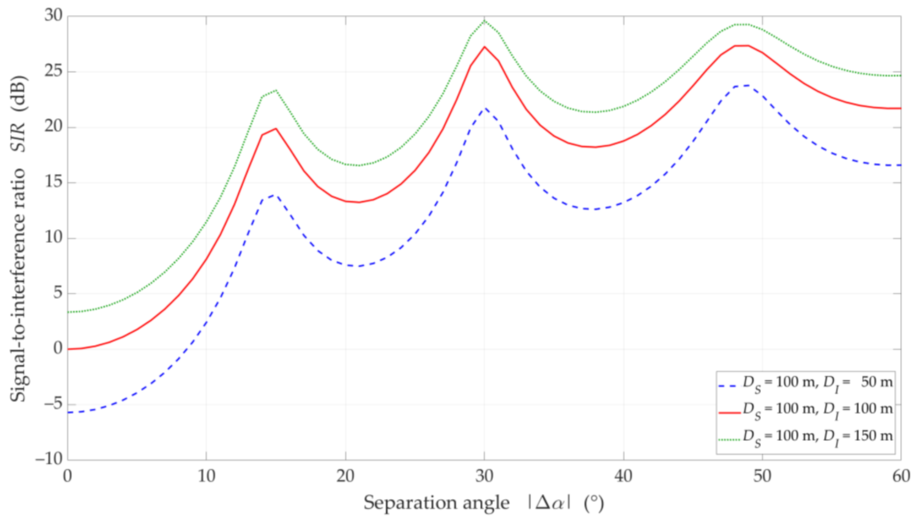

Figure 10. SIR versus separation angle for UL scenario, selected D_I = {50, 100, 150} m, D_S = 100 m, and LOS (TDL-D) conditions.

The increase in the separation angle reduces the downlink interference between the reference beam providing services to the UE and the interference beam. However, the nature of the SIR graphs is not uniform. For $\Delta\alpha = \{15°, 30°, 48°\}$, there are local maxima. We may observe this effect both for LOS and NLOS conditions. It results from considering side lobes in the realistic patterns of the base station beams. As the distance D increases, these maxima are less and less significant. We obtain the similar results in [32] for the carrier frequency of 3.5 GHz.

On the other hand, the obtained results differ significantly from those presented in [43], where some stabilization may be seen in the SIR graphs. In [43], two simplifications are assumed. Firstly, the Gaussian main lobe pattern without side lobes is modeling as the beam. Secondly, the beam gain is constant regardless of its radiation direction. Whereas, in the real beamforming antenna array, the beam gain depends on its direction. This second fact influences importantly on the differences in the presented results.

The comparison of the CDFs (see Figure 8) shows that for 80% of the results of the LOS simulation tests, we obtain up to 20 dB better beam separation compared to NLOS conditions. In the absence of a direct propagation path, we can observe an increase in the

SIR value by 5 dB in over 80% of the results, whereas this increase is below 1 dB for LOS conditions. Figure 9 illustrates the SIR versus the gNodeB-UE distance for selected $\Delta\alpha$, under LOS and NLOS conditions.

Analyzing the obtained results, we can see that as the distance increases, the SIR is reduced. The rationale for this effect is as follows. In the simulation study scenarios, we assume that the environment is homogeneous in terms of propagation properties. This means that the PDP is constant in all directions of electromagnetic wave emission. This assumption complies with the conditions of the propagation phenomena analysis described and recommended by 3GPP [14]. In relation to the model MPM, this means that an increase in the gNodeB-UE distance causes an apparent increase in large and a decrease in small semi-axes of all half-ellipsoids. As a result, the reception of the propagation paths which originate from the main lobe of the interfering beam is focused on the direction of maximum reception of the UE antenna. This causes an increase in the interference level relative to the power of the useful signal by about 7 dB. However, for $\Delta\alpha = 20°$, we see an evident influence of the side lobes on the increase of the interference level, which results in the reduction of the SIR to 13 dB in LOS simulations. The concentration of the interfering paths on the direction of maximum reception also occurs in the NLOS conditions. In this case, the uniformity of the spreading of all propagation paths lowers the range of SIR variation about 10 dB and reduces the differentiation of the side lobes' influence.

For LOS conditions, we can also observe that, despite the larger separation angle for $\Delta\alpha = 20°$, we obtain a lower useful beam resistance to interference compared to $\Delta\alpha = 15°$. This effect is the result of the concentration of the received power on the side-lobe direction and the first minimum of the useful Rx beam, respectively. Figure 10 shows that this phenomenon does not occur under NLOS propagation conditions. The scattering phenomenon of electromagnetic waves under these conditions makes it impossible to concentrate the received power in the Tx-Rx direction.

5.2. UL Scenario

In Figures 10–13, the simulation results are depicted for the UL scenario. Figures 10 and 11 present the SIR curves versus separation angles for selected distances between the gNodeB and UE-I, under LOS and NLOS conditions, respectively. Figure 12 shows the CDFs of SIR for the UL scenario, which were obtained based on curves in Figures 10 and 11.

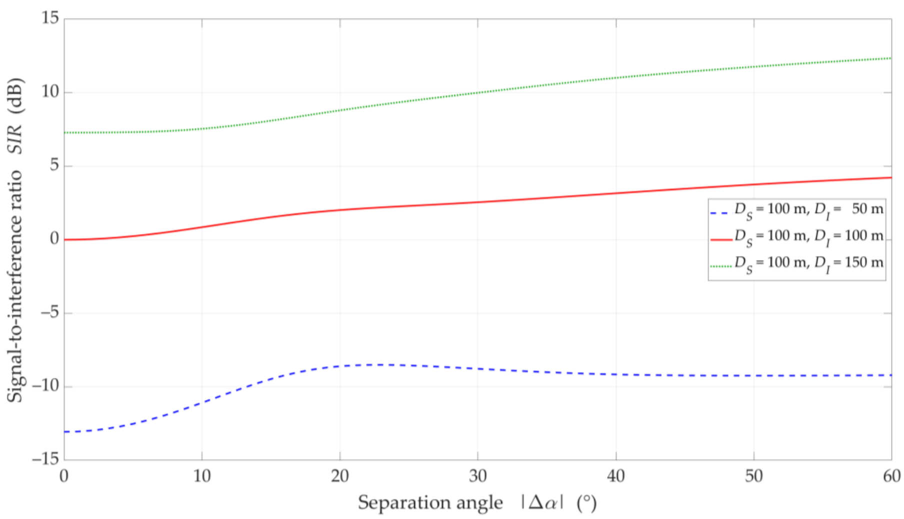

Figure 11. SIR versus separation angle for UL scenario, selected D_I = {50, 100, 150} m, D_S = 100 m, and NLOS (TDL-B) conditions.

[13]

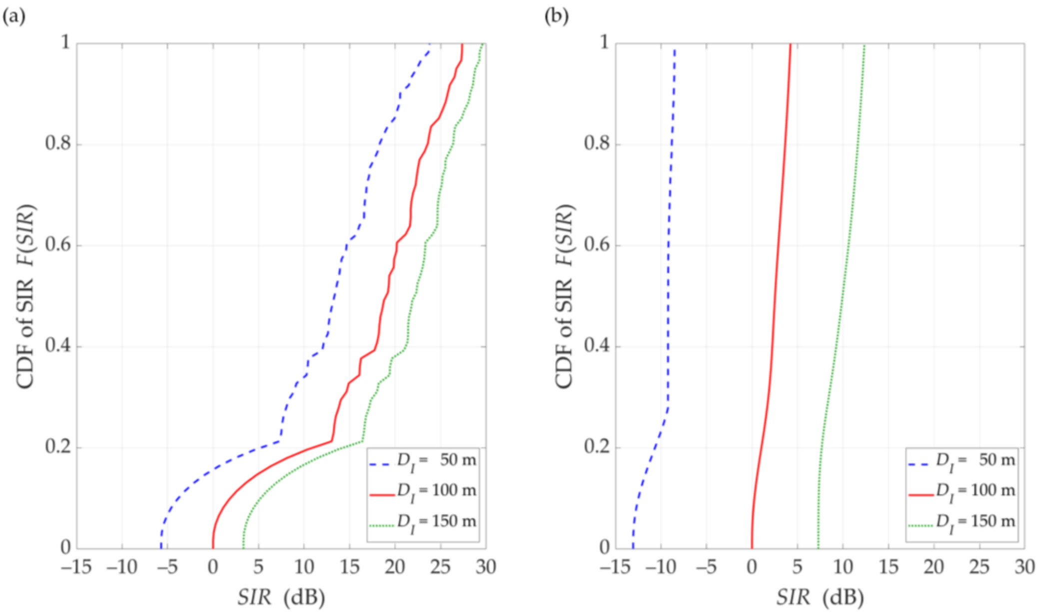

Figure 12. CDFs of SIR for UL scenario, selected D_I = {50, 100, 150} m, D_S = 100 m, (**a**) LOS (TDL-D) and (**b**) NLOS (TDL-B) conditions.

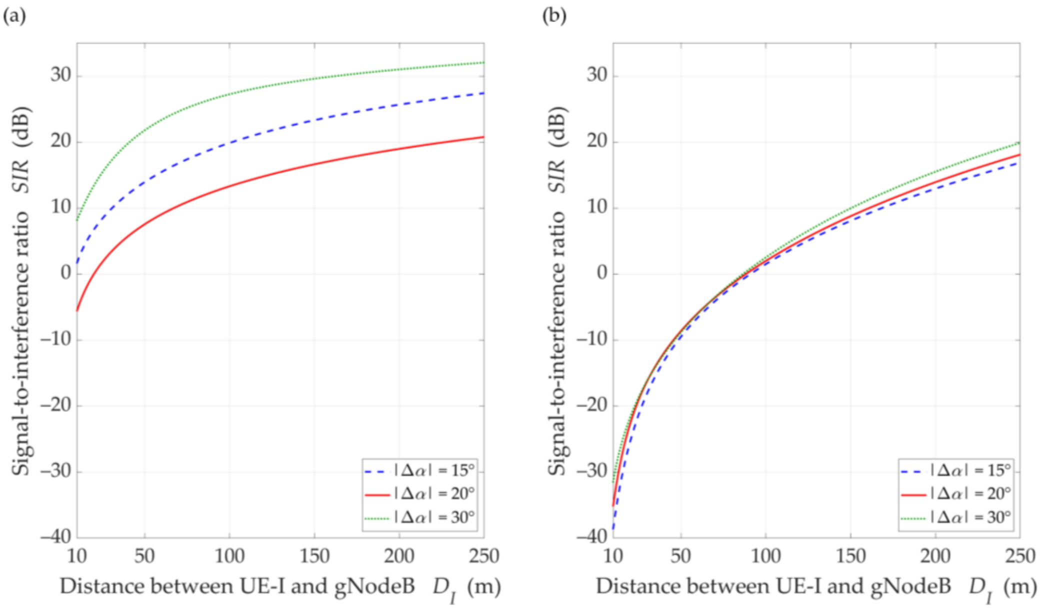

Figure 13. SIR versus distance D_I for UL scenario, selected $\Delta\alpha$ = {15°, 20°, 30°}, D_S = 100 m, under (**a**) LOS (TDL-D) and (**b**) NLOS (TDL-B) conditions.

The obtained results are evident because the SIR graphs correspond to the inversion of the gNodeB beam pattern for the useful link. This testifies the correctness of the developed simulation procedure. The comparison of graphs in Figures 10 and 11 shows the smoothing effect of a multipath propagation environment on changes in the SIR as a function of $\Delta\alpha$. Figure 11 shows that as the distance between the UE-I and gNodeB increases, the shape of the analyzed graph becomes similar as to the graph for LOS conditions. In this case, the distance increase contributes to the convergence of the signal reception directions to the distribution concentrated around the UE-I-gNodeB direction. Similar as to the DL scenario, the comparative analysis of the CDFs (see Figure 12) shows better beam separation with respect to the NLOS conditions. In this case, for 80% of the simulation test results, the SIR value may be about 25 dB greater. The graphs illustrated in Figures 10 and 11 also show that under both LOS and NLOS conditions, to ensure the desired quality of the received signal, i.e., a given value of the SIR, the separation angle decreases with increasing the distance. From a practical viewpoint, this conclusion is obvious. However, the possibility of quantitative SIR assessment in multi-beam radio links operating under NLOS conditions determines the originality of the presented solution. This fact is a premise for the practical use of the developed method in the process of planning and power control in radio links with multi-beam antenna systems.

Figure 13 displays the SIR charts versus D_I for $D_S = 100$ m, selected $\Delta\alpha$, under LOS and NLOS conditions. The presented results are obtained for $\Delta\alpha$ equal to 15°, 20°, and 30°. For these values, the gNodeB beam pattern of the serving link reaches the first minimum, maximum of the first side-lobe, and second minimum, respectively (see Figure 10).

Analyzing the results for LOS conditions, we can see the same effect as for the DL simulation study scenario. Despite the larger separation angle for $\Delta\alpha = 20°$, we obtain a lower useful beam resistance to interference compared to $\Delta\alpha = 15°$. Of course, the reason for this effect is the same as in the DL scenario. For NLOS conditions, the scattering phenomenon of electromagnetic waves under these conditions makes it impossible to concentrate the received power in the Tx-Rx direction. Therefore, we do not see this effect in Figure 13b. The obtained results show the possibility of the SIR evaluation for various propagation conditions enabling optimal management of co-channel beams, which is the basis for interference mitigation, minimizing energy and spectral resources of wireless networks.

5.3. Exemplary Comparison of MPM with 3GPP Approach for DL Scenario

In this section, we provide an example comparison of the proposed MPM-based approach with another solution. In our opinion, choosing a different propagation model that can be the basis for a similar analysis of the inter-beam interference level is not easy. It results from the fact that only a few propagation models make it possible to consider the parameters and patterns of antennas and the environmental scattering of signals occurring in a radio channel. The statistical model based on the 3GPP standard [14] is one of them. Moreover, the choice of the 3GPP model was dictated by three reasons. Firstly, the analysis carried out in this paper with the use of the MPM is based on TDLs defined in the same standard [14]. Secondly, in both simulators we considered the same antenna patterns created according to the 3GPP recommendation [42]. Thirdly, we were able to use a proprietary simulator of the 3GPP statistical model, which was developed in the MATLAB environment and is used for generating the results contributed to the 3GPP, as an input to 5G standardization or research studies (e.g., [9,44]).

Exemplary interference comparison determined based on the MPM and 3GPP model was carried out for the DL scenario and the distance $D = 100$ m. To obtain the average SIR, SIR_{avg}, the Monte Carlo method with 1000 repetitions of statistical channel model realizations was used in the 3GPP simulator. Based on the set of obtained results, confidence intervals for SIR_{avg} with the standard deviation σ_{SIR} were also determined. The same parameters as in Section 5.1 were adopted in the research.

To compare the MPM and 3GPP approaches, we ran the MPM simulator also in Monte Carlo mode for 1000 runs. Thus, the mean results, SIR_{avg}, with the confidence intervals, $SIR_{\text{avg}} \pm \sigma_{SIR}$, were determined. The results of the MPM and 3GPP comparison for the DL scenario and the distance $D = 100$ m between the gNodeB and UE are illustrated in Figures 14 and 15 for LOS and NLOS conditions, respectively.

[13]

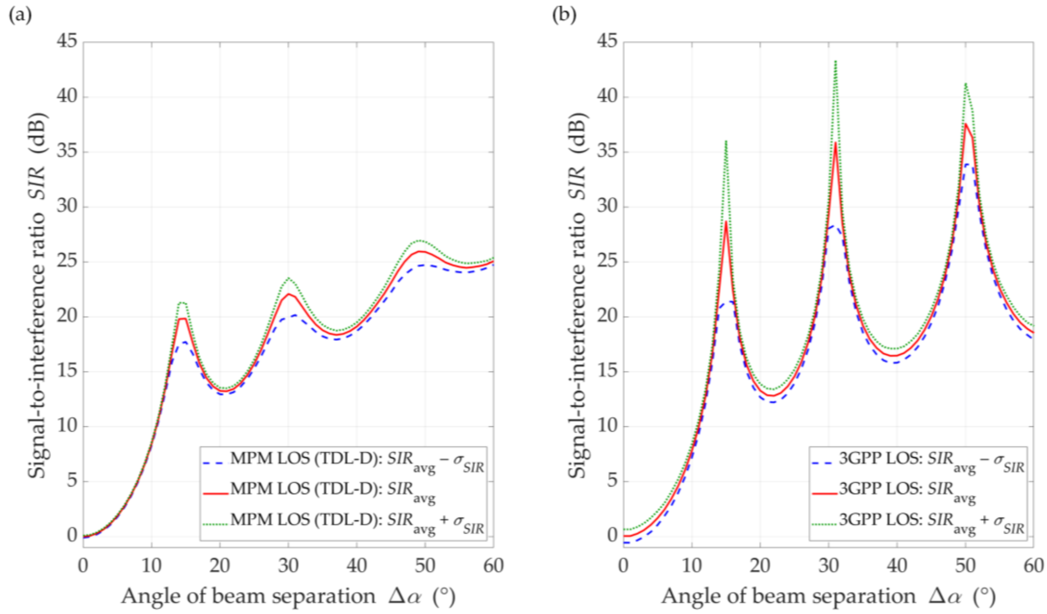

Figure 14. SIR comparison between (**a**) MPM and (**b**) 3GPP model for DL scenario, D = 100 m, and LOS conditions.

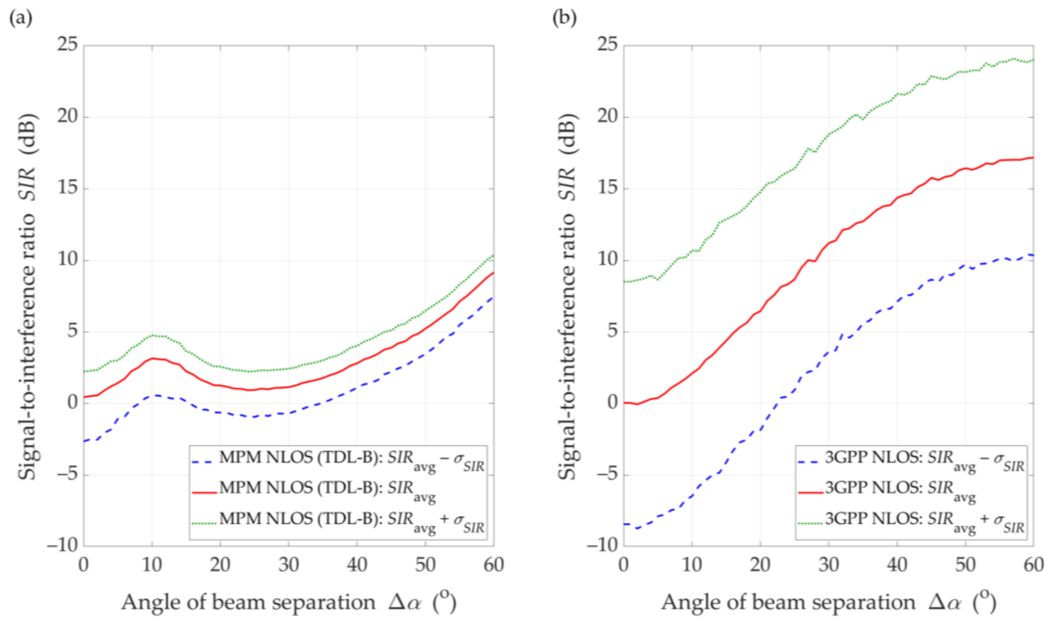

Figure 15. SIR comparison between (**a**) MPM and (**b**) 3GPP model for DL scenario, D = 100 m, and NLOS conditions.

Overall, we might conclude that the results are similar. The SIR results are more similar for LOS conditions (see Figure 14), where we may see characteristic extremes resulting from the use of the same gNodeB antenna pattern. In this case, both the maxima and the minima fall for the same separation angles. This is due to the presence of a direct path that enhances or reduces the influence of the pattern side lobes in certain directions relative to its main lobe (see Figures 4 and 5). Therefore, the optimal directions' selection for the adjacent beams in the gNodeB based on the MPM and 3GPP approaches will be identical or very similar. In this case, we would like to emphasize that the MPM approach gives the possibility to obtain an average result from a single simulation, while the 3GPP statistical model requires the time-consuming Monte Carlo methodology.

Under NLOS conditions (see Figure 15), the dynamics of SIR changes is lower than for LOS conditions. The results for the MPM and the 3GPP model show that the multipath propagation environment for NLOS conditions and the lack of a direct path provide to minimize the impact of the transmitting antenna pattern lobes. Thus, the selection of optimal directions for the adjacent gNodeB beams should be made based on an analysis for LOS conditions. On the other hand, we would like to highlight that other propagation models available in the literature also indicate result differences with the 3GPP model, e.g., [45–48].

With regard to the presented above comparative analysis, it is also worth providing the mean values of the standard deviation, $\overline{\sigma}^{Model}_{LOS/NLOS}$, obtained for the MPM: $\overline{\sigma}^{MPM}_{LOS} = 0.58$ dB and $\overline{\sigma}^{MPM}_{NLOS} = 1.69$ dB, and 3GPP model: $\overline{\sigma}^{3GPP}_{LOS} = 0.97$ dB and $\overline{\sigma}^{3GPP}_{NLOS} = 7.51$ dB under LOS and NLOS conditions, respectively. The differentiation of the obtained results is related to the different spatial nature of scatterings (i.e., spatial dispersion) in the two analyzed propagation models. In the MPM, we use a multi-ellipsoidal geometric structure which is defined based on the TDL of the 3GPP standard [14]. On the other hand, the 3GPP statistical model has greater flexibility in the spatial location of potential scatterers. A more detailed comparison of the MPM and 3GPP model will be presented in the prepared next paper focusing on the 3.5 GHz band used in 5G massive-MIMO systems. A more detailed description of the 3GPP model and simulator will be presented there.

6. Conclusions

This paper is devoted to assessing the limitations that exist in multi-beam antenna systems. Here, the SIR is the primary metric that is used to evaluate the level of interference between the intra-cell beams. The presented procedure for assessing this parameter is based on the PAS analysis, which is determined by simulation tests. By using the channel transmission characteristics (i.e., TDL or PDP) to create the geometric MPM structure, the results of assessing the received power are closely related to the different propagation environment type. Using the MPM allows mapping the impact of the antenna beam radiation patterns on the PAS. The presented methodology allows evaluating changes in the PAS as a function of antenna beam shape and parameters such as the maximum radiation direction, main and side-lobes beamwidths. Additionally, the ability to evaluate the SIR under both LOS and NLOS conditions justifies using this method in the network planning process of energy and spectral management of 5G system with the multi-beam antenna systems. In the multipath propagation environment, in most cases to evaluate fluctuations in the received signal level, the Rician and Rayleigh distributions are used for LOS and NLOS conditions, respectively. The SIR assessment is the basis for determining the parameters of these characteristics. Due to the association of the SIR with the propagation properties of the environment, it is justified to use the presented SIR assessment methodology in the 5G network planning. The ability to adapt the developed model to any environment, weather conditions, and multi-beam antenna system distinguishes this SIR determination method from among the methods used so far. The comparison of the mean results for the proposed methodology with a similar approach based on the 3GPP statistical model shows that the same optimal directions for the adjacent gNodeB beams might be determined faster based on the MPM approach. A more detailed comparison of the two solutions with regard to the interference level assessment in the 3.5 GHz band will be presented in the authors' next work [49]. In the future, we also plan to conduct empirical research for selected scenarios that will allow us to verify the approach presented in this paper.

Author Contributions: Conceptualization, J.M.K. and C.Z.; methodology, K.B., J.M.K., and C.Z.; software, K.B. and J.M.K.; validation, K.B. and J.M.K.; formal analysis, C.Z.; investigation, K.B. and J.M.K.; resources, K.B. and J.M.K.; data curation, K.B. and J.M.K.; writing—original draft preparation, K.B., J.M.K., C.Z., and L.N.; writing—review and editing, K.B., J.M.K., C.Z., and L.N.; visualization, J.M.K.; supervision, C.Z.; project administration, J.M.K. and C.Z.; funding acquisition, J.M.K. All authors have read and agreed to the published version of the manuscript.

Funding: This research was funded by the POLISH MINISTRY OF DEFENSE, grant number GBMON/13-996/2018/WAT on "Basic research in sensor technology field using innovative data processing methods" and grant number UGB/22-730/2020/WAT on "Impact of various propagation conditions on effectiveness of wireless communication and electronic warfare systems".

Institutional Review Board Statement: Not applicable.

Informed Consent Statement: Not applicable.

Data Availability Statement: The data presented in this study are available on request from the corresponding author. The data are not publicly available due to project restrictions.

Acknowledgments: The authors would like to express their great appreciation to the *Sensors* journal Editors and anonymous Reviewers for their valuable suggestions, which have improved the manuscript quality.

Conflicts of Interest: The authors declare no conflict of interest.

Abbreviations

3D	three-dimensional
3GPP	3rd Generation Partnership Project
5G	fifth-generation
AOA	angle of arrival
AOD	angle of departure
CDF	cumulative distribution function
DL	downlink
GBM	geometry-based model
gNodeB	5G base station
ITU	International Telecommunication Union
LOS	line-of-sight
MIMO	multiple-input-multiple-output
mmWave	millimeter-wave
MPM	multi-ellipsoidal propagation model
NLOS	non-line-of-sight
NR	New Radio
PAS	power angular spectrum
PDP	power delay profile
Rx	receiver
SIR	signal-to-interference ratio
TDL	tapped delay line
Tx	transmitter
UE	user equipment
UE-I	interfering UE
UE-S	serving UE
UMa	urban macro
UL	uplink

Symbols

(θ, ϕ)	AOA of individual propagation path
(θ_T, ϕ_T)	AOD of individual propagation path
$\lvert g(\theta, \phi)\rvert^2$	normalized power pattern of receiving antenna
$\lvert g_I(\theta_T, \phi_T)\rvert^2$	normalized power pattern of interfering transmitting antenna
$\lvert g_S(\theta_T, \phi_T)\rvert^2$	normalized power pattern of serving transmitting antenna
α_R	direction of receiving beam
α_{RI}	direction of interfering receiving beam
α_{RS}	direction of serving receiving beam
α_T	direction of transmitting beam
α_{TI}	direction of interfering transmitting beam

[13]

α_{TS}	direction of serving transmitting beam
$\Delta\alpha$	separation angle between serving and interference beams
ΔPL	path loss correction coefficient (relationship between attenuation of propagation environment for different distances)
γ_θ	angular dispersion of local scattering components in elevation plane
γ_ϕ	angular dispersion of local scattering components in azimuth plane
θ	elevation AOA of individual propagation path
θ_T	elevation AOD of individual propagation path
Φ_0	direction of receiving (gNodeB) beam in relation to direction of cell sector center in UL scenario
Φ_I	direction of interfering transmitting (gNodeB) beam in relation to direction of cell sector center in DL scenario
Φ_S	direction of serving transmitting (gNodeB)beam in relation to direction of cell sector center in DL scenario
ϕ	azimuth AOA of individual propagation path
ϕ_T	azimuth AOD of individual propagation path
σ_{SIR}	standard deviation of SIR for confidence interval analysis
$\overline{\sigma}^{3GPP}_{LOS}$	standard deviation of SIR for 3GPP model and LOS conditions
$\overline{\sigma}^{3GPP}_{NLOS}$	standard deviation of SIR for 3GPP model and NLOS conditions
$\overline{\sigma}^{Model}_{LOS/NLOS}$	standard deviation of SIR for Model and LOS/NLOS conditions
$\overline{\sigma}^{MPM}_{LOS}$	standard deviation of SIR for MPM and LOS conditions
$\overline{\sigma}^{MPM}_{NLOS}$	standard deviation of SIR for MPM and NLOS conditions
τ_n	delay of nth time-cluster in PDP/TDL
a	auxiliary variable used to compute r_T
a_{xn}	major semi-axis of nth ellipsoid along x-axis
b_{yn}	minor semi-axis of nth ellipsoid along y-axis
C_0	normalizing constant
c	lightspeed
c_{zn}	minor semi-axis of nth ellipsoid along z-axis
D	distance between Tx and Rx or between gNodeB (Rx) and UE (Tx) in DL
D_I	distance between UE-I (Tx) and gNodeB (Rx) in UL
D_S	distance between UE-S (Tx) and gNodeB (Rx) in UL
$F(SIR)$	CDF of SIR
$f(\widetilde{p})$	distribution of path power
$f_0(\theta,\phi)$	2D von Mises distribution describing local scattering components
$f_I(\theta_T,\phi_T)$	distribution of AOD for interfering link
$f_S(\theta_T,\phi_T)$	distribution of AOD for serving link
G	gain of receiving beam
G_I	gain of interfering transmitting beam
G_S	gain of serving transmitting beam
$\mathrm{I}_0(\cdot)$	zero-order modified Bessel function of imaginary argument
N	number of all time-clusters in analyzed PDP/TDL
n	number of analyzed time-cluster in PDP/TDL
P_I	power of interfering signal
P_S	power of serving signal
PL	path loss
$PL(D_I)$	path loss for wireless links between UE-I and gNodeB at distance D_I
$PL(D_S)$	path loss for wireless links between UE-S and gNodeB at distance D_S
$\widetilde{p}$	power of individual propagation path
p_n	mean power of nth time-cluster in PDP/TDL (nth local extreme of PDP/TDL)
$p_I(\theta,\phi)$	PAS seen at the output of receiving antenna for interfering link
$p_S(\theta,\phi)$	PAS seen at the output of receiving antenna for serving link
$\widetilde{p}_I(\theta,\phi)$	PAS in vicinity of receiving antenna for interfering link
$\widetilde{p}_S(\theta,\phi)$	PAS in vicinity of receiving antenna for serving link
r_T	radial coordinate in spherical system with origin in Tx
SIR	SIR
SIR_{avg}	average SIR for confidence interval analysis
$SIR_{\mathrm{avg}} \pm \sigma_{SIR}$	confidence intervals of SIR

[13]

References

1. Gupta, A.; Jha, R.K. A Survey of 5G network: Architecture and emerging technologies. *IEEE Access* **2015**, *3*, 1206–1232. [CrossRef]
2. Agiwal, M.; Roy, A.; Saxena, N. Next generation 5G wireless networks: A comprehensive survey. *IEEE Commun. Surv. Tutor.* **2016**, *18*, 1617–1655. [CrossRef]
3. Araújo, D.C.; Maksymyuk, T.; de Almeida, A.L.; Maciel, T.; Mota, J.C.; Jo, M. Massive MIMO: Survey and future research topics. *IET Commun.* **2016**, *10*, 1938–1946. [CrossRef]
4. Busari, S.A.; Huq, K.M.S.; Mumtaz, S.; Dai, L.; Rodriguez, J. Millimeter-wave massive MIMO communication for future wireless systems: A survey. *IEEE Commun. Surv. Tutor.* **2018**, *20*, 836–869. [CrossRef]
5. Yacoub, M.D. Fading distributions and co-channel interference in wireless systems. *IEEE Antennas Propag. Mag.* **2000**, *42*, 150–160. [CrossRef]
6. Rui, X.; Jin, R.; Geng, J. Performance analysis of MIMO MRC systems in the presence of self-interference and co-channel interferences. *IEEE Signal Process. Lett.* **2007**, *14*, 801–803. [CrossRef]
7. Fernandes, F.; Ashikhmin, A.; Marzetta, T.L. Inter-cell interference in noncooperative TDD large scale antenna systems. *IEEE J. Sel. Areas Commun.* **2013**, *31*, 192–201. [CrossRef]
8. Guidolin, F.; Nekovee, M. Investigating spectrum sharing between 5G millimeter wave networks and fixed satellite systems. In Proceedings of the 2015 IEEE Globecom Workshops (GC Wkshps), San Diego, CA, USA, 6–10 December 2015; pp. 1–7. [CrossRef]
9. Kim, S.; Visotsky, E.; Moorut, P.; Bechta, K.; Ghosh, A.; Dietrich, C. Coexistence of 5G with the incumbents in the 28 and 70 GHz bands. *IEEE J. Sel. Areas Commun.* **2017**, *35*, 1254–1268. [CrossRef]
10. Hattab, G.; Visotsky, E.; Cudak, M.; Ghosh, A. Toward the Coexistence of 5G Mmwave Networks with Incumbent Systems beyond 70 GHz. *IEEE Wirel. Commun.* **2018**, *25*, 18–24. [CrossRef]
11. Cho, Y.; Kim, H.-K.; Nekovee, M.; Jo, H.-S. Coexistence of 5G with satellite services in the millimeter-wave band. *IEEE Access* **2020**, *8*, 163618–163636. [CrossRef]
12. Kim, T.; Park, S. Statistical Beamforming for massive MIMO systems with distinct spatial correlations. *Sensors* **2020**, *20*, 6255. [CrossRef] [PubMed]
13. Arshad, J.; Rehman, A.; Rehman, A.U.; Ullah, R.; Hwang, S.O. Spectral efficiency augmentation in uplink massive MIMO systems by increasing transmit power and uniform linear array gain. *Sensors* **2020**, *20*, 4982. [CrossRef] [PubMed]
14. 3GPP. *Study on Channel Model for Frequencies from 0.5 to 100 GHz*; 3rd Generation Partnership Project (3GPP), Technical Specification Group Radio Access Network: Valbonne, France, 2019.
15. Kilzi, A.; Farah, J.; Nour, C.A.; Douillard, C. Mutual successive interference cancellation strategies in NOMA for enhancing the spectral efficiency of CoMP systems. *IEEE Trans. Commun.* **2020**, *68*, 1213–1226. [CrossRef]
16. Hassan, N.; Fernando, X. Interference mitigation and dynamic user association for load balancing in heterogeneous networks. *IEEE Trans. Veh. Technol.* **2019**, *68*, 7578–7592. [CrossRef]
17. Ali, K.S.; Elsawy, H.; Chaaban, A.; Alouini, M. Non-orthogonal multiple access for large-scale 5G networks: Interference aware design. *IEEE Access* **2017**, *5*, 21204–21216. [CrossRef]
18. Mahmood, N.H.; Pedersen, K.I.; Mogensen, P. Interference aware inter-cell rank coordination for 5G systems. *IEEE Access* **2017**, *5*, 2339–2350. [CrossRef]
19. Elgendi, H.; Mäenpää, M.; Levanen, T.; Ihalainen, T.; Nielsen, S.; Valkama, M. Interference measurement methods in 5G NR: Principles and performance. In Proceedings of the IEEE 16th International Symposium on Wireless Communication Systems (ISWCS), Oulu, Finland, 27–30 August 2019; pp. 233–238. [CrossRef]
20. Wang, H.; Khilkevich, V.; Zhang, Y.; Fan, J. Estimating radio-frequency interference to an antenna due to near-field coupling using decomposition method based on reciprocity. *IEEE Trans. Electromagn. Compat.* **2013**, *55*, 1125–1131. [CrossRef]
21. Fan, J. Near-field scanning for EM emission characterization. *IEEE Electromagn. Compat. Mag.* **2015**, *4*, 67–73. [CrossRef]
22. Liu, E.; Zhao, W.; Wang, B.; Gao, S.; Wei, X. Near-field scanning and its EMC applications. In Proceedings of the IEEE International Symposium on Electromagnetic Compatibility Signal/Power Integrity (EMCSI), Washington, DC, USA, 7–11 August 2017; pp. 327–332. [CrossRef]
23. Shu, Y.; Wei, X.; Yang, Y. Patch antenna radiation pattern evaluation based on phaseless and single-plane near-field scanning. In Proceedings of the IEEE International Conference on Computational Electromagnetics (ICCEM), Shanghai, China, 20–22 March 2019; pp. 1–3. [CrossRef]
24. Zhao, Y.; Baharuddin, M.H.; Smartt, C.; Zhao, X.; Yan, L.; Liu, C.; Thomas, D.W.P. Measurement of near-field electromagnetic emissions and characterization based on equivalent dipole model in time-domain. *IEEE Trans. Electromagn. Compat.* **2020**, *62*, 1237–1246. [CrossRef]
25. Xue, Q.; Li, B.; Zuo, X.; Yan, Z.; Yang, M. Cell Capacity for 5G Cellular Network with Inter-Beam Interference. In Proceedings of the IEEE International Conference on Signal Processing, Communications and Computing (ICSPCC), Hong Kong, China, 5–8 August 2016; pp. 1–5. [CrossRef]
26. Elsayed, M.; Shimotakahara, K.; Erol-Kantarci, M. Machine Learning-based inter-beam inter-cell interference mitigation in mmWave. In Proceedings of the IEEE International Conference on Communications (ICC), Dublin, Ireland, 7–11 June 2020; pp. 1–6. [CrossRef]
27. Lee, H.; Park, Y.; Hong, D. Resource Split Full duplex to mitigate inter-cell interference in ultra-dense small cell networks. *IEEE Access* **2018**, *6*, 37653–37664. [CrossRef]

[13]

28. Xu, S.; Li, Y.; Gao, Y.; Liu, Y.; Gačanin, H. Opportunistic coexistence of LTE and WiFi for future 5G system: Experimental performance evaluation and analysis. *IEEE Access* **2018**, *6*, 8725–8741. [CrossRef]
29. Ziółkowski, C.; Kelner, J.M. Antenna pattern in three-dimensional modelling of the arrival angle in simulation studies of wireless channels. *IET Microw. Antennas Propag.* **2017**, *11*, 898–906. [CrossRef]
30. Ziółkowski, C.; Kelner, J.M. Statistical evaluation of the azimuth and elevation angles seen at the output of the receiving antenna. *IEEE Trans. Antennas Propag.* **2018**, *66*, 2165–2169. [CrossRef]
31. Kelner, J.M.; Ziółkowski, C. Multi-elliptical geometry of scatterers in modeling propagation effect at receiver. In *Antennas and Wave Propagation*; Pinho, P., Ed.; IntechOpen: London, UK, 2018; pp. 115–141. ISBN 978-953-51-6014-4. [CrossRef]
32. Bechta, K.; Ziółkowski, C.; Kelner, J.M.; Nowosielski, L. Downlink interference in multi-beam 5G macro-cell. In Proceedings of the IEEE 23rd International Microwave and Radar Conference (MIKON), Warsaw, Poland, 5–8 October 2020; pp. 140–143. [CrossRef]
33. Parsons, J.D.; Bajwa, A.S. Wideband characterisation of fading mobile radio channels. *IEE Proc. F Commun. Radar Signal Process.* **1982**, *129*, 95–101. [CrossRef]
34. Ziółkowski, C.; Kelner, J.M. Estimation of the reception angle distribution based on the power delay spectrum or profile. *Int. J. Antennas Propag.* **2015**, *2015*, e936406. [CrossRef]
35. Abdi, A.; Barger, J.A.; Kaveh, M. A parametric model for the distribution of the angle of arrival and the associated correlation function and power spectrum at the mobile station. *IEEE Trans. Veh. Technol.* **2002**, *51*, 425–434. [CrossRef]
36. Vaughan, R.; Bach Andersen, J. *Channels, Propagation and Antennas for Mobile Communications*; IET Electromagnetic Waves Series; Institution of Engineering and Technology: London, UK, 2003; ISBN 978-0-86341-254-7.
37. Rappaport, T.S.; MacCartney, G.R.; Samimi, M.K.; Sun, S. Wideband millimeter-wave propagation measurements and channel models for future wireless communication system design. *IEEE Trans. Commun.* **2015**, *63*, 3029–3056. [CrossRef]
38. ITU. *Recommendation ITU-R P.837-7: Characteristics of Precipitation for Propagation Modelling*; P Series Radiowave Propagation; International Telecommunication Union (ITU): Geneva, Switzerland, 2017.
39. ITU. *Recommendation ITU-R P.838-3: Specific Attenuation Model for Rain for Use in Prediction Methods*; P Series Radiowave Propagation; International Telecommunication Union (ITU): Geneva, Switzerland, 2005.
40. Han, C.; Duan, S. Impact of atmospheric parameters on the propagated signal power of millimeter-wave bands based on real measurement data. *IEEE Access* **2019**, *7*, 113626–113641. [CrossRef]
41. Huang, J.; Cao, Y.; Raimundo, X.; Cheema, A.; Salous, S. Rain statistics investigation and rain attenuation modeling for millimeter wave short-range fixed links. *IEEE Access* **2019**, *7*, 156110–156120. [CrossRef]
42. 3GPP. *Evolved Universal Terrestrial Radio Access (E-UTRA) and Universal Terrestrial Radio Access (UTRA); Radio Frequency (RF) Requirement Background for Active Antenna System (AAS) Base Station (BS)*; 3rd Generation Partnership Project (3GPP): Valbonne, France, 2019.
43. Kelner, J.M.; Ziółkowski, C. Interference in multi-beam antenna system of 5G network. *Int. J. Electron. Telecommun.* **2020**, *66*, 17–23. [CrossRef]
44. Bechta, K.; Du, J.; Rybakowski, M. Rework the radio link budget for 5G and beyond. *IEEE Access* **2020**, *8*, 211585–211594. [CrossRef]
45. Almesaeed, R.; Ameen, A.S.; Mellios, E.; Doufexi, A.; Nix, A.R. A proposed 3D extension to the 3GPP/ITU channel model for 800 MHz and 2.6 GHz bands. In Proceedings of the IEEE 8th European Conference on Antennas and Propagation (EuCAP). Hague, The Netherlands, 6–11 April 2014; pp. 3039–3043. [CrossRef]
46. Ademaj, F.; Taranetz, M.; Rupp, M. 3GPP 3D MIMO Channel Model: A Holistic Implementation Guideline for Open Source Simulation Tools. *EURASIP J. Wirel. Commun. Netw.* **2016**, *2016*, 55. [CrossRef]
47. Rappaport, T.S.; Sun, S.; Shafi, M. Investigation and Comparison of 3GPP and NYUSIM Channel Models for 5G Wireless Communications. In Proceedings of the IEEE 86th Vehicular Technology Conference (VTC-Fall), Toronto, ON, Canada, 24–27 September 2017; pp. 1–5. [CrossRef]
48. Sheikh, M.U.; Jäntti, R.; Hämäläinen, J. Performance Comparison of Ray Tracing and 3GPP Street Canyon Model in Microcellular Environment. In Proceedings of the IEEE 27th International Conference on Telecommunications (ICT), Bali, Indonesia, 5–7 October 2020; pp. 1–5. [CrossRef]
49. Bechta, K.; Ziółkowski, C.; Kelner, J.M.; Nowosielski, L. Modeling of downlink interference in massive MIMO 5G macro-cell. *Sensors* **2021**, *21*, 597. [CrossRef] [PubMed]

Coexistence of 5G With the Incumbents in the 28 and 70 GHz Bands

Seungmo Kim, Eugene Visotsky, *Member, IEEE*, Prakash Moorut, Kamil Bechta, Amitava Ghosh, *Fellow, IEEE*, and Carl Dietrich, *Senior Member, IEEE*

***Abstract*— A promising way of realizing the fifth generation (5G) wireless systems is to operate 5G deployments at higher frequency bands, specifically in the millimeter-wave (mmW) spectrum (30–300 GHz). Access to such spectrum bands will enable future 5G wireless systems to meet the 5G requirements of peak rate greater than 10 Gb/s, and cell edge rate of up to 1 Gb/s. However, the emerging 5G systems will need to coexist with a number of incumbent systems in these bands. This paper provides an extensive study of the co-channel coexistence of 5G in two critical mmW bands, 27.5–28.35 GHz (28 GHz) and 71–76 GHz (70 GHz) bands, where fixed satellite service (FSS) and fixed service (FS), such as wireless backhaul, are the predominant incumbent users. In the 28-GHz study, we show that interference from 5G into the FSS space stations can be kept below the FSS interference protection criterion. We also characterize the minimum separation distance between the FSS earth stations (ESs) and 5G in order to protect the 5G system from interference due to the ESs transmissions. In the 70-GHz study, we show that the 5G-to-FS interference could be a potential issue in certain scenarios, but we introduce techniques to significantly suppress this interference, while maintaining acceptable performance of the 5G systems. For each study, we suggest appropriate deployment strategies for a 5G system based on our results.**

***Index Terms*— 5G, coexistence, spectrum sharing, mmW, 28 GHz, 70 GHz, FSS, FS, wireless backhaul.**

I. Introduction

THE millimeter wave (mmW) bands previously have been best suited for satellite or fixed microwave applications. However, recent technological breakthroughs, such as the capability to integrate a very large numbers of antennas into future the 5th generation (5G) User Equipments (UEs) and Access Points (APs), have newly enabled advanced mobile services in these bands, notably including very high speed and low latency services [5]. Thus, disadvantages in propagation due to high frequency in mmW bands can be mitigated by using large antenna arrays at both transmitter and receiver ends of 5G wireless links, creating a massive Multiple Input-Multiple Output (MIMO) communication system. The ideas of deploying massive MIMO arrays in mmW bands have been well-covered in recent work such as [2] and [3].

There is high international interest (including USA, Japan and South Korea) in making the 27.5-28.35 GHz (28 gigahertz, GHz) band available for mobile use [5]. In addition, the 71-76 GHz (70 GHz) band was identified at the International Telecommunication Union (ITU)'s World Radiocommunication Conference (WRC) 2015 [6] as a possible band for future 5G wireless system deployments. In the 28 GHz band, Fixed Satellite Service (FSS) uplink–i.e., the communication links from Earth Stations (ESs) to Space Stations (SSs)–is in wide use, whereas in the 70 GHz band, the Fixed Service (FS) Wireless Backhaul (WB) for other cellular systems–e.g., the 4th generation (4G)–is the predominant incumbent.

There is related work that discusses various models of coexistence [7]–[14], and a body of prior work that discusses the techniques of interference reduction [15]–[19]. There is also recent work that has been performed in the area of spectrum sharing in mmW bands [20]–[26].

In this paper, we discuss coexistence between 5G and two incumbents at 28 GHz and 70 GHz, the FSS and FS systems, respectively. Showing that 5G can coexist with these incumbent systems is critical to the introduction of 5G in mmW bands. One relevant discussion of the coexistence of the 5G systems is provided in [21]. Our work is more extensive than [21] for the following three reasons. Firstly, we discuss both co-channel interference scenarios of 5G-to-FSS and FSS-to-5G at 28 GHz, whereas in [21] only FSS ES-to-5G interference is discussed. In fact, the authors identified analysis of the 5G-to-SS interference as their future work. Secondly, we additionally study coexistence of 5G with FS at 70 GHz. Thirdly, motivated by our results at 70 GHz, we propose several techniques that mitigate interference from 5G APs and UEs to the incumbent systems while interference mitigation at 70 GHz is another future work area that is identified in [21].

The proposed interference mitigation schemes in this work are novel for several reasons. Firstly, while the prior schemes [23]–[25], [25] focus on inter-cell interference in 5G systems, we address coexistence of 5G with incumbent systems. Secondly, our schemes are more efficient than those proposed in [15]–[18], since (i) they are standalone techniques in the sense that they do not require assistance from infrastructure, such as the Spectrum Access System (SAS) adopted as a solution for coexistence at 3.5 GHz [4], and (ii) they are straightforward to implement in realistic deployments, as the proposed schemes solely rely on the native beam management protocols defined

Manuscript received December 18, 2016; revised March 2, 2017; accepted March 02, 2017. Date of publication April 12, 2017; date of current version June 1, 2017. *(Corresponding author: Seungmo Kim.)*

S. Kim and C. Dietrich are with the Department of Electrical and Computer Engineering, Virginia Polytechnic Institute and State University, Blacksburg, VA 24061, USA (e-mail: seungmo@vt.edu).

E. Visotsky, P. Moorut, and A. Ghosh are with the Nokia Bell Labs, Arlington Heights, IL 60004, USA.

K. Bechta is with the Nokia Bell Labs, 53-661 Wrocław, Poland.

Color versions of one or more of the figures in this paper are available online at http://ieeexplore.ieee.org.

Digital Object Identifier 10.1109/JSAC.2017.2687238

as part of the 5G air interface. Thirdly, this paper discusses detailed methods of compensating the performance degradation of 5G systems incurred when mitigating 5G interference towards the incumbent systems. Finally, this paper assesses the UE-to-FS interference that is not discussed in [18] and [19], and proposes a novel method of mitigating it.

Specifically, the contributions of this paper are as follows:

- We provide detailed analysis and supporting simulation results of the co-channel coexistence between 5G and uplink FSS systems in the 28 GHz band. With respect to the 5G system modeling, we concentrate on APs, as interference generated and observed at the APs is much more significant than that at the UEs. Hence, we analyze the AP-to-SS and ES-to-AP interference. Based on our results, we conclude that (i) potentially on the order of hundreds to thousands of APs can simultaneously transmit in a given 5G service area without harming an SS receiver and (ii) a separation distance on the order of a few kilometers is required between an ES and the 5G system for acceptable operation of 5G.
  We also provide an initial set of results on the UE-to-SS interference assessment. In general, characterization of the UE-to-SS interference is heavily dependent on the deployment scenario and such system parameters as the percentage of UEs indoors or below clutter, as well as the particulars of the UE antenna array design. Hence, a detailed study of the UE-to-SS interference is outside the scope of this paper. Nevertheless, we provide a number of preliminary results on UE-to-SS interference, indicating that under reasonable UE deployment assumptions, the number of active UEs supported can far exceed the number of active APs in a 5G service area.
- We analyze the co-channel coexistence between 5G and FS at 70 GHz. We assume the FS system to be a point-to-point WB for another cellular system such as 4G. Unlike the coexistence at 28 GHz, all of the four directions of interference are possible in this band: AP to FS, FS to AP, UE to FS, and FS to UE. It is because: (i) both directions of an FS link operate at 70 GHz, and (ii) UE has higher probabilities of Line-of-Sight (LoS) in a 5G-FS coexistence topology since the beam of an FS's antenna is placed terrestrially and pointed closer toward the ground. We find that compared to the FS-to-5G interference, the one from 5G to FS (both AP to FS and UE to FS) is more significant since an interference is aggregated among multiple cells.
- Motivated from the finding, we propose techniques that mitigate AP-to-FS and UE-to-FS interference. The main idea for mitigation of the AP-to-FS interference is to establish exclusion zones at each region of AP, in order to ensure that the transmit beam gain toward the FS is attenuated sufficiently. Mitigation of the UE-to-FS interference is to force a UE to generate an uplink beam that is away enough from the direction toward FS. The proposed techniques can be applied to other coexistence situations, as long as the incumbent system operates terrestrially.

The coexistence models adopted in this paper rely on realistic channel and beamforming models that strive to truthfully capture the interaction between the multipath environment observed at the APs and UEs (according to the channel model of [35]) and the selection process of the AP and UE transmit and receive beamforming weights. Given the selected weights, the resulting distribution of the AP and UE transmit and receive beamforming gains is central for characterizing the interference scenarios considered in this paper. Unfortunately, the multipath fading model in [35] is stochastic in nature and is quite complex, which makes closed-form mathematical analysis of the interference distributions of interest intractable. Thus, in this work we resort to a semi-analytical approach, whereby the interference distributions of interest are evaluated via Monte-Carlo simulations.

This paper is organized as follows. In Section II, we discuss coexistence of 5G with FSS at 28 GHz. Section III studies coexistence of 5G with FS at 70 GHz. Section IV describes our proposed techniques that mitigate interference from 5G to the incumbent system, followed by evaluation results in Section V. Conclusions are drawn in Section VI.

II. Coexistence of 5G With Fixed Satellite Service at 28 GHz

At 28 GHz, the FSS operates in the uplink only (from ES to SS). Therefore, for coexistence with 5G, the possible scenarios of interference are 5G to SS and ES to 5G. Note that we consider the case of co-channel interference only.

In general, we expect APs to be the dominant source of interference from 5G. The reason is that in comparison to AP-to-SS interference, the UE-to-SS interference has much smaller impact since the Effective Isotropically Radiated Power (EIRP) of a UE is likely far lower than that of an AP. In addition, a UE is far more likely than an AP not to have a line-of-sight (LoS) propagation path toward an SS, which further reduces the potential for the UE-to-SS interference. These observations are confirmed by our results on the UE-to-SS interference, indicating that the number of active UEs permitted in a 5G service area far exceeds that of active APs.

For the FSS-into-5G direction, only ES-to-AP interference is considered as interference observed at the APs is expected to be the bottleneck for 5G system deployments. The UEs likely to have smaller antenna gains and experience much higher propagation losses from the ES transmitters than APs. Hence, the directions of interference that we consider in this study are AP-to-SS, UE-to-SS and ES-to-AP.

Finally, we note that the distribution of UEs in the system plays an important role in both directions of the interference. The reason is that the position of a UE determines the UE's and the serving AP's beamforming directions, which in turn affects both the AP-to-SS, UE-to-SS and ES-to-AP interference. As in Table I, the cell site of an AP is divided into three sectors, each of which spans 120 degrees (°). The distribution of UEs follows Poisson Point Process (PPP) [27] in a sector region.

TABLE I

PARAMETERS FOR 5G

Parameter	AP	UE
Carrier frequency	28 GHz	
System layout	UMi [35]	
Inter-site distance (ISD)	200 m	
Cell density	29 cells/km^2	
Cell sectorization	3 sectors/site	
Duplexing	Time-division duplexing (TDD)	
Transmission scheme	Singler-user (SU)-MIMO	
Bandwidth	850 MHz	
Temperature	290 K	
Max antenna gain	5 dBi per element	
Transmit power	21 dBm per element	14 dBm per element
Number of antennas ($\lambda/2$ array)	8×8 and 16×16	4×4
Noise figure	7 dB	9 dB
Antenna height	10 m	1.5 m

TABLE II

PARAMETERS FOR FSS SS

Parameter	Class 1	Class 2	Class 3
Elevation angle (degrees)	15-55	15-55	5-50
Orbit distance (km)	36,000	36,000	9,000
Max antenna gain (dBi)	58	58	27
Temperature (K)	1000	650	570
Thermal noise (dBm/Hz)	-168.6	-170.5	-171.0
Path loss models between 5G and FSS SS (dB)	LoS: FSPL + 4 NLoS: FSPL + 24		
Interference protection criterion (I/N, dB)	$TH_{fss} = \{-12.2, -6, 0\}$		

TABLE III

RESULTS OF 5G AP-TO-FSS SS INTERFERENCE

SS class, Los/NLoS mix		Result			
		Mean individual-sector interference (dBm/Hz)	Maximum number of simultaneously transmitting sectors		
			$TH_{fss} =$ -12.2 dB	6 dB	0 dB
		AP EIRP = 62 dBm/100 MHz (8×8 array)			
Class 1	50% LoS / 50% NLoS	-213	2,000	8,000	32,000
	25% LoS / 75% NLoS	-216	3,800	15,200	60,800
	10% LoS / 90% NLoS	-220	9,000	36,000	144,000
Class 2	50% LoS / 50% NLoS	-213	1,200	4,800	19,200
	25% LoS / 75% NLoS	-216	2,300	9,200	36,800
	10% LoS / 90% NLoS	-220	5,400	21,600	86,400
Class 3	50% LoS / 50% NLoS	-217	2,200	8,800	35,200
	25% LoS / 75% NLoS	-219	4,400	17,600	70,400
	10% LoS / 90% NLoS	-223	10,000	40,000	160,000
		AP EIRP = 74 dBm/100 MHz (16×16 array)			
Class 1	50% LoS / 50% NLoS	-213	2,000	8,000	32,000
	25% LoS / 75% NLoS	-216	3,800	15,200	60,800
	10% LoS / 90% NLoS	-220	9,000	36,000	144,000
Class 2	50% LoS / 50% NLoS	-213	1,200	4,800	19,200
	25% LoS / 75% NLoS	-216	2,300	9,200	36,800
	10% LoS / 90% NLoS	-220	5,400	21,600	86,400
Class 3	50% LoS / 50% NLoS	-211	600	2,400	9,600
	25% LoS / 75% NLoS	-214	1,300	5,200	20,800
	10% LoS / 90% NLoS	-218	3,000	12,000	48,000

TABLE IV

RESULTS OF 5G UE-TO-FSS SS INTERFERENCE

SS class, Los/NLoS mix		Result			
		Mean individual-UE interference (dBm/Hz)	Maximum number of simultaneously transmitting UEs		
			$TH_{fss} =$ -12.2 dB	6 dB	0 dB
Class 1	25% LoS / 75% NLoS	-225	283,000	1,132,000	4,528,000
	10% LoS / 90% NLoS	-228	566,000	2,264,000	9,056,000
	100% NLoS	-238	6,226,000	24,904,000	99,616,000
Class 2	25% LoS / 75% NLoS	-217	28,000	112,000	448,000
	10% LoS / 90% NLoS	-220	57,000	228,000	912,000
	100% NLoS	-230	627,000	2,508,000	10,032,000
Class 3	25% LoS / 75% NLoS	-223	64,400	257,800	1,031,200
	10% LoS / 90% NLoS	-227	162,000	648,000	2,591,800
	100% NLoS	-237	1,781,900	7,127,500	28,510,100

A. Interference From 5G AP and UE to FSS SS

1) System Model: Tables I and II provide parameters for the 5G AP/UE and FSS SS, respectively. For the SS, the interference protection criterion is defined as the threshold of interference-to-noise ratio (I/N), which is denoted by TH_{fss}. Regarding the path loss between an AP/UE and an SS, various combinations of LoS and Non-Line-of-Sight (NLoS) channel conditions are considered. Note that a large percentage of LoS sites appears to be unrealistic given real-world vegetation/foliage losses and practical deployment cases of 5G. Moreover, we note that LoS channel conditions will occur with very low probabilities at 28 GHz, where propagation of a microwave signal is adversely affected not only by blockage due to buildings and other structures but also by vegetation. Therefore, only realistic subsets of LoS/NLoS combinations are reported in our final results given in Tables III and IV.

The path loss models are elaborated as follows. In LoS conditions, we assume a free space path loss (FSPL) model [28] plus additional atmospheric and polarization losses of 4 dB In the NLoS channel conditions, an FSPL model is again used, with additional 20 dB of clutter loss in addition to the 4 dB of atmospheric and polarization losses [29]. Thus, the total additional loss assumed in the NLoS model is 24 dB. Recall that *clutter loss* is the loss due to various conditions on the terrain (such as buildings) over a wide area, and hence it also accounts for the *diffraction loss* [30], which is the loss due to propagation bending around an object such as a building or a wall. Note that our assumption of a 20 dB of clutter loss is worst case with respect to interference modeling, as diffraction losses can be significantly higher depending on the ray angles of incidence and departure toward the satellite. This potentially higher clutter loss may result in an even lower AP/UE-to-SS interference in practice.

The threshold TH_{fss} of -12.2 dB in Tables III and IV is derived from [31]. There is, however, general recognition in the satellite community that this interference level was developed when satellite networks were considered to be power limited, whereas today satellite networks tend to be interference limited and, as such, this protection level is very conservative [6]. Therefore more realistic and less stringent protection criteria of TH_{fss} of -6 dB and 0 dB are used in this paper. It is to be noted that TH_{fss} of -6 dB and 0 dB corresponding to 1dB and 3 dB desensitization (desense) interference thresholds, which represent the increase in the noise floor of the system due to interference, are also typically used for mobile terrestrial systems [32], [33]. We use the same -6 dB and 0 dB I/N as the protection criteria for satellite systems in addition to -12.2 dB, since without the knowledge of the receiver characteristics of the satellite systems, it is difficult to derive a more precise value of the I/N protection criteria for the FSS SS and ES receivers. For 5G, TH_{5g} of -12.2 dB was also used in addition to -6 dB and 0 dB to be consistent with the FSS interference results.

2) Analysis of Interference: As a metric that measures AP/UE-to-SS interference, we calculate the number of simultaneously transmitting APs/UEs such that TH_{fss} at the FSS SS is not violated.

Here we provide an analysis framework for the AP-to-SS interference. With straightforward modifications, this framework can be also applied to the UE-to-SS interference. To compute such an aggregate interference, an interference from the downlink transmission of a single sector is computed by averaging over all possible downlink directions according

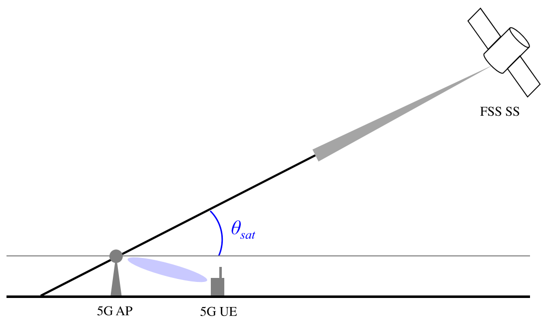

Fig. 1. Topology of coexistence between a 5G system and an FSS SS on elevation plane.

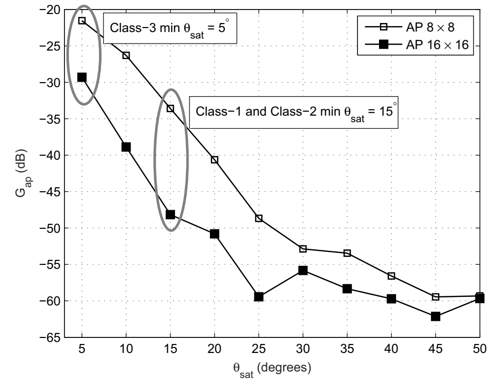

Fig. 2. Normalized mean AP antenna gain into FSS SS vs. the elevation angle θ_{sat}.

to position of the UE, which is given by

$$I_{5g} = \frac{1}{\left|\mathcal{R}_k^2\right|} \int_{x_{ue}^{(k)} \in \mathcal{R}_k^2} \frac{P_{T,ap} G_{ap,a}(x_{ue}) G_{ap,e}(x_{ue}) G_{ss,3db}}{PL_{ap\rightarrow ss}} dx_{ue} \quad (1)$$

where $\mathcal{R}_k^2$ is region of a sector and thus $\left|\mathcal{R}_k^2\right|$ is the area of a sector; x_{ue} is position of a UE in an $\mathcal{R}_k^2$; $P_{T,ap}$ is transmit power of an AP; $G_{ap,a}$ and $G_{ap,e}$ are the azimuth and elevation beamforming gains of a downlink transmission to a UE in the direction toward the SS; $G_{ss,3db}$ is the beamforming gain of the SS receiver antenna within its 3dB-contour; $PL_{ap\rightarrow ss}$ is the path loss between the AP and the SS.

For a 5G AP, the attenuation patterns of an antenna element on the elevation and azimuth plane are given by [35]

$$\begin{aligned} A_a(\phi) &= \min\left\{12\left(\frac{\phi}{\phi_{3db}}\right)^2, A_m\right\}, \\ A_e(\theta) &= \min\left\{12\left(\frac{\theta - 90^\circ}{\theta_{3db}}\right)^2, A_m\right\} \text{ [dB]} \end{aligned} \quad (2)$$

where ϕ and θ are angles of a beam on the azimuth and elevation plane, respectively; $(\cdot)_{3db}$ denotes an angle at which a 3-dB loss occurs. Then the antenna element pattern that is combined in the two planes is given by

$$A(\theta, \phi) = \min\left(A_a(\phi) + A_e(\theta), A_m\right) \text{ [dB]} \quad (3)$$

where A_m is a maximum attenuation (front-to-back ratio). It is defined $A_m = 30$ dB in [35], but it can be higher in practice. Finally, an antenna gain that is formulated as

$$G(\phi, \theta) = G_{max} - A(\phi, \theta) \text{ [dB]} \quad (4)$$

where G_{max} is a maximum antenna gain.

Note that $G_{ap,a}$ and $G_{ap,e}$ are lower than the maximum azimuth and elevation beamforming gains. The reason is depicted in Fig. 1. Generally, a beam of an AP is pointed away from an SS since transmitting to a UE that is placed at a lower elevation than the AP. The elevation angles that are shown in Table II for each class of SS [29] are obtained in this manner.

Based on (1), we calculate an *aggregate* interference, which is given by

$$I_{aggr}(\mathbb{N}[\mathcal{S}_{5s}]) = I_{5g} \times \mathbb{N}[\mathcal{S}_{5s}] \quad (5)$$

where $\mathcal{S}_{5s}$ is a set of 5G sectors; $\mathbb{N}[\cdot]$ is the number of elements in a set. Now, we can obtain the number of simultaneously transmitting APs, $\mathbb{N}[\mathcal{S}_{5s}]$, such that I_{aggr} does not exceed TH_{fss}, which is given by

$$\arg\max_{\mathbb{N}[\mathcal{S}_{5s}]} I_{aggr}(\mathbb{N}[\mathcal{S}_{5s}]) < 10^{0.1TH_{fss}} \quad (6)$$

within an area that a satellite beam forms on the Earth surface. The receive antenna on board an SS forms a spot where a solid angle formed by the receive beam subtends the surface of the Earth; and this is typically known as a *spot beam*. It is assumed that the entire 5G system deployment falls within the 3dB-contour of an SS receiver spot beam.

3) Evaluation of Interference: Tables III and IV record our final results of (i) a mean individual-sector/UE interference power received at an SS receiver, I_{5g}/W from (1) where W is bandwidth of 5G, and (ii) the maximum number of simultaneous 5G sectors/UEs that can transmit under a TH_{fss}, $\arg\max_{\mathbb{N}[\mathcal{S}_{5s}]} I_{aggr}(\mathbb{N}[\mathcal{S}_{5s}])$ from (6). No specific interference control techniques were assumed at the UEs.

AP-to-SS Interference: Table III shows that potentially very large numbers of simultaneously transmitting sectors can be supported. For example, even using a very conservative -12.2 dB of TH_{fss}, Table III shows that with increased EIRP of an AP from 62 to 74 dBm/100 MHz, the number of active AP sectors that can simultaneously transmit is kept the same for both Class 1 and Class 2 FSS systems, although the number drops for Class 3 FSS systems. This result has certain implications on the deployment of 5G systems. Specifically, an environment with higher NLoS yields lower interference into an SS receiver, due to higher attenuation of the interfering signal power. In other words, a higher density of 5G sectors can be deployed in urban areas than in suburban areas.

Fig. 2 provides a justification for this drop. It depicts the *normalized* (assuming maximum antenna gain is normalized to 0 dBi) transmit antenna gain of a sector toward an SS, which is given by $G_{ap} = -A(\phi, \theta)$ from (4) with $G_{max} = 0$. In general, an AP has a lower antenna gain toward an SS with a larger antenna array, since the beamwidth is reduced with increasing number of transmit antennas. Conversely, the antenna gain toward an SS is increased with higher number of transmit antennas if an SS falls within the main beam of an AP. The main difference between Class 3 and the other two classes is the elevation angle θ_{sat}, as depicted in Fig. 1.

According to Table II, Class 3 SSs operate at a lower elevation angle than the other two classes, thus they experience higher interference due to increased transmit antenna count at the APs.

Due to several reasons, the numbers given in Table III likely underestimate the actual number of APs that could be deployed without violating TH_{fss}. Firstly, in real-world networks, it is unlikely that all 5G sectors simultaneously transmit. In fact, in current deployments, network loading rarely exceeds 30% [29], thus allowing a roughly three-fold increase in the number of sectors given in Table III without adversely impacting FSS links. Secondly, the results only consider *outdoor* deployments. Indoor APs will not contribute to aggregate interference levels observed at the SS receivers due to very high penetration losses that occur in mmW bands. Finally, this study assumes that all APs are synchronized and analyzes interference during a downlink period when all APs are in transmit mode. If geographically-adjacent network deployments of several operators are not synchronized, then their respective downlink periods will not occur simultaneously. Thus, even a smaller percentage of APs will be in transmit mode simultaneously, whereas the remainder of active APs will be receiving uplink transmissions from UEs. As transmission of a UE is expected to have much smaller impact on an SS, the overall interference from a 5G deployment area will be further reduced. In summary, fractional network loading, indoor deployments, and unsynchronized network deployments result in a more favorable scenario than what was modeled to obtain the results in Table III.

UE-to-SS Interference: Here we provide an initial set of results on the UE-to-SS interference. The interference calculation steps mirror those for the AP-to-SS interference given in (1)-(6), but with the UE parameters given in Table I. Namely, based on the statistics of the UE antenna array gains into an SS receiver, a per-UE average interference value is computed in Table IV. From that, the number of *simultaneously transmitting* UEs is derived, given a certain interference threshold at the SS. Note that unlike on the downlink where under heavily loaded APs continuously transmit, UE transmissions on the uplink are scheduled periodically, as all available uplink slots are shared between the active UEs in a 5G cell. Assuming a typical *heavy-load* approximation of 10 active UEs per sector, the number of *active* UEs per sector becomes roughly 10 times that of the simultaneously transmitting UEs. The final numbers of supported active UEs in a 5G deployment area under various LoS/NLoS channel conditions are given in Table IV. Note that the highest probability of LoS for the UE-to-SS links was assumed to be 25%.

We make two key observations on the UE-to-SS results: i) the number of active UEs supportable in a 5G system far exceeds the number of simultaneously transmitting APs given in Table III. This is mainly due to the increased probability of NLoS for the UEs and the intermittent nature of the UE uplink transmissions, where we have assumed a per UE transmission duty cycle of 10% to convert the number of simultaneously transmitting UEs into the number active UEs.; (ii) these results may still significantly underestimate the total number of active 5G UEs that can be supported in a 5G system, as a significant fraction the UEs may be situated indoors or inside vehicles and have very high path loss towards the SS receivers.

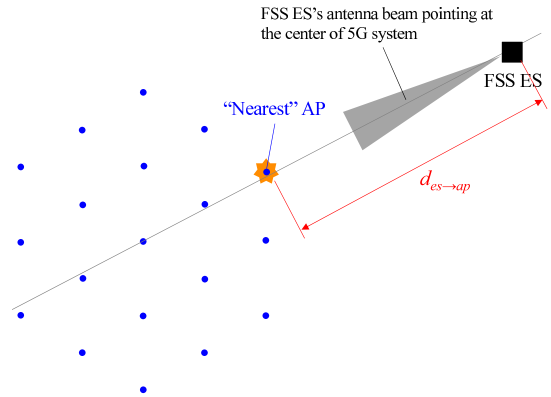

Fig. 3. Azimuth plane of a 5G-FSS ES coexistence topology.

B. Interference From FSS ES to 5G AP

1) System Model: The analysis is based on a link-level protection criterion that is defined as an I/N observed at a 5G AP receiver. Specifically for our results, the link-level protection thresholds, denoted by TH_{5g}, are set to -12.2, -6, and 0 dB of I/N. Based on the link-level protection criterion, we define a system-level interference protection criterion as the minimum distance between an FSS ES and the *edge* of the 5G system deployment, such that 95% of the 5G uplink connections in the cell nearest to the ES transmitter are protected under TH_{5g}. The distance to the edge of the system deployment is defined as the minimum distance between the ES and the 5G AP that is nearest to it. Fig. 3 illustrates an example of the 5G system layout and the definition of the minimum protection distance. The parameters used for this study refer to Table I. For the terrestrial propagation between an ES transmitter and APs, the following three models are assumed: FSPL [28], Urban Macro (UMa), and Rural Macro (RMa) [35].

Each AP activates an elevation and azimuth beam to receive the intended uplink transmission based on the preferred azimuth and elevation beam index feedback from the UE. Each UE selects its preferred elevation and azimuth beam from the elevation and azimuth codebook based on the long-term received power measurements obtained for all beams in the codebooks. For the results reported here, a codebook with 16 entries was used for beam selection in the azimuth and elevation dimensions. The beam patterns are symmetric in elevation and azimuth planes.

2) Analysis of Interference: Given the preferred azimuth and elevation beam, an interference received from an ES at a 5G AP is computed as

$$I_{es} = \frac{P_{T,es} G_{es,a} G_{ap,a}(\chi_{ue}) G_{ap,e}(\chi_{ue})}{PL_{es\to ap}(d_{es\to ap})} \tag{7}$$

where the parameters are defined in the same manner as in (1). The transmit power of the ES node is denoted by $P_{T,es}$. The azimuth pattern of an ES, $G_{es,a}$, is defined in [34]. For the interference analysis, the value of $EIRP_{es} = P_{T,es} + G_{max,es}$

[14]

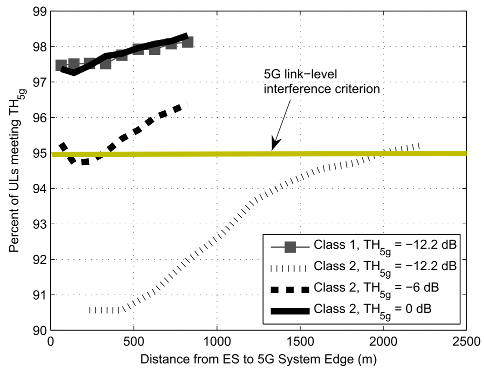

Fig. 4. 5G uplinks with Classes 1 and 2 ES under FSPL.

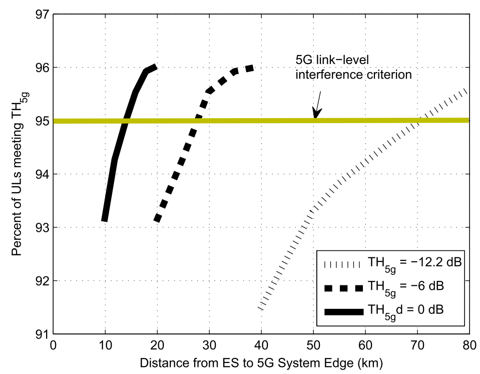

Fig. 5. 5G uplinks with Class 3 ES under FSPL.

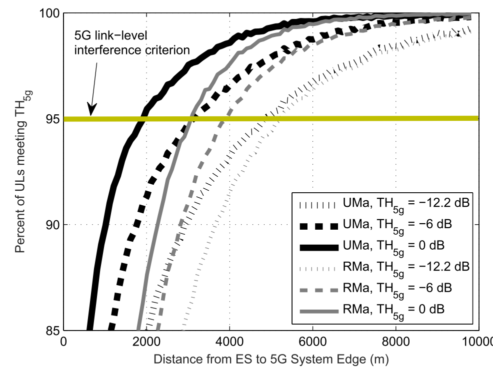

Fig. 6. 5G uplinks with Class 3 ES under UMa and RMa.

TABLE V
REQUIRED SEPARATION DISTANCE UNDER UMa AND RMa

	UMa			RMa		
TH_{5g} (dB)	-12.2	-6	0	-12.2	-6	0
Required $d_{es\rightarrow ap}$ (m)	4,900	3,000	2,000	5,100	4,000	3,000

(where $G_{max,es}$ is the maximum transmit antenna gain for the ES node) is specified according to the three classes of ES transmitters [29] given by: 12.2, 24.1, and 48 dBm/MHz for Class 1, 2, and 3, respectively.

Given a certain level of $EIRP_{es}$ and position of the ES relative to the 5G system layout, an ES-to-5G interference is calculated for every UE attached to the *nearest* AP. Each calculation is performed with randomized positions of the UEs in the system and randomized positions of the ES around the 5G system layout, with variation of $d_{es\rightarrow ap}$. It is assumed that the ES antenna azimuth is always directed toward the center of the 5G system layout.

3) Evaluation of Interference: Figs. 4 and 5 demonstrate cumulative distribution functions (CDFs) of the uplink connections computed over all UE positions in the nearest cell as a function of $d_{es\rightarrow ap}$ for Classes 1 and 2, and for Class 3, respectively. Given the 95% protection target, the minimum $d_{es\rightarrow ap}$ can be determined from Figs. 4 and 5. As evident in the figures, the required $d_{es\rightarrow ap}$ is highly dependent on TH_{5g} as well as $EIRP_{es}$ toward the 5G system.

Based on the above results, we observe that the required values of $d_{es\rightarrow ap}$ are reasonable in most cases of interest and will not place an overly restrictive set of constraints on future 5G system deployments. With a protection margin of -6 dB I/N, the distance where less than 5% of links fall below the protection threshold TH_{5g} is less than 400 m for Class 2 ESs and less than 50 m for Class 1 ESs. While our calculations show that Class 3 ESs nominally could interfere with 5G systems at a distance of 28 km with a -6 dB of I/N threshold, we believe that this distance could be significantly smaller in practice due to additional clutter loss between 5G APs and ES transmitters not accounted in the FSPL model.

To more accurately model the terrestrial propagation effect, such as the clutter loss, we also generated results using the 3GPP UMa and RMa models [35] for Class 3 ES transmitters. The 3GPP UMa and RMa path loss models exhibit much higher path loss exponents than the FSPL and are more appropriate for terrestrial propagation modeling. Fig. 6 exhibits the percent of 5G uplinks below TH_{5g} in presence of interference from an FSS ES based on Class 3. Compared to Fig. 5, $d_{es\rightarrow ap}$ is dramatically reduced. This implies that a 5G system experiences lower interference from an ES when deployed in an environment with higher attenuation–mainly due to higher probability of NLoS propagation conditions.

Table V shows the results with both 3GPP path loss models for Class 3 ES transmitters for various I/N thresholds. As expected, the RMa model requires a larger distance for interference protection, since in general it predicts higher LoS probability as a function of distance and has a lower path loss exponent than UMa. Specifically, the table indicates that the worst case of protection distance of 5,100 m occurs with RMa and the most restrictive threshold of TH_{5g} (-12.2 dB).

III. COEXISTENCE OF 5G WITH FIXED SERVICE AT 70 GHz

In this section, we discuss co-channel coexistence of 5G at 70 GHz where the Fixed Service (FS) is the incumbent system. We consider a point-to-point Wireless Backhaul (WB) system that adopts highly directional antennas to connect distant radio towers. Note that the FS system provides backhaul for another cellular system, thus it is uncoordinated with the 5G.

Unlike the 28-GHz coexistence problem, there are four possible interference scenarios: FS to AP, AP to FS, FS to UE, and UE to FS. The reasons are as follows: (i) both directions of an FS system's wireless link transmit in the 70 GHz band; (ii) a UE has higher probability of LoS than in the coexistence

TABLE VI
PARAMETERS FOR 70-GHz COEXISTENCE

Parameter	5G		FS
Carrier frequency	73.5 GHz		
Path loss model [35]	UMa and UMi		
Bandwidth	1 GHz		
System	AP	UE	WB
Transmit power	15 dBm per element	14 dBm per element	19 dBm
Max antenna gain	8 dBi per element	5 dBi per element	50 dBi
Temperature	290 K	290 K	290 K
Noise figure	7 dB	9 dB	5 dB
Antenna height	10 m	1.5 m	25 m
Number of antennas	8×8 and 16×16 ($\lambda/2$ array)	Omni and 4×4 ($\lambda/2$ array)	

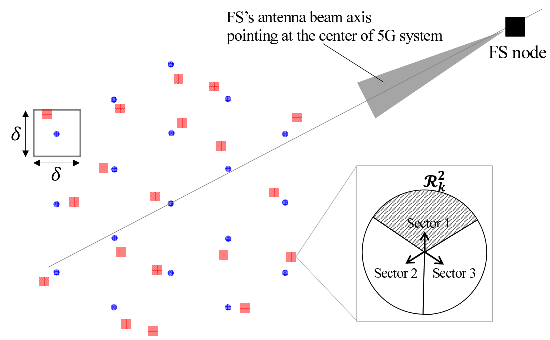

Fig. 7. Topology of a 5G-FS coexistence.

at 28 GHz since the beam of an FS's antenna is placed terrestrially and pointed closer toward the ground.

Note that this analysis framework is sufficiently general in that it can be readily applied to coexistence scenarios between 5G and other terrestrial incumbent system.

A. System Model

The parameters for 5G and FS are summarized in Table VI. Note that the parameters of 5G are different from the ones used in the 28 GHz coexistence of Section II. Since the rules are still under discussion by the FCC for the 70 GHz band, the parameters are obtained from a standard 3GPP evaluation model [37]. We assume 19 cell sites–equivalently 19 APs–where in total $\mathbb{N}[\mathcal{S}_{5s}] = 57$ sectors exist.

Fig. 7 describes a *drop*–or an instance–of topology for coexistence. There are two important assumptions: (i) the FS node is regarded as a transmitter in an FS-to-5G interference scenario while it is a receiver in a 5G-to-FS interference situation; (ii) the FS node points its beam at the center of the 5G system. The interference between the 5G and the FS nodes is a function of at least four variables corresponding to the positions of transmitters and receivers in the interferer and victim systems. Since the FS node is always assumed to point its beam at the center of the 5G system, position of the FS receiver in the FS-to-5G scenario and position of FS transmitter in the 5G-to-FS scenario can be excluded from consideration. In Fig. 7, the FS node is placed outside of the 5G system, at 176 different positions on an r-θ coordinate: $r = [0 : 500 : 10,500]$ and $\theta = [0 : \frac{\pi}{4} : \frac{7\pi}{4}]$ in reference to the center of the 5G system.

The blue circles in Fig. 7 correspond to positions of the APs in a classical hexagonal cell layout with Inter-Site Distance (ISD) of 200 m. The actual positions of APs (red squares) are *dithered* within δ m relative to the locations of the hexagonal cells, to achieve a more realistic system layout. Furthermore, we uniformly and randomly distribute 10 UEs in the kth sector region, denoted by $\mathcal{R}_k^2$. The distribution of UEs can be modeled as a homogeneous PPP [27] whose density is kept constant to be $\lambda_{ue} = 10$ over $\mathcal{R}_k^2, k = 1, 2, \cdots, \mathbb{N}[\mathcal{S}_{5s}] = 57$.

For the path loss model, we use the 3GPP UMa and UMi [35]. The models are used both for the 5G-FS and AP-UE links. Again, although 3GPP defines path loss models for outdoor and indoor scenarios, this paper discusses the 5G placed outdoor only since the FS devices are likely placed outdoors and penetration losses at 70 GHz are very high.

The antenna element pattern for the 5G system refers to (2) through (4) in Section II-A. The antenna beam pattern for an FS device is provided in [36] as

$$G_{fs}(\theta) = \begin{cases} G_{max} - 2.5 \times 10^{-3} \left(\frac{D}{\lambda}\theta\right)^2, & 0^\circ < \theta < \theta_m \\ G_1, & \theta_m \le \theta < \theta_r \\ 32 - 25 \log \theta, & \theta_r \le \theta < 48^\circ \\ -10, \ [\text{dB}] & 48^\circ \le \theta \le 180^\circ \end{cases} \tag{8}$$

where G_{max} is a maximum gain; D is antenna diameter; λ is a wavelength; $G_1 = 2 + 15 \log \frac{D}{\lambda}$: gain of the first sidelobe; $\theta_m = \frac{20\lambda}{D}\sqrt{G_{max} - G_1}$ in degrees; $\theta_r = 15.85 \left(\frac{D}{\lambda}\right)^{-0.6}$ in degrees.

B. Analysis of Interference

1) Coexistence Topology: We now discuss a general framework for interference analysis that is applicable to all the four scenarios of interference, where the key is to analyze how antenna gains are determined for: (i) the interferer system's transmitters and (ii) the victim system's receivers. Let $\mathrm{x} = (x, y)$ denote position of a node on a two-dimensional Cartesian coordinate plane. Subscripts "i" and "v" indicate the "interferer" and "victim", respectively, and "t" and "r" denote "transmitter" and "receiver", respectively. Without loss of generality, we consider the AP-to-FS interference where $\mathrm{x}_{i,t}$, $\mathrm{x}_{i,r}$, and $\mathrm{x}_{v,r}$ denote the positions of an AP, a UE, and the FS receiver respectively. The method can be extended to the other scenarios (i.e., FS to AP, UE to FS, and FS to UE).

Fig. 8 illustrates the azimuth plane of an AP-to-FS interference scenario. There are two angles that determine the interference level between a 5G AP and the FS node: the off-axis angle, ϕ_{off}, and the steering angle, ϕ_{str}. A ϕ_{str} is an angle between the direction of a beamforming and the antenna's physical orientation. Such an electrical steering is only assumed for the 5G (i.e., APs and UEs), whereas the FS assumed to be equipped with fixed beam antennas. Also, we define an *interference axis* to be a line connecting the interfering transmitter (the AP) and the victim receiver (the FS receiver). A ϕ_{off} is an angle between the direction of a beamforming and the interference axis. These angles will be used in the analysis to represent discrimination of antenna gain from: (i) electrical steering and (ii) pointing away from the FS receiver, respectively.

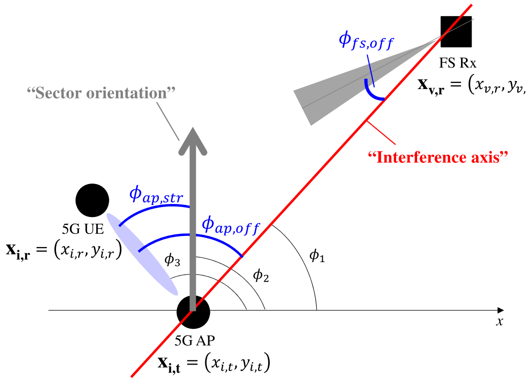

Fig. 8. 5G AP as interferer on the azimuth plane (Cell orientation of 90°).

For defining the angles, we put an azimuth-plane geometry on a quadrant and set $\mathrm{x}_{i,t}$ at the origin of the quadrant. The angle formed by the interference axis with respect to the X-axis is denoted by ϕ_1. The angle of a sector's physical orientation is denoted by and set as $\phi_2 = 90°$. The beamforming angle with respect to the X-axis of the quadrant is denoted as ϕ_3. Now we can define ϕ_{off} and ϕ_{str} for the 5G AP and FS receiver as

$$\phi_{ap,off}\left(\mathrm{x}_{i,t}, \mathrm{x}_{i,r}, \mathrm{x}_{v,r}\right) = \phi_3 - \phi_1 \tag{9}$$

$$\phi_{ap,str}\left(\mathrm{x}_{i,t}, \mathrm{x}_{i,r}\right) = \phi_3 - \phi_2 \tag{10}$$

$$\phi_{fs,off}\left(\mathrm{x}_{i,t}, \mathrm{x}_{v,t}, \mathrm{x}_{v,r}\right) = \arccos\left(\frac{\left(\mathrm{x}_{v,t} - \mathrm{x}_{v,r}\right) \cdot \left(\mathrm{x}_{i,t} - \mathrm{x}_{v,r}\right)}{\|\mathrm{x}_{v,t} - \mathrm{x}_{v,r}\| \|\mathrm{x}_{i,t} - \mathrm{x}_{v,r}\|}\right) \tag{11}$$

where $(\cdot)$ in (11) indicates a dot product between two vectors, and

$$\phi_1 = \arctan\left(\mathrm{x}_{v,r}, \mathrm{x}_{i,t}\right) = \arctan\left(\frac{y_{v,r} - y_{i,t}}{x_{v,r} - x_{i,t}}\right) \tag{12}$$

$$\phi_3 = \arctan\left(\mathrm{x}_{i,r}, \mathrm{x}_{i,t}\right) = \arctan\left(\frac{y_{i,r} - y_{i,t}}{x_{i,r} - x_{i,t}}\right). \tag{13}$$

Now, denote azimuth and elevation planes by subscripts "a" and "e," respectively. Then two types of attenuation, $A_{ap,a,off}\left(\phi_{ap,off}\right)$ and $A_{ap,a,str}\left(\phi_{ap,str}\right)$, can be obtained by substituting $\phi_{ap,off}$ and $\phi_{ap,str}$ into $A_a(\phi)$ in (2), where $\phi_{ap,off,3db} = 6°$ and $\phi_{ap,str,3db} = 65°$ [35].

Fig. 9 describes an elevation plane of the interference scenario of interest. Similarly to the azimuth-plane analysis, the off-axis angles of the interfering transmitter and the victim receiver, $\theta_{ap,off}$ and $\theta_{fs,off}$, are defined with respect to the interference axis. The angles can be calculated based on locations and heights, which are given by

$$\theta_{ap,off} = \arctan\left(\frac{h_{v,r} - h_{i,t}}{\|\mathrm{x}_{v,r} - \mathrm{x}_{i,t}\|}\right) + \theta_{ap,str} \tag{14}$$

$$\theta_{fs,off} = \arctan\left(\frac{h_{v,r} - h_{v,t}}{\|\mathrm{x}_{v,r} - \mathrm{x}_{v,t}\|}\right). \tag{15}$$

Note that although it is set $h_{v,t} = h_{v,r}$ in Fig. 9, it can be generalized as in (15). Again, by substituting $\theta_{ap,off}$ into $A_e(\theta)$ in (2), we can obtain $A_{ap,e,off}\left(\theta_{ap,off}\right)$ with $\theta_{ap,off,3db} = 6°$ and $\theta_{ap,str,3db} = 65°$ [35].

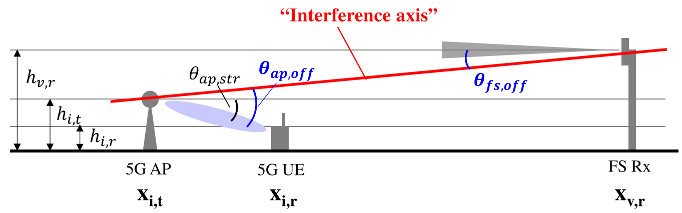

Fig. 9. 5G AP as interferer on the elevation plane.

Also, for the FS receiver, the azimuth and elevation off-axis angles, $\phi_{fs,off}$ and $\theta_{fs,off}$, are substituted into (8) to obtain the $G_{fs}\left(\phi_{fs,off}\right)$ and $G_{fs}\left(\theta_{fs,off}\right)$.

2) Analysis Framework: An interference power received at a victim receiver is computed as

$$I = \frac{P_T G_i\left(\phi_i, \theta_i\right) G_v\left(\phi_v, \theta_v\right)}{PL\left(\mathrm{x}_{i,t}, \mathrm{x}_{v,r}\right)} \tag{16}$$

where P_T denotes a transmit power of the interferer system's transmitter; $G(\cdot)$ denotes an antenna gain that is given in (4). Again, for a 5G device (either AP or UE), the angles $\phi_{i \text{ or } v}$ and $\theta_{i \text{ or } v}$ include ϕ_{off} and ϕ_{str}, and θ_{off} and θ_{str}. It is important to note that although not explicitly expressed, an I is a function of $\left(\mathrm{x}_{i,t}, \mathrm{x}_{v,t}, \mathrm{x}_{v,r}\right)$ in an FS-to-5G interference and $\left(\mathrm{x}_{i,t}, \mathrm{x}_{i,r}, \mathrm{x}_{v,r}\right)$ in a 5G-to-FS interference, which can be expressed through (9) and (11) and written as

$$I = \begin{cases} I_{fs \to ap}\left(\mathrm{x}_{i,t}, \mathrm{x}_{v,t}, \mathrm{x}_{v,r}\right) \\ I_{ap \to fs}\left(\mathrm{x}_{i,t}, \mathrm{x}_{i,r}, \mathrm{x}_{v,r}\right). \end{cases} \tag{17}$$

Also, $PL(\cdot)$ is a path loss that is a function of $\mathrm{x}_{i,t}$ and $\mathrm{x}_{v,r}$. By generalizing an expression for path loss given in [35] as $PL = \xi d^{\alpha}$ where d is a distance, one can rewrite (16) as

$$I = P_T G_i\left(\phi_i, \theta_i\right) G_v\left(\phi_v, \theta_v\right) \xi^{-1} \|\mathrm{x}_{i,t} - \mathrm{x}_{v,r}\|^{-\alpha}. \tag{18}$$

3) 5G as Interferer: Based on (18), we can calculate 5G-to-FS interference. The analysis focuses on the AP-to-FS interference only but can readily be extended to the UE-to-FS scenario. We consider an aggregate AP-to-FS interference with the 5G system that is fully loaded in both downlink and uplink. An aggregate interference is defined as an interference that is received at a *victim* FS receiver at $\mathrm{x}_{v,r}$ from all the 5G sectors, which can be formulated as

$$\begin{aligned} I_{aggr} &= \sum_{k=1}^{\mathbb{N}[\mathcal{S}_{5s}]} I_{ap \to fs}^{(k)}\left(\mathrm{x}_{i,t}^{(k)}, \mathrm{x}_{i,r}^{(k)}, \mathrm{x}_{v,r}\right) \\ &= P_T \xi^{-1} \sum_{k=1}^{\mathbb{N}[\mathcal{S}_{5s}]} G_i^{(k)}\left(\phi_i, \theta_i\right) G_v^{(k)}\left(\phi_v, \theta_v\right) \|\mathrm{x}_{i,t}^{(k)} - \mathrm{x}_{v,r}\|^{-\alpha} \end{aligned} \tag{19}$$

where a superscript (k) indicates that the quantity is defined for a sector region, $\mathcal{R}_k^2$; a set of AP sectors is denoted by $\mathcal{S}_{5s}$.

Now we need to compute the mean of aggregate interference over all the possible positions of $\mathrm{x}_{i,t}^{(k)}$, $\mathrm{x}_{i,r}^{(k)}$ and $\mathrm{x}_{v,r}$, which is given by

$$
\begin{aligned}
&\bar{I}_{aggr} \\
&= \mathbb{E}\left[I_{aggr}\right] \\
&= \underbrace{\frac{1}{\mathbb{N}\left[\mathcal{S}_{fs}\right]}\sum_{\mathcal{S}_{fs}}}_{\text{average of } \mathrm{x}_{v,r}} \sum_{k=1}^{\mathbb{N}[\mathcal{S}_{5s}]} \underbrace{\frac{1}{\delta^2}\int_{\mathrm{x}_{i,t}^{(k)}}}_{\text{average of } \mathrm{x}_{i,t}^{(k)}} \underbrace{\frac{1}{\left|\mathcal{R}_k^2\right|}\int_{\mathrm{x}_{i,r}^{(k)}\in\mathcal{R}_k^2}}_{\text{average of } \mathrm{x}_{i,r}^{(k)}} \\
&\qquad \left(I_{ap\rightarrow fs}^{(k)}\right) d\mathrm{x}_{i,r}^{(k)} d\mathrm{x}_{i,t}^{(k)} \\
&= \frac{P_T\xi^{-1}}{\delta^2\left|\mathcal{R}_k^2\right|\mathbb{N}\left[\mathcal{S}_{fs}\right]}\sum_{\mathcal{S}_{fs}}\sum_{k=1}^{\mathbb{N}[\mathcal{S}_{5s}]}\int_{\mathrm{x}_{i,t}^{(k)}}\int_{\mathrm{x}_{i,r}^{(k)}\in\mathcal{R}_k^2} \\
&\quad \left(G_i^{(k)}\left(\phi_i,\theta_i\right)G_v^{(k)}\left(\phi_v,\theta_v\right)\left\|\mathrm{x}_{i,t}^{(k)}-\mathrm{x}_{v,r}\right\|^{-\alpha}\right) d\mathrm{x}_{i,r}^{(k)} d\mathrm{x}_{i,t}^{(k)}
\end{aligned}
\tag{20}
$$

where $\mathcal{S}_{fs}$ denotes a set of positions of the FS node. The integral expression in (20) is not amenable to analytic evaluation due to high complexity in calculation. Therefore, in the rest of the paper we evaluate (20) via Monte-Carlo simulations.

4) 5G as Victim: The FS-to-5G interference is a *per-sector* interference power averaged over the $\mathbb{N}[\mathcal{S}_{5s}] = 57$ sectors. As above and without loss of generality, we analyze the FS-to-AP interference scenario in detail, and this analysis is applicable to the FS-to-UE interference scenario by replacing parameters for the AP with those for the UE. From (19), the average interference that is received at an AP located at $\mathrm{x}_{v,r}^{(k)}$ and pointing its receive beam at a UE located at $\mathrm{x}_{v,t}^{(k)}$ in $\mathcal{R}_k^2$ can be formulated as

$$
I_{avg} = \frac{1}{\mathbb{N}\left[\mathcal{S}_{5s}\right]}\sum_{k=1}^{\mathbb{N}[\mathcal{S}_{5s}]} I_{fs\rightarrow ap}^{(k)}\left(\mathrm{x}_{v,t}^{(k)}, \mathrm{x}_{v,r}^{(k)}, \mathrm{x}_{i,t}\right). \tag{21}
$$

Similarly to (20), an average of (21) over all the possible positions of $\mathrm{x}_{v,t}^{(k)}$, $\mathrm{x}_{v,r}^{(k)}$, and $\mathrm{x}_{i,t}$ can be calculated as

$$
\begin{aligned}
\bar{I}_{avg} &= \mathbb{E}\left[I_{avg}\right] \\
&= \mathbb{E}\left[\frac{1}{\mathbb{N}\left[\mathcal{S}_{5s}\right]}\sum_{k=1}^{\mathbb{N}[\mathcal{S}_{5s}]} I_{fs\rightarrow ap}^{(k)}\left(\mathrm{x}_{v,t}^{(k)}, \mathrm{x}_{v,r}^{(k)}, \mathrm{x}_{i,t}\right)\right].
\end{aligned}
\tag{22}
$$

C. Evaluation of Interference

Similarly to the ES-to-AP interference study, we adopt I/N as our coexistence interference metric, which is defined according to the direction of interference as

$$
(\mathrm{I/N})_{ap \text{ or } ue\rightarrow fs} = \bar{I}_{aggr}/N_{th,fs} \tag{23}
$$

$$
(\mathrm{I/N})_{fs\rightarrow ap \text{ or } ue} = \bar{I}_{avg}/N_{th,ap \text{ or } ue} \tag{24}
$$

where $N_{th,(\cdot)}$ is the thermal noise power of a receiver device according to the system type.

As mentioned in Section II, TH_{5g} of -6 and 0 dB are typically used for mobile terrestrial systems. An TH_{fs} of -10 dB was chosen for the FS as per [38].

Recall from (20) and (22) that the 5G-to-FS interference metric is aggregated whereas the FS-to-5G interference is

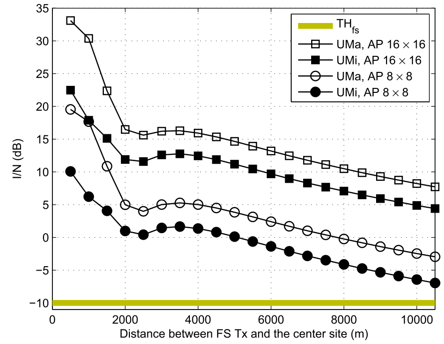

Fig. 10. Interference from 5G APs to FS.

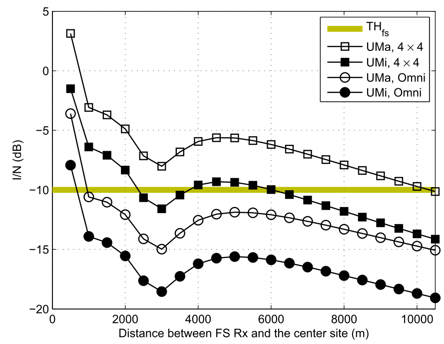

Fig. 11. Interference from 5G UEs to FS.

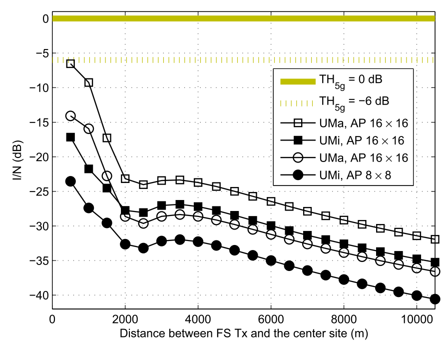

Fig. 12. Interference from FS to 5G APs.

averaged over $\mathbb{N}[\mathcal{S}_{5s}] = 57$ sectors in the 5G system. This is why 5G-to-FS interference is more significant, as observed in Figs. 10 through 13. It is shown in Figs. 10 and 11 that the 5G-to-FS interference is above the interference protection criterion of the FS, $TH_{fs} = -10$ dB of I/N, in many cases where the FS node is situated in the proximity of the 5G system. On the other hand, Figs. 12 and 13 show that the FS-to-5G interference is below the interference protection criterion of the 5G, $TH_{5g} = -6$ and 0 dB of I/N, in all cases of interest. Comparing both sets of figures, it is consistently observed that UMi yields lower interference than UMa, in both scenarios of 5G-to-FS and FS-to-5G interference. This is because UMi predicts a higher propagation loss which in turn leads to a lower interference signal power.

One interesting observation is that an *inflection point* is observed in the region of 2,000 to 4,000 m, in all of Figs. 10 through 13. To analyze this phenomenon, we consider a single AP and place it at the center of the 5G system (see Fig. 7 for

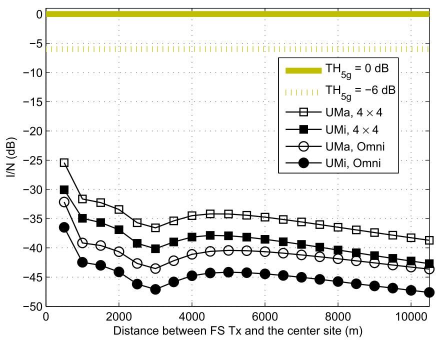

Fig. 13. Interference from FS to 5G UEs.

the layout). We found two dominant factors contributing to the AP-to-FS interference: (i) the elevation antenna gain of the FS node, $G_{fs,e}(\theta_{fs,off})$, and (ii) the path loss from the AP to the FS as a function of distance, $PL_{5g\to fs}$. Fig. 14 shows the two factors separately, and the resulting I/N with the two factors combined. In Fig. 14a, around the region of 3,000 to 3,500 m, $G_{fs,e}(\theta_{fs,off})$ increases by 8.35 dB while $PL_{5g\to fs}$ drops by only 2.3 dB in Fig. 14b. Therefore, in Fig. 14c, the resulting I/N increases by 5.73 dB which causes an inflection point. We note that the elevation antenna gain curve is the result of the FS antenna beam pattern model adopted by the ITU [36]. Hence, the behavior of I/N is dependent on the specific properties of the FS node antenna pattern.

IV. Mitigation of Interference From 5G Into Fixed Service

As demonstrated in Section III, in the coexistence between 5G and FS, the 5G-to-FS interference is more problematic due to aggregation of interference from multiple 5G sectors. This section proposes practical mechanisms to mitigate AP-to-FS and UE-to-FS interference. Although the proposed mechanisms refer to the system model and parameters discussed in Section III, these mechanisms can be applied to any interference scenario where a 5G system adopting high-gain steerable directional antennas coexists with a terrestrial incumbent system.

The key idea of the proposed mitigation methods is to prohibit transmissions from 5G nodes (APs or UEs) with transmit beams pointing at the victim FS receiver. In other words, the 5G transmitters are driven to point the beams away enough from the FS receiver so that they have sufficiently attenuated transmit gains toward the FS.

A. Mitigation of AP-to-FS Interference

Without loss of generality, let us consider beam restriction techniques on the azimuth plain. For an AP, $\phi_{ap,off}$ and $\phi_{ap,str}$ are recalled from Fig. 8 as an off-axis angle and a steering angle. Note that the antenna gain of an AP's beam attenuates as it: (i) points further away from the FS receiver and (ii) gets further away from the sector's physical orientation. The victim FS receiver can undergo a lower interference if the transmit beam from an AP is sufficiently attenuated based on the two factors. To measure the two types of attenuation, we define the thresholds Φ_{off} and Φ_{str} that $\phi_{ap,off}$ and $\phi_{ap,str}$ must exceed, respectively. Fig. 15 illustrates the thresholds. If a beam is with $\phi_{ap,off} \le \Phi_{off}$, it means that the beam points closer at the FS receiver than allowed. Similarly, if $\phi_{ap,str} \le \Phi_{str}$, the beam is attenuated less than allowed by electrical steering.

Therefore, we shut down a beam if it does not meet $\phi_{ap,off} > \Phi_{off}$ and $\phi_{ap,str} > \Phi_{str}$ at the same time, which is formulated based on (4) as

$$G_{ap}\left(\phi_{ap,off},\phi_{ap,str}\right) = \begin{cases} G_{ap}\left(\phi_{ap,off},\phi_{ap,str}\right), & \phi_{ap,off} > \Phi_{off} \text{ and } \phi_{ap,str} > \Phi_{str} \\ 0, & \text{otherwise.} \end{cases} \tag{25}$$

Now, we can rewrite (16) to depict that an AP is the interfering transmitter and the FS is the victim receiver as

$$I^{(k)}_{ap\to fs} = \frac{P_{T,ap}G_{ap}\left(\phi_{ap,off},\phi_{ap,str}\right)G_{fs}\left(\phi_v,\theta_v\right)}{PL_{ap\to fs}\left(\mathrm{x}_{ap},\mathrm{x}_{fs}\right)} \tag{26}$$

where $P_{T,ap}$ denotes transmit power of an AP. Thus, an AP-to-FS interference aggregated over the $\mathbb{N}[\mathcal{S}_{5s}] = 57$ sectors is obtained by substituting (26) into (19), which now reflects the proposed interference mitigation method.

As mentioned in Section I, this proposed method enables each AP to autonomously (without the need of an inter-system infrastructure) identify the beams that are to be avoided and perform the interference mitigation. The reason is that for the computation of Φ_{off}, the only information that an AP needs is location of the victim FS receiver. It can be learned from the license data registered to the FCC because all the FS devices in the 70 GHz band are required to register.

The proposed method is integrated into a realistic protocol that utilizes 5G interface as follows:

1) Define (a) Beam Exclusion Zone(s) at Each AP: Each AP constructs (an) exclusion zone(s), which is defined as an intersection (highlighted in light green in Fig. 15) of two fan-shaped areas that are formed by the following two inequalities: (i) $\phi_{ap,off} < \Phi_{off}$ and (ii) $\phi_{ap,str} < \Phi_{str}$.

2) Shut Down the Interfering Beams: The interfering beams are identified as the beams in the exclusion zones. Downlink pilot transmissions corresponding to these beams are also shut down (or transmitted at reduced power levels) during the 5G beam scanning intervals. This enables 5G UEs to exclude such interfering beams during their initial beam attachment or periodic beam re-selection process. A UE requesting an attachment in an exclusion zone is handed over to another sector through a re-selection process.

B. Mitigation of UE-to-FS Interference

The method of mitigating UE-to-FS interference is also a two-step process as follows:

1) Identify the Interfering UE Based on its Uplink Reference Signal: The proposed UE-to-FS interference mitigation technique is similar to the AP-to-FS interference mitigation. It aims to reduce interference caused by UEs, based on identification of the specific beams causing unacceptable interference at the FS receiver. Hence it also refers to (26), but with the parameters for the UE.

[14]

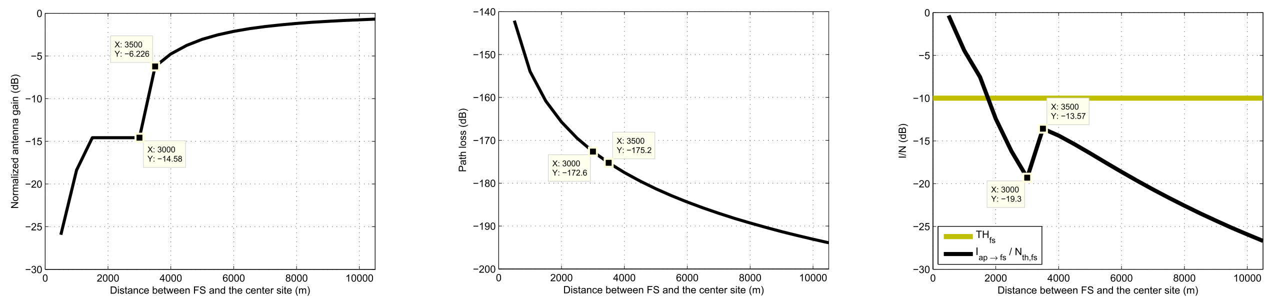

(a) $G_{fs,e}\left(\theta_{fs,off}\right)$ (b) $PL_{5g\rightarrow fs}$ (c) Resulting AP-to-FS interference

Fig. 14. Non-convexity in 5G-to-FS interference.

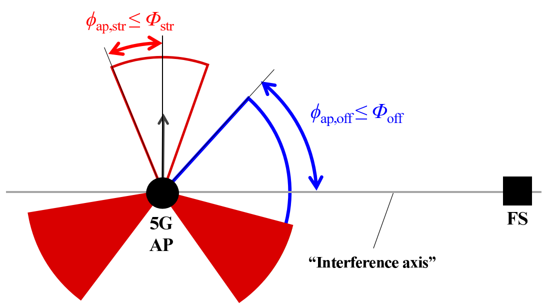

Fig. 15. Definition of exclusion zone at a 5G AP.

However, the key problem with identification of the interfering UEs is that in general only the AP is aware of which of its UEs are assigned to transmit during a certain uplink time slot. As a solution, this paper proposes a *probe-based* method where a 5G probe device is co-located with the victim FS receiver. The probe measures and reports its uplink Reference Signal Received Power (RSRP) measurements to the 5G system server. The probe device is frame-synchronized with the 5G system and may rely on the uplink 5G air-interface beam measurement procedures. Also, the antenna characteristics of the probe device should match those of the FS node (Table VI), which enables the probe to accurately track UE-generated interference as received by the FS node.

To enable interfering UE identification by the 5G system, it is proposed for the emerging 5G air interface to embed a cell-specific identification signal into the uplink Demodulation Reference Signal (DMRS). The cell-specific identification signal can take a form of a pseudo-noise (PN) sequence with a particular index of the sequence tied a particular 5G cell in which the uplink transmission was performed. Given the probe's RSRP report and the identity of the cell in which the interfering transmission has occurred, the 5G system can readily identify the interfering UE(s) by learning the particular frame and cell of the interfering transmission(s).

2) Hand Over the Interfering UEs to Another Sector: Given that the interfering UEs have been successfully detected and identified, the 5G system initiates a handover of the interfering UEs to another sector. Because of the highly directional transmit beams deployed by the 5G UEs on the uplink, simply handing over the interfering UEs will very likely change the direction of the UEs' transmit beams even if the UEs remains stationary. This change in the transmit beam direction will mitigate or even fully eliminate the interference observed at the FS node prior to the handover.

V. Evaluation of the Proposed Interference Mitigation Technique

We evaluate performance of the interference mitigation methods that are discussed in Section IV. The settings and parameters for the evaluation refer to Table VI of Section IV.

A. Evaluation Method

We assess the proposed interference mitigation techniques in the following two aspects: (i) 5G-to-FS interference and (ii) impact on performance of the 5G system itself. Firstly, the improvement in the 5G-to-FS interference is calculated based on (23). Secondly, the application of the proposed AP and UE interference mitigation methods will invariably lead to performance degradation of the 5G system, since the AP interference mitigation technique restricts the selection of beams available for UE attachment on the downlink and forces handover to a possibly suboptimum attachment point for the UE interference mitigation on the uplink. We characterize this performance degradation by computing downlink SINR and uplink SNR before and after applying the downlink and uplink interference mitigation techniques.

For the downlink, a signal-to-interference-plus-noise ratio (SINR) that is measured at a UE in the jth sector, $\mathcal{R}_j^2$, is calculated as

$$\text{SINR} = \frac{P^{(j)}_{R,ue} G_{ue} G_{ap}}{N_{th,ue} + \sum_{k\in\mathbb{N}[\mathcal{S}_{5s}],k\neq j} P^{(k)}_{R,ue}}. \tag{27}$$

where $P^{(j)}_{R,ue}$ denotes the signal power that the UE receives from the jth sector's antenna. Note that this SINR does not include the interference from the FS; referring to Fig. 12, the FS-to-AP interference is insignificant compared to the noise level observed at the UEs.

For the uplink, a signal-to-noise ratio (SNR) at an AP is obtained as

$$\text{SNR} = \frac{P^{(j)}_{R,ap} G_{ap} G_{ue}}{N_{th,ap}}. \tag{28}$$

where $P^{(j)}_{R,ap}$ denotes a signal power received at the jth sector. Similarly, the FS-to-UE interference is excluded since it has

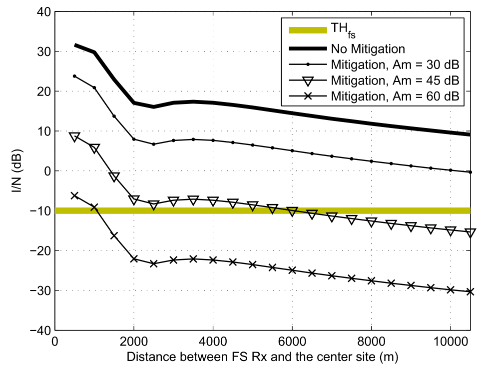

Fig. 16. Mitigation of AP-to-FS interference.

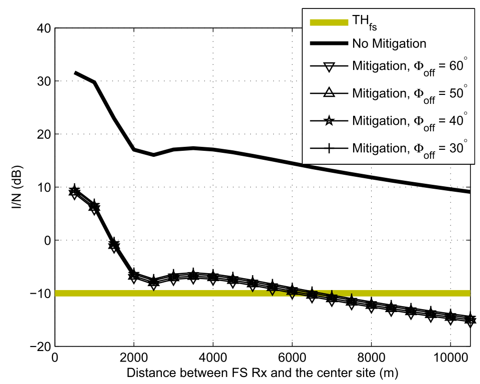

Fig. 17. Reduction of Φ_{off} ($\Phi_{str} = 60°$, $A_m = 45$ dB).

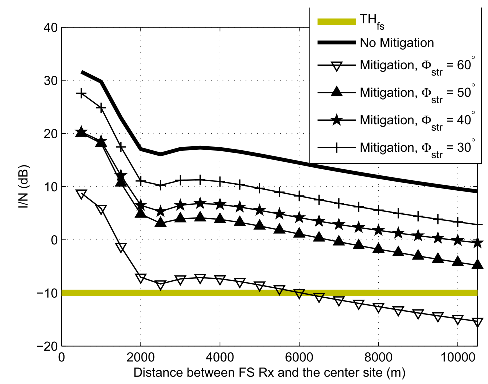

Fig. 18. Reduction of Φ_{str} ($\Phi_{off} = 60°$, $A_m = 45$ dB).

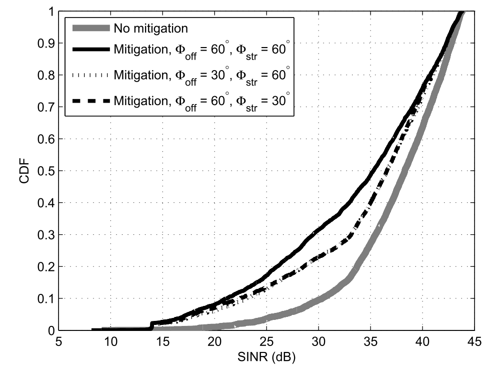

Fig. 19. Impact of Φ_{off} and Φ_{str} on the 5G downlink SINR.

little impact on the SNR as observed from Fig. 13. As a further simplification, we note that the uplink performance is noise-limited due to lower UE transmit powers and also exclude inter-cell interference from calculation of the uplink SNR.

B. AP-to-FS Interference Mitigation

Fig. 16 shows the impact of the proposed interference mitigation technique on the AP-to-FS interference. Note that the decrease in AP-to-FS interference follows the corresponding increase in sector antenna's front-to-back ratio, A_m; this is especially pronounced in the region of AP-to-FS distance of 2,000 m or more. That is, a 15 dB increase in A_m roughly results in a 15 dB decrease in I/N. This effect demonstrates that the dominant interfering beams in the sectors that are pointed directly at the FS node have been suppressed and the interference is now largely dependent on the power received from the sectors that are pointed away from the FS node.

As the performance of the 5G system can be adversely affected by the size of a beam exclusion zone, here we explore the sensitivity of the resulting I/N at the FS node to the size of the exclusion zone at an AP. Reduction of exclusion zone can be achieved by reduction of either Φ_{off} or Φ_{str}, defined above in Fig. 15. Impacts of reduction of the two thresholds are shown in Figs. 17 and 18. Reducing the exclusion zone according to Φ_{off} does not result in a significant increase in AP-to-FS interference, as shown in Fig. 17. On the other hand, Fig. 18 shows that reduction of exclusion zone according to Φ_{str} significantly increases AP-to-FS interference.

The reason for this behavior is explained in Fig. 20. Each subfigure shows a cumulative snapshot of 10 drops with 10 UEs dropped per sector. For consistency with the topology shown in Fig. 15, the victim FS node is fixed at $(x, y) = (500, 0)$ which is on the right side of the cell; thus the interference axis is defined as a horizontal line passing through the AP at $(0, 0)$ in each subfigure. The red dots represent the UEs in the exclusion zone, while the blue ones indicate those outside of the zone where downlink transmissions are allowed. Let us begin with the case of $\Phi_{off} = 60°$, $\Phi_{str} = 60°$ that is given in Fig. 20a. The cases where the thresholds Φ_{off} and Φ_{str} are reduced are presented in Figs. 20b and 20c, respectively. In Fig.20b, reduction of Φ_{off} opens up a beam transmission area that is further away from the interference axis, which does not translate into increased interference at the FS node. On the other hand, in Figs. 20c, reduction of ϕ_{str} opens up an area with interfering beam transmissions that is closer to the interference axis, resulting in significant interference increase at the FS node.

We further note that reducing either of the two thresholds results in a similar level of improvement in SINR for the 5G downlink which is given in (27). Fig. 19 displays a CDF of the downlink SINRs with no interference mitigation and three different Φ_{off} and Φ_{str} settings. The figure shows that reduction of either Φ_{off} or Φ_{str} improves the SINRs since both of these thresholds about equally reduce the beam exclusion zone at each AP. This is also evident in Figs. 20b and 20c, where the sizes of the exclusion zones (areas with red dots) are roughly equal after reduction. As a consequence, it is much more efficient to adjust Φ_{off} for controlling the size of

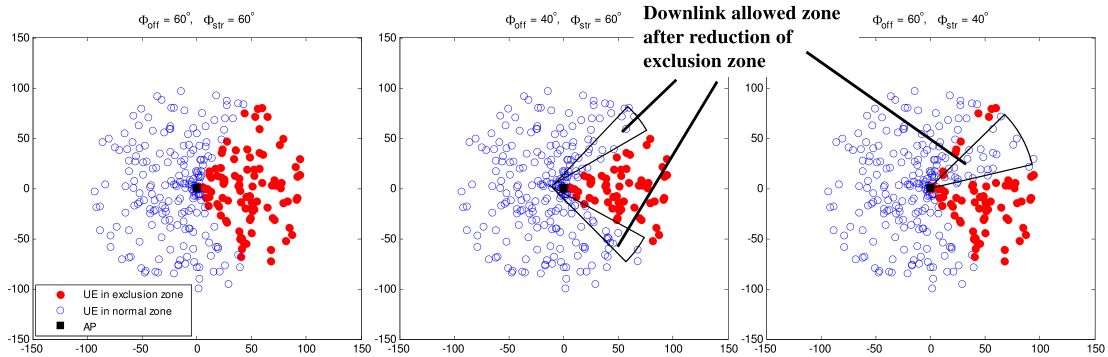

(a) $\Phi_{off} = 60°, \Phi_{str} = 60°$ (b) $\Phi_{off} = 40°, \Phi_{str} = 60°$ (c) $\Phi_{off} = 60°, \Phi_{str} = 40°$

Fig. 20. Example of reduction of the thresholds, Φ_{off} and Φ_{str}.

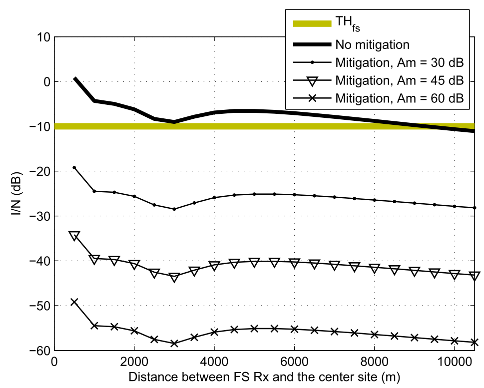

Fig. 21. Mitigation of UE-to-FS interference.

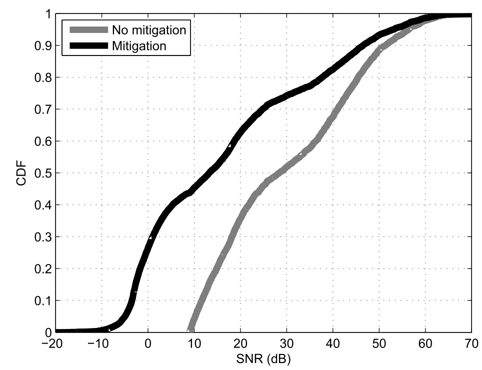

Fig. 22. Impact of UE-to-FS interference mitigation on the 5G uplink SNR.

the exclusion zone, while keeping Φ_{str} fixed, since adjusting Φ_{off} yields a similar level of downlink SINR improvement but without increasing the AP-to-FS interference.

C. UE-to-FS Interference Mitigation

Fig. 21 evaluates the UE-to-FS interference with application of the proposed mitigation technique. Similar to the trend observed in Fig. 16, the change in residual interference level observed at the FS node roughly follows the change in the UEs' antenna front-to-back ratio, A_m. We again conclude that the proposed mitigation technique on the UE side is effective in suppression of the beams pointed directly at the FS node, as it is observed that the residual interference becomes a function of the energy received from the back side of a UE's antenna.

Fig. 22 presents the impact of the UE-to-FS interference mitigation technique on the uplink 5G system performance. Maximum degradation observed with this mitigation technique is approximately 15 dB, which is due to forcing the interfering UEs to re-attach to a sector that provides a sub-optimum uplink signal strength.

D. Discussion on Performance of 5G

In general, 5G systems will be expected to provide a high degree of coverage and reliability even in the most severe propagation environments. In [20], typical values of SINR for uplink and downlink at mmW frequencies are displayed. According to the results in [20], SINRs as low as -10 dB could be observed at these frequencies in challenging propagation conditions, and 5G systems are expected to remain fully operational even in these very low SINR conditions.

From Figs. 19 and 22, one can see that the "worst-case" downlink SINR and uplink SNR of a 5G system adopting the proposed interference mitigation techniques are also in the range of -10 dB. Thus, we conclude that despite some degradation in both downlink and uplink due to incumbent interference mitigation, the performance of a 5G system will remain acceptable.

VI. Conclusion

This paper performed a detailed analysis of coexistence scenarios for 5G in mmW bands, namely co-channel coexistence of 5G with FSS uplink at 28 GHz and with FS WB at 70 GHz. The first part of our 28 GHz study discussed the AP-to-SS and UE-to-SS interference. We showed that 5G can satisfy interference protection criteria of the FSS while allowing simultaneous transmissions from at least several thousands of sectors and tens of thousands of UEs under various LoS and NLoS channel conditions and with various sets of parameters for the FSS. In the analysis of ES-to-AP interference, we characterized the separation distances in order to guarantee that higher than 95% of uplink transmissions in the nearest cell are protected. The required separation distances are not overly restrictive for deployment of 5G systems, and our results further validate that the 28 GHz band is viable for future 5G system deployments. In the 70 GHz study, we demonstrated that the 5G-to-FS interference is more significant than the FS-to-5G interference, due to aggregation of interference among all of the sectors. Motivated by this observation, we proposed the mechanisms that mitigate the interference from APs and UEs into the FS system. Our results showed that the proposed techniques can effectively suppress the interference at the FS receiver while maintaining operable performance of 5G.

REFERENCES

[1] Z. Pi and F. Khan, "An introduction to millimeter-wave mobile broadband systems," *IEEE Commun. Mag.*, vol. 49, no. 6, pp. 101–107, Jun. 2011.

[2] C. T. Neil, M. Shafi, P. J. Smith, and P. A. Dmochowski, "On the impact of antenna topologies for massive MIMO systems," in *Proc. IEEE ICC*, Jun. 2015, pp. 2030–2035.

[3] C. T. Neil, M. Shafi, P. J. Smith, and P. A. Dmochowski, "Deployment issues for massive MIMO systems," in *Proc. IEEE ICC*, Jun. 2015, pp. 1298–1303.

[4] *Report and Order and Second Further Notice of Proposed Rulemaking, in the Matter of Amendment of the Commission's Rules With Regard to Commercial Operations in the 3550–3650 MHz Band*, document GN Docket 12-354, FCC, Washington, DC, USA, Apr. 2015.

[5] *Report and Order and Second Further Notice of Proposed Rulemaking, Use of Spectrum Bands Above 24 GHz for Mobile Radio Services*, document GN Docket 14–177, FCC, Washington, DC, USA, Jul. 2016.

[6] *Resolution COM6/20: Studies on Frequencyrelated Matters for International Mobile Telecommunications Identification Including Possible Additional Allocations to the Mobile Services on a Primary Basis in Portion(s) of the Frequency Range Between 24.25 and 86 GHz for the Future Development of International Mobile Telecommunications for 2020 and Beyond*, World Radiocommunication Conference (WRC15), Geneva, Switzerland, 2015.

[7] A. Khawar, A. Abdelhadi, and T. C. Clancy, "A mathematical analysis of cellular interference on the performance of S-band military radar systems," in *Proc. Wireless Telecommun. Symp. (WTS)*, Apr. 2014, pp. 1–8.

[8] Y. Noam and A. J. Goldsmith, "Blind null-space learning for MIMO underlay cognitive radio with primary user interference adaptation," *IEEE Trans. Wireless Commun.*, vol. 12, no. 4, pp. 1722–1734, Apr. 2013.

[9] K. W. Sung, M. Tercero, and J. Zander, "Aggregate interference in secondary access with interference protection," *IEEE Commun. Lett.*, vol. 15, no. 6, pp. 629–631, Jun. 2011.

[10] P. A. Dmochowski, P. J. Smith, M. Shafi, J. G. Andrews, and R. Mehta, "Interference models for heterogenous sources," in *Proc. IEEE ICC*, Jun. 2012, pp. 4049–4054.

[11] M. Ghorbanzadeh, E. Visotsky, P. Moorut, W. Yang, and C. Clancy, "Radar inband and out-of-band interference into LTE macro and small cell uplinks in the 3.5 GHz band," in *Proc. IEEE WCNC*, Mar. 2015, pp. 1829–1834.

[12] J. H. Reed *et al.*, "On the co-existence of TD-LTE and radar over 3.5 GHz band: An experimental study," *IEEE Wireless Commun. Lett.*, vol. 5, no. 4, pp. 368–371, Aug. 2016.

[13] M. Tercero, K. W. Sung, and J. Zander, "Impact of aggregate interference on meteorological radar from secondary users," in *Proc. IEEE WCNC*, Mar. 2011, pp. 2167–2172.

[14] F. Hessar and S. Roy, "Spectrum sharing between a surveillance radar and secondary Wi-Fi networks," *IEEE Trans. Aerosp. Electron. Syst.*, vol. 52, no. 3, pp. 1434–1448, Jun. 2016.

[15] E. Obregon, K. W. Sung, and J. Zander, "On the sharing opportunities for ultra-dense networks in the radar bands," in *Proc. IEEE DYSPAN*, Apr. 2014, pp. 215–223.

[16] E. Obregon, K. W. Sung, and J. Zander, "Exploiting temporal secondary access opportunities in radar spectrum," *Wireless Pers. Commun.*, vol. 72, no. 3, pp. 1663–1674, Mar. 2013.

[17] S. Kim, J. Choi, and C. Dietrich, "PSUN: An OFDM-pulsed radar coexistence technique with application to 3.5 GHz LTE," *Hindawi Mobile Inf. Syst.*, vol. 2016, 2016, Art. no. 7480460.

[18] S.-S. Raymond, A. Abubakari, and H.-S. Jo, "Coexistence of power-controlled cellular networks with rotating radar," *IEEE J. Sel. Areas Commun.*, vol. 34., no. 10, pp. 2605–2616, Oct. 2016.

[19] A. Lackpour, M. Luddy, and J. Winters, "Overview of interference mitigation techniques between WiMAX networks and ground based radar," in *Proc. IEEE WOCC*, Apr. 2011, pp. 1–5.

[20] M. Akdeniz *et al.*, "Millimeter wave channel modeling and cellular capacity evaluation," *IEEE J. Sel. Areas Commun.*, vol. 32, no. 6, pp. 1164–1179, Jun. 2014.

[21] F. Guidolin and M. Nekovee, "Investigating spectrum sharing between 5G millimeter wave networks and fixed satellite systems," in *Proc. IEEE Globecom*, Dec. 2015, pp. 1–7.

[22] G. R. MacCartney, Jr., and T. S. Rappaport, "73 GHz millimeter wave propagation measurements for outdoor urban mobile and backhaul communications in New York City," in *Proc. IEEE ICC*, Jun. 2014, pp. 4862–4867.

[23] O. Holland and M. Dohler, "Geolocation-based architecture for heterogeneous spectrum usage in 5G," in *Proc. IEEE Globecom*, Dec. 2015, pp. 1–6.

[24] D. A. Wassie, G. Berardinelli, F. M. L. Tavares, T. B. Sorensen, and P. Mogensen, "Experimental verification of interference mitigation techniques for 5G small cells," in *Proc. IEEE VTC Spring*, May 2015, pp. 1–5.

[25] T. K. Vu, M. Bennis, S. Samarakoon, M. Debbah, and M. Latva-Aho, "Joint in-band backhauling and interference mitigation in 5G heterogeneous networks," in *Proc. IEEE Eur. Wireless*, May 2016, pp. 1–6.

[26] G. Li, T. Irnich, and C. Shi, "Coordination context-based spectrum sharing for 5G millimeter-wave networks," in *Proc. IEEE CROWNCOM*, Jun. 2014, pp. 32–38.

[27] D. Stoyan *et al.*, *Stochastic Geometry and its Applications*, vol. 2. Chichester, U.K.: Wiley, 1995.

[28] *International Telecommunications Union*, document ITU-R P.525, Dec. 2016.

[29] Verizon, AT&T, Nokia, Ericsson, Samsung, and T-Mobile, "Letter to Federal Communications Commission on GN Docket No. 14-177 and IB Docket No. 15-256," Tech. Rep., May 2016.

[30] H. Anderson, *Fixed Broadband Wireless System Design*. Hoboken, NJ, USA: Wiley, 2003.

[31] *International Telecommunications Union*, document ITU-R S.1432, Apr. 2016.

[32] *International Telecommunications Union*, document ITU-R M.2030, 2003.

[33] [Online]. Available: http://www.vcomm-eng.com/wp-content/uploads/2014/01/12-35704-18-2013Verizon7022285928.pdf

[34] *Antenna Performance Standards*, document 47 CFR 25.209, FCC, Washington, DC, USA, 2010. [Online]. Available: https://www.gpo.gov/fdsys/granule/CFR-2010-title47-vol2/CFR-2010-title47-vol2-sec25-209

[35] *Channel Model for Frequency Spectrum Above 6 GHz (Release 14)*, document TR 38.900, v1.0.0, 3GPP, Jun. 2016.

[36] *International Telecommunications Union*, document ITU-R F.699-7, Dec. 2010.

[37] *Further Advancements for E-UTRA Physical Layer Aspects*, document TR 36.814 (Release 9), 3GPP, Sophia-Antipolis, France, 2010.

[38] *International Telecommunications Union*, document ITU-R F.758-6, Sep. 2015.

Seungmo Kim received the B.S. and M.S. degrees in electrical communications engineering from the Korea Advanced Institute of Science and Technology, Daejeon, South Korea, in 2006 and 2008, respectively. He is currently pursuing the Ph.D. degree with the Bradley Department of Electrical and Computer Engineering, Virginia Polytechnic Institute and State University, Blacksburg, VA, USA. His current research interests include the coexistence of heterogeneous wireless systems and efficient communications protocols for Internet of Things applications. He was a recipient of the Best Paper Award at the IEEE WCNC 2016 International Workshop on Smart Spectrum.

Eugene Visotsky (M'12) received the B.S., M.S., and Ph.D. degrees from the University of Illinois at Urbana–Champaign, in 1996, 1998, and 2000, respectively, all in electrical engineering. In 2000, he joined the Communication Systems Research Laboratory, Motorola Labs, Schaumburg, IL, USA. Since 2011, he has been with Nokia Bell Labs, where is involved in advanced signal processing techniques for spread spectrum communication systems, link adaptation, multicarrier modulation techniques, and multihop protocols applied in cellular systems. He has authored or co-authored a number of issued and pending U.S. patents. His current research interests include advanced inter-cell interference coordination, cooperative transmission algorithms, 3D MIMO techniques, and 5G coexistence issues.

Prakash Moorut received the M.S.E.E. degree from École Supérieure d'Electricité, Paris, France. He is currently the North America Spectrum Lead with Nokia Bell Labs, where he is involved in regulators, operators, and industry members to open more useable commercial spectrum in North America. Prior joining Nokia Bell Labs, he was with Motorola, where he created and led a Customer Facing Spectrum Engineering Group, in USA, France, and China. He has over 19 years of experience in Europe and USA on numerous wireless communications system, including GSM, CDMA, UMTS, TETRA/Public Safety, WiMAX, LTE, LTE-Advanced, and is currently enabling Small Cells, 5G technologies, and Spectrum Sharing. He also has extensive experience in spectrum regulation and strategy, standardization, spectrum coexistence analysis/simulations and developing efficient spectrum usage solutions for products and operators worldwide. He has earned industry recognition and is regularly invited to speak at various FCC workshops and other venues about spectrum management. He holds several publications and patents related to spectrum usage.

Kamil Bechta received the M.Sc. degree in electronics engineering from the Military University of Technology, Warsaw, Poland, in 2010. He was a Research Assistant with the Military University of Technology and in 2011 he joined Nokia Siemens Networks as a 3GPP RAN4 Standardization Specialist, where he was involved in the RF and RRM requirements of HSPA and LTE. Since 2015, he has been a 5G Senior Radio Research Engineer with Nokia Bell Labs, he has been leading the team and responsible for spectrum and co-existence studies for 5G. Since 2017, he has been a Senior System Engineer, where he was involved in the development of advanced baseband platforms in Nokia.

Amitava Ghosh (F'15) received the Ph.D. degree in electrical engineering from Southern Methodist University, Dallas, TX, USA. He joined Motorola, in 1990, after his Ph.D. Since joining Motorola, he was involved in multiple wireless technologies from IS-95, cdma-2000, 1xEV-DV/1XTREME, 1xEV-DO, UMTS, HSPA, 802.16e/WiMAX, and 3GPP LTE. He is currently a Nokia Fellow and the Head of Small Cell Research with the Nokia Bell Labs. He is currently involved in 3GPP LTE-Advanced and 5G technologies. He has co-authored a book *Essentials of LTE and LTE-A*. He holds 60 issued patents, has written multiple book chapters, and has authored numerous external and internal technical papers. His research interests are in the area of digital communications, signal processing, and wireless communications. He was a recipient of the 2016 IEEE Stephen O. Rice Prize.

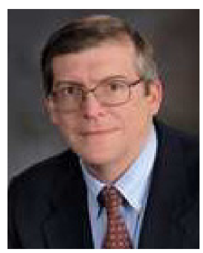

Carl Dietrich (SM'13) received the B.S. degree in electrical engineering from Texas A&M University, College Station, TX, USA, and the Ph.D. and M.S. degrees from the Bradley Department of Electrical and Computer Engineering, Virginia Polytechnic Institute and State University, Blacksburg, VA, USA. He is also a Licensed Professional Engineer in Virginia. His current research interests include spectrum sharing, cognitive radio, software defined radio, multi-antenna systems, and radio wave propagation. He has chaired the Wireless Innovation Forums Educational Special Interest Group, and is a member of the IEEE Eta Kappa Nu and ASEE.